Magnetotelluric Studies of the Zambezi Valley Mobile Belt, Northern Zimbabwe

David Bailey

A thesis submitted in fulfilment of the requirements
for the degree of Doctor of Philosophy
to the
University of Edinburgh
1998

Abstract

The Mana Pools and Lower Zambezi Karoo sedimentary basins lie within the Zambezi mobile belt in northern Zimbabwe. The subsurface apparent resistivities measured at both locations are extremely low. This thesis models the resistivity structure of these two basins and the underlying material. New and pre-existing magnetotelluric data and the available seismic reflection data are used to determine the basin structure and the depth to the electrical basement.

Long period magnetotelluric data were collected at 5 stations along a 60 km profile running north-south across the Mana Pools basin and onto the escarpment to the south. These data are used to augment an existing audiofrequency dataset from the same area. After processing of both datasets the estimated impedance tensor is decomposed, showing that the resistivity structure of the Mana Pools basin can be modelled two-dimensionally. Minimum structure models for the Mana Pools and Lower Zambezi basins are produced and compared, the latter obtained from a pre-existing magnetotelluric dataset. There are significant differences between the structure of the two basins. The major conductive feature in the Mana Pools basin is contained within the Upper Karoo sedimentary layer and does not extend into the basement below, which is, however, of an extremely low resistivity for basement rock. The electrical basement in the Lower Zambezi basin is not detected. A good conductor is again found in the Upper Karoo sediments but extends to below 11.6 km, within the gneissic rocks of the seismic basement. The resistivity structure of the Mana Pools basin is well modelled as a series of resistive layers whose boundaries are defined by the seismic data. However, the resistivity structure of the Lower Zambezi basin cannot be matched easily to the seismic structure; additional structure with no seismic expression is required.

The resistivity structure of the Mana Pools basin supports its previous description as a half graben basin of approximately 7 km depth. The resistivity and seismic structure of the Lower Zambezi basin are markedly different; however, both the MT and seismic data are not in disagreement with the prior suggestion that it is a pull-apart basin. The conductive feature in the two basins exploits the Upper Karoo sandstone layer, but extends below the seismic basement beneath the lower Zambezi basin. This indicates that they may represent different types of feature in the two basins. A resistive unit is present within the sediments in the Lower Zambezi basin which may represent intercalated basalt dykes which give an anisotropic MT response. The presence of thin basalt layers within the sedimentary layering of the Mana Pools basin cannot be rejected but is not indicated by the data. The low resistivity of the basement, particularly beneath the Lower Zambezi basin, is remarkable and may result from a high degree of either chemical or tectonic alteration to the underlying rocks due to metamorphic processes and tectonic disruption during rift formation. The presence of the Lower Zambezi basin conductor at depths greater than the seismic basement is consistent with observations to the west, in the adjacent Damara mobile belt, where similar conductors have been seen in regions with no sedimentary cover. The conductor in the Mana Pools basin is quite different to those elsewhere in the orogenic belt in that it is a feature purely of the sedimentary fill; the resistivity of the basement is low but no localised conductor is observed. The reason for the differences in the resistivity structure of the two basins cannot be definitely ascertained from the data available but it is possible that they arise from the contrast in their modes of formation.

Acknowledgements

I would first like to thank my supervisor Prof. Kathy Whaler for four years of help and assistance and for her careful and patient reading of the drafts of this thesis. My thanks also to NERC for funding this project and paying for a costly field campaign in Zimbabwe. I would also like to thank Dr. Andreas Junge for giving me my first fieldwork experience, allowing me to use his software and for his continued patience in answering my questions. Many other people also helped me to gain fieldwork experience before going to Zimbabwe and I would particularly like to mention Dr. O. Ritter, G. Dawes and Dr. D. Nascimento all of whom took me on their field experiments and from whom I learnt a lot.

I owe a large debt to the many people who helped me prepare for, and during, the field campaign in Zimbabwe. In Edinburgh the members of the NERC geophysical equipment pool, M. Valiant, P. Kearney and J. Stevenson who prepared the equipment and stopped me from forgetting anything. Special thanks go to Alf Ball for teaching me how to use the logging units and software and for donating his technical expertise and muscle power to the fieldwork itself. Without Alf's help the amount of data collected in Zimbabwe would have been a mere fraction. I would also like to thank Alex Jackson for his help in preparing a backup set of electrodes. In Zimbabwe, thanks go to Dr. Oswald Gwavava for the time he spent doing paperwork and for his diplomatic skills which greatly eased the passage of the equipment through customs, allowing the fieldwork to start on time. Oswald also assisted me in the field with Dr. T. Zengeni and Samson Takaedza and I thank all of them for their help. Particular thanks go to Samson for his hard work and for being a good humoured friend through a long hot two months. I am also grateful to the University of Zimbabwe for the loan of numerous small items during the fieldwork and also their Landrover. I thank Dr. G. Schwarz who provided me with a set of electrodes and managed to get them insured when it looked unlikely that I could. The staff of Mana Pools national park were extremely helpful and provided us with storage space for our equipment and access to an electricity generator. Thanks also to the Zimbabwean department of national parks and wildlife management who were kind enough to grant us the permit to work in the national park and to the British Council who contributed financially to the work and lent us their Landrover. I also thank everyone at the University of Zimbabwe and their families for making me feel welcome in Harare and making my stay there more pleasurable. The Zimbabwe geological survey made the MT data from the Lower Zambezi basin available to me and I thank Keith Fisk at the ministry of mines from whom I obtained copies of the seismic sections of the Zambezi valley basins.

In Edinburgh my gratitude goes to the members of the MT group, past and present, for their advice and many interesting discussions. My thanks to those already mentioned and to Dr. R. Banks, Dr. B. Hobbs, Dr. R. Hutton, Dr. M Ingham, Dr. A Wilson, Dr. K. Macdonald, Dr. T. Volti, Dr. P. Ritter, Dr. R. Holme,

G. Balasis, S. Tauber and A. Vickery. I also thank Dr. Alan Jones for his very useful MTnet web page from which I obtained much of the software that I have used, and those contributers to it who have made their software freely available to students like myself in the MT community. Dr. R. Holme must also be mentioned for being good at maths, approachable and willing to spend time on thickies like me. The support of my fellow research students has also been greatly appreciated and I thank everyone for their assistance and for their knowledge of spodery which they have kindly shared with me. I am grateful to the departmental computing officers, Dr. I. Chisholm, S. Voss and J. MacNeil for their abundant help and keeping the geology department online all year round. I also thank Dr. Max Meju for his enthusiasm, without which I probably would never have applied for this project. Lastly but by no means least I would like to thank my parents for their patience in reading early drafts of this thesis and for their unfailing love and support over the past 7 years.

Contents

List of Tables

List of Figures

Chapter 1

Introduction

The work in this thesis adds to a body of work studying the resistivity structure of the southern African crust. The African continent has been largely divided into stable cratonic blocks and mobile belts during its tectonic history. This differentiation dates back to the end of the Archean period but the mobile belts have a long and complex history of movement stretching to the end of the Pan-African orogeny, approximately 600 Ma ago. Subsequent rifting of the African continent between the late Permian and the early Tertiary led to the formation of a number of Karoo basins within the mobile belt terranes. DC resistivity soundings (eg. Van Zijl, 1977) taken in a variety of different tectonic settings indicate that there are a number of distinct resistivity layers which are continuous across large parts of the southern African continent. One of these layers is very conductive and has been observed as a thin region at depths of approximately 40 km in cratonic blocks. It is also observed to be developed more strongly in mobile belt regions where its upper surface is detected at shallower depths. Geomagnetic depth sounding (GDS) surveys (De Beer *et al.*, 1976, 1982a) have detected this conductor as a continuous feature running from the Atlantic coast in Namibia and exploiting the Damara mobile belt to run across Botswana and connect with the Zambezi belt in the east. Studies of this feature, the southwest African conductor, have concentrated mainly on the Damara belt where the conductor's position has been mapped in more detail. Resistivity soundings (eg. De Beer *et al.*, 1982a) tend to favour an association between the conductor and the Pre-Damara basement, although the conductor is detected at only 3 km depth within the mobile belt (Van Zijl and De Beer, 1983; De Beer *et al.*, 1982a). While the position of the conductor has been mapped in some detail, its origin remains a mystery. Several hypotheses exist using high heat-flows, saline-water filled fractures and serpentinised ultramafic material to explain it. These hypotheses cannot be separated due to the overlap in their physical properties. Other relevant information to discriminate between them, such as heat flow measurements, is lacking.

Until recently, the possible extension of the southwest African conductor into the Zambezi mobile belt had not been investigated by geophysical techniques. The tectonic development of this area has largely been controlled by movement along two major crustal shear zones, the Mwembeshi shear zone and the Mzarabani fault. These are believed to be responsible (Orpen *et al.*, 1989) for the formation of three Karoo age (Lambiase, 1989) basins, the Mid Zambezi, Lower Zambezi and Mana Pools basins within the Zambezi mobile belt. The Lower Zambezi basin and Mid Zambezi basin lie in two different rift zones, the Lower Zambezi rift and the Mid Zambezi rift, and the Mana pools basin lies at their

junction. The Mana Pools basin has only lately been defined and was first discussed by Orpen *et al.* (1989); we have therefore, until recently, known little about it. A seismic survey (Hiller and Buttkus, 1996) by Mobil has helped to delineate the structure of the basins. The Mid Zambezi basin is a half graben with a depocentre at its northern boundary. The Lower Zambezi basin is not a graben; Orpen *et al.* (1989) suggest it to be a pull-apart basin. The Mana Pools basin is also a half graben but with a warped basement creating a second, shallower depocentre adjacent to its southern boundary. The main depocentre is offset to the north against the basin's faulted margin.

While the structural styles of the basins have recently been determined by the seismic studies their resistivity structure is not well understood. The Lower Zambezi basin was investigated using magnetotelluric (MT) methods by Losecke *et al.* (1988). This study revealed a three layer resistivity structure with a resistive layer being sandwiched by a good conductor above and a very good conductor below. The data from an audiofrequency-magnetotelluric (AMT) survey of the Mana Pools basin (Whaler and Zengeni, 1993) were modelled one-dimensionally and a three layer basin structure was also suggested, similar to that in the Lower Zambezi basin with a very good conductor at depth. Attempts to correlate this layering and data from potential field surveys (Bosum and Geipel, 1988; Zhou, 1988) has left the question of the depth to basement in each basin very confused. The recent seismic data solve this problem but prompt the need for a re-assessment of the resistivity structure of both basins. In particular it is not clear what the relation between the conductive features in each basin and the basement interface is. It is also not clear whether the structures interpreted from the seismic and MT data are consistent: for the Lower Zambezi basin there seem to be features in Losecke *et al.*'s MT model that do not appear in the seismic structure. The attempts to interpret the layering in the two basins jointly have not been able to show whether the conductive features are related and, if so, how. Just as the relationship of the conductive features in the two basins is uncertain, their possible link, if any, to the southwest African conductor in the west is also unknown.

This thesis aims to answer some of these difficult questions, particularly addressing the problems of interpreting the resistive layering within the two basins. The relationship of the conductive features to the basement interface is examined and a comparison between the MT and seismic models is made to both test their compatibility and aid the interpretation of the resistivity sections. A field survey is documented in which new long period magnetotelluric (LMT) data were collected for the Mana Pools basin. This dataset augments the existing AMT dataset of Whaler and Zengeni (1993) revealing the basement, previously at the penetration limit of the AMT data. Local distortions are removed from the impedance estimates and the combined dataset modelled using a 2-D minimum structure algorithm (Smith and Booker, 1991). The resulting model is the first two-dimensional model of the resistivity structure of the basin and agrees with the structural features of the Mobil seismic data (Hiller and Buttkus, 1996). The resistivity model shows the Mana Pools basin to be a half graben with a northerly dipping basement and a depocentre of approximately 7 km adjacent to the northern boundary fault. The basement has an extremely low resistivity of 20-30 Ωm and may have been tectonically altered. The MT data for the Lower Zambezi basin are also modelled using a two-dimensional minimum structure inverse technique and the results are found to be in broad agreement with those of Losecke *et al.* (1988).

The resistivity models for each basin are used to fix the layer resistivities in an MT forward modelling study of the seismic structure which tests whether the models from these two methods are compatible. There is agreement between the two models for the Mana Pools basin and the conductor is shown to

be a feature of the sedimentary layering. The Lower Zambezi basin is more complex and the resistivity model is difficult to reconcile with the seismic data. The difficulty found in simultaneously modelling the E- and H-polarisation data, it is suggested, indicates anisotropy within the Upper Karoo layer. This might be due to basalt dykes within the sedimentary fill, which are not present in the Mana Pools basin. The Lower Zambezi conductor lies mainly within the seismic basement. The position of the conductive feature in the Mana Pools basin is different from that in the Lower Zambezi basin and in the Damara belt to the west where the southwest African conductor is also seen within the basement. A second conductor may exist beneath the Mana Pools basin but the data in the appropriate frequency range are shown to be downward biased by the results of a ρ^+ (Parker and Booker, 1996) study of the H-polarisation data. It remains uncertain whether there is a connection between the conductor seen in the Mana Pools basin and that within the Lower Zambezi basin and whether either are related to the southwest African anomaly which exploits the Damara belt. A study of the Chewore Inlier which separates these two basins would greatly help to answer this question.

An outline of what is known of the geological history of the southern African mobile belts and from geophysical studies of them is given in chapter 2. The discovery of the southwest African conductor in the Damara orogen is discussed and its connection to the Zambezi belt in the east. The tectonic origins of the Mana Pools and Lower Zambezi basins are outlined and their exploration, using electrical and electromagnetic methods, to search for a continuation of the southwest African conductor, is reviewed. Chapter 3 gives a brief outline of the theory behind the MT method with a description of the field survey and data processing in chapter 4. Chapter 4 gives a first assessment of the data using a simple Swift (1967) rotation technique on the assumption that the basin structure is two-dimensional. This assumption is largely supported by the appearance of the data and the calculated skew values. A full study of the impedance tensors for both the AMT and LMT datasets is given in chapter 5. The tensors are first assessed for the degree of structure they contain using a Mohr circle technique (Lilley, 1993a,b) and the Bahr distortion class method (Bahr, 1991). The majority of the data are found to be two-dimensional, with varying degrees of local distortion, and justify a decomposition of the impedance tensor using the Groom and Bailey (1989) technique. An approximately east-west strike direction was found for a large majority of the impedance tensors and the data were rotated to this coordinate system prior to modelling in chapter 6. The modelling shows the resistivity structure of the basin to be in agreement with the structure revealed by the Mobil seismic data (Hiller and Buttkus, 1996). The LMT data show that the basement resistivity is extremely low, 20-30 Ωm, but no zone of localised low resistivity is found such as is observed beneath the Lower Zambezi basin (Losecke *et al.*, 1988) or in the Damara belt (De Beer *et al.*, 1976, 1982a). The BGR data (Losecke *et al.*, 1988) from the Lower Zambezi basin are modelled in chapter 7 using a two-dimensional minimum structure inverse technique. The resistivity models from both basins are used to fix the resistivity of the layers revealed by the seismic data. The resulting resistivity sections are forward modelled to generate MT responses and assess the compatibility of the models obtained from the two techniques, and to aid the interpretation of the resistivity structure. This work helps clarify the relationship of the conductors within each basin to the basement position and shows the Mana Pools conductor to be a sedimentary feature while the Lower Zambezi conductor lies within the basement. The conclusions from this thesis are summarised in chapter 8 and suggestions for useful further work are made.

Chapter 2

The Mobile Belts of Southern Africa

2.1 Introduction

This chapter reviews the geological history of southern Africa's mobile belts and the Karoo basins that lie within them. The southwest African conductor in Botswana, Namibia and Zimbabwe is discussed and the exploration of both Namibia's Damara orogenic belt and the basins of the Zambezi mobile belt. The exploration of these areas with a variety of geophysical techniques has revealed similarities, particularly in electrical structure, between them. This has led to the desire for a coherent interpretation of the conductive structures seen and for some link to connect the Damara and Zambezi mobile belts. Finding a joint interpretation for the anomalies seen in the Zambezi valley basins and reconciling these with the results from the Damara orogenic belt to the west has proved difficult. This has illustrated the need to step back from this goal to find a firmer starting point from which to achieve it. This starting point is sought through a detailed study of the results from different geophysical techniques employed in the Mana Pools basin and the derivation of a combined model for its structure.

2.2 The Pre-Karoo Geology of Southern Africa

The ensuing outline of the geology and tectonics of southern Africa is taken largely from the PhD thesis of Barber (1994) and the work of Orpen *et al.* (1989). Thickening of the crust of the Kaapval craton was caused by its collision with the Zimbabwe craton (Windley, 1995). The development of the Limpopo belt in this thickened crust and the formation of the main greenstone bodies completed the evolution of the Archean basement complex in Zimbabwe between 3100 and 2500 Ma. During the period following this collisional event, major cratonic-scale strike-slip deformation zones were formed. This occurred prior to or coincidentally with the emplacement of the Great Dyke at about 2461 Ma. Reactivation of the Archean shear zones occurred c.2100 Ma with associated rifting, volcanism and basin evolution. These events were followed between 2000 and 1750 Ma by the reactivation of the Limpopo belt and an episode of basin deformation which was associated with volcanism, thrusting and strike-slip faulting within the Zimbabwe craton. From 1000 to 600 Ma deposition occurred in basins situated along the

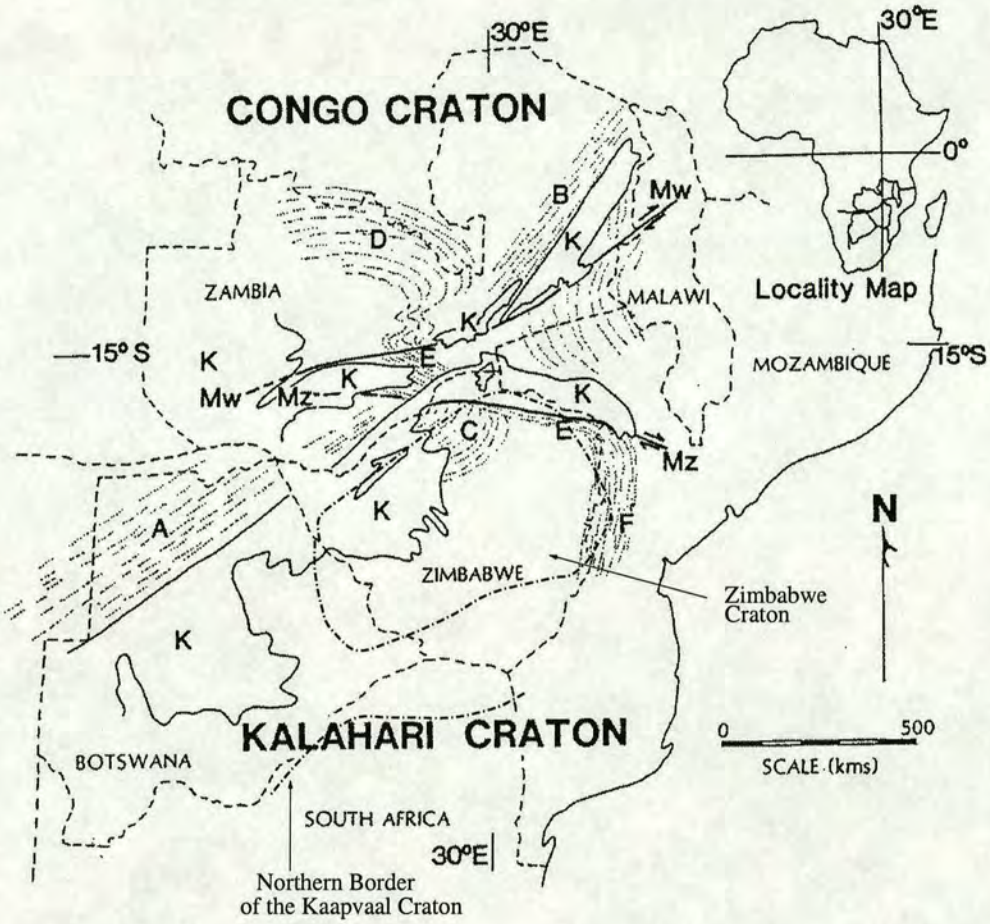

Figure 2.1. The mobile belts of Central Africa, after Orpen *et al.* (1989). The Karoo basins are marked with a K and the mobile belts are identified as A = Damaran; B = Irumide; C = Magondi; D = Lufilian Arc; E = Zambezi; F = Mozambique. The Mwembeshi shear zone (Mw) and Mzarabani fault (Mz) are also labelled. The boundaries of the Zimbabwe craton are reproduced from Ranganai (1995).

northwestern and northern margins of the Zimbabwe craton. Later the Pan-African orogeny caused the deformation of the northern margins of the shield and led to the late Proterozoic basinal sediments being thrust southwest on to the Zimbabwe craton (Orpen *et al.*, 1989) and the reworking of the marginal terranes.

The Pan-African orogeny occurred between 1100 and 600 Ma and was the last major tectonic event of the Precambrian to affect central and southern Africa (Barber, 1994). The Pan-African orogeny created a large number of mobile belts in central Africa, with numerous fold, fracture and thrust trends. Figure 2.1 shows the distribution of these mobile belts whose margins, following the final phase of convergence, are commonly defined by ductile shear zones (Barber, 1994). The Pan-African orogeny comprised two different phases. The first phase from 1100 to 667 Ma involved 285° orientated pull-apart forces and completed the structural differentiation of the continent into cratonic and mobile belt environments. This phase created the Pan-African intra-cratonic and proto-oceanic basins in south and west Africa. During this period the Lufilian belt and Zambezi belt (figure 2.1) were sites of major thrust

activity. It has been suggested (Daly, 1986; Barber, 1994) that the Mwembeshi shear zone acted as a major dextral transform for these two opposing thrust belts and allowed the separation of the Congo and Kalahari cratons. This initial phase of the orogeny was characterised by wrench movement along the Zambezi belt which runs along the north, northwest and west margins of the Zimbabwe craton. Minor north-south and NE-SW convergence were also associated with this wrenching episode. Between 667 and 600 Ma, the second phase of the orogeny occurred; this was caused by the east-west convergence of the proto-African and South America plates and caused the closure of the Pan-African basins.

The Mzarabani shear zone is a zone of NE and ENE trending anastomosing fractures with a sinistral sense of movement, attributed to extension at 110° (Barber, 1994); it intersects the Zambezi mobile belt and the margins of the adjacent cratonic blocks. The southern boundary of this belt is believed to mark the site of a major thrust zone (Coward and Daly, 1984) responsible for the transportation of the Zambezi belt rocks WSW over the Zimbabwe craton during the second phase of the Pan-African orogeny. The boundary of this shear zone trends approximately east-west in northern Zimbabwe and should form a steeply dipping lateral ramp with a sinistral wrench component to accommodate this movement (Orpen *et al.*, 1989). Some authors (De Swardt *et al.*, 1965; Orpen *et al.*, 1989) argue that between 170 and 150 km of sinistral displacement were taken up across the Zambezi mobile belt during the Pan African orogeny. This movement is believed to have occurred along the Mzarabani shear zone. The Great Dyke lies adjacent to the southern boundary fault of the Lower Zambezi basin and its lack of major displacement implies that the Mzarabani shear zone must lie to the north of the present escarpment. Several dextral wrench faults do cut the northern portion of the Great Dyke with an east to NE trend but the total displacement along these faults only amounts to approximately 25 km (Barber, 1994). This faulting is believed to have occurred late in the history of the Pan-African orogeny and is probably unrelated to the major faulting discussed earlier. Figure 2.2 shows the northern portion of the Great Dyke. It is difficult to account for the amount of sinistral movement required on the Mzarabani shear zone during thrusting of the Proterozoic basinal sediments onto the Zimbabwe craton. One possibility is that a relationship exists between the Great Dyke and the layered ultramafic rocks found in the Chewore inliers (Orpen *et al.*, 1989). The Chewore complex lies approximately 130 km northwest of the northern end of the Great Dyke in the Lower Zambezi basin. Assuming that the Chewore complex originally formed a more northerly part of the Great Dyke, a sinistral displacement of at least 150 km along the Mzarabani shear zone could be deduced (Orpen *et al.*, 1989).

The east-west convergence in the eastern part of the Zimbabwe craton towards the end of the Pan-African orogeny was followed between 650 and 400 Ma by WNW to NNW directed shortening. This occurred along the northern, north-western and western margins of the craton. Daly (1986) found that the east trending portion of the Zambezi mobile belt had lineations and thrust geometries indicative of two separate directions of tectonic transport, one to the WSW and a second to the south. This resulted in the emplacement of low grade Proterozoic meta-sediments along the front of the belt and southward thrusting of folded meta-sediments over the northeastern margins of the Zimbabwe craton. During the early Ordovician, north-south extensional forces began the Cape orogeny and the development of the Cape basin in South Africa (Barber, 1994). Rift development in the Cape orogeny was controlled by pre-existing zones of weakness from earlier tectonic events and the regional subsidence was accompanied by a northerly marine transgression (Barber, 1994). The Cape basin was closed during the late

Figure 2.2. Schematic showing the possible structural correlation of the Great Dyke and the Chewore complex, after Orpen *et al.* (1989). Where C = Chewore basement inliers and K = Karoo sediments, in faulted contact with the crystalline basement along the Mzarabani fault B, also shown in figure 2.1.

Carboniferous by compressional north-south forces. This closure marked the final stages of Cape tectonism in South Africa and the last major event prior to the onset of Karoo rifting.

2.3 Karoo and Later Tectonics

The tectonic history of Africa after the late Paleozoic is dominated by rifting events. Seven major extensional tectonic events have been identified since the early Permian (Lambiase, 1989), three of which comprise the Karoo rifting events and four of which are related to the break up of Gondwanaland. Following the work of Lambiase (1989); rifting commenced in the early Permian with the first of the Karoo events. This event was restricted to just a few basins along the present-day east coast of Africa and Madagascar (Lambiase, 1989). While there was little motion of plates relative to each other during this event, the whole region was affected indicating that the breakup of southern Gondwanaland had begun (Lambiase, 1989). The second episode of Karoo rifting occurred in the late Permian/early Triassic and affected eastern and southern Africa with the formation of new basins, such as those in northern Zimbabwe (Lambiase, 1989), and the reactivation of pre-existing rifts. Extension in the late Triassic/early Jurassic in northwest Africa ultimately led to a third rift event which is not classified with the other Karoo events (Lambiase, 1989). This extension led to the separation of North America and Africa and the formation of rift basins in northwest Africa. The subsequent period, through which the southern African region of Gondwanaland was under tensional stress, led to the third Karoo event in the Early/Middle Jurassic. This event was accompanied by the onset of sea-floor spreading and the break away of southern Africa from Antarctica (Cannon *et al.*, 1981; Martin and Hartnady, 1986) and India

(Lambiase, 1989) as the proto-Indian Ocean was formed. As in other continental rifting events (Bryan, 1986) the resulting extensional fracturing of Gondwanaland was largely taken up along pre-existing Pan-African mobile belts between the cratonic blocks. This final Karoo event initiated a major change in deposition with the first wide-spread and persistent marine deposition as the sea transgressed from the north. This affected basins mainly in eastern Africa and as far south as Kenya (Lambiase, 1989).

Later rifting events in the Cretaceous and Tertiary continued the breakup of Gondwanaland. Middle Cretaceous rifting separated west Africa from South America and initiated formation of the South Atlantic Ocean (Lambiase, 1989) with reactivation of some rift structures in Central Africa (Orpen *et al.*, 1989). The greatest extension however was further north in the East African rift system where an early Tertiary rifting event was followed by development of the rift system and the evolution of the Red Sea and the Gulf of Aden during a period of middle Tertiary rifting (Lambiase, 1989).

2.4 The Southwest African Conductivity Anomaly

Geological investigation of southern Africa's rift systems has been hampered by Tertiary, and later, Kalahari sediments which cover most of Botswana and the eastern part of Namibia (De Beer *et al.*, 1976). Information has instead been gained from measurements, made at the surface, of the electrical resistivity of the underlying rocks. There is more than one technique to do this but early efforts used the geomagnetic depth sounding (GDS) method. One of the first GDS surveys was made in 1972 by De Beer *et al.* (1976) prompted by the work of Reeves (1972) on the seismicity of Botswana. Reeves concluded that the epicentres of Botswana's seismic events consisted of two distinct spatial populations, that of the Okavango Delta and that of the Central Kalahari lying either side of the Ghanzi ridge, shown in figure 2.3. De Beer *et al.* (1976) wanted to look for possible contrasts in the electrical resistivity of the crust and upper mantle associated with this seismicity in Botswana and the Swakop and Otavi regions of the Damara basin.

The GDS survey involved deployment of an array of 25 3-component magnetometers in Namibia, Botswana and northwest Zimbabwe recording between December 1971 and February 1972. A large anomaly was seen in both the northward horizontal and vertical magnetic fields in the period range from 21 to 171 minutes. Reversals in the vertical magnetic field between several pairs of adjacent sites were also seen in magnetogram plots. Analysis of these results showed a conductor trending east-west beneath the western section of the array and northeast beneath the eastern part; see figure 2.3. Although no quantitative information is obtained from GDS studies, De Beer *et al.* (1976) were able to deduce from the anomalies' induction vectors that it was a crustal structure with a maximum depth of approximately 50 km.

As can be seen from figure 2.3 the conductor extends eastwards from the eastern Damara basin in Namibia, into Botswana and then north eastwards along the southern borders of the Okavango swamp. At the eastern point of the array the conductor underlies the Mid Zambezi rift valley which is a southwestward extension of the Luangwa rift in Zambia. Reeves (1972) also found that the Kalahari seismic axis forms a southwest extension of the Luangwa rift. In eastern Botswana the conductor is in good alignment with the regional fault trends and coincides spatially with much of the known seismic activity. Based on this evidence De Beer *et al.* (1976) suggested that the conductor formed an extension of

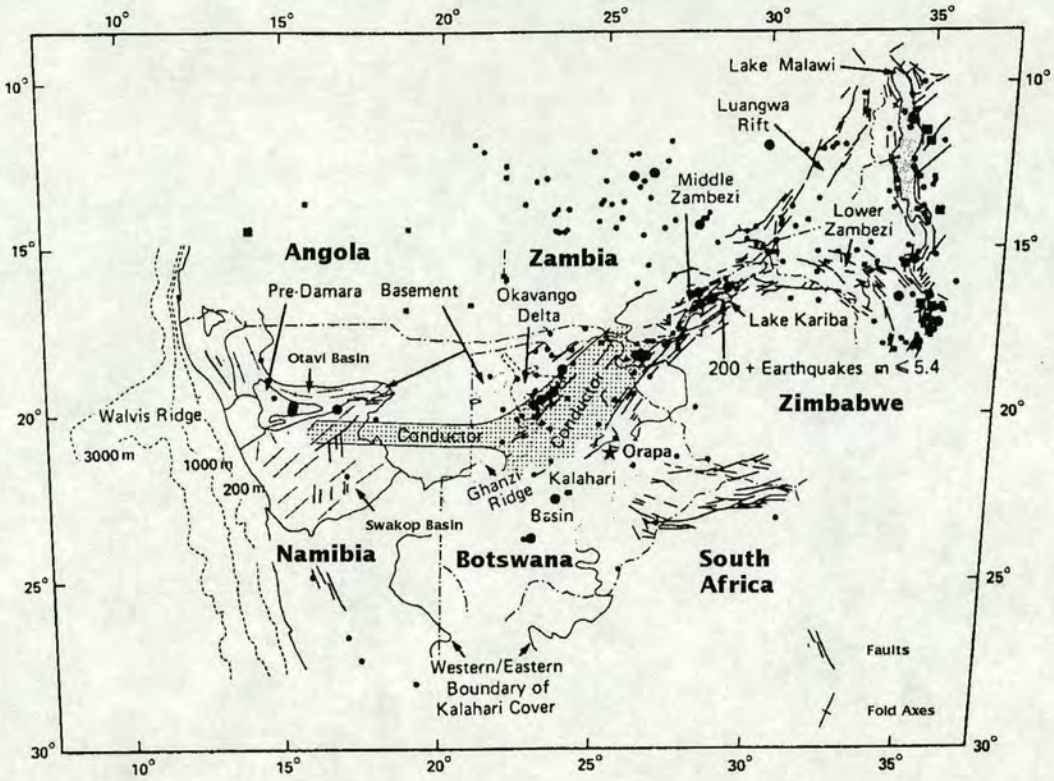

Figure 2.3. The southwest African conductor in relation to the seismicity and tectonics of southern central Africa. After De Beer *et al.* (1975). Earthquake magnitudes are indicated by small dots, $2 \leq m \leq 4$; large dots, $m > 4$. Small squares are intensities ≤ 3; large squares > 3.

the Zambezi rift system along old weak zones in the lithosphere.

While the southwest African conductor parallels the linear features of figure 2.3 within the Okavango delta, further west in Namibia it cuts obliquely across the structural trends of the Damara basin. The Damara basin lies in the Damara orogenic belt, another of the late Precambrian Pan-African mobile belts. It consists of two branches, (Martin and Porada, 1977) one running sub-parallel to the present-day Atlantic coast, the other, intra cratonic branch crosses Namibia and may be connected with the Zambezi belt (De Beer *et al.*, 1976). The desire to extend the magnetometer survey of De Beer *et al.* (1976) into the Damara belt to search for a westward continuation of the southwest African conductor led to a second magnetometer survey in 1977 (De Beer *et al.*, 1982a). Twenty seven three component magnetometers were deployed across the width of Namibia between latitudes 19 and 22° S. The aim of this second survey was to find the hypothesised structural connection between the intra-cratonic branch of the Damara belt and the Zambezi belt in the east.

The rocks of the intra cratonic Damara sequence underlie most of the magnetometer stations; this sequence can be lithologically subdivided into two different provinces, shown on figure 2.4. The Swakop group is in the south with large volumes of both syn- and post-tectonic granitic rock (Martin and Porada, 1977) in its northern half, the Otavi group lies to the north. These two provinces meet in a transition zone approximately 40 km wide that is marked by a string of Pre-Damara basement inliers, the largest

Figure 2.4. A simplified geological map of the Damara orogen. Numbered dots mark the centre positions of Schlumberger resistivity soundings. From Van Zijl and De Beer (1983).

of which is the Kamanjab inlier marked on figure 2.4. Using data from several geomagnetic disturbances, De Beer *et al.* (1982a) delineated that the conductor extended approximately east-west from the Botswana border (21° E) to 17° E before bending southwest and continuing to the Atlantic coast. The effects of the conductor on the vertical magnetic field were seen to be very local to the structure, which De Beer *et al.* (1982a) suggested was an indication that the conductor may be narrow in a north-south direction.

The Damara orogenic belt has been investigated with deep Schlumberger resistivity soundings (Van Zijl, 1977, 1978; Van Zijl and De Beer, 1983), their locations are given on figure 2.4. Very deep Schlumberger soundings outside the region in which the GDS studies defined the conductor have detected low resistivities at greater depth. Soundings taken 10 km to the south of the GDS conductor with electrode spacings up to 200 km were interpreted as showing a conductive layer underlying a 23 km thick, 5000 Ωm layer (Van Zijl, 1977). This sounding was taken at a site that was occupied by a magnetometer and which failed to detect the conductor. The Schlumberger soundings also give quantitative estimates for the resistivity of the conductive zone and its depth. In places, the conductive structure is only 3 km below the surface and has a resistivity of below 20 Ωm (Van Zijl and De Beer, 1983). Comparable soundings taken at locations outside the conductive structure give resistivity values for the upper crust in the range 5000 Ωm to, on the Kamanjab inlier, more than 20000 Ωm (De Beer *et al.*, 1982a). The

Schlumberger results indicate that the magnetometer studies only locate the conductor at its closest to the surface. The evidence of a deeper conductor outside the GDS conductive zone, if related, could indicate that the conductor deepens towards the boundaries of the mobile belt. The depth at which the conductor is found by soundings both inside and outside the zone in which the GDS survey located it suggests that it lies within the basement below the Damara rocks. It also confirm that the conductor is a crustal structure (De Beer *et al.*, 1982a).

De Beer *et al.* (1982a) concluded that the westward continuation of the structure discovered in 1972 curves south-west rather than continuing the east-west trend of the section from the Botswana border to Otjiwarongo. As with the conductor in Botswana, the westward continuation runs along the dominant local structural trends. In Botswana the conductor parallels the structural trends of the Zambezi belt, but in Namibia it follows the trends of the Swakop group of the Damara belt paralleling the major faults in the region (Martin and Porada, 1977). Although there is no obvious connection between the lithologies of the Damara rocks and the low resistivities measured, the northern edge of the conductor appears to mark the northern boundary of Swakop Group rocks (De Beer *et al.*, 1982a). This may be coincidental, as the Schlumberger resistivity data indicate that the cause of the anomaly is probably in the Pre-Damara basement rock.

The conductor in northeast Botswana paralleled the structural trends of the Zambezi belt and correlates well spatially with the seismicity recorded there (De Beer *et al.*, 1975). These two observations are not unrelated and reflect exploitation of an older fracture zone by the current stress regime. Due to the sparsity of seismological observatories within Namibia, no correlation between seismicity and the location of the conductor is possible. The nature of the Damaran crust is however revealed by the occurrence of fourteen Post-Karoo alkaline igneous complexes along the line of the conductor (De Beer *et al.*, 1982a). These intrusive complexes represent the youngest igneous activity in the Damara belt and, as with other alkaline igneous complexes in Namibia and Angola, form north-east trending lineaments. It has been suggested that these lineaments lie along small circles around the Cretaceous pole of rotation for the opening of the South Atlantic Ocean (De Beer *et al.*, 1982a). Sykes (1978) suggested that intrusive rocks and tectonic features younger than the opening of present-day oceans were often found in old zones of weakness near the ends of major transform faults. Sykes (1978) suggested that in regions such as the Damara orogenic belt, this alkaline magmatism may have an asthenospheric source and be controlled by deep fractures penetrating the entire lithosphere. The spatial correlation between the alkaline magmatic complexes and the conductor within Namibia supports the theory of De Beer *et al.* (1975) that the conductor marks and may be exploiting an older zone of weakness in the lithosphere. That an anomaly is detected along this line of weakness implies a difference in physical properties between the crustal material inside and outside of the anomalous structure.

2.5 The Origin of the Southwest African Anomaly

The southwest African conductor, linking the Damara and Zambezi mobile belts is not unique in the distance over which it extends; a list of other such anomalies can be found in Haak and Hutton (1986). Determining the origin of these features is difficult and the anomaly in the Damara belt is no exception.

One cause of anomalously low resistivities is high heat flow; a good correlation between these two parameters has been reported by Gough (1974) for anomalies within the United States. This is unlikely to be the cause of the Damara belt anomaly. The most recent magmatic activity in the region is thought to be the alkaline igneous complexes previously discussed, which are dated at more than 120 Ma (De Beer *et al.*, 1982a). Lack of subsequent igneous activity implies that the heat flow in the area is probably too low to be responsible for the low resistivities measured. However, in the absence of appropriate measurements for the area, this explanation for the low resistivities cannot be eliminated. It is clear that the southwest African conductor is associated with an old weak zone in the lithosphere. This weakness may have originated in the formation of the Pan-African basins during the Precambrian and be both the cause of the conductive zone and the reason for its location. The Damara basin is believed to have originated in three graben systems which developed toward widely spaced aulacogens; a second stage of subsidence caused them to merge, forming the basin (De Beer *et al.*, 1982a). The formation process would involve significant faulting and crustal thinning of the high resistivity Pre-Damara basement which is believed to be similar to the rock that forms the Kamanjab inlier. The extensive faulting and fracturing could cause a decrease in electrical resistivity by virtue of the increased porosity and electrolytic conduction associated with it (Van Zijl, 1977, 1978). The high resistivity layer in the upper crust of the Kamanjab inlier measured by the Schlumberger soundings does not extend south into the Damara orogenic belt itself. This lack of continuity supports the hypothesis of tectonic alteration of the Pre-Damara rocks within the orogenic belt.

This explanation for the origin of the southwest African conductor relies on the assumption that the high resistivity Pre-Damara crust seen in the Kamanjab inlier existed beneath the Damara belt but has been tectonically altered. If this assumption is incorrect then a different explanation for the origin of the conductor is required. One possibility is that the Damara and Zambezi belts the conductor exploits mark a suture zone where a paleo-ocean has been subducted (Burke *et al.*, 1977). Slabs of oceanic lithosphere wedged between continental lithosphere would be capable of producing such an induction anomaly. Similar anomalies in other parts of the world such as the Southern Cape conductive belt have been ascribed (De Beer *et al.*, 1982b) to such suture zones and the presence of buried segments of oceanic floor. Work done by Drury and Hyndman (1979) amongst others has demonstrated that the resistivity contrast would certainly be large enough particularly if some degree of serpentinisation of the oceanic crust is allowed for (Stesky and Brace, 1973).

Van Zijl and De Beer (1983), in an excellent paper on the tectonic significance of electrical studies in the Damara belt, discuss the deep Schlumberger sounding results collected for the region. Their work brings together elements both from a serpentinite model and a model involving tectonic alteration of the Pre-Damara basement. Van Zijl and De Beer (1983) prefer a tectonic explanation for the origin of the conductor. They suggest that the moderate resistivities measured across the orogenic belt and southward beyond its borders into the Pre-Damara basement rocks indicate deformation and fracturing so intense that it affected the basement. Rejecting a high heat flow hypothesis Van Zijl and De Beer (1983) instead examined the fault patterns and the position of the conductive structure. They noticed that the faults were better aligned with the trend of the conductor at locations directly above the anomaly than they were at locations outside the conductor's geophysically defined boundaries. To date these faults Van Zijl and De Beer (1983) made a comparison of the resistivities of different units within the Damara basin. The Donkerhuk Granite (figure 2.4) is highly resistive, massive and unfractured and was

probably emplaced after deformation. The more northerly Pre-Damara Kamanjab inlier is also highly resistive but much older and because of its size probably acted as a stable crustal block experiencing a much smaller degree of deformation (Van Zijl and De Beer, 1983). Other of the Pre-Damara inliers are less resistive than the Kamanjab inlier and the faults are probably of an age intermediate between them and the Donkerhuk Granite. Their trend within the boundaries of the conductor is predominantly north-easterly. This parallels the dominant deformation trend immediately prior to the metamorphic phase resulting in the formation of the granites of the central zone of the Damara basin (Miller, 1979). The Donkerhuk granite is one of these granites and the age of this deformation event fits in with the dating required by the resistivity measurements. Van Zijl and De Beer (1983) on the basis of these observations suggested that the conductor may be associated with this phase of deformation or a metamorphic event immediately following it. There are however problems with attributing the conductor to a region of severe faulting. Most seriously, a zone of more intensive faulting corresponding to the position of the conductor is not visible and there is no evidence of low resistivities in the upper crust overlying it. If a model is suggested where the fractured zone is being exploited by saline water then this is a problem, the porosity and conductivity of such a structure should rise towards the surface. This could be overcome by invoking a model which involves a layer of fresh water in stable stratification above a layer of saline water but Van Zijl and De Beer (1983) prefer a serpentinite model instead. A serpentinite model would fit the available geophysical data and would also help to explain the relatively high magnetic intensity observed over the Central Zone of the Swakop basin (Van Zijl and De Beer, 1983). The origin of such a serpentinite anomaly could not be determined with the geological and geophysical data available. Emplacement of ophiolitic material in a suture zone by subduction or the shallow emplacement of asthenospheric material in a weak zone in the lithosphere are equally likely. The origin and availability of the large quantities of water required during serpentinisation remain a problem with this model (Van Zijl and De Beer, 1983).

While the discussions in this section have concentrated on the southwest African conductor, it is not a unique feature in Africa. A comparison of this conductor with other such features within Africa is given by Van Zijl and De Beer (1983). From electrical sounding measurements made over various tectonic provinces they proposed a 5 zone generalised geoelectrical model of the southern African lithosphere. This model contains a conductive zone 3, present within both cratonic and mobile belt areas at depths of between 25 and 40 km. The resistivity of this zone has been estimated at 50 Ωm and its longitudinal conductance (thickness-conductivity product) increases dramatically in mobile belts (Van Zijl and De Beer, 1983). Zone 3 is found to be continuous across the Limpopo mobile belt into the adjacent Zimbabwe and Kaapval cratonic nuclei (Van Zijl and De Beer, 1983). Its existence and continuity in southern Africa is widespread, as is its development in fractured mobile belt environments. The deep Schlumberger soundings on the Kamanjab inlier and north of the Donkerhuk Granite reveal a 20 Ωm conductive zone identified with zone 3 present at estimated depths of 37 and 24 km respectively. The evidence from other regions of Africa favours a connection between the conductive structure within the Damara belt and the conductive zones to the north and south (Van Zijl and De Beer, 1983). Van Zijl and De Beer (1983) suggest that the base of the conductor may represent the present-day isotherm at which serpentinite reverts back to olivine.

There are clearly many explanations for the possible origins and development of the southwest African conductor and the mobile belt which it occupies. On present geological and geophysical data it is

impossible to say how this weak zone originated or what property or material gives rise to the low resistivities measured. However, the magnetometer studies (De Beer *et al.*, 1976, 1982a) show the conductive belt to have a close association with the Damara belt in the west and the Zambezi belt in the east. This conductor provides a connection between these two Pan-African mobile belts.

2.6 The Geology of the Zambezi Valley

The preceding sections have concentrated on the study of the Damara belt. As has been seen, the southwest African conductor links the Damara belt with the Zambezi belt to the east. The main features controlling the tectonic processes in the Zambezi area are shown in figure 2.1. The Mwembeshi shear zone along which the Kalahari and Congo cratons separated dextraly during the Pan-African orogeny (Daly, 1986) runs NE-SW across the region. This shear zone bounds the Zambezi belt to the west while to the east the belt continues until it merges with the north-south trending Mozambique belt. The second major control on tectonics in the Zambezi valley is the Mzarabani shear zone which is also shown on figure 2.1 and trends east-west across the area. As was discussed in § 2.2, Daly (1986) and Coward and Daly (1984) proposed that the southern margin of the Zambezi belt is a major thrust zone. The inferred transport of Zambezi rocks southwest onto the Zimbabwe craton during the Proterozoic requires the Mzarabani shear zone to have a sinistral wrench component with a steep dip and the geometry of a lateral ramp. The lack of sinistral displacement of the northern portion of the Great Dyke implies that this shear zone either coincides with the Zambezi escarpment or lies to the north of it beneath the Karoo cover. The estimated sinistral displacement along the Mzarabani shear zone is 150km (Orpen *et al.*, 1989).

The majority of the Karoo basins in central and southern Africa appear to be grabens. Aeromagnetic and gravity data have enabled a broad analysis of the geometry of the basins in figure 2.5 to be made. The depth to magnetic basement in the basin depocentres is found to be typically greater than 6 km. The Lower Zambezi, Mana Pools and Mid Zambezi basins lie within the Zambezi valley. The Mid Zambezi basin contains Karoo rocks and lies between the stable Zambia and Zimbabwe cratons. Between Botswana and Kariba Gorge it trends NE-SW. Karoo strata continue eastwards along the Zambezi valley into Mozambique and lie within the Lower Zambezi basin. The western boundary of the Lower Zambezi basin is formed by the Chewore inliers (Orpen *et al.*, 1989). These form a horst of Precambrian rocks extending south from Zambia into the Karoo sediments of northern Zimbabwe and are shown on figure 2.5. This created a separate graben with an estimated depocentre of 5 km which was named the Mana Pools basin (Orpen *et al.*, 1989) and lies between the Chewore inliers and Kariba Gorge in the west. The rift zones occupied by these basins are defined using the nomenclature of Rosendahl *et al.* (1986). The Mid Zambezi rift zone trends NE-SW and contains the Passarge and Mid Zambezi basins and the Lower Zambezi rift zone trends east-west and contains the Lower Zambezi basin. The Mana Pools basin is situated at the junction of these two rift systems (Barber, 1994).

Looking first at the structure of the basins in the Mid Zambezi rift valley; figure 2.5 shows how the northwest margins of the Mid Zambezi rift basins and the Luangwa basin in the Luangwa rift are in a close linear alignment. Structurally however, there are differences between the Luangwa basin and those of the Mid Zambezi rift valley which are very similar. The Luangwa basin is fault bounded whereas

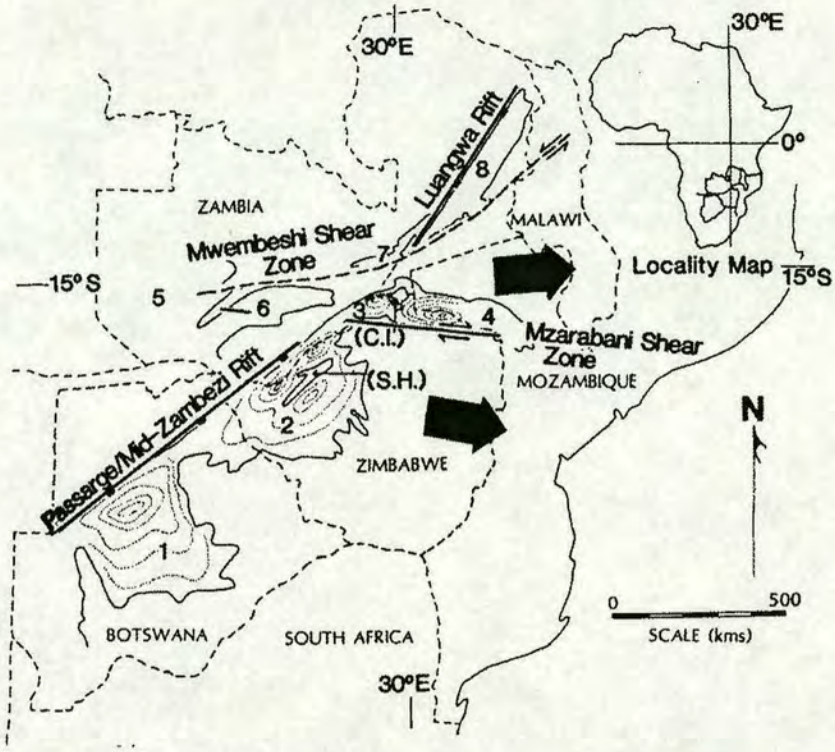

Figure 2.5. The central African Karoo sedimentary basins, after Orpen *et al.* (1989). Approximate basement contours derived from potential field methods are shown and the basins are numbered: 1, Passarge; 2, Mid Zambezi; 3, Mana Pools; 4, Lower Zambezi; 5, Western Zambian; 6, Kafue; 7, Luano 8, Luangwa. The Sijarira horst (S.H.) separates sub-basins within the Mid Zambezi basin, and the Mana Pools and Lower Zambezi basins are separated by the Chewore inlier (C.I.).

the Mid Zambezi and Passarge basins have lobate southeastern margins with a passive unconformable relationship between the sediments and the basement. The basement contours on figure 2.5 show the depocentres of both the Mid Zambezi and Passarge basins to be adjacent to their faulted northwest margins giving both an asymmetric cross-profile perpendicular to the depositional axis (Orpen *et al.*, 1989). The Mid Zambezi basin is the better exposed of the two with major internal basin faults striking sub-parallel to the northwest marginal fault, which should more accurately be termed a fault zone, with numerous en echelon northeast-southwest trending faults. Isolated basement horsts such as the Sijarira horst in figure 2.5 have developed within the basin because of this normal faulting. The southeast margin of the basin gently tilts down to the northwest, forming a hinged flank to the basin (Orpen *et al.*, 1989). The Passarge basin is obscured by the Kalahari cover and little is known of the faults controlling sedimentation within it. The similarity however in geometry between the Mid Zambezi and Passarge basins and the alignment of their northwest boundaries implies their structural similarity. This suggests that any tectonic model for one basin should apply to both.

The structure of the Lower Zambezi basin has been determined from measurements made using geophysical and geological techniques. They show it to be significantly different from the Mid Zambezi and

Passarge basins. The Lower Zambezi basin is bounded to the south by the Mzarabani fault. The major syn-sedimentary faults within the basin strike obliquely to it and downstep towards an approximately 10 km depocentre close to the southern margin. The northern margin of the basin is more complex. Satellite imagery reveals several northwest striking faults which splay off a main east-west escarpment fault (Orpen *et al.*, 1989). The Lower Zambezi basin therefore has an asymmetric cross profile like the Mid Zambezi and Passarge basins but in this case the basement slopes down to the south rather than the north. This implies that a tectonic model different to that for the Mid Zambezi rift basins is required to explain the origin of the basin in the Lower Zambezi.

To summarise, looking first at the Mid Zambezi rift basins, there are similarities between the two basins; both are bounded to the northwest by major rift escarpment faults aligned with each other and along a major plane of crustal weakness in Pan-African mobile belt terranes. Both basins have lobate southeast margins where the sediments lie unconformably on the basement. Their depocentres are adjacent to their northwest margins giving both an asymmetric cross profile with internal faults creating basement horst structures within each. The Luangwa basin to the northeast is also reasonably aligned with the Mid Zambezi rift and may lie on the same plane of weakness with a similar tectonic history as the Mid Zambezi and Passarge basins. The Luangwa basin is however fault bounded and without the same lobate southeast margin as the Mid Zambezi rift basins. The internal fault geometry of the Mid Zambezi basin has led Daly *et al.* (1987) to postulate an ESE extension regime for it, this is shown in figure 2.5. The structural features of the Mid Zambezi basin indicate a half-graben as the most likely tectonic model for its origin; this model can also be applied to the neighbouring Passarge basin. The Luangwa basin with its faulted boundaries does not fit a half-graben model and may be a full graben; for a discussion of the Luangwa basin see Rosendahl *et al.* (1986) and Daly *et al.* (1987). Stratigraphically the important features of the Mid Zambezi basin are the heavily faulted Lower Karoo sediments unconformably overlain by less disrupted Upper Karoo sediments which onlap onto the basement. The sedimentary pile is overlain by basaltic cap rocks but volcanic rocks do not appear within the sedimentary layering. Orpen *et al.* (1989) argued that the sedimentation followed by volcanism indicates a passive rifting event while the relationship of the Upper and Lower Karoo sequences and the onlap of the Upper Karoo onto the basement implies a "rift-phase" and a subsequent "sag-phase" during basin evolution. This would be compatible with the emplacement of asthenospheric material beneath the basin causing crustal thinning, followed by a period of subsidence as the lower part of the plate slowly cooled (McKenzie, 1978).

The Lower Zambezi basin is markedly different from the Mid Zambezi basin. It is bounded to the south by the Mzarabani fault which has a history of movement stretching back to the Proterozoic. Satellite imagery reveals the northern margin of the basin to also be fault bounded with a complex pattern of faults splaying off a main escarpment fault. Within the basin the main syn-sedimentary faults strike oblique to the Mzarabani fault, downstepping towards a depocentre in the southern portion of the basin and giving the basin an asymmetric cross profile. Orpen *et al.* (1989) propose that the Lower Zambezi basin is a pull-apart basin formed by wrenching along the Mzarabani fault; the oblique, northwest trending intrabasin faults at the western end of the basin indicate that basin formation would have required a dextral reactivation of the previously sinistral Mzarabani Fault (Mann *et al.*, 1983), as shown in figure 2.5. The evolution of the Mana Pools basin, at the intersection of the two rift systems, is not understood; satellite imagery (Orpen *et al.*, 1989) shows that the Mzarabani Fault continues westward from the Lower Zambezi basin to bound the southern margin of the Mana Pools basin. The NNW

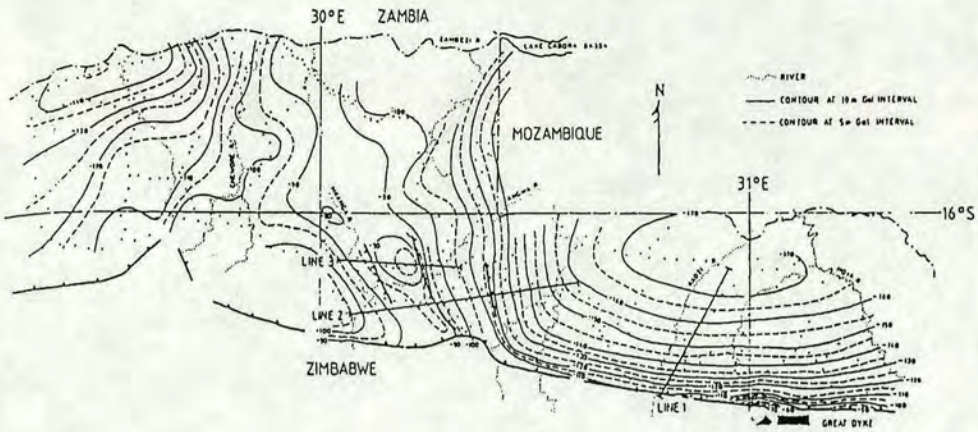

Figure 2.6. A bouguer anomaly map of the Mana Pools and Lower Zambezi basins. Major faults are indicated with downthrown sides ticked and gravity stations by dots. After Orpen *et al.* (1989).

margin of the Mana Pools basin is also fault bounded; satellite data show that the marginal fault splays off the Luangwa trough system west of the Chewore inliers and runs along the margin of the basin. The tectonic controls on the Mana Pools basin remain unknown although the geometry of the basin suggest that it is a half graben (Orpen *et al.*, 1989). The conclusions of Orpen *et al.* (1989) contradict the work of Burke and Dewey (1973) who argued that the Mid Zambezi, Lower Zambezi and Luangwa basins represent a failed Karoo triple junction formed by a plume-generated uplift. While a triple junction model can be applied to these three basins there is no real evidence to support it and the interpretation of Orpen *et al.* (1989) is more convincing given the available facts. Figure 2.5 is a simplified summary of the preferred interpretation of Orpen *et al.* (1989); the Karoo basins developed along two major planes of weakness in the Central African crust. The northeast-southwest plane developed normal faults and half-graben basins, while the east-west plane is a strike-slip fault developing pull-apart basins.

2.7 Geophysical Studies in the Zambezi Valley

The data from a 1986 gravity survey of the Zambezi valley (Zhou, 1988) supports the broad structural outline of the Lower Zambezi basin given in § 2.6. The Bouguer anomaly map for the Zambezi valley shown in figure 2.6 shows the Mana Pools and Lower Zambezi basins as two large gravity 'lows'. The margins of the basins are seen as areas where the gravity isolines are much closer together; this marks a rapid change in the depth to basement indicating that the basins are fault bounded. The Mzarabani fault can clearly be seen running across the bottom of figure 2.6 and the Lower Zambezi basin is clearly delineated as a large elliptical gravity low which contacts the southern boundary of the Zambezi valley along the Zambezi escarpment (Zhou, 1988). An anomaly of approximately 800g.u. relative to the escarpment occurs near the border with Mozambique and this is assumed to mark the deepest part of the basin; no gravity data exist for the basin in Mozambique (Zhou, 1988). To the west, the northward bend of the isolines marks where the basement rises abruptly, probably at a faulted boundary. The basement also rises gradually to the east (Zhou, 1988). The abrupt northward bend of the isolines at around 30°30′E in figure 2.6, indicating a rapid rise in basement towards the west, was investigated by Orpen *et al.* (1989). They modelled an east-west gravity traverse across this feature. The resulting

model showed two NNW-SSE faults, the eastern one downthrowing to the east and the western one downthrowing to the west. These two faults truncate the Lower Zambezi basin to the west, with the western one bringing basement almost to the surface. Together with a fault further west, downthrowing to the west, these faults may be extensions to the block-faulted boundary of the Chewore inlier (Bosum and Geipel, 1988). West of this, the gravity survey over the Mana Pools basin indicates a basement depth of approximately 5 km with a depocentre offset towards the NNW faulted margin of the basin.

EM and electrical sounding measurements taken in the Zambezi valley (see fig 2.7) could indicate whether the southwest African conductor extends along Zimbabwe's northern border to lie beneath the Lower and Mid Zambezi basins. In 1988 a MT survey of the Lower Zambezi basin was made by Losecke *et al.* (1988); one of the aims of this survey was to determine the sediment thickness within the basin. This was prompted by the results of an aeromagnetic survey (Bosum and Geipel, 1988), flown in 1982 during a Uranium prospecting study of the Zimbabwe section of the Zambezi valley. The aeromagnetic survey located two magnetic horizons at depths of 2 km and 6 to 10 km respectively within the Lower Zambezi basin. This three layer structure has proved difficult to interpret. It may correspond to a non-magnetic cover overlying a layer of either weakly magnetic basement or intercalated basalt sills and sediments with a layer of magnetic or non-magnetic material below (Bosum and Geipel, 1988). What is not clear from the aeromagnetic data is which, if either, of the magnetic horizons corresponds to the magnetic basement and what the consequent sedimentary thickness of the basin is. Two magnetic horizons were also found in the Mana Pools basin at depths of 0.8 and 3 to 4 km.

The MT survey of Losecke *et al.* (1988) was part of a hydrocarbon prospect assessment of the Lower Zambezi basin. The survey area covered the region between $30^o15'$E and $31^o15'$E on the Zimbabwe side of the Zimbabwe-Mozambique border. It was assumed that the basin would consist of a graben, striking east-west along the dominant trend of the Zambezi valley and therefore could be approximated by a two-dimensional resistivity structure. Survey lines were layed out north to south over the region extending for some distance onto the cratonic blocks bounding the basin. Soundings were taken for these profiles and data were collected using a remote reference technique for periods between 0.2 and 2000 s, this was extended further to 10000 s at some sites. The objectives of the survey were to gain a large scale picture of the electrical resistivity distribution within the basin and its surrounding region, to determine the basin configuration and to get an estimate of its sediment thickness (Losecke *et al.*, 1988). The answer to the last of these aims should help in the interpretation of the two magnetic horizons recorded by the aeromagnetic survey (Bosum and Geipel, 1988).

The two-dimensional model for a profile of the Lower Zambezi basin proposed from forward modelling studies by Losecke *et al.* (1988) is shown in figure 2.8. There are three zones to the model; zone 1 is a good conductor of resistivity 2 to 10 Ωm extending to between 1 and 4 km deep and thinning southward toward the Zambezi escarpment. Zone 2 is much more resistive, typically 1000 Ωm and between 2 and 12 km thick; its maximum thickness is adjacent to the southern escarpment and it tapers severely to the north. Beneath zone 2 is zone 3, an extremely good conductor of resistivities dropping to below 0.5 Ωm. Losecke *et al.* (1988) claim that zone 3 continues to a depth of 30 km and that its base is not resolved. It is unlikely that this is accurate. For such low resistivities at this period range the electromagnetic signals probably do not have sufficient penetration to resolve the structure to such depth. Zone 3 will probably act as a barrier to deeper penetration of the basin and such a large estimate of its vertical extent can not be supported. The depth and resistivity of zone 3 increases to the south and the west as the escarpment

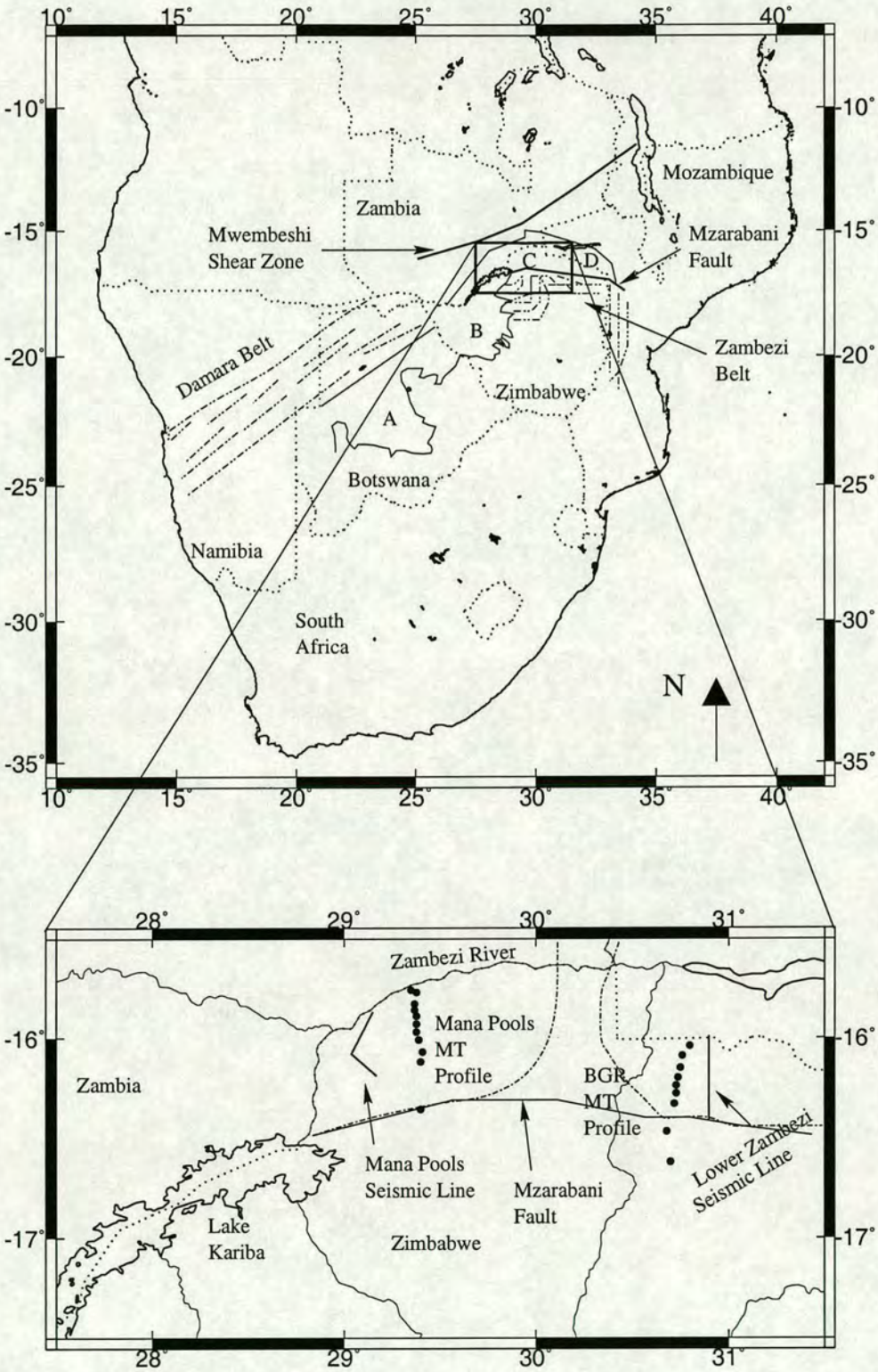

Figure 2.7. The location of the seismic and MT surveys of the Zambezi valley basins in relation to the main political and geological features of southern Africa. In the upper map: A = Passarge basin; B = Mid Zambezi basin; C = Mana Pools basin and D = Lower Zambezi basin. National boundaries are marked with dotted lines. The lower map shows a smaller area of the Zambezi valley with the approximate boundaries of the Mana Pools and Lower Zambezi basins marked with dash-dot lines.

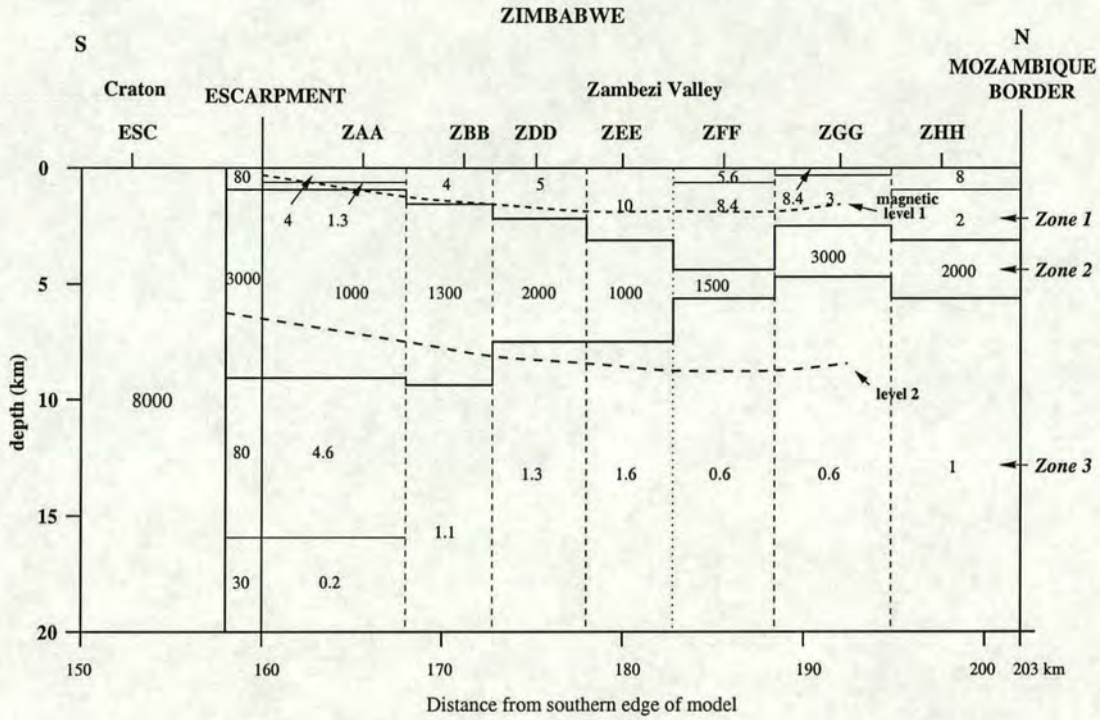

Figure 2.8. Two-dimensional resistivity model of the Lower Zambezi basin, figures indicate resistivity in Ωm, after Losecke *et al.* (1988). The magnetic levels represent the two magnetic horizons observed in the aeromagnetic survey (Bosum and Geipel, 1988).

and Chewore complex respectively are approached; this may indicate a change in the conductor's nature (Losecke *et al.*, 1988). The contrast between the electrical structure on the Zimbabwe craton and that in the mobile belt is evident in figure 2.8. The cratonic rocks are much more resistive; the model estimates values of 8000 Ωm to a depth of at least 20 km.

Losecke *et al.* (1988) used the existing potential field data to try to constrain the interpretation of their 2-D model. The resistivity of zone 1 and its low density, determined from modelling of the gravity data (Zhou, 1988), are consistent with non-metamorphic sediments of post Karoo and Karoo age. Many of the Karoo basins of central and southern Africa are capped by basaltic rocks but no thick resistive basalts are discernible in the MT model, although thinner conductive or intercalated basalt layers are possible (Losecke *et al.*, 1988). Borehole data are not available in this area to resolve this difficulty. There is agreement between the MT and potential field data on two possible interpretations of zone 2, either as the upper part of the crystalline basement or a layer of consolidated sediments containing intercalated basalt sills. The resistivity and density of these two rock types overlap considerably making them indistinguishable by these methods (Losecke *et al.*, 1988). If the latter explanation is correct then the sedimentary thickness of the basin cannot be determined using MT measurements while the former would make the crystalline basement much less resistive than the craton. This could be explained if the resistivity of the basement in the Lower Zambezi basin has been reduced by deformation or is of a different material to that comprising the craton (Losecke *et al.*, 1988). A cause for the extremely low resistivities of zone 3 cannot be suggested from the MT data (Losecke *et al.*, 1988)and the aeromagnetic data do not constrain the nature of this zone at all. Both Bosum and Geipel (1988) and Losecke *et al.*

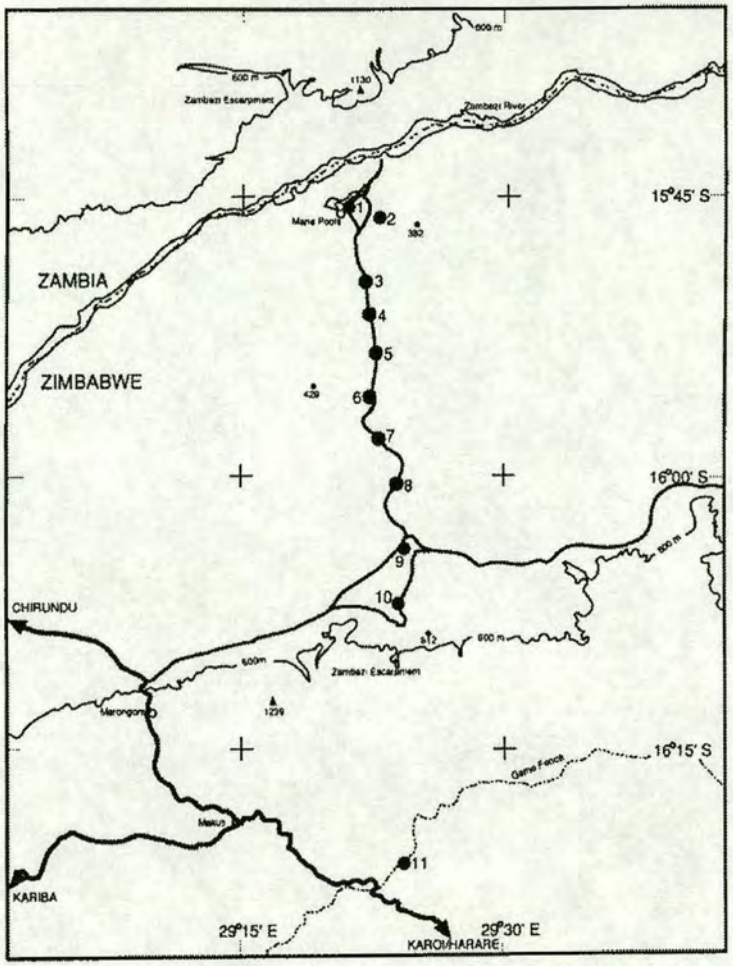

Figure 2.9. The Mana Pools AMT survey, numbers indicate sounding sites. After Whaler and Zengeni (1993).

(1988) suggest that the rocks at this depth may be at temperatures above the Curie temperature with the lower magnetic horizon and the top of zone 3 representing the Curie surface. This hypothesis cannot be tested without borehole temperature gradient measurements.

The increase in resistivity of zone 3 westward in the Lower Zambezi valley may indicate a termination of the conductor by the Chewore inliers or a move to greater depth such as seen in the Kamanjab inlier by Van Zijl and De Beer (1983). This is an important question; if the latter hypothesis is true then the Lower Zambezi basin anomaly may be a continuation of the southwest African conductor described by De Beer *et al.* (1982a). Losecke *et al.* (1988) concluded that these two features were not related but that a survey to the west in the Chewore area would be helpful in resolving the matter. Following the MT survey of the Lower Zambezi basin, no electrical studies of the Chewore area have been made but the Mana Pools basin, west of the Chewore inliers, was surveyed in 1987 using MT methods (Whaler and Zengeni, 1993). AMT data were collected at 10 sites along a north-south profile extending 40 km from the Zambezi River in the north to the Zambezi escarpment in the south. A further station was set up on the craton south of the profile and data collected at all sites for a frequency range of 0.016 to 128 Hz.

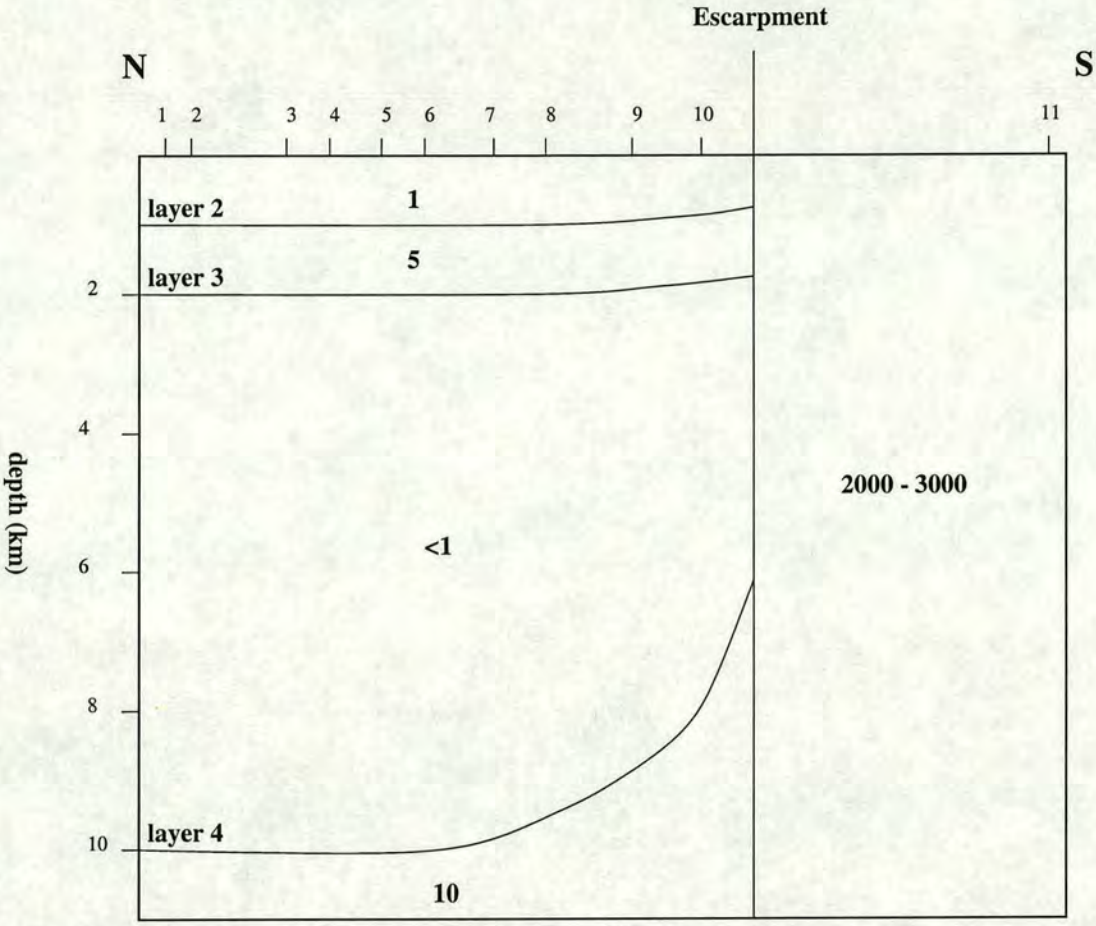

Figure 2.10. A schematic resistivity section for the Mana Pools basin; numbers refer to the sounding sites in figure 2.9. Resistivity values are given in Ωm.

The layout of this profile and site locations are shown in figure 2.9. Whaler and Zengeni's aims were to determine the sedimentary thickness within the basin and to compare the results with existing models for the other Zambezi valley basins. From field stacks and one-dimensional modelling they observed a large contrast between the resistivity of the southern craton and that within the basin. Values of 2000 to 3000 Ωm were modelled for the craton while the basin consists of a variable thickness low resistivity layer up to 10 km thick, over a 10 Ωm layer possibly representing the geological basement (Whaler and Zengeni, 1993). If the identification of the geological basement is correct, then its resistivity is extremely low even for a mobile belt with such a long history of movement. The implications of this observation are similar to those of Losecke *et al.* (1988) and De Beer *et al.* (1982a) for the Lower Zambezi basin and the Damara basin respectively. The basement is either extremely fractured and deformed or of a radically different composition to that encountered on the craton. These two hypotheses are not exclusive and a both fractured and compositionally altered basement may explain the low resistivity. Whaler and Zengeni (1993) tentatively interpreted the overlying 10 km layer as a sedimentary succession with variations in resistivity being identified with different stratigraphic units. They identified three different layers within this 10 km sequence and their positions were mapped with 1-D D^+ models (Parker, 1980); a schematic resistivity section for the Mana Pools basin is shown in figure 2.10. A thin

conductive layer of approximately 1 Ωm extends to a depth of 0.8 to 1 km and overlies a 5 Ωm unit extending to 2 km depth. Below this is an extremely good conductor with resistivities down to less than 1 Ωm extending to depths of between 6 and 10 km. The one-dimensional models indicate that this deeper layer shallows rapidly and increases in resistivity towards the southern escarpment. This increase in resistivity was also seen for the good conductor in the Lower Zambezi basin (Losecke *et al.*, 1988), but there the conductor was observed to deepen. The resolution of the data were assessed using D^+ (Parker, 1982) and show the penetration depth to increase towards the escarpment to mirror this drop in resistivity. The penetration depth increases accordingly from 6 to 10 km across most of the basin to an estimated 21 and 29 km at sites 9 and 10 respectively (Whaler and Zengeni, 1993). The implication of this is that, within the basin, the sediment-basement interface is just at the resolution depth of the data and therefore may not be properly resolved.

If the division of the sedimentary fill into three layers (Whaler and Zengeni, 1993) is maintained then there is an obvious similarity between the Mana Pools and Lower Zambezi basins. The three postulated sedimentary layers in the Mana Pools basin are labelled as layers 2, 3 and 4. Layer 1 is a very thin surface resistor which is also sometimes detected (Whaler and Zengeni, 1993). The three layers within the Lower Zambezi basin are named zones 1, 2 and 3 (Losecke *et al.*, 1988). In both basins the resistivity structure is similar, with two conductors sandwiching a resistive layer. The lower conductor in each case has the lowest resistivity but this increases towards the margins of the basin. The aeromagnetic data also show similarities. The two magnetic horizons in each basin, if related, are at the top and bottom of resistive layer 3 in the Mana Pools basin and the zone 2 resistor in the Lower Zambezi basin. The similarities apparent from these two techniques may indicate that the two basins are closely related and that a consistent interpretation of their features may be possible. This combined interpretation relies on the difference in depth between the two basins, estimated from the gravity data (Orpen *et al.*, 1989; Zhou, 1988).

When comparing the results of the MT surveys from both basins it is difficult to determine which boundary marks the basement. The Lower Zambezi basin can be interpreted as consisting of sediments confined to zone 1 overlying crystalline basement in zones 2 and 3. This hypothesis is consistent with the data for zone 1. Zone 1 is a good conductor with a thickness of up to 4 km and has a density of 2200 kgm^{-3}, determined from modelling of the gravity data (Zhou, 1988). If this interpretation is correct, then for the correlation of layering to hold between the two basins the nearer surface good conductor in the Mana Pools basin must also correspond to the sediment thickness. This layer only extends to a depth of approximately 800 m, whereas the sediment thickness is estimated by the potential field methods to be significantly greater in both basins. The base of layer 2 is unlikely to mark the sediment-basement interface in the Mana Pools basin. A better agreement with the other techniques is reached if the interface lies at the base of layer 4, at depths of typically 6 km. Differing stratigraphic sequences within the sediments, known to exist from the work of Barber (1994), could account for the variations in resistivity with depth in the top few kilometres (Whaler and Zengeni, 1993). If this boundary is the sediment-basement interface then there is a sedimentary thickness of between 5 and 8 km across the majority of the Mana Pools basin, with a rapid decrease adjacent to the escarpment. It is unlikely that the sediment thickness in the Lower Zambezi basin extends to over 30 km depth and the correlation between the two basins depends on the depth of this layer being overestimated. If the Mana Pools conductor is identified with the southwest African conductor then its position in the Mana

Pools basin contrasts radically with its position in the Damara belt. The conductor in the Damara belt is identified with the Pre-Damara basement (De Beer *et al.*, 1982a) and is thought to extend into the adjacent cratonic blocks. This suggests that the good conductor is associated with the basement, and not the sedimentary pile as is seen here in the Mana Pools basin; this is a clear problem in the reconciliation of these two features with each other.

The Mana Pools results tend to rule out the hypothesis examined by Losecke *et al.* (1988) that the temperature in the third zone of the Lower Zambezi basin must be above the Curie temperature, lowering the resistivity and explaining the absence of a magnetic signal from that zone. The same explanation for the highly conducting fourth layer and the magnetic horizon around 3 to 4 km in the Mana Pools basin would imply excessively large temperature gradients.

2.8 Seismic Reflection Studies in the Zambezi Valley

Some of the ambiguities in the interpretation of the basin structure using the MT data were resolved by a reflection seismic survey by Mobil Exploration Zimbabwe Incorporated in 1990 and 1991. The Mobil licence area in the Zimbabwe section of the Zambezi rift covers 30120 km^2 downstream from Victoria falls and upstream from lake Cabora Bassa (Hiller and Buttkus, 1996). The objective of the survey was to provide a reconnaissance grid over the basinal areas that were thought to contain prospective hydrocarbon accumulations. The wide line spacing meant that prospects were unlikely to be delineated, merely structural information and leads obtained (MOBIL, 1993); the primary goal was to provide depth estimates to the Precambrian basement (Hiller and Buttkus, 1996). Seismic data were collected during 1990 and 1991 for the Lower Zambezi, Mana Pools and Mid Zambezi basins and a report on the structural style of the basins published by Hiller and Buttkus (1996). Stacking velocities were used to estimate average seismic velocities in the absence of other types of velocity data. These were used to calculate reflection time-depth relations for each of the basins and the depth to reflectors and horizon thicknesses from two-way time maps. The simplified geological structures of the three basins, based on the seismic interpretation, are shown in figure 2.11. Three separate dip lines for the Mid Zambezi basin, whose locations are given in the map inset, are shown in figure 2.11. The Mid Zambezi basin consists of three alternating half grabens involving faulting of the basement (Hiller and Buttkus, 1996), each of these half grabens are between 50 and 70 km wide, dip at between 5 and 10° and are divided into a series of smaller grabens by internal faulting. The southwest half graben is shown in profile A to B on figure 2.11 and dips down to the northwest reaching a depth of nearly 6 km. The central half graben is plotted on profile C to D and dips to the southeast, reaching a maximum basement depth of almost 3.5 km northwest of the Chizarira high shown on figure 2.11. The northerly half graben illustrated on profile E to F dips to the northwest again, away from the Chizarira high, attaining a depth of approximately 2 km of sediments close to the Zambia border. The maximum sediment thickness seen in the Mid Zambezi basin is estimated to be approximately 5.3 km.

As is implied by the plots of geological structure, the top of the seismic basement forms a distinct and continuous reflector across the entire basin; this is true for all three of the basins surveyed (Hiller and Buttkus, 1996). The Upper/Lower Karoo boundary also appears as a distinct reflector and is traceable over large parts of the Mid Zambezi and Lower Zambezi basins; this reflector does not appear in the

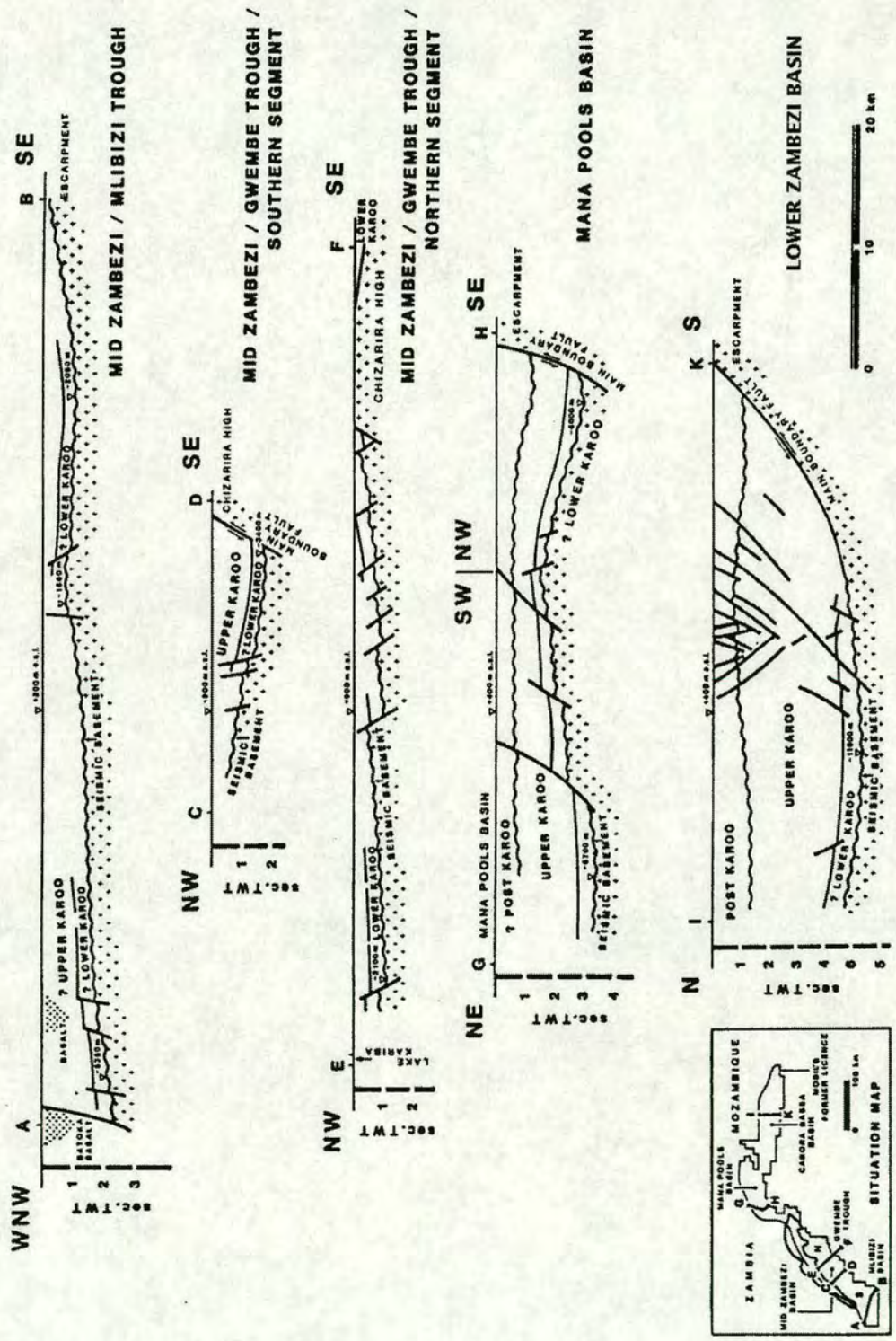

Figure 2.11. The structure of the Zambezi valley basins, interpreted from the Mobil reflection seismic data, after Hiller and Buttkus (1996).

Mana Pools basin whose lack of outcrop makes its structural interpretation a lot less certain (Hiller and Buttkus, 1996). Work in the Mana Pools basin was confined to its western section, and a geological interpretation of one of the dip lines, G to H, is shown in figure 2.11. The basin contains two lows which parallel the graben rims and are separated by an ENE-WSW trending basement high (Hiller and Buttkus, 1996). The deeper of the two basin lows is at the northeast end of the profile near the Zambezi river at a depth of nearly 7 km; the shallower is approximately 6 km deep and adjacent to the southeastern escarpment. Hiller and Buttkus (1996) suggest that these two basement lows may deepen further to the east where the MT profile is located. The Lower Zambezi basin is the deepest of the three Zambezi rift basins with an estimated maximum sedimentary thickness of 11.6 km; the geological interpretation of the seismic data is shown in profile I to K in figure 2.11. Hiller and Buttkus (1996) interpret the basin fill to be structurally dominated by a saddled, hanging-wall anticline parallel to the main southern boundary fault. This structure is flanked to the north and south by two synclines, the shallower to the south and a deeper one to the north, reaching the maximum sedimentary thickness adjacent to the border with Mozambique.

There seems to be good agreement between the results from the seismic survey and the other geophysical methods employed in the Zambezi valley basins. The depth to the seismic basement within each of the three basins is well constrained by the seismic data and answers some of the questions posed by the interpretation of the MT and aeromagnetic results. The seismic evidence also allows a reassessment of the existing hypotheses for the structure and mode of formation of each of the basins. The data clearly support a half graben structure for the Mid Zambezi basin, while the Mana Pools basin also seems graben-like, though slightly deformed and displaying a warped basement. The warping of the basement seems to have deepened the basin adjacent to the southern escarpment creating a second shallower depocentre. The northern depocentre is 7 km deep which is in reasonable agreement with the gravity data and the preferred interpretation of Whaler and Zengeni (1993) for the MT data from the basin. The depth to basement in the Lower Zambezi basin is in good agreement with the depth of the lower magnetic horizon and the depth estimate given by the gravity data. It also resolves the problem of the interpretation of zone 2 in the resistivity model of Losecke *et al.* (1988); zone 2 cannot contain crystalline basement at only 4 km depth, this would be seen in the seismic data. The Lower Zambezi basin does not appear to fit the graben model; its structure is markedly different to that of the other two basins, implying that it experienced a different tectonic mode of emplacement. From the available seismic data it is difficult to assign a particular method of formation to the Lower Zambezi basin; the hypothesis of a pull-apart basin cannot be further supported or rejected but it does not appear to conflict with the data.

2.9 Summary

The work of Losecke *et al.* (1988) and Whaler and Zengeni (1993) has provided what appears to be the foundation for a common geoelectric interpretation of the structure of the Lower Zambezi basin and the Mana Pools basin. Correlation between the layering in these two basins is supported by evidence from both electromagnetic work and potential field methods. Yet this seeming correlation has led to many problems in finding a common interpretation for the nature of each layer and the structure of the two basins, most notably in identifying the depth to basement and whether the extremely good deep

conductor in each basin lies within the sedimentary pile or beneath it. Further problems are generated by the work undertaken in the 1970's in the Damara orogenic belt mapping the southwest African conductor (De Beer *et al.*, 1976; Van Zijl and De Beer, 1983; De Beer *et al.*, 1982a, 1975; Van Zijl, 1977, 1978). The results from these studies show a conductor within the basement and extending at depths of approximately 40 km into the neighbouring cratons. If the anomalies observed in the Lower Zambezi and Mana Pools basins are related to this feature then they should also lie within the basement. The conductor in zone 3 in the Lower Zambezi basin, according to the seismic data, lies either partially or completely within the basement but the preferred interpretation of the electrical structure of the Mana Pools basin has the conductor entirely within the sediments. This is a problem that is difficult to overcome.

Since the discovery of the southwest African conductor, many of the studies in the Zambezi valley have aimed to try to find a link between the Damara mobile belt to the west and the Zambezi mobile belt to the east, believing these conductors would provide this link. Whaler and Zengeni (1993), from their work in the Mana Pools basin, considered the deeper conductor in that basin to link the southwest Africa conductor and the Lower Zambezi conductor of Losecke *et al.* (1988). The latter author, admittedly working prior to the former's work, considered there to be no such link between the two. The transition of the Lower Zambezi conductor to a deeper resistor to the west in their opinion precluded any such statement until a full survey of the Chewore inlier region had been made. This region remains unsurveyed, but there is no reason to consider it as terminating the conductive structure; it may simply mark the transition of the conductor to a deeper thinner structure as is observed by Van Zijl and De Beer (1983) in the massive inliers of the Damara basin.

There are many similarities between the electromagnetic data collected in all these regions and a coherent interpretation is very desirable. The common fact that all these anomalies share is their location within Pan-African mobile belt terranes; these mobile belts crossing much of southern Africa have had a major control on its subsequent tectonic history and evolution and have no doubt led to similarities between the structures within them. There are however differences too: the formation of the Lower Zambezi basin is thought to have occurred by pull-apart forces along the Mzarabani Fault while the Mid Zambezi and Mana Pools basins are believed to be half-graben basins formed along the Mwembeshi shear zone. Debate also continues on the origin of the Damara basin in Namibia; the main models are critically assessed by Martin (1983), yet the possibility of either a rifting origin or a subduction origin still exists. Neither at present is the cause of the conductive anomalies within the Karoo basins known and, without further information, particularly heat flow measurements, only hypotheses can be proposed. Although a regional interpretation of all the features discussed within this chapter is the aim of any study of this kind, an interpretation involving data from many different techniques for a smaller region could provide a better start from which a larger interpretation can be made. It is the aim of this thesis to provide that firm starting point with a detailed study of the structure of the Mana pools basin.

Chapter 3

The Magnetotelluric Method

3.1 Introduction

The magnetotelluric (MT) method is an electromagnetic (EM) induction technique. MT soundings are used to determine the resistivity distribution of the subsurface from measurements, at the ground surface, of natural time-varying magnetic and electric (telluric) fields. This chapter gives a brief outline of the theory underlying the MT method, starting from Maxwell's equations and ending with expressions for the MT impedance tensor and its form in environments with different degrees of structure. A brief review of the major scientific contributions to the development of the method is given and an outline of the natural sources which MT measurements rely upon. Diffusion equations explaining the propagation of electromagnetic waves in the earth are derived from Maxwell's equations. Propagating electric and magnetic waves are then sought as solutions to these equations from which expressions for the MT impedance and the apparent resistivity and phase are developed. Subsequent chapters develop relevant aspects of the theory further as is required.

3.2 The Development of the Method

The source for the MT method is the transient portion of the Earth's magnetic field, which has a frequency range of between 10^{-4} and 10^{3} Hz. The signal amplitude drops rapidly with increasing frequency, a minimum being reached at approximately 1 Hz, this allows a convenient division of the source field into two types, each type having its origin in a different activity. The main source of MT fields of frequencies above 1 Hz is worldwide atmospheric thunderstorm activity (Vozoff, 1972) with solar activity responsible for periods longer than 0.125 seconds. This primary magnetic field penetrates the ground inducing telluric currents and secondary magnetic fields; the fields combine and components of the total resultant electric and magnetic fields can be measured at the surface. The energy from these sources can be used to probe the resistivity structure of the earth over a large range of depths, down to many hundreds of kilometres.

An MT survey involves the measurement of orthogonal electric and magnetic field variations at one or a

number of sites simultaneously. Two electrodes are deployed in the ground at a fixed distance l apart and the electric field is measured as their voltage difference divided by their separation l. The magnetic field is measured using a variety of sensors depending on the frequency range of interest. For short period signals, in the range between 10^{-4} s and 1 s, known as 'audiofrequency-magnetotellurics' (AMT), induction coils are used, while flux-gate magnetometers are used at longer periods. The measured electric and magnetic fields are used to deduce the information about the spatial variation of the Earth's resistivity.

The origins of the MT method can be traced back to the 1950's. Tikhonov (1950) first showed the possibility of electrical exploration of the Earth through a comparison of magnetic and electric field measurements. Later Cagniard (1953) gave a fuller theoretical treatment, developing solutions for the horizontal components of the electric and magnetic fields at the surface due to telluric currents in the Earth. Cagniard described the ratio of these horizontal components and their relative phases as diagnostic of the structure and resistivity of the subsurface and developed formulae and a set of master curves for calculating the resistivity and depths to interfaces for both a two and three layer 1-D problem. Cagniard was quick to see the general applicability of the MT method to a variety of situations, particularly the investigation of sedimentary basins for petroleum traps. While use of periods shorter than 1 s was, at that time, technically difficult, first being recorded by Strangway *et al.* (1973), Cagniard predicted the use of the MT method at these frequencies in civil engineering problems, mineral prospecting and the search for underground water. The assumption of Cagniard (1953) that the incident fields could be treated as plane waves was questioned by Wait (1954) and the shape of the source field was further examined by Price (1962) and Wait (1962). Madden and Nelson (1964) settled this problem concluding that the effects of source geometry were not sufficient to invalidate Cagniard's assumption of an infinite horizontal wavelength. Madden and Nelson suggested that lateral variations in the Earth's resistivity structure was a far more serious problem and required the development of a tensor treatment of the data. The treatment of the magnetotelluric impedance as a rank two tensor in situations where the resistivity varied laterally was first discussed by, amongst others, Rokityanski (1961) and Berdichevski (1960). Bostick and Smith (1962) and later Swift (1967) were among the first to rotate the impedance tensor into a preferred electrical strike direction by minimisation of the auxiliary impedance elements.

3.3 Geoelectromagnetic Theory

The theory behind geophysical induction studies is based on Maxwell's equations which describe the behaviour of an electromagnetic field. The differential forms of Maxwell's equations assuming that no dielectric or magnetic material is present are

$$\nabla \cdot \mathbf{B} = 0 \tag{3.1}$$

$$\nabla \cdot \mathbf{D} = q \tag{3.2}$$

$$\nabla \times \mathbf{E} = -\frac{\partial \mathbf{B}}{\partial t} \tag{3.3}$$

$$\nabla \times \mathbf{H} = \frac{\partial \mathbf{D}}{\partial t} + \mathbf{J}. \tag{3.4}$$

All the fields involved are functions of position and of time. $\mathbf{H}$ and $\mathbf{E}$ are the magnetic and electric field strengths respectively, $\mathbf{B}$ is the magnetic induction, $\mathbf{D}$ is the electric displacement, $\mathbf{J}$ and q represent the electric current and electric charge densities respectively and ω denotes the angular frequency. A right handed Cartesian coordinate system is assumed with x,y and z defined to be positive when pointing towards the north, the east and vertically downwards, respectively.

Physically, equation 3.3 describes the generation of electric fields from time-varying magnetic induction fields and equation 3.4 represents the fact that magnetic fields are caused by electric current flow, both through conduction and displacement currents. Equation 3.1 states the condition that there are no magnetic monopoles while equation 3.2 implies Coulomb's law and the property that the charge on an insulated conductor migrates towards its outer surface.

For a general conducting medium the scalar electrical conductivity σ is defined by Ohm's law as,

$$\mathbf{J} = \sigma \mathbf{E}. \tag{3.5}$$

The relations between the magnetic field $\mathbf{H}$ and the magnetic induction $\mathbf{B}$ and that between the electric field $\mathbf{E}$ and the electric displacement $\mathbf{D}$ are given by:

$$\mathbf{B} = \mu \mathbf{H} \tag{3.6}$$

$$\mathbf{D} = \epsilon \mathbf{E} \tag{3.7}$$

where μ is the magnetic permeability and ϵ is the electrical permittivity. Both μ and ϵ are assumed to be constant and frequency-independent. The free space values of these constants are $\mu_o = 4\pi \times 10^{-7}[\frac{Vs}{Am}]$ and $\epsilon_o = (\mu_o c^2)^{-1} \approx 8.85 \times 10^{-12}[\frac{C}{Vm}]$, where c is the speed of light. Equations 3.5 to 3.7 are the constitutive relations for a linear isotropic medium and σ, ϵ and μ are referred to as the constitutive constants and are usually frequency dependent.

Taking Maxwell's equations as a starting point it is straight forward to derive the wave equations characterising the behaviour of electromagnetic fields in a medium. Taking the curl of equation 3.4 and using the constitutive equations 3.5, 3.6 and 3.7 we obtain the expression

$$\nabla \times \nabla \times \mathbf{H} + \mu\varepsilon \frac{\partial^2 \mathbf{H}}{\partial t^2} + \mu\sigma \frac{\partial \mathbf{H}}{\partial t} = 0 \tag{3.8}$$

and the curl of equation 3.3 gives:

$$\nabla \times \nabla \times \mathbf{E} + \mu\sigma \frac{\partial \mathbf{E}}{\partial t} + \mu\varepsilon \frac{\partial^2 \mathbf{E}}{\partial t^2} = 0. \tag{3.9}$$

For materials with normal values of ϵ and μ that do not differ appreciably from ϵ_o and μ_o and for the typical values of conductivity encountered in earth materials, at the frequencies used in MT soundings the charge distribution decays very rapidly and it can be assumed that, with a uniform conductor, no charges will accumulate (eg. Telford *et al.*, 1990; Pain, 1993). This condition enables equation 3.2 to be simplified by setting q to zero. Using the vector identity $\nabla \times \nabla \times \mathbf{F} = \nabla(\nabla \cdot \mathbf{F}) - \nabla^2 \mathbf{F}$ where $\mathbf{F}$ is either of the fields $\mathbf{E}$ or $\mathbf{H}$ and remembering that $\nabla \cdot \mathbf{E} = 0$ and $\nabla \cdot \mathbf{H} = 0$ for homogeneous media,

we have that,

$$-\nabla^2\mathbf{H} = \nabla \times \nabla \times \mathbf{H} \quad \text{and} \quad -\nabla^2\mathbf{E} = \nabla \times \nabla \times \mathbf{E} \tag{3.10}$$

giving

$$\nabla^2\mathbf{H} = \mu\varepsilon\frac{\partial^2\mathbf{H}}{\partial t^2} + \mu\sigma\frac{\partial\mathbf{H}}{\partial t} \tag{3.11}$$

and

$$\nabla^2\mathbf{E} = \mu\varepsilon\frac{\partial^2\mathbf{E}}{\partial t^2} + \mu\sigma\frac{\partial\mathbf{E}}{\partial t}. \tag{3.12}$$

Equations 3.11 and 3.12 are the differential wave equations for the magnetic and electric fields in the time domain. They describe the propagation of damped waves where $(\mu\sigma\frac{\partial\mathbf{F}}{\partial t})$ is the damping term. The effect of the damping term is to cause conduction currents to flow. If $\sigma = 0$, for example in air, the damping term disappears. Most materials however have finite conductivity. The conduction currents are dissipated irreversibly through ohmic heating, resulting in a loss of energy from the wave as it propagates.

If we assume harmonic time dependence of the electromagnetic fields $\mathbf{F}$, where

$$\mathbf{F} \sim e^{i\omega t}, \tag{3.13}$$

then the relationship between the time and frequency domain can be written using a Fourier integral representation:

$$\mathbf{F}(\mathbf{r}, t) = \int \mathbf{F}(\mathbf{r}, \omega)e^{i\omega t}d\omega. \tag{3.14}$$

Equations 3.11 and 3.12 can then be re-expressed in the frequency domain giving Helmholtz equations in $\mathbf{H}$ and $\mathbf{E}$.

$$\nabla^2\mathbf{H} - (i\mu\sigma\omega - \mu\varepsilon\omega^2)\mathbf{H} = 0, \tag{3.15}$$

and

$$\nabla^2\mathbf{E} - (i\mu\sigma\omega - \mu\varepsilon\omega^2)\mathbf{E} = 0 \tag{3.16}$$

or simply,

$$\nabla^2\mathbf{H} - \gamma^2\mathbf{H} = 0 \quad \text{and} \quad \nabla^2\mathbf{E} - \gamma^2\mathbf{E} = 0, \tag{3.17}$$

where

$$\gamma^2 = (i\mu\sigma\omega - \mu\varepsilon\omega^2). \tag{3.18}$$

In this form, the two fields ($\mathbf{E}$ and $\mathbf{H}$) have been separated from frequency and the constitutive constants,

which are properties of the rock, all of which have been grouped together into a single term, γ^2. γ^2 is the wave number and allows σ, μ and ε and frequency to be treated as a single parameter which characterises the interaction of the EM fields with the medium. For earth materials at the frequencies employed in MT work, $\mu\varepsilon\omega^2 \ll \mu\sigma\omega$ (Telford *et al.*, 1990). Thus the conduction currents predominate over displacement currents, which we neglect; under these conditions the dependence of γ on ε disappears and the EM field simply diffuses. Equations 3.15 and 3.16 therefore simplify to

$$\nabla^2\mathbf{H} - i\mu\sigma\omega\mathbf{H} = 0 \tag{3.19}$$

$$\nabla^2\mathbf{E} - i\mu\sigma\omega\mathbf{E} = 0 \tag{3.20}$$

which are diffusion equations. In this case, the wave number is approximated by

$$\gamma^2 = (i\mu\sigma\omega) \tag{3.21}$$

and γ has equal real and imaginary parts:

$$\gamma = (\frac{\mu\sigma\omega}{2})^{\frac{1}{2}} + i(\frac{\mu\sigma\omega}{2})^{\frac{1}{2}}. \tag{3.22}$$

Diffusion applies for real earth materials and is the reason for the inherent lack of resolution of the EM prospecting methods. Fields are attenuated during propagation and the field strength is large enough to measure only up to some penetration depth; the diffusive nature of the EM signals causes a smoothing out of Earth structure.

3.4 1-D Solutions of Wave Equations

In the previous section, equations were derived to describe the behaviour of geoelectric and magnetic fields; in this section we look for one-dimensional fields that will satisfy these equations. Consider the propagation of a plane-polarised electric field with a simple harmonic time dependence in a conducting homogeneous earth. The electric field is considered to vary in one direction only, where $\mathbf{E} = \hat{\mathbf{i}}E_x$ and $\hat{\mathbf{i}}$ is the unit vector in the x-direction. E_x is constant over a plane normal to the direction of propagation and so,

$$\frac{\partial E_x}{\partial x} \quad \text{and} \quad \frac{\partial E_x}{\partial y} = 0.$$

Applying this assumption to equation 3.20 gives the expression:

$$\frac{\partial^2 E_x}{\partial z^2} - i\mu\sigma\omega E_x = 0. \tag{3.23}$$

Concentrating on the E_x oscillation and using the assumptions that we have made, a solution to the wave equation can be proposed where $E_x = E_o e^{iwt} e^{-kz}$ in the positive z direction. E_o is the incident electric field at the earth's surface and k is an unknown constant. Substituting this solution into equation 3.20

gives the expression

$$\begin{aligned} E_o k^2 e^{iwt} e^{-kz} &= \mu\sigma E_o i\omega e^{iwt} e^{-kz} \\ \text{or} \quad k^2 &= i\omega\mu\sigma \end{aligned} \tag{3.24}$$

so that

$$\pm k = \left(\frac{\omega\mu\sigma}{2}\right)^{\frac{1}{2}} + i\left(\frac{\omega\mu\sigma}{2}\right)^{\frac{1}{2}} = s + is, \tag{3.25}$$

where

$$s = \left(\frac{\omega\mu\sigma}{2}\right)^{\frac{1}{2}}. \tag{3.26}$$

Equation 3.24 and 3.21 are equivalent, so the constant k equals the wavenumber γ. The assumed solution is a correct one-dimensional solution to the wave equation and E_x is of the form,

$$\begin{aligned} E_x &= E_o e^{\pm(\sqrt{\frac{\omega\mu\sigma}{2}})z} e^{(i\omega t \pm isz)} \\ &= E_o e^{\pm sz} e^{i(\omega t \pm sz)} \end{aligned} \tag{3.27}$$

Since the intensities of **E** and **H** decrease with increasing depth in the earth due to the transformation of electromagnetic energy into heat, only the e^{-sz} solution of the above equation meets the conditions of the physical model. Therefore,

$$E_x = E_o e^{-sz} e^{i(\omega t - sz)} \tag{3.28}$$

is an acceptable solution of the wave equation. An EM field will be reduced in amplitude by a factor $\frac{1}{e}$ (eg. Cagniard, 1953; Pain, 1993) at a distance within a medium described by the skin depth δ, defined as (eg. Vozoff, 1972),

$$\delta = \frac{1}{s} = (\frac{2}{\omega\mu\sigma})^{\frac{1}{2}} = 503(\frac{1}{f\sigma})^{\frac{1}{2}} \tag{3.29}$$

where f = frequency in Hz. The skin depth in metres is obtained from equation 3.29 if all the other quantities are also expressed in S. I. units. Equation 3.29 shows that the penetration depth of a MT sounding depends on both the period of the signal being measured and the conductivity of the medium (assuming μ to be constant). The longer the period measured or the smaller the conductivity of the medium, the deeper the electromagnetic fields penetrate.

3.5 Basic Concepts of Magnetotelluric Theory

The previous sections have concentrated on the development, from Maxwell's equations, of equations which describe the behaviour of electromagnetic fields in conducting media. Solutions to these equations in the form of propagating fields have been derived for the one-dimensional case. In this section we consider the relationship between the electric and magnetic components of the EM wave and look

at the extension of the induction problem to two dimensions.

Maintaining the assumption of a homogeneous earth, equations 3.19 and 3.20 describe a pure diffusion process and can be re-written as

$$\frac{\partial^2 E_x}{\partial z^2} - i\mu\sigma\omega E_x = 0 \tag{3.30}$$

$$\frac{\partial^2 H_y}{\partial z^2} - i\mu\sigma\omega H_y = 0. \tag{3.31}$$

Because of the assumption of plane polarised waves, the incident source field E_x only induces a perpendicular H_y magnetic field component. It was shown in the previous section that for a plane wave in a half space,

$$E_x = E_o e^{iwt} e^{-\gamma z} \tag{3.32}$$

where $\gamma = (1+i)(\frac{\omega\mu\sigma}{2})^{1/2}$, the wave equation for the magnetic field is of the same form as the electric field and the magnetic field solution is of the same form as equation 3.32. The wave H_y can be expressed in the form $H_y = H_o e^{i(wt-\phi)} e^{-\gamma z}$, this implies that there is a phase difference, ϕ, between the two fields with H_y lagging behind E_x. The MT impedance, **Z**, is defined as the ratio of the electric to the magnetic fields such that,

$$\mathbf{Z} = \frac{E_x}{H_y} = \frac{E_o}{H_o} e^{i\phi} \tag{3.33}$$

The frequency-dependent impedance tensor **Z** contains information about the conductivity distribution of the sub-surface. The MT method involves estimation of this impedance tensor by measurements of orthogonal components of the electric and magnetic fields at the Earth's surface. **Z** is also called a response function of the Earth. Applying equation 3.6 to equation 3.3 gives the expression

$$\frac{\partial E_x}{\partial z} = -\mu \frac{\partial H_y}{\partial t}; \tag{3.34}$$

taking the derivatives and using equation 3.32 gives

$$-\gamma E_x = -i\omega\mu H_y. \tag{3.35}$$

Combining equations 3.33 and 3.35 gives an alternative expression for the impedance (Pain, 1993):

$$\mathbf{Z} = \frac{1+i}{\sqrt{2}} (\frac{\omega\mu}{\sigma})^{\frac{1}{2}} = (\frac{\omega\mu}{\sigma})^{\frac{1}{2}} e^{i\phi} \tag{3.36}$$

Equation 3.36 shows that **Z** is a complex quantity with a magnitude of $(\frac{\omega\mu}{\sigma})^{\frac{1}{2}}$ and that the magnetic field lags 45° behind the electric field.

We have thus far looked at the propagation of plane-polarised waves in a linear, homogeneous and isotropic conductor. If the conductivity structure is two-dimensional, so that σ varies in both the vertical (z) and one horizontal direction, in this case y, then Maxwell's equations de-couple into two sets of

equations,

$$\begin{aligned}\frac{\partial H_z}{\partial y} - \frac{\partial H_y}{\partial z} &= \sigma E_x \\ \frac{\partial E_x}{\partial z} &= -iw\mu_o H_y \\ \frac{\partial E_x}{\partial y} &= i\omega\mu_o H_z,\end{aligned} \tag{3.37}$$

and

$$\begin{aligned}\frac{\partial E_z}{\partial y} - \frac{\partial E_y}{\partial z} &= -i\omega\mu_o H_x \\ \frac{\partial H_x}{\partial z} &= \sigma E_y \\ \frac{\partial H_x}{\partial y} &= -\sigma E_z.\end{aligned} \tag{3.38}$$

Equation 3.37 refers to the E-polarisation and describes the field components (E_x, H_y and H_z) observed when E_x is parallel to the structure and in the direction of constant conductivity, the electrical strike. Equation 3.38 describes the H-polarisation mode and relates the field components (H_x, E_y and E_z) when the currents are perpendicular to electrical strike. The impedances calculated for the two modes will be different (O'Brien and Morrison, 1967) because the conductivity is no longer isotropic. Equations 3.37 and 3.38 are usually solved numerically by application of either finite difference techniques (eg. Swift, 1967; Brewitt-Taylor and Weaver, 1976) or the finite element method (eg. Coggon, 1971; Wannamaker *et al.*, 1987). The magnitude of the impedance estimates can be used to define a quantity with units of resistivity, referred to as the apparent resistivity, ρ_a, such that

$$\rho_{a_{ij}}(\omega) = \frac{1}{\omega\mu_o}|Z_{ij}(\omega)|^2. \tag{3.39}$$

The indices i and j refer to either the x or y component of the horizontal electric and magnetic field respectively, and determine which impedance estimate is used in the calculation of ρ_a. The expression for the impedance phase is

$$\phi_{ij}(\omega) = \arctan\left(\frac{Im\{Z_{ij}(\omega)\}}{Re\{Z_{ij}(\omega)\}}\right) \tag{3.40}$$

In the 3-D case Maxwell's equations do not decouple into E and H-polarisations and the resulting system of equations is much more difficult to solve. Typically an integral equation technique is applied to the problem (eg. Hohmann, 1975; Weidelt, 1975) or more recently a difference equation technique was used by Mackie *et al.* (1993).

3.6 The 3-D Magnetotelluric Impedance Tensor

In regions where the Earth has a structure more complicated than a plane-layered model, the conductivity is dependent upon the lateral heterogeneities of the structure. The electric and magnetic fields are no longer orthogonal; this is true for the two-dimensional case in the previous section when the field

components are measured in directions other than parallel and perpendicular to the electrical strike. The impedance relationship between the two field components is described by a pair of linear equations (eg. Cantwell, 1960; Rokityanski, 1961; Wait, 1962; Vozoff, 1972):

$$E_x = Z_{xx}H_x + Z_{xy}H_y \tag{3.41}$$

and

$$E_y = Z_{yx}H_x + Z_{yy}H_y \tag{3.42}$$

These two equations can be expressed using a tensor relationship,

$$\begin{bmatrix} E_x \\ E_y \end{bmatrix} = \begin{bmatrix} Z_{xx} & Z_{xy} \\ Z_{yx} & Z_{yy} \end{bmatrix} \begin{bmatrix} H_x \\ H_y \end{bmatrix} \tag{3.43}$$

Elements Z_{xy} and Z_{yx} of the impedance tensor are known as the principal impedances while Z_{xx} and Z_{yy} are the auxiliary impedances.

The general case of a 3-D earth involves the variation of resistivity in all directions and is described by the impedance tensor of equation 3.43. The 1-D and 2-D cases can be seen to be special cases of equation 3.43 where the auxiliary impedances are zero. For a 1-D earth where conductivity varies only with depth the impedance tensor simplifies to (Zhang *et al.*, 1987; Park, 1989; Bahr, 1988, 1991)

$$\mathbf{Z_{1-D}} = \begin{bmatrix} 0 & Z_{xy} \\ -Z_{xy} & 0 \end{bmatrix}. \tag{3.44}$$

The off-diagonal elements have the same magnitude but the lower off-diagonal element is given a negative sign to indicate that the phase of this element is in the third rather than the first quadrant. For a 2-D resistivity model, the resistivity does not vary along the axis of strike and the auxiliary impedances are zero when referred to axes in the strike and dip directions. The 2-D impedance tensor can be expressed (Groom and Bailey, 1989, 1991; Bahr, 1988, 1991; Chakiridi *et al.*, 1992; Jones and Groom, 1993; Park, 1989; Zhang *et al.*, 1987),

$$\mathbf{Z_{2-D}} = \begin{bmatrix} 0 & Z_{xy} \\ Z_{yx} & 0 \end{bmatrix} \tag{3.45}$$

where the auxiliary impedances are zero but the off-diagonal elements are now of different magnitude. In the general 2-D case, the fields will not have been recorded in directions parallel and perpendicular to electrical strike. The strike direction can be obtained by a straightforward tensor rotation

$$\mathbf{Z}'(\theta) = \mathbf{R}(\theta)\mathbf{Z}\mathbf{R}^{\mathbf{T}}(\theta). \tag{3.46}$$

$\mathbf{Z}'(\theta)$ is the impedance tensor in a reference frame rotated θ degrees from the measurement axes and has the form of equation 3.45. In practise, measurement errors mean that the diagonal elements will not vanish. The electrical strike direction has traditionally been chosen as that angle which minimises the sum of the squares of the auxiliary impedance elements (Swift, 1967). The rotation operator, $\mathbf{R}$, is

given by (eg. Bostick and Smith, 1962; Swift, 1967),

$$\mathbf{R} = \begin{bmatrix} \cos\theta & \sin\theta \\ -\sin\theta & \cos\theta \end{bmatrix} \tag{3.47}$$

which corresponds to an anticlockwise rotation by an angle θ. The components of the rotated impedance tensor are (eg. Vozoff, 1972; Kaufman and Keller, 1981),

$$Z'_{xx} = Z_2 + Z_3 \sin 2\theta + Z_4 \cos 2\theta \tag{3.48a}$$

$$Z'_{xy} = Z_1 + Z_3 \cos 2\theta - Z_4 \sin 2\theta \tag{3.48b}$$

$$\begin{aligned} Z'_{yx} &= -Z_1 + Z_3 \cos 2\theta - Z_4 \sin 2\theta \\ &= -Z'_{xy}(\theta + \pi/2) \end{aligned} \tag{3.48c}$$

$$\begin{aligned} Z'_{yy} &= -Z_2 - Z_3 \sin 2\theta - Z_4 \cos 2\theta \\ &= -Z'_{xx}(\theta + \pi/2) \end{aligned} \tag{3.48d}$$

where

$$Z_1 = (Z_{xy} - Z_{yx})/2 \tag{3.49a}$$

$$Z_2 = (Z_{xx} + Z_{yy})/2 \tag{3.49b}$$

$$Z_3 = (Z_{xy} + Z_{yx})/2 \tag{3.49c}$$

$$Z_4 = (Z_{xx} - Z_{yy})/2 \tag{3.49d}$$

The skew parameter, k (Swift, 1967), can be extracted from $\mathbf{Z}'$ and indicates the extent to which the impedance tensor departs from the zero-diagonal form of 1-D and 2-D earth structure. The skew is calculated from Z_2 and Z_1, both of which are rotationally invariant, using

$$k = |Z_2|/|Z_1|, \tag{3.50}$$

and is therefore also rotationally invariant, taking a value of zero in both the 1-D and 2-D cases.

Chapter 4

Data Acquisition and Processing

4.1 Introduction

Vozoff (1972) showed that MT studies can often provide a useful dataset for the study of sedimentary basins, since there is usually a good electrical conductivity contrast between the sediments and underlying basement. The combination of MT data with controls provided by other geological and geophysical data can overcome the non-uniqueness problem in MT data inversion and lead to meaningful modelling of sedimentary thicknesses.

This chapter discusses the acquisition of an LMT dataset to augment an earlier AMT one for the Mana Pools basin. This dataset was processed as single site data using a robust regression-M method (Huber, 1981), an approach with a proven success record for single site data. The resulting set of impedance estimates are shown to be adequate to resolve the basin structure beneath the conductors, which are known to lie within it. A preliminary assessment of the dimensionality of the data is made but it is clear that a more sophisticated analysis must be performed before a modelling strategy is decided upon.

4.2 The Existing AMT Database

The SPAM MK. II system developed by Graham Dawes was used in 1987 and 1990 to collect AMT measurements in the Mana Pools basin (Whaler and Zengeni, 1993); an account of the instrument and its operation is given in Dawes (1984). SPAM MK. II consists of three connected parts, the sensors, the analogue box and the computer. It is capable of some processing and real time data analysis, allowing an in-field assessment of data quality and helping to catch problems in the equipment and setup early.

Two pairs of grounded porous pot Cu-$CuSO_4$ electrodes were used as electric sensors; these were connected to the sensor box, mid-way between them, typically by 50 m cables and laid out in 100 m long north-south and east-west lines at all sites. It is extremely important for the success of the MT method to have as noise-free an environment as possible. At least regarding cultural noise, the Mana Pools basin provides near ideal conditions; there is no detectable electrical noise in the data because

there is no mains supply to the basin, virtually no use of generators, and it is about 100 km from the Kariba Dam hydroelectric project. Noise due to vibrations caused by wind and traffic is more of a problem; it is not possible to travel far from the roads within the valley but the traffic is minimal. Wind noise may particularly affect sites within the northern part of the profile as much of this region, between sites 2 and 6, is covered in thick scrub more than 2 m in height amongst which some of the sites had to be located.

Variations in the Earth's horizontal magnetic field were measured using two ECA CM11e induction coils with a sensitivity of 50 $mVnT^{-1}$, these are aligned with their long axes parallel to magnetic north-south and east-west and accurately levelled. The measured magnetic field signals are pre-amplified and then passed with the electric field signals to the analogue box. The sensors and analogue box are separated by a 50 or 100 m cable to minimise the chance of magnetic interference affecting the data. Within the analogue box, the signals are amplified and filtered in order to eliminate the high frequencies and DC levels which lie beyond the equipment's measurement range. The data are then divided into four, overlapping frequency bands and amplified again prior to digitisation.

The digitised data are recorded and analysed within the computer box. Prior to recording, the computer checks all filter and amplifier selections and the amplitude and phase response functions of the band pass filters are compared with earlier calibrations to detect any variations. Data acceptance criteria can be defined, for instance the magnitude of the signal power in the magnetic components or the multiple predicted coherency of impedance tensors may have to exceed certain limits. Windows not meeting these criteria are rejected; if the criteria are met then 512-sample time series are recorded for each band and a cosine bell function is used to decimate these down to windows of 256 samples. The data are then converted into the frequency domain using a Fast Fourier Transform (FFT) routine and tensors are calculated using cross- and auto-spectral averages. The accepted time series windows are transferred to floppy disk so that more rigorous processing can be done later.

4.3 Long Period Magnetotelluric Measurements

A long period magnetotelluric (LMT) survey was undertaken in 1995 along the same profile as the earlier AMT survey, the objective being to probe the geoelectric structure of the Mana Pools basin to a greater depth and to constrain the unresolved deeper features from the earlier survey. The LMT equipment was provided by NERC and incorporated a Datataker geologger for recording the signals. The magnetic measurements were made using an EDA fluxgate magnetometer with a sensitivity of 50 $mVnT^{-1}$, consisting of three mutually orthogonal fluxgate magnetometers in a sealed drum. The drum is attached to a spike driven into the ground at the bottom of a hole and then buried. The magnetometers are accurately levelled and orientated to point north, east and vertically downwards and are separated from, and connected to, the geologger by a 30 m cable to reduce any magnetic interference with the rest of the equipment.

The electric sensors were a set of Ag-AgCl electrodes kindly provided by Gerhard Schwarz from the Free University of Berlin. They each consist of an Ag-AgCl kernel made by Jean Filloux, which is surrounded by approximately 1 litre of KCl brine, made up of distilled water and about 30 wt% of KCl. Each probe is about 10 cm in diameter and about 20 cm high; ground contact is made by 4 ceramics

measuring 12 mm in diameter, on the side near the base of each probe. When buried, the electrodes were placed into a hole in the ground in a plastic net filled with a stiff heavy mud of Bentonite clay, the electrode was placed centrally and the net filled with mud up to about four fifths of the electrode's height. The mud is carefully pressed against the walls of the electrode in order to give good electrical contact. The clay mud was used to retain moisture and prevent the electrodes drying out. Although the use of Bentonite has been criticised because it alters the local ground properties, in the conditions prevailing in the area it is extremely difficult to maintain a good electrical contact and prevent drift without it. The electrodes were deployed in an L-shaped configuration with one common and two other electrodes, one to the north and one to the east; electrode line lengths of 100 m were used at each site with the telluric box located at the common electrode. The self potentials of each electrode compared to a designated control electrode were measured in Harare prior to the fieldwork and the electrodes were divided into groups of 3 with similar self potentials. These readings were again checked once the electrodes were deployed in the field and the electrode wire resistance along each line was also measured. The recorded telluric signals are passed through an amplifier with a fixed gain of 100 before any filtering is performed and a further gain of 10, 25 or 100 could be applied using the variable post-amplifier in the NERC LMT system. All the equipment and cables were buried to reduce noise from vibration and to try to ensure a stable temperature environment for the magnetometers. It was hoped that burying the loggers and cables would help reduce system failure due to the extreme heat of the Zambezi Valley and also protect them from the numerous wild animals within the national park; elephants have a habit of pulling on exposed cables.

Only the variations in electric and magnetic fields are important, so electronics within the logger are used to back off the d.c. component of the magnetic field and the self potential between the electrodes; this increases the dynamic range of the recording equipment. The sampling rates used varied between 2 s and 20 s; aliasing effects were avoided by using a low pass, two pole Butterworth filter of 40 s. A 3000 s high pass filter was also used to exclude signals produced by diurnal temperature changes affecting the magnetometer circuitry; this was necessary due to the large variations of as much as 15°C experienced in the region.

All five signals are recorded in the geologger on a 1 Megabyte memory card which can hold up to 10 days data at a 20 s sampling rate. Each logger was powered by a 12 V car battery recharged by an attached solar panel; the solar panels were very effective and meant that the batteries could be left unchanged for the entire 5 weeks of recording. Data acquisition was started and terminated using a laptop PC program supplied by NERC. The software was also used to suspend data logging while the memory cards were replaced. A portable card reading unit was used to read the cards and the time series recorded by the Datataker were viewed in the field using the PC; this enabled some degree of instrument trouble-shooting in situ. The laptop was used to restart the recording once the memory card in the logging unit had been replaced.

4.4 Site Location and Success of the Field Survey

Figure 4.1 shows the site locations from both surveys and table 4.1 lists all the sites and the frequency range of data obtained from each. As can be seen from the site location map, there are no urban areas

Site No.	Site Name	Lat.	Long.	AMT Data	LMT Data	LMT Recording Period	Successful LMT Rec. Time %
1	N1MP	15.76 S	29.35 E	X	X	18.9 - 20.10.95	100
2	-	15.77 S	29.38 E	X	-	-	-
3	-	15.83 S	29.37 E	X	-	-	-
4	-	15.86 S	29.37 E	X	-	-	-
5	-	15.89 S	29.38 E	X	-	-	-
6	N2MP	15.93 S	29.38 E	X	X	19.9 - 20.10.95	93
7	-	15.97 S	29.38 E	X	-	-	-
8	N3MP	16.01 S	29.39 E	X	X	22.9 - 20.10.95	44
9	-	16.07 S	29.41 E	X	-	-	-
10	RUCK	16.12 S	29.40 E	X	X	21.9 - 20.10.95	53
11	VUTI	16.36 S	29.40 E	X	X	16.9 - 21.10.95	83

Table 4.1. Site identification, locations and the dates of recording.

or artificial sources of noise such as power cables within the survey area. Due to the combination of the higher frequencies used and the extremely low resistivity of the region, the anomaly sampled by the earlier AMT profile was not fully resolved at depth. The base of the conductor observed and the structure beneath it were right at the penetration limit of the data. It was hoped that data collected in the LMT period range would be sufficient to "see" beneath the conductor and give a quantitative estimate of its depth extent. Sites from the earlier AMT survey were reoccupied where preliminary analysis of their data indicated them to be of a high quality. Five of the six available LMT systems were used, reserving one as a backup; each system was deployed at a site with the inter-site spacing as even as possible to aid later modelling. Within these limitations, systems were deployed at sites beneath which preliminary analysis also indicated the conductor to lie. The craton site was reoccupied to map the differences in geoelectric structure between the different tectonic regimes of the craton and the valley mobile belt. Two of the new generation Narod LMT loggers were also freighted to Zimbabwe, these were to be deployed in tandem with the older fluxgate systems to gain a comparison of their performance. Unfortunately the two systems were damaged beyond repair during transit and we were unable to use either in the field.

The equipment was deployed between 14th September and 21st October 1995; during this period, the equipment was successfully logging for just over 70% of the total possible recording time of all five sites. All loggers recorded with both their inbuilt filters set, 40s low pass and 3000s high pass and sampling rates initially of 10s; later, once all stations were deployed and it was no longer possible to service them as regularly, the sampling rate was increased to 20s. Figure 4.2 shows a particularly good section of data recorded at a 20 s sampling rate at site 10; the events recorded are of relatively high amplitude for the data as a whole. It should be noted that the vertical magnetic field is very small even with the strong horizontal magnetic fields recorded over this time interval.

Some minor problems with the equipment were encountered such as the filter boards within the Datatakers becoming dislodged during road transit and a few dry solder joints were revealed due to the very high temperatures; these were quickly rectified. The extreme daytime heat of September-October in the Zambezi valley caused problems; daytime temperatures were recorded by the logging units in the mid 40's Celsius and, in light of this, all possible efforts were made to keep them cool. Initial failures at

some sites were suspected to be caused by the excessive temperatures but these were largely overcome.

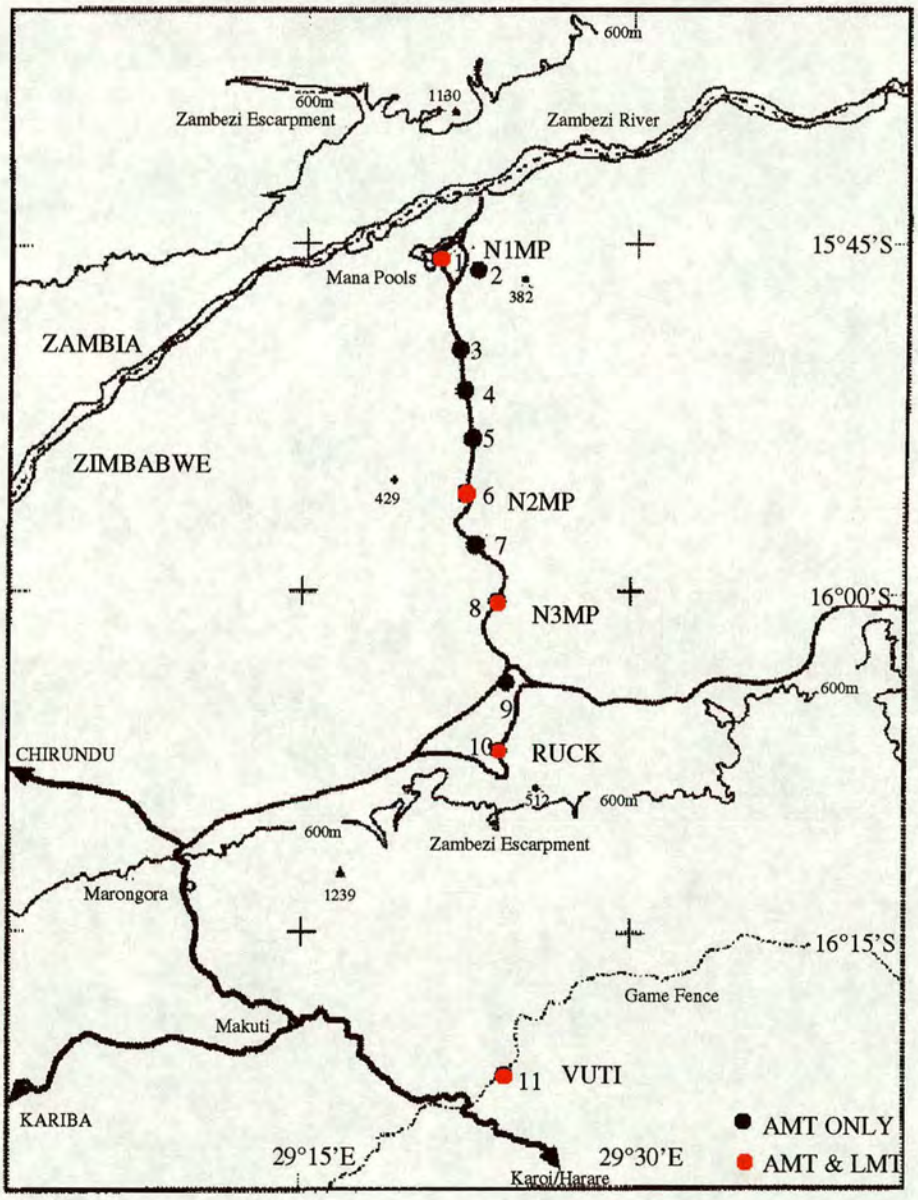

Figure 4.1. Site location map.

A small amount of data was lost from the Datataker memory cards due to flattening of the batteries within the cards. The batteries are only designed to operate up to a maximum temperature of 50°C and were close to this limit throughout much of the daytime. No problems were experienced with the electrodes at any of the sites, following their burial they were saturated with water and took, on average, 24 hours to stop drifting, after which time they remained extremely stable. One site suffered more serious problems peculiar to itself; site 8 failed to record at all between 22nd September and 7th October, a large section of the total recording period. The logger deployed at the site seemed to reset itself on a

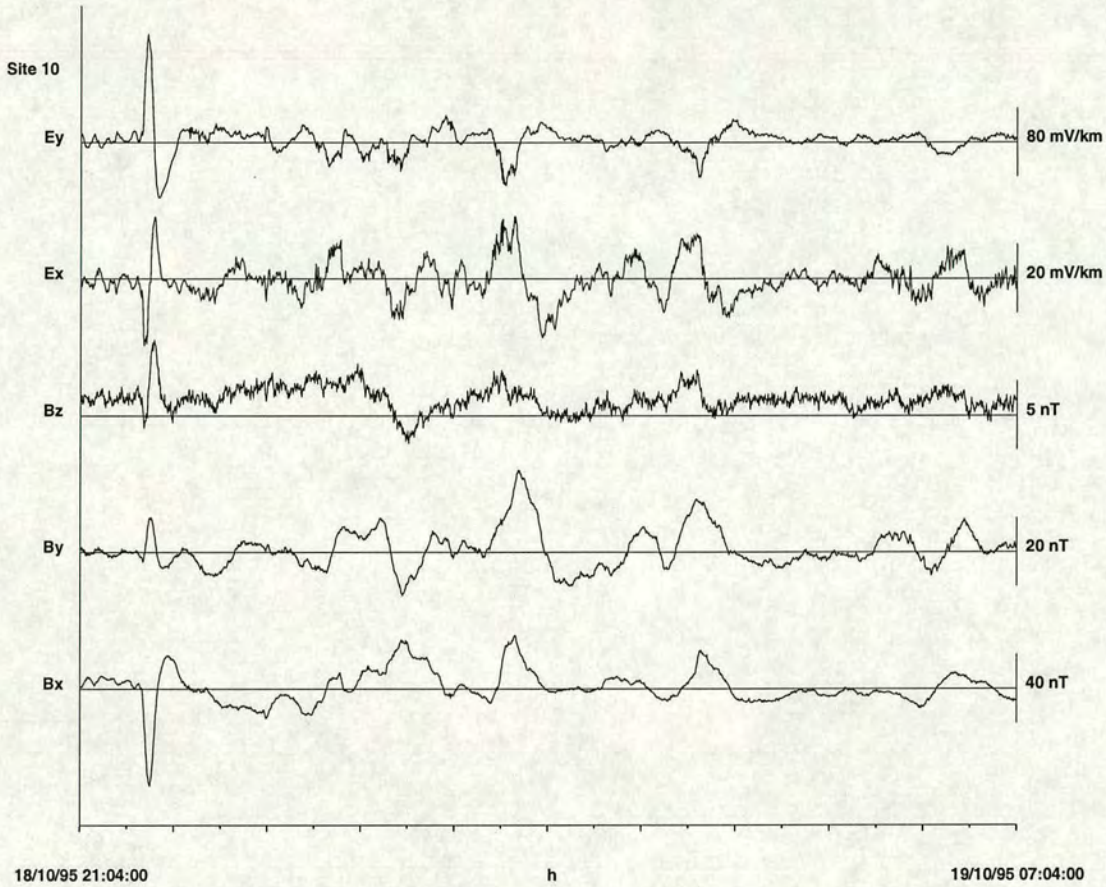

Figure 4.2. A section of time series recorded at site 10. The horizontal axis is time and the vertical axes are individually scaled for each magnetic and electric channel in nT and mV/km respectively. The stated scales refer to the full height of the plotted bar.

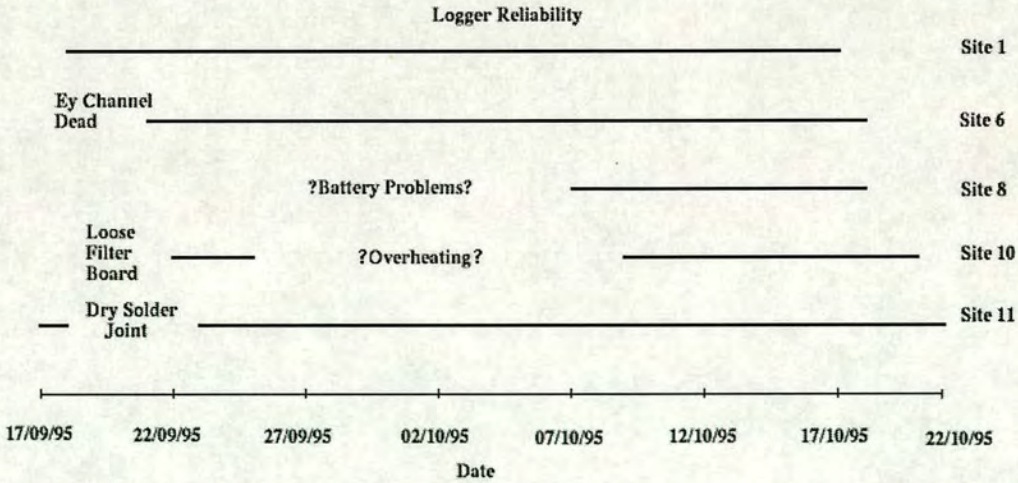

Figure 4.3. Logger reliability and faults.

regular basis losing all its logging schedules, and the time series retrieved from the data cards showed large power spikes on all channels prior to the termination of logging. The cause of these problems was never definitely isolated but may have been associated with the battery used to run that site. This was replaced along with the logger, and the solar panel output voltage was lowered slightly which overcame the problem. Most of the problems were minor and easily overcome without detracting significantly from the experiment. With the exception of site 8, significant periods of simultaneous recording were achieved; figure 4.3 shows a plot of each station and its periods of successful operation.

4.5 The Theory of MT Time Series Analysis

Before the calculation of transfer functions, the data are pre-processed to remove gross data errors such as artificial power spikes. This is done by an averaging procedure using adjacent data points, or simply, by discarding 'poor' sections of the time series. The recorded data are next subsampled; the subset size being chosen based on the lowest frequency of interest and a target value for the final number of degrees of freedom (Chave and Thomson, 1989). These data windows are tapered to reduce spectral leakage (Percival and Walden, 1993) and Fourier-transformed giving many estimates of the spectral components for each frequency. The quality of each estimate is measured against some acceptance criteria, such as coherency, and those accepted are used to calculate transfer function estimates. Estimates of longer periods are made by applying a decimation filter to the recorded time series prior to subsampling it; the sampling interval increases but the number of samples in the data window remains the same. The choice of periods estimated is controlled at high frequencies by the low-pass filter used during recording, and, at low frequencies, by the length of the recorded time series and whether the number of spectral estimates available is sufficient to maintain the required number of degrees of freedom. For the remainder of this section, it is assumed that such pre-processing steps have been taken and that "data" refers to Fourier transforms of windowed subsets of the electric and magnetic fields. These data are then used to calculate the impedance tensor, $\mathbf{Z}$, for frequencies at the centre of narrow frequency bands under the assumption that $\mathbf{Z}$ varies slowly with frequency within each band (Travassos and Beamish, 1988).

The aim of all MT time series processing methods is to achieve accurate, unbiased and repeatable estimates of the impedance tensor as a function of frequency and location (Travassos and Beamish, 1988); this is done by trying to either remove or suppress noise on each of the recorded data channels. The impedance tensor, also known as a transfer function, is a second rank tensor which relates the magnetic field measurements $\mathbf{H} = (H_x, H_y)$ to the electric field measurements $\mathbf{E} = (E_x, E_y)$ via the linear relationship

$$\mathbf{E} = \mathbf{Z}\mathbf{H} + \mathbf{e_E} \tag{4.1}$$

where $\mathbf{e_E}$ is the noise component on the output electric channel. Both $\mathbf{H}$ and $\mathbf{E}$ are complex quantities as they consist of both an in-phase and an out-of-phase component.

Many methods exist for the calculation of the impedance tensor, the simplest of these being a least squares approach to minimise the output channel noise under the assumption that the input magnetic channel is noise free (Sims *et al.*, 1971). A brief description of the least squares estimation procedure for MT data is given here; more detailed descriptions can be found in, amongst others, Travassos and

Beamish (1988), Egbert and Booker (1986) and Larsen (1989). Estimates of $\mathbf{Z}$ are made by solving the system of equations represented by the expression,

$$\mathbf{Z^d} = [\mathbf{H^T H}]^{-1}[\mathbf{H^T E}] \tag{4.2}$$

where [ ] represent power spectral matrices since their elements are the product of two Fourier spectral estimates at the same frequency; $\mathbf{H^T}$ is the transpose of the magnetic field vector. Estimation of the impedance tensor by the method of equation 4.2 proceeds by minimisation of the noise on the electric channel; the magnetic channel is assumed to be noise free. This assumption is unrealistic and the random noise on the magnetic channel is correlated in the auto power terms of each of the equations represented by equation 4.2. Equation 4.3 gives an expression for the calculation of estimates of the impedance elements,

$$Z_{ij} = \frac{(E_i H_j^* \cdot H_i H_i^* - E_i H_i^* \cdot H_i H_j^*)}{(H_x H_x^* \cdot H_y H_y^* - H_x H_y^* \cdot H_y H_x^*)} \tag{4.3}$$

where H_i^* represents the complex conjugate of H_i and each product represents either a cross or auto power spectrum; i and j are subscripts that can represent either the x or y component of the magnetic or electric field. The correlated random noise in the magnetic channels increases the magnitude of the denominator term and causes the impedance estimate to be too small; $\mathbf{Z^d}$ is known as a downward biased estimate of the impedance tensor, $\mathbf{Z}$ (Sims *et al.*, 1971; Travassos and Beamish, 1988; Egbert and Livelybrooks, 1996). An upward biased estimate of the impedance tensor can also be calculated if we define an admittance tensor $\mathbf{Y}$ where,

$$\mathbf{H} = \mathbf{YE} + \mathbf{e_H}. \tag{4.4}$$

This time the output channel is the magnetic channel and the input is the electric channel. In this case, noise is considered only to affect the output magnetic channel and an estimate of the MT admittance $\mathbf{Y}$ can be calculated by solving the system of equations,

$$\mathbf{Y} = [\mathbf{E^T E}]^{-1}[\mathbf{E^T H}]. \tag{4.5}$$

This estimate minimises noise on the output magnetic channel and, by the same process of correlation, gives an impedance value $\mathbf{Z^U}$ which is upward biased by the noise on the electric field, where,

$$\mathbf{Z^U} = \mathbf{Y^{-1}}. \tag{4.6}$$

Equations 4.2 and 4.6 give two different methods for estimating the impedance tensor $\mathbf{Z}$. From these two equations it can be shown (Sims *et al.*, 1971) that there are a possible six least squares estimates for each pair of impedance elements. Each of these six estimates will contain auto power spectral estimates, such as those forming the denominator in equations 4.2 and 4.5, which include a squared random noise term and it is these which cause the least squares impedance estimates to be either upward or downward biased (Gamble *et al.*, 1979). Without more than the basic, single-site four measured fields, a separation of the signal and noise component on each channel is impossible (Travassos and Beamish, 1988). Therefore the upward- and downward-biased estimates are used in order to put some kind of

bound on the true impedance value.

Data collected simultaneously at two sites enables additional remote channels to be added into the analysis and the impedance tensor to be estimated by what is called a remote reference (RR) method (Gamble *et al.*, 1979). The RR method is effective in removing the bias seen in magnetotelluric impedance computations; the two magnetotelluric stations are occupied simultaneously providing two concurrent sets of electric and magnetic field observations. The difference between the computation of the impedance tensor by the two methods can be seen by comparing equation 4.3 to equation 4.7 (see Kaufman and Keller, 1981; Gamble *et al.*, 1979)

$$Z_{ij} = \frac{(E_i H_{jr}^* \cdot H_i H_{ir}^* - E_i H_{ir}^* \cdot H_i H_{jr}^*)}{(H_x H_{xr}^* \cdot H_y H_{yr}^* - H_x H_{yr}^* \cdot H_y H_{xr}^*)} \tag{4.7}$$

where each product represents a cross power spectrum and H_{ir} is the ith component of the magnetic field from the second 'reference' site. Equations 4.3 and 4.7 are used to estimate the components of $\mathbf{Z}$ in the least squares minimisation procedure. There are no auto power terms in the remote reference equation and this eliminates the bias caused by random noise in the auto power terms used in equation 4.3 for the single site estimates.

It has been found that the least squares approach can often produce unsatisfactory impedance estimates because the method assumes that the data have zero mean and independent, identically distributed Gaussian errors. Chave and Thomson (1989) and Egbert and Booker (1986), however, observed that the error variance seemed to depend on the signal power over at least a part of the data series. Egbert and Booker (1986) found that, in many cases, because of the finite spatial scale of the magnetic source fields, the least squares modelling assumptions fail at periods from 5 minutes to several hours. They argue that this failure is due to the assumption that all sources are plane waves of infinite horizontal extent; a part of the misfit between the least squares model and the data is due to deviations from this ideal source field geometry. The size of this portion of the misfit will be related to the power of the inducing source and therefore the assumption of statistical independence cannot hold. Egbert and Booker (1986) estimated the magnitude of the error variance as a function of signal power using plots of squared residuals versus power in the magnetic field. Their results showed that the statistical independence between error variance and signal power could only be justified for data at periods less than 300 s. At longer periods the variances seem to increase systematically with increasing signal power, and, at periods close to an hour, noise power and signal power are essentially proportional. This situation would lead to an extreme violation of the assumptions inherent in the least squares method.

There are also difficulties with the assumption that the data errors are identically distributed; as Chave and Thomson (1989) pointed out, active source field events may produce morphologically complex, small spatial scale current systems and finite duration transient features in the geomagnetic field, causing outliers to occur in patches. These strong signal-active source field events at mid-latitudes tend to occur in the early phase of magnetic storms which are well known to correspond to times of source field complexity (Chave and Thomson, 1989), when the uniform source field assumption is broken. This has ramifications for the assumption that the data errors are evenly distributed and uncorrelated; the bunching of source-related errors in time domain patches may, through Fourier transformation, propagate similar source errors into a broad band of frequencies.

Clearly, the main reason these statistical assumptions are invalidated is a breaking of the modelling assumption of a plane source field of infinite horizontal extent. The failure of this model assumption makes large deviations and hence significant outliers possible, a situation that is poorly modelled by a Gaussian error distribution. The variation of power distribution with time or non-stationarity of both signal and noise in MT data means that the error distribution in the frequency domain not only contains outliers but can often conform more to a long tailed asymptotic distribution than a Gaussian one (Egbert and Livelybrooks, 1996). The failure of all three modelling assumptions means that least squares estimates of the transfer functions and their errors are not robust.

Some of the problems of the least squares method can be overcome by applying a weighted least squares methodology to the problem. This can be done most simply by rescaling the field components by dividing by a calculated standard deviation σ_i for each data point i. This overcomes the unequal variance distribution within the data.
Thus, for a system,

$$\mathbf{E} = \mathbf{ZH} + \mathbf{e} \tag{4.8}$$

rescaled field components can be defined where,

$$\begin{aligned} \mathbf{E_i'} &= (\mathbf{E_i}/\sigma_i) \\ \mathbf{H_i'} &= (\mathbf{H_i}/\sigma_i) \\ \mathbf{e_i'} &= (\mathbf{e_i}/\sigma_i) \end{aligned}$$

so that,

$$\mathbf{E_i'} = \mathbf{ZH_i'} + \mathbf{e_i'} \tag{4.9}$$

where $\mathrm{var}(\mathbf{e_i'}) \equiv 1$.

Egbert and Booker (1986) calculated an error scale by assuming a linear relationship between the error variance and signal power; this relationship is frequency dependent and estimated using empirical signal to noise power plots. The least squares minimisation is then expressed,

$$\sum_{i=1}^{N} (\mathbf{E_i'} - \mathbf{ZH_i'})^2 \tag{4.10}$$

this can further be expressed as,

$$\sum_{i=1}^{N} w_i r_i^2 = \sum_{i=1}^{N} w_i (\mathbf{E_i} - \mathbf{ZH_i})^2 \tag{4.11}$$

where N is the number of estimates and w_i are proportional to $1/\sigma_i^2$, r_i are the residuals between the observed and modelled points. Use of the weighted least squares estimates can overcome the problem of unequal variances within the data and, according to the Gauss-Markov theorem (Graybill, 1976, p.219), will give the best linear unbiased estimate of the transfer function **Z**.

A weighted least squares approach gives more acceptable transfer functions because it does not give too much weight to high signal power events, whereas with traditional least squares estimates these events can sometimes dominate the calculation of the transfer function and, as we have seen, are likely to outlie the Gaussian distribution. Weighted least squares also guarantees the validity of the equal variance assumption upon which the calculation of estimation errors relies. However, Chave and Thomson (1989) argue that a weighted least squares approach is rarely satisfactory for MT data due to the non-stationarity of the error variance structure itself and the common failure of our modelling assumptions often leads to transfer function estimates with unrealistically small error estimates (Smith and Booker, 1988). Clearly we have to abandon the least-squares assumptions and look for a basis from which to estimate the MT impedance tensor for a non-Gaussian error distribution; this new method should be robust so that a few bad data points cannot cause the whole process to fail.

A robust alternative to the least squares estimate is the 'regression M-estimate' (RME) (Huber, 1981); this has been advanced by many authors including Egbert and Booker (1986), Chave and Thomson (1989), Egbert and Livelybrooks (1996) and Sutarno and Vozoff (1991). Robust methods are useful because they remove contamination by outliers and other deviations from the optimal Gauss-Markov regression estimates (Chave and Thomson, 1989). They are robust in the sense that they are relatively insensitive to moderate amounts of non-stationarity and outliers or small inadequacies of the model, and they react gradually rather than abruptly to perturbations of either (Chave and Thomson, 1989). Robust methods are sensitive only to outliers in the dependent variable (**E**), however, as already discussed, the response functions will also be biased downwards by noise in the independent (**H**) variable; this can again be overcome by using a remote reference methodology (Chave and Thomson, 1989). However, the assumption that noise is restricted to the output channel is approximately valid if the magnetic field can be measured much more accurately than the electric field; the assumption is normally valid in practice, except when the magnetic channel is contaminated by artificial noise (Sutarno and Vozoff, 1991). The RME both minimises the difference between prediction and observations and prevents data sections with a few bad points from dominating the estimate. To do this, estimates of the transfer function **Z** are sought which minimise the expression,

$$\sum_{i=1}^{n} \rho\left(r_i/\sigma\right) = \sum_{i=1}^{n} \rho\left\{\left(E_i - \sum_{j=1}^{2} Z_j H_{ij}\right) \Big/ \sigma\right\} \tag{4.12}$$

for n observations of the ith electric field component where j=1,2 correspond to x,y magnetic field components, Z_j will have elements corresponding to the MT impedance elements Z_{xj} and Z_{yj}. Here $\rho(r)$ is some error dependent weighting of the minimisation term known as the loss function and σ is an error scale parameter. The loss function $\rho(r)$ can take many forms; a standard hybrid (Huber, 1981) is used by Egbert and Booker (1986) and Sutarno and Vozoff (1991) and takes the form,

$$\rho(r) = \begin{cases} \frac{r^2}{2}, & |r| < r_o \\ r_o|r| - \frac{r_o^2}{2}, & |r| \geq r_o \end{cases} \tag{4.13}$$

r_o is known as the tuning constant and a value of r_o=1.5 is used because it gives better than 95 % efficiency with outlier-free Gaussian data (Chave and Thomson, 1989).

By phrasing the problem in this form, the algorithm can behave in a different manner depending on

the size of the residual error it encounters. For small errors, the minimisation follows an L_2 form; this implies a Gaussian error distribution, and the term L_2 means that the measure of misfit that is minimised is equal to the Euclidean length squared, as in the least squares method. For higher errors, the algorithm can follow an L_1 minimisation; this implicitly assumes that the data follow a long-tailed exponential distribution and downweights outliers (Menke, 1984, pp.190-194). The term L_1 means that the measure of misfit that is being minimised is the modulus of the length (Parker, 1994, pp 13-14). This results in robustness of the M-estimator for data with a "least informative" distribution (Huber, 1981). The transition between these two different approaches occurs at a value of σr_o for the unscaled residuals, where σ is the error scale employed in equation 4.12. We can therefore use the error scale to decide what magnitude of residual is considered to be large. The value of r_o=1.5 times the standard deviation of the ideal Gaussian error distribution works well for a Gaussian error distribution contaminated by a few outliers (Egbert and Booker, 1986).

The minimum of equation 4.12 can be found by differentiating the expression, setting it equal to zero and solving the resulting set of equations.

$$\sum_{i=1}^{n} \psi(r_i/\sigma) H_{ij} = \sum_{i=1}^{n} \psi \left\{ \left(E_i - \sum_{j=1}^{2} Z_j H_{ij} \right) \Big/ \sigma \right\} H_{ij} = 0 \tag{4.14}$$

where $\psi(r) = d\rho(r)/dr$, and is known as the influence function. The solution of this expression can be computed iteratively using a least squares algorithm which downweights outliers by setting

$$w(r) = \frac{\psi(r)}{r} \tag{4.15}$$

where $w(r)$ now weights the data points according to their residual misfit. So, starting with a least squares estimate of the transfer function $\hat{\mathbf{Z}}_o$ and error scale $\hat{\sigma}_o$ we can calculate predicted and residual electric fields from equation 4.14.

$$\begin{aligned} \hat{E}_{io} &= \sum_{j=1}^{2} \hat{Z}_{jo} H_{ij} \\ \text{and;} \quad r_{io} &= E_i - \hat{E}_{io} \end{aligned}$$

a modified 'observation' can then be calculated depending on the size of r_{io} where

$$E_{i1} = \hat{E}_{io} + w\left(r_{io}/\hat{\sigma}_o\right) r_{io}. \tag{4.16}$$

For ρ given in equation 4.13, the corresponding Huber weight function is

$$w(r) = \begin{cases} 1, & |r| < r_o \\ \frac{r_o}{|r|}, & |r| \geq r_o. \end{cases}$$

This means that if the residuals are less than r_o, the weighted observation is identical to the original one, whereas if the residual is greater than r_o, the observation is downweighted and pulled closer to its predicted value. The modified observations are now used instead of the original ones and a new least

squares estimate of the transfer function can be calculated,

$$\hat{\mathbf{Z}}_1 = (\mathbf{H}^{\mathbf{T}}\mathbf{H})^{-1}(\mathbf{H}^{\mathbf{T}}\mathbf{E}_1) \tag{4.17}$$

along with a new error scale estimate $\hat{\sigma}_1$.

Egbert and Booker (1986) apply this procedure iteratively until convergence to the solution of equation 4.14 is achieved. The algorithm performs as a sort of weighted least squares procedure with a data adaptive weighting scheme. Because the Huber weighting system falls off slowly for large residuals, never descending to zero, inadequate protection is provided against the severe outliers observed in magnetotelluric data. To eliminate the worst outliers completely two final iterations are performed using a more severe weighting function (Sutarno and Vozoff, 1991; Chave and Thomson, 1989).

The RME is an improvement on other methods of transfer function estimation in most situations. On long period (> 10 s) MT data, the period range of measurement for this LMT study, the superiority of the robust RME has been clearly demonstrated (Egbert and Booker, 1986; Egbert and Livelybrooks, 1996). Problems with the technique have been highlighted by some authors. Egbert and Livelybrooks (1996) found that, within the dead band, the low signal-to-noise ratio can lead the regression-M method to throw the rare good data points away as outliers while retaining the noise. Similar behaviour can occur in a much wider frequency band for particularly badly contaminated data sets; weighted section averaging can lead to the downweighting of a section with only a very few large outliers and if all sections are contaminated with outliers there may be no clean sections of any useful duration (Larsen, 1989). For such particularly contaminated data sets, more complex robust methods may need to be used, such as that outlined by Larsen *et al.* (1996).

The problem with all the methods of time series analysis discussed here is their reliance on Fourier transform methods. The Fourier transform method is favoured over other mathematical decompositions because often the energy at any frequency interval of the Fourier power spectrum is directly related to the energy in the same frequency interval for the signal source (Chant and Hastie, 1992). For this to be true, the stationary source assumption has to be made; this assumption as we have seen does not hold. Chant and Hastie (1992) discuss time-frequency distribution (TFD) analysis techniques as an alternative method of transfer function estimation and a way of minimising the non-stationary bias; algorithms to achieve this are currently under development but are not discussed here.

4.6 Error Calculation on Impedance Estimates

It is important that the error bounds placed on the impedance tensor estimates are consistent with the observed data and their associated errors. Inversion procedures implicitly assume that the data and model parameters sought are related; the parameter is estimated on the basis of the data and the data errors will tend to be mapped onto the model parameters (Menke, 1984). This in turn implies that the estimated transfer functions are themselves random variables which can be described by a distribution in the same way that the data can. We can therefore use a simple statistical approach to calculate error bounds on each frequency estimate of the transfer function; this is done by defining a property of the data called the covariance. The covariance is the correlated data equivalent of the variance and similarly

describes the overall width of the distribution; this is a function of the data quality, such that noisy data will give a wide distribution while good data will give a narrower one. In the simple univariate case, the variance is calculated by multiplying the distribution by a function that is zero near the centre and grows on either side of the peak; the function used is the parabola $(x - \langle x \rangle)^2$, where $\langle x \rangle = \hat{E}(x)$ is the mean or expected value of the random variable x, where

$$\hat{E}(x) = \int_{-\infty}^{+\infty} xP(x)dx \tag{4.18}$$

and $P(x)$ is the probability distribution. The area under the resulting function is the variance σ^2 and its square root σ is a measure of the width of the distribution (Menke, 1984).

$$\sigma^2 = \int_{-\infty}^{+\infty} (x - \langle x \rangle)^2 P(x)dx \tag{4.19}$$

Expanding this concept to the correlated data situation that we experience with magnetotelluric data, we can define a joint distribution $P(\mathbf{x})$, which is the probability that the first datum will lie close to x_1, the second close to x_2, etc. (Menke, 1984). In the case of magnetotelluric data we can define x_1 to be an estimate of the power in the magnetic field at a discrete frequency and x_2 a like electric field estimate. We would expect to see a correlation between these data, and the joint distribution is constructed to take account of this (Menke, 1984). We can use the function $[x_1 - \langle x_1 \rangle][x_2 - \langle x_2 \rangle]$ to divides the (x_1, x_2) plane into four quadrants of alternating sign, centred on the centre of the joint distribution. Uncorrelated distributions tend to lie equally in all four quadrants of the (x_1, x_2) plane while correlated distributions tend to concentrate in two opposing quadrants. The covariance is a measure of this correlation and is calculated by multiplying the distribution by this function and summing the area under the resulting curve. Values close to zero are obtained for uncorrelated distributions while correlated distributions give positive or negative areas depending on the sense of correlation.

$$cov(x1, x2) = \int_{-\infty}^{+\infty} \cdots \int_{-\infty}^{+\infty} [x_1 - \langle x_1 \rangle][x_2 - \langle x_2 \rangle]P(\mathbf{x})dx_1 \cdots dx_N \tag{4.20}$$

The covariance characterises the basic shape of the distribution; its diagonal elements are a measure of the width of the data distribution, and the off-diagonal elements indicate the degree to which pairs of data are correlated (Menke, 1984).

If the data distribution is known, then the distribution for any function of the data, including estimated model parameters, can be found (Menke, 1984). In the case of a linear function such as $\mathbf{Z} = (\mathbf{H^T H})^{-1}(\mathbf{H^T E})$ then the covariance of the resulting distribution is given by (Meju, 1994),

$$\begin{aligned} Cov(\mathbf{Z}) &= \mathbf{L}[Cov(\mathbf{E})]\mathbf{L^T} \\ \text{where; } \mathbf{L} &= (\mathbf{H^T H})^{-1}\mathbf{H^T} \end{aligned} \tag{4.21}$$

and for a discrete function (Huber, 1981),

$$Cov(\mathbf{Z}) = \frac{1}{n-p}\left(\sum r_i^2\right)(\mathbf{H^T H})^{-1} \tag{4.22}$$

The assumptions made in this formulation are that the data are Gaussian, uncorrelated and of equal

variance. The square roots of the diagonal estimates of $Cov(\mathbf{Z})$ may be taken as the standard deviations of the least squares parameter estimates and may be used to define confidence limits for the model parameters (Meju, 1994).

In the robust RME case, the errors on the calculated impedance estimates are also derived from the parameter covariance matrix $Cov(\mathbf{Z})$; however none of the aforementioned assumptions are tenable. Instead Huber (1981) defines the asymptotic covariance matrix of the robust estimate $\mathbf{Z}$ to be,

$$Cov(\mathbf{Z}) = \frac{\sigma^2 \hat{E}\psi^2}{[\hat{E}\psi']^2}(\mathbf{H^T H})^{-1} \tag{4.23}$$

where ψ' is the derivative of the influence function.
If we consider the final (nth) iteration of the RME algorithm and apply the discrete approximations for $\hat{E}\psi^2$, $\hat{E}\psi'$ and σ^2, then this expression can be approximated to (Egbert and Booker, 1986),

$$\frac{\frac{\hat{\sigma}^2}{N-4}\sum_i \psi(\frac{r_{in}}{\hat{\sigma}_n})^2}{\left[\frac{1}{N}\sum_i \psi'(\frac{r_{in}}{\hat{\sigma}_n})\right]^2}(\mathbf{H^T H})^{-1} = \frac{\frac{1}{N-4}\sum_i r_{in}^2(\mathbf{H^T H})^{-1}}{\left[\frac{1}{N}\sum_i \psi'(\frac{r_{in}}{\hat{\sigma}_n})\right]^2} \tag{4.24}$$

where N is the number of estimates and $\sum_i r_{in}^2$ is computed from the modified observations of equation 4.16 and for ρ given by equation 4.13. ψ' will take values of 0 or 1 depending on the magnitude of the residual for that estimate (Egbert and Booker, 1986). This means that the denominator in equation 4.24 is simply the fraction of data points that are considered good.

This approach is not the only method of transfer function error estimation. Other parametric approaches exist as do non-parametric techniques, such as the popular jackknife method; this is not discussed here, but details can be found in Efron (1982), Chave and Thomson (1989) and Thomson and Chave (1989).

4.7 Time Series Analysis of the MT Data

Sutarno and Vozoff (1991) have shown that the robust M-estimation technique can produce usable MT impedance functions even under conditions of severe noise contamination and in the absence of remote reference data. The difficulties we experienced with equipment failure and synchronising the logging units in the bush prohibited the realistic use of the remote reference method with the LMT data collected in 1995. Therefore it was decided to process the LMT data as single site data using Gary Egbert's robust RME code obtained from the Internet. A brief description of the software package is given here; for a more detailed account the reader is referred to the release notes supplied with it.

The transfer function estimation software is split into three separate stages. Stage 1 uses the program **clean** to clean up any isolated outliers in the time domain. The cleaning routine takes very short sections of the time series, typically 7 samples, and calculates the mean data point for that section and the largest absolute deviation of the data from the mean. If this maximum deviation is higher than an arbitrary value, dependent on the sampling rate, the level of source-field activity and the sensitivity of the sensors, then that window is cleaned by checking each point individually and averaging suspected outliers with their surrounding samples.

Clean outputs the cleaned time series in a format which can then be read by stage 2, **dnff**, the windowing and Fourier transformation routine. The Fourier transform used is a hybrid between a standard FFT routine and a cascade decimation procedure (Wight and Bostick, 1986); the goal is to use data segments that are as short as possible given the desired resolution in the frequency domain, since shorter segments reduce the quantity of data affected by individual correlated error clusters. Windows of 128 data points overlapping by 32 were taken for sampling rates of 10 and 20 s; from these we can calculate Fourier coefficients for the highest frequencies of interest. Longer period coefficients are obtained by passing the data window through a digital low pass filter and decimating the resulting smooth time series. Four levels of decimation were performed; each subsamples the previous level at every fourth point and windows of 128 samples are again taken. For data sampled at 10 s, this gives windows of a total length of 1270 s for decimation level 1 (undecimated), 5080 s for level 2, 20320 s for level 3 and 81280 s for level 4. Corresponding sampling rates are therefore 10 s, 40 s, 160 s and 640 s respectively. The data are tapered using a pi-prolate spheroidal data window (Thomson, 1982) and pre-whitened (see Percival and Walden, 1993, p218-220) to protect against spectral leakage (Percival and Walden, 1993). **Dnff** corrects the time series for clock drifts and applies filter corrections to all five channels. The magnetic and electric channels are corrected for variations with frequency of the instrument response using NERC response functions and software supplied by Dr. Andreas Junge (pers. comm., 1995). The magnetometer and telluric box serial numbers are passed to a subroutine which calculates both the instrument response and the filter responses at each of the frequencies at which coefficients are calculated. The data are converted to physical units and output to a file to be read into stage 3 of the code, **tranmt**, which calculates the transfer functions from the stored Fourier coefficient data. Program **tranmt** calculates robust transfer functions and their uncertainties by the RME method discussed in § 4.5 and outputs Parkinson vectors, apparent resistivities and phases and the full MT impedance tensor with uncertainties. **Tranmt** is supplied with a band set-up file by the user, detailing the frequency bands to stack. The approach taken to frequency band selection involves calculating all possible Fourier coefficients for each decimated data section and then calculating bands for equally spaced log-period values. Care was taken that the frequency bands for adjacent periods didn't overlap and that each period estimate was therefore independent of its neighbours in the frequency domain. Bands were selected so that, wherever possible, frequencies were calculated using Fourier coefficients from the lowest decimation level possible. This keeps the data windows as short as possible, increasing the number of estimates available and reducing the probability of an individual window and its coefficients being contaminated by a correlated error cluster resulting from the breaking of the stationary source assumption.

4.8 The Processed Data

The processed LMT data are shown in figures 4.4 to 4.8 along with the AMT data processed using the same software by Dr. Phil Jones (pers. comm., 1995). The data are displayed in their unrotated measurement axes, with the xy-component representing a north-south directed electric field and the yx-component representing the east-west electric fields. Apparent resistivity and phase are plotted with the phase for both components displayed in the first quadrant. The cross correlation between the measured electric field and that predicted by computation using the calculated impedance elements and

the measured magnetic field is averaged over all estimates to give an estimated coherence between the observed and predicted electric fields for each frequency. This is plotted and can be used to assess the quality of the recorded data in terms of both the amount of noise on the data and the amount of deviation from the assumed linear relationship between the observed magnetic and electric fields. The higher the coherence, the lower the amount of signal introduced by non-linear factors such as source field effects and measurement errors. While coherency can be affected by non-random noise sources it does give a guide to the validity of the assumptions under which we process and model the data.

The linearity assumption is expressed by equations 3.41 and 3.42, and the predicted coherencies can be written as,

$$Coh_x(\omega) = \overline{E_{x,i} \cdot E^*_{x,p,i}} \tag{4.25}$$

$$Coh_y(\omega) = \overline{E_{y,i} \cdot E^*_{y,p,i}} \tag{4.26}$$

where the overbar indicates that the estimate is an average of all the spectra available. The predicted electric field components $E^*_{x,p,i}$ and $E^*_{y,p,i}$ are given by

$$\begin{aligned} E^*_{x,p,i} =& \Re(Z_{xx}) \cdot \Re(H_{x,i}) - \Im(Z_{xx}) \cdot \Im(H_{x,i}) \\ &+ \Re(Z_{xy}) \cdot \Re(H_{y,i}) - \Im(Z_{xy}) \cdot \Im(H_{y,i}) \\ &- i[\Re(Z_{xx}) \cdot \Im(H_{x,i}) + \Im(Z_{xx}) \cdot \Im(H_{x,i}) \\ &+ \Re(Z_{xy}) \cdot \Im(H_{y,i}) + \Im(Z_{xy}) \cdot \Re(H_{y,i})] \end{aligned} \tag{4.27}$$

and

$$\begin{aligned} E^*_{y,p,i} =& \Re(Z_{yx}) \cdot \Re(H_{x,i}) - \Im(Z_{yx}) \cdot \Im(H_{x,i}) \\ &+ \Re(Z_{yy}) \cdot \Re(H_{y,i}) - \Im(Z_{yy}) \cdot \Im(H_{y,i}) \\ &- i[\Re(Z_{yx}) \cdot \Im(H_{x,i}) - \Im(Z_{yx}) \cdot \Im(H_{x,i}) \\ &+ \Re(Z_{yy}) \cdot \Im(H_{y,i}) - \Im(Z_{yy}) \cdot \Re(H_{y,i})] \end{aligned} \tag{4.28}$$

after Kaufman and Keller (1981), where $\Re$ and $\Im$ indicate the real and imaginary part respectively.

An initial assessment of the tensor dimensionality is given by the skew plots. Section 3.6 shows how the impedance tensor takes different forms depending on whether the geological structure is one-, two- or three-dimensional. For a tensor measured along its principal axes, that is with the (x,y) cartesian co-ordinates parallel and perpendicular to electrical strike, the auxiliary impedance elements are equal to zero or at least very small for one- and two-dimensional structures. For a three-dimensional structure, the auxiliary elements will be larger and the difference in the diagonal elements smaller. Swift (1967) defined the skewness parameter, k, as

$$k = \frac{|Z_{xx} + Z_{yy}|}{|Z_{xy} - Z_{yx}|}. \tag{4.29}$$

Skew is invariant to rotation and is small (< 0.2) (e.g. Ritter, 1995) for one- and two-dimensional structures.

Data curves are also shown after the data have been rotated into principal co-ordinate directions; the

rotation this requires from the measurement co-ordinate system is determined and performed using the method proposed by Swift (1967). Since the earth is never perfectly one- or two-dimensional and the data never measured without some error there is no co-ordinate system the data can be rotated into which will zero the auxiliary impedance elements. Instead, the data are rotated to the angle which minimises the auxiliary elements and maximises the magnitude of the two off-diagonal elements; Swift (1967) defined the principal axes as those which maximise the quantity,

$$\left|Z'_{xy}(\theta_o)^2 + Z'_{yx}(\theta_o)^2\right|. \tag{4.30}$$

The expression for the necessary rotation, after Swift (1967), is then given by,

$$\theta_o = \frac{1}{4}\arctan\frac{(Z_{xx} - Z_{yy})(Z^*_{xy} + Z^*_{yx}) + (Z^*_{xx} + Z^*_{yy})(Z_{xy} + Z_{yx})}{|Z_{xx} - Z_{yy}|^2 - |Z_{xy} + Z_{yx}|^2} \tag{4.31}$$

where θ_o is the angle that rotates the measurement axes anticlockwise to the principal axes. This can be applied via equations 3.47 to 3.48d.

Vertical magnetic field measurements were also taken during the LMT survey, allowing calculations of the magnetic transfer functions to be made. The vertical magnetic field component is induced by the horizontal magnetic components when they encounter lateral changes in resistivity (Parkinson, 1959); this is expressed by the equation,

$$H_Z(\omega) = Z_H(\omega)H_X(\omega) + Z_D(\omega)H_Y(\omega) \tag{4.32}$$

where Z_H and Z_D are the complex frequency-dependent magnetic transfer functions. These transfer functions are represented visually in figure 4.9 in terms of Parkinson vectors (Parkinson, 1962). Introducing the notation of Hobbs (1992) where, $A_I = \Im Z_H$, $A_R = \Re Z_H$, $B_I = \Im Z_D$ and $B_R = \Re Z_D$, the lengths of the two Parkinson vectors are defined as,

$$\sqrt{A_R^2 + B_R^2} \quad \text{and} \quad \sqrt{A_I^2 + B_I^2} \tag{4.33}$$

for the real and imaginary vectors respectively, and their orientations are given by.

$$\arctan\left(\frac{-B_R}{-A_R}\right) \quad \text{and} \quad \arctan\left(\frac{B_I}{A_I}\right) \tag{4.34}$$

In the Parkinson convention, the vectors point towards regions of relatively lower resistivity. The behaviour of the two induction vectors depends on the proximity of lateral resistivity changes and the frequencies of investigation. Induction arrows are largest close to lateral resistivity changes and decrease with increasing distance from them. The scale of the resistivity anomaly relative to the skin depth of the electromagnetic signals affects the relative orientation of the two vectors. If the induction anomaly is at a depth which greatly exceeds the skin depth, then both vectors have zero magnitude. For a two-dimensional earth, induction vectors lie parallel or anti-parallel to each other; for a near surface anomaly with a depth extent that is small relative to the skin depth, the real and imaginary arrows will point in the same direction. However, for anomalies within the range of the skin depth, the real and imaginary induction vectors point in opposite directions to each other (Ritter, 1995). More complicated relationships are generated by a three-dimensional earth.

4.9 Discussion of the Results

Figures 4.4 to 4.8 show the data for both frequency bands at sites for which LMT data were collected. The data for the two surveys do not overlap - there is a narrow gap between periods of 23 and 93 s. The effective data gap, however, covers a wider frequency range because of the poor quality of certain estimates, as can be seen by a study of the data coherence plots. For modelling the data it would be unwise to accept data of too low coherency; Vozoff (1972) claims that data of coherency less than 0.90 do not usually give reasonable results but I have found in practice that data down to a coherency of 0.80 are generally acceptable. Between 0.5 s and 10 s, we see the MT dead band where the source signal strength is low. There is a corresponding drop in coherency in this range where the fields measured become dominated more by random noise and less by coherent signal; this effect can be seen particularly at sites 1, 6 and 11. Typically we also see poor coherency at the highest frequencies of the LMT survey, often the desired coherency is not achieved until periods of at least 200 s. The reasons for this are suspected to be a high background noise level on the magnetic channels and the poor sensitivity of the fluxgate magnetometers in this period range. The degree to which these effects are seen varies considerably between the sites.

The data gap exaggerated by the range of frequencies over which the coherency is poor makes it more difficult to assess whether the two surveys are consistent with each other or if there is some offsetting bias between the two sections of the resistivity curves. On inspection, the two frequency bands appear consistent; the increase in resistivity seen in the LMT data is rapid up to approximately 1000 s but then is seen to level off at the longest periods. For the sites that overlie the Mana Pools basin, the LMT resistivity curves separate so that the unrotated yx data are more resistive than the xy data; this is also seen in the AMT data at the low frequency end of its measurement range. A separation in the phase curves is apparent with increasing period, which would seem to indicate an increase in dimensionality of the basin geology with period; certainly, the apparent resistivity and phase appear very one-dimensional at high frequencies. In the northern portion of the basin, the skew values remain very low for all periods barring those for which the coherency is poor; this indicates a one- or two-dimensional environment across the entire period range. For the southern sites, adjacent to and on the Zimbabwe craton, the skew values are higher at longer periods, rising to above 0.4 for the longest periods at site 11, implying that the two-dimensional assumption will not hold for these periods at this site. The data from site 11 are different to those from the other sites, in that we see the xy data with a higher resistivity than the yx data over the LMT period range. This represents the effect of the transition from the sedimentary basin environment to a cratonic environment with a different electrical structure. The offset between the xy and yx apparent resistivity curves in the higher frequencies at site 11 suggests that the data are affected by a static shift and makes it difficult to interpret their behaviour over the AMT frequency range. Static shift is more of a problem at sites with highly resistive surface layers (Jones, 1988) and no significant static shift is discernible at any of the sites within the basin where we would expect to see a more conductive near surface structure.

The rotation angle applied to the data from equation 4.31 is quite variable across the AMT frequency range; this may be due to the near one-dimensional nature of the data over much of the higher frequencies. For the lower end of the AMT frequency range and for the LMT data, the rotation angle tends to a very low value; this indicates that the measurement axes are very close to the principal axes.

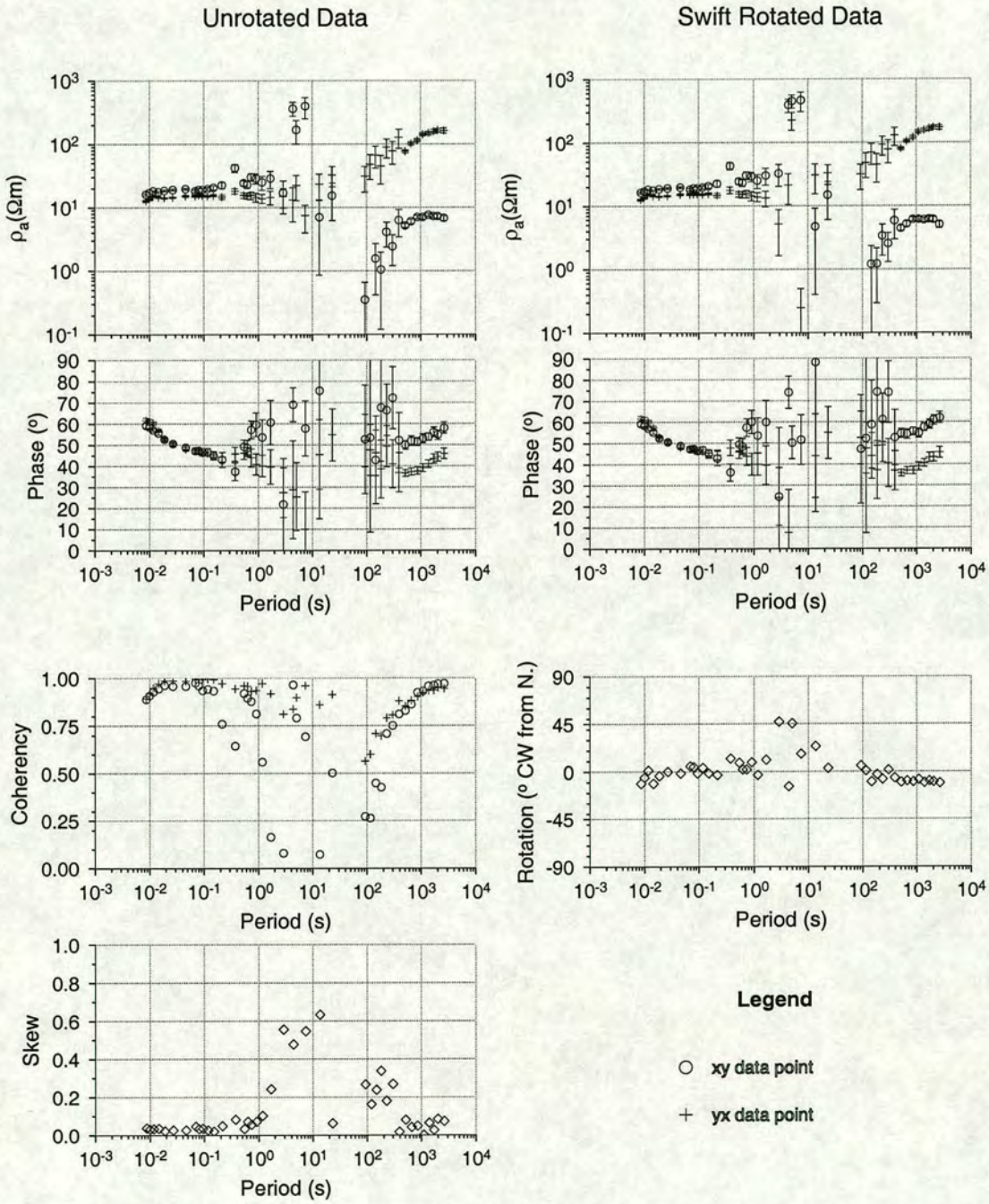

Figure 4.4. The processed data from site 1, plotted with 2 standard deviation error bars.

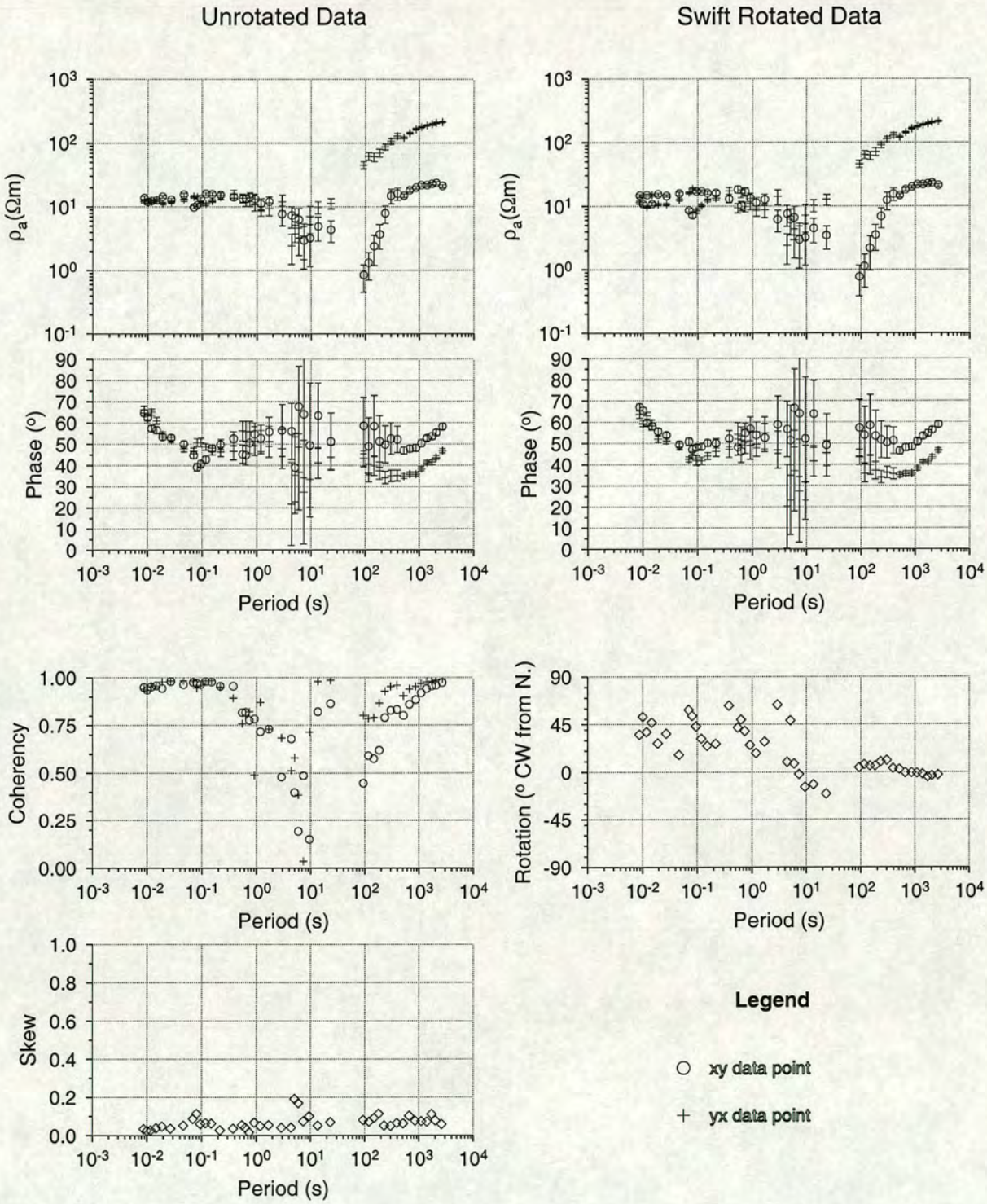

Figure 4.5. The processed data from site 6, plotted with 2 standard deviation error bars.

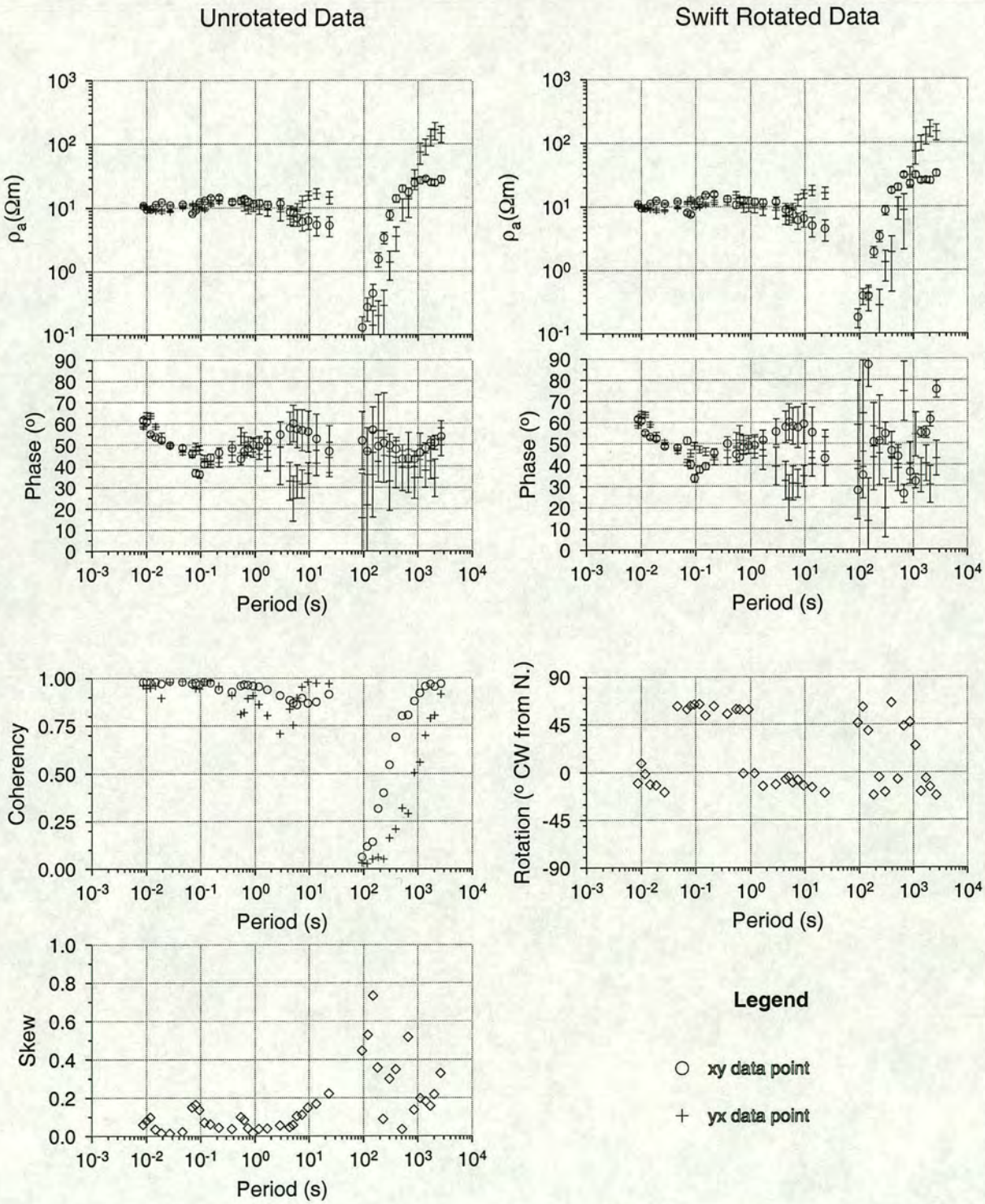

Figure 4.6. The processed data from site 8, plotted with 2 standard deviation error bars.

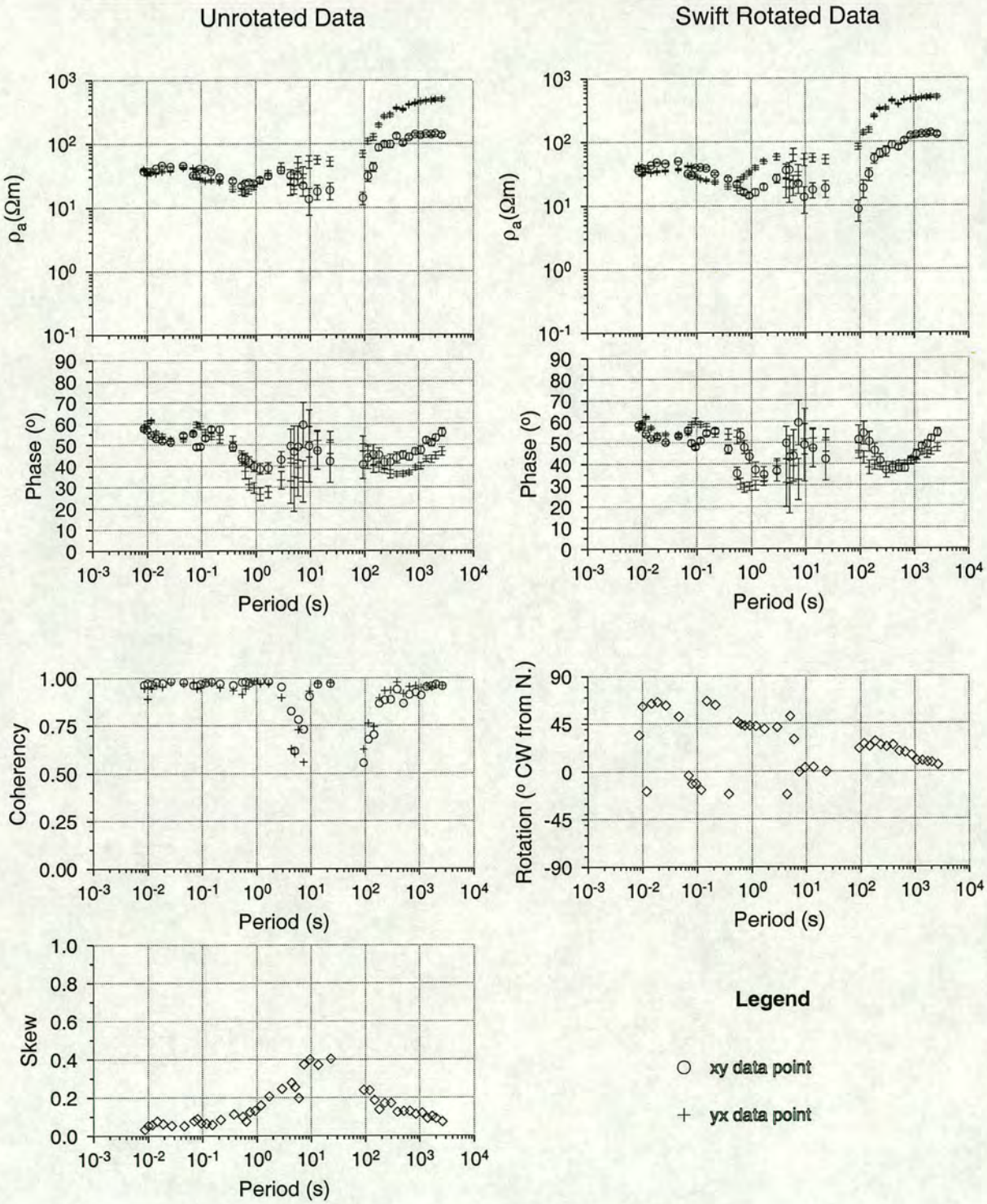

Figure 4.7. The processed data from site 10, plotted with 2 standard deviation error bars.

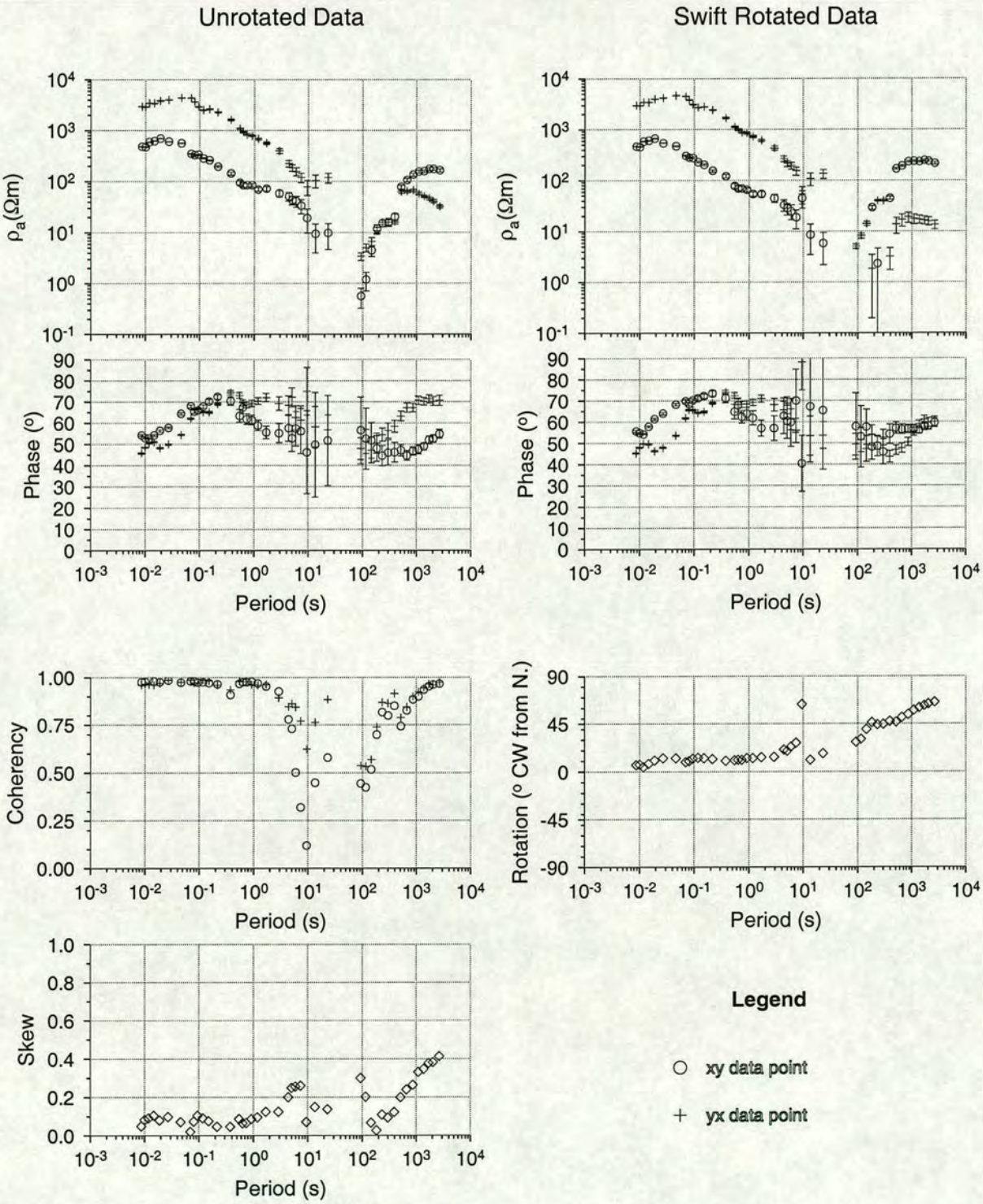

Figure 4.8. The processed data from site 11, plotted with 2 standard deviation error bars.

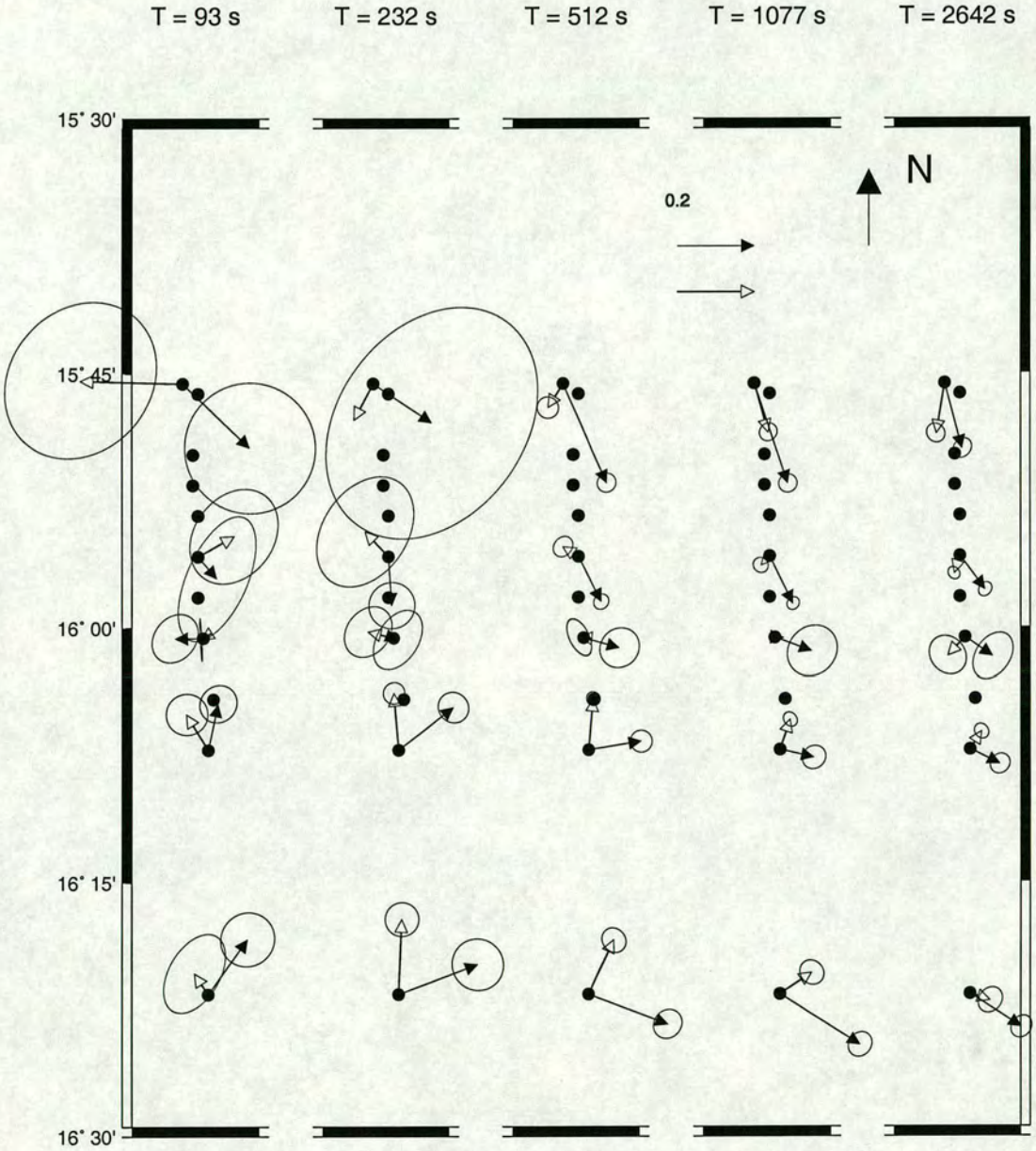

Figure 4.9. Parkinson vectors and their error ellipses calculated for the LMT data at a number of periods. Real arrows have solid heads and imaginary arrows have hollow heads. Positions of all sites are shown (see fig 4.1 for longitude information). The error ellipse for the imaginary vector at site 1 and a period of 232 s exceeds the edge of the plot and is not shown.

From the geological information (see chapter 2), we can define the electrical strike within the basin to be approximately east-west and as such xy will represent the B-polarisation and yx the E-polarisation data. At site 11, the rotation angle increases with increasing period; this reflects that on the craton the principal direction of current flow is no longer east-west and that the geological structure is different to that within the basin.

Figure 4.9 shows the real and imaginary Parkinson vectors calculated at five frequencies for the LMT data. It can be clearly seen from this diagram that, for each frequency, the largest induction vectors are seen at the extremal sites of the profile, 1 and 11. This, coupled with the direction of these vectors, suggests a conductive structure lying between them in the centre of the profile running approximately east-west. As the period of investigation increases, there is an observed clockwise rotation of the vectors in both the northern and southern sections of the profile; this may indicate a slight change in orientation of the anomaly with depth to a more south-easterly strike direction. The magnetic transfer functions are particularly poorly constrained at the higher frequencies, as shown by the size of the error ellipses; this is due to the extremely small signal strength of the vertical magnetic field.

It is difficult to make any deductions about geological structure based on the relative geometry of the real and imaginary induction vectors; however, for the two longest periods plotted, the real and imaginary vectors point in approximately the same direction. This is significant and indicates that the conductive feature is of a small depth extent relative to the skin depth at this period, and the data are sampling the structure beneath the conductor. The complexity of the relations between the two parts of the complex induction vector demonstrated by figure 4.9 necessitates a more detailed look at the measured impedance tensor dimensionality before a modelling strategy is decided upon.

4.10 Summary

The LMT fieldwork of 1995 built on an earlier AMT survey conducted mainly in 1987. The key aim of this later study was to constrain the depth extent of the conductive features found in the Mana Pools basin and to gain information about the structure beneath the basin. The field campaign was largely successful with instruments recording data for over 70% of the total possible recording time, at sites evenly spaced along the earlier profile. The difficulties we had in synchronising the recording equipment in the taxing working conditions meant that the application of a remote reference processing technique was not possible. After careful examination of the options, it was decided to use a robust regression-M estimate code to calculate transfer functions because of the proven success of this method even with single site data.

The calculated impedance estimates discussed in this section provide a good data set from which to model the electrical structure of the Mana Pools basin. We see a reasonable agreement between the data collected in the AMT and LMT frequency ranges in spite of the 8 year time gap between their acquisition. Preliminary assessments of the data using the MT parameters seem to indicate a conductive structure running east-west across the profile.

There is little evidence for static shifting of the data except at site 11 on the craton, but the dimensionality of the electrical structure is difficult to ascertain. Skew values seem to support a one- or

two-dimensional structure for most of the sites over a large part of the frequency range, except site 11 which appears more three-dimensional at long periods. Magnetic transfer functions show a more complex picture which is difficult to interpret; this necessitates a detailed look at the structure of the impedance tensor before any modelling strategy can be chosen and applied.

The structure of the apparent resistivity and phase curves and the long period induction vectors suggest that the frequencies of investigation used in the LMT survey are penetrating beneath the major conductive features of the basin. Therefore this data set should be adequate to constrain the base of the conductors observed within the Mana Pools basin.

Chapter 5

Analysis of the Measured Impedance Tensors

5.1 Introduction

Distortion of MT sounding curves by the build up of charge on the boundaries of small, near-surface three-dimensional resistivity anomalies is a major problem in the study and modelling of MT data. This charge build-up causes deviations in current flow referred to as current channelling (Jones, 1983; Jiracek, 1990). The effects of current channelling on MT data are threefold (Groom and Bahr, 1992). A frequency-independent multiplicative factor is applied to the measured apparent resistivity curves, the so-called "static shift". Secondly, for a two-dimensional structure, current channelling can lead to incorrect estimation of the regional strike direction. The consequent mixing of the regional impedances alters the level, shape and phase of the impedance estimates. Thirdly, at sufficiently high frequencies anomalous magnetic fields can be generated which can also alter the phase estimates. These effects have led to the development of a model to analyse measured impedance tensors which cannot be described by the layered earth model of Cagniard (1953) or the two-dimensional model of Swift (1967). This third model is described by Groom and Bailey (1989) as a one- or two-dimensional induction model coupled with the effects of galvanic telluric distortion.

A number of methods which evaluate all four complex elements of the MT impedance tensor have been developed (Groom and Bailey, 1989, 1991; Groom and Bahr, 1992; Bahr, 1988, 1991; Zhang *et al.*, 1993; Eggers, 1982; Spitz, 1985; La Torraca *et al.*, 1986; Yee and Paulson, 1987; Chave and Smith, 1994) to correct for the effects of galvanic distortions. These fall broadly into two categories (Bahr, 1991), involving either the extraction of the parameters of an a priori resistivity model or the mathematical description of the impedance tensor as a rank two matrix with no simplifying assumptions made. The former are of more general applicability with experimental data (Bahr, 1991). These techniques make the simplifying assumption that, for the distorting bodies, the electromagnetic fields are at the galvanic limit and induction within the anomaly may be neglected. This reduces the effects of such bodies to real electrostatic distortion. Usually the further assumption is made that the effects of magnetic galvanic distortion are small compared to those of electric galvanic distortion and the former are neglected,

exceptions to this being the techniques of Zhang *et al.* (1993) and Chave and Smith (1994). All of these methods aim to separate the effects of galvanic distortion from the inductive anomaly and retrieve both the two-dimensional regional strike and accurate impedance estimates. This chapter introduces this aspect of magnetotelluric processing and applies the Groom and Bailey (1989) decomposition method to the Mana Pools data, reviewing the parameters obtained.

5.2 Galvanic Distortion

The physical principles responsible for galvanic distortion of an electric field flowing in a non-uniform earth are discussed by Price (1973) and in an excellent tutorial by Kaufman (1985). Price (1973) demonstrates the effects which can occur at a conductivity boundary using the example of the perturbation, by a vertical conductivity discontinuity, of a system of alternating currents flowing in a half-space conductor. Figure 5.1, redrawn from Price (1973), shows the lines of current flow for the H-polarisation field

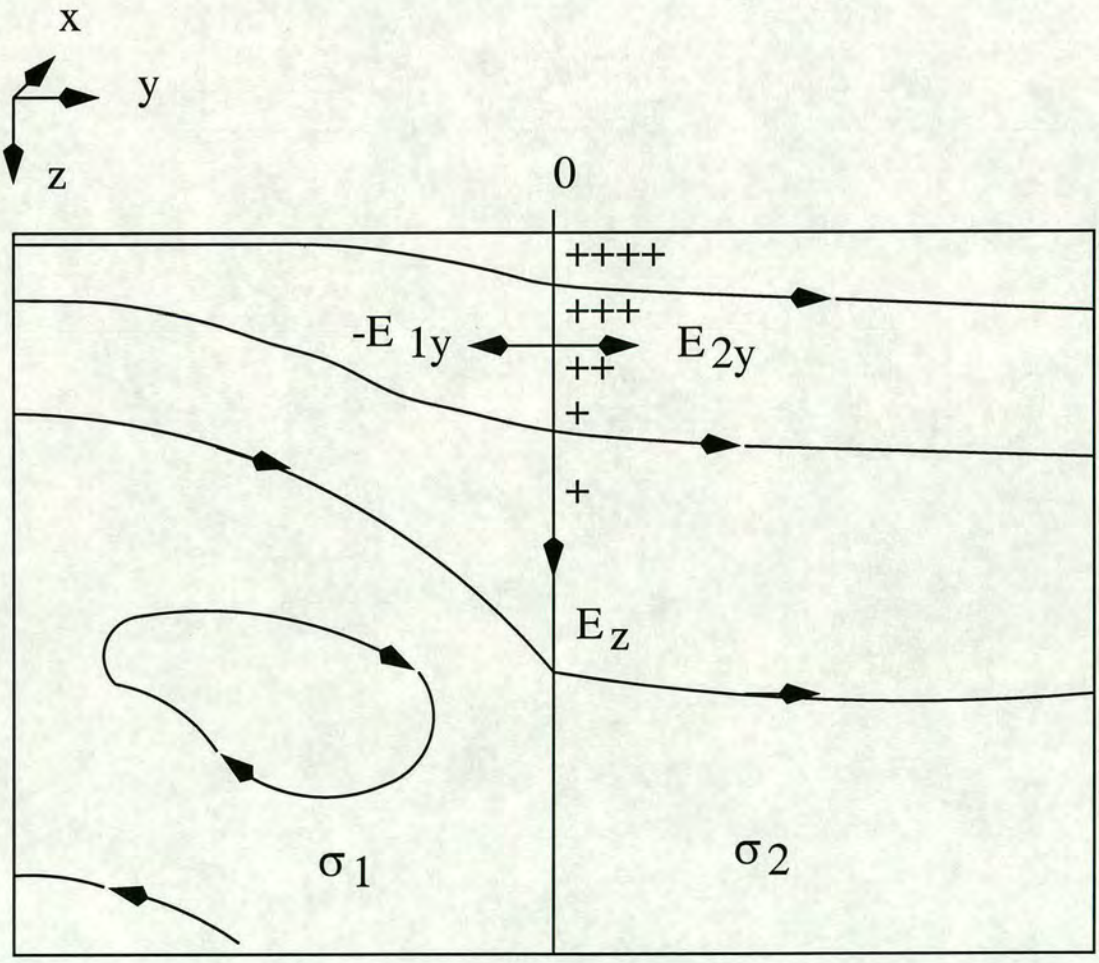

Figure 5.1. Current lines and surface charges near a vertical discontinuity. After Price (1973).

in the vicinity of such a vertical discontinuity at a particular instant, t, when the current is flowing from a good conductor into a poorer one ($\sigma_1 > \sigma_2$). At a sufficient 'adjustment distance' (Jones, 1983) from

the conductivity discontinuity, the currents will flow horizontally and are distributed according to the skin depth relation of equation 3.29 (Price, 1973). The deviations in current flow from this behaviour are due to an alternating surface charge continually being placed on the boundary by the impinging current flow (Price, 1973; Jones, 1983). This built up surface charge, τ, leads to a net difference in the component of the displacement field, D_y, in the two regions, normal to the conductivity discontinuity, where (Price, 1973; Jones, 1983; Kaufman, 1985)

$$D_{1y} - D_{2y} = \tau. \tag{5.1}$$

The rate of change of this disparity, and hence the surface charge, causes a difference in current flow normal to the boundary (Price, 1973; Jones, 1983; Kaufman, 1985)

$$J_{1y} - J_{2y} = \dot{\tau}, \tag{5.2}$$

where J_y is the y component of the electric current density. This current will be of the same order of magnitude as the displacement current and hence is ignored in the formulation of the MT problem where the assumption is made that $\sigma \gg \omega\epsilon$ (Price, 1973). The size of the current means that the associated magnetic field required to generate it is negligible (Price, 1973), and that the assumption of a non-divergent current is not violated. The surface charge τ however, has an electrostatic field associated with it which cannot be ignored (Price, 1973; Jones, 1983),

$$E_{1y} = \frac{D_{1y}}{\epsilon_1} \quad \text{and} \quad E_{2y} = \frac{D_{2y}}{\epsilon_2} \tag{5.3}$$

ϵ_1 and ϵ_2 are the electrical permittivities in the two media and are of the order of 10^{-10} (Jones, 1983). These two fields are oppositely directed and the exciting electrical field is reduced by E_1 in σ_1 and increased by E_2 in σ_2. The surface charge decreases with depth due to the decrease of current density with depth by the skin effect (Price, 1973). This leads to a downward electric field which is the same in both media due to the constraints of the tangential boundary conditions (Jones, 1983); when combined with the horizontal electric field caused by the discontinuity, the result is current refraction in σ_1.

Kaufman (1985) developed expressions for the distribution of volume and surface charges in a non-uniform conducting media using equations for the conservation of charge in a time-varying field and Gauss's formula for the electrical induction due to an enclosed charge. From these it can be shown that, for a general case of an EM field which varies with time, the volume charge density δ_v obeys the differential equation (Kaufman, 1985)

$$\frac{\partial \delta_v}{\partial t} + \frac{\delta_v}{\rho\epsilon_o} = -\mathbf{E} \cdot \nabla\sigma \tag{5.4}$$

which can be expressed as,

$$\delta_v = \frac{-\epsilon_o \mathbf{E} \cdot \nabla\sigma}{\sigma + i\omega\epsilon_o} \tag{5.5}$$

if a harmonic time dependence of the form $e^{i\omega t}$ is assumed for the EM fields. Equation 5.5 highlights two features of galvanic distortion. A charge build up will only arise if a component of the electric field occurs in the direction of the conductivity gradient, i.e., there must be both an electric field and a

conductivity change. It is also clear that if displacement currents are neglected as in the quasi-static MT assumption ($\sigma \gg \omega\epsilon_o$), then from equation 5.5 the volume charge generated is frequency-independent and real, and therefore in-phase with the exciting electric field. At a conductivity discontinuity, this volume charge density reduces to a surface charge density which will be minute due to the small value of the permittivity term; however the electrostatic field produced will not be minute, again due to the small values of the permittivity term in equation 5.3.

From the foregoing discussion it is clear that galvanic charge build up will occur on conductivity gradients and discontinuities within the earth. This becomes a problem in MT data when such charges build up on bodies which are too shallow or too small to be involved in the induction process at the relevant period range. These bodies have no true two- or three-dimensional inductive response but do cause a galvanic distortion of the measured electric fields which can lead to serious modifications of the measured MT impedance tensor. Such three-dimensional surface structure causes the observed impedance estimates to be location-dependent mixtures of the regional responses; this can include distortion of both their magnitudes and phases (Chave and Smith, 1994).

5.3 Models for the Analysis of the Impedance Tensor

Interpretation of the impedance tensor is easiest in cases where the measured structure is one- or two-dimensional and comparatively difficult when it is three-dimensional (Groom and Bailey, 1989). For many measured impedance tensors, there is no rotation direction for which the diagonal elements of the tensor are zero and therefore it does not conform to either a simple one- or two-dimensional model. Groom and Bailey (1989) suggest three possible explanations for the deviation of an impedance tensor from the one- or two-dimensional form. Firstly, the measured structure may be one- or two-dimensional but data errors cause the tensor to be three-dimensional; secondly, the structure may be three-dimensionally inductive, or thirdly, the impedance tensor may represent a one- or two-dimensional inductive structure affected by a frequency-independent galvanic distortion such as described in § 5.2. In the third case, practical analysis of the MT data requires correction of the responses for galvanic distortion (Chave and Smith, 1994) and some form of decomposition of the impedance tensor, so that the information pertaining to the inductive structure can be retrieved.

While experimental data rarely conform to either a pure one- or two-dimensional model, the diagonal elements of the impedance tensor may be sufficiently small that an approximation to a model that is less than three-dimensional can be made over significant portions of the frequency range (Groom and Bahr, 1992). This, combined with the comparative difficulty of calculating three-dimensional inductive responses, has meant that it has, in the past, usually been assumed that the tensor represents a one- or two-dimensional inductive anomaly contaminated by data errors (Groom and Bailey, 1989). Two a priori models have then been used to explain the measured tensor. Namely, the model of Cagniard (1953) for a one-dimensional layered earth, which contains two parameters, the magnitude and phase of the complex impedance which vary smoothly with frequency, and that of Swift (1967) where the structure of interest is two-dimensional. In the Swift (1967) model, the strike is determined by a rotation of the tensor to minimise the diagonal elements, five parameters are extracted, two complex impedances varying smoothly with frequency and a strike angle which should remain approximately constant.

Recent improvements in instrumentation and field techniques have shown that this explanation is unsatisfactory in many cases, and that a one- or two-dimensional structure distorted by galvanic effects is often more appropriate (Groom and Bailey, 1989). This model describes distortion of the MT impedance tensor by galvanic charge build up on small-scale, near-surface conducting inhomogeneities. The effects of these distortions are seen in both the magnitudes and directions of the measured electric and magnetic fields and can alter the measured impedance tensor in three ways (Groom and Bahr, 1992). Firstly, by the addition of a frequency-independent, or static shift, factor to the magnitude of the impedance estimates. Secondly by mixing the two impedances of a two-dimensional inductive structure in an arbitrary coordinate system, altering the shape, magnitude and phase of the impedance estimates recovered. Thirdly, at sufficiently high frequencies the effects generate anomalous magnetic fields which in turn alter the background phases. Clearly, while the application of a two-dimensional model such as that of Swift (1967) may often be appropriate to the inductive structure, the effects of galvanic distortions upon experimental data mean that the measured impedance tensor can deviate significantly from two-dimensionality. Thus the parameters recovered may be significantly in error, making conventional techniques which rotate the tensor assuming a pure two-dimensional structure inappropriate and misleading (Groom and Bailey, 1989).

5.4 Methods for Decomposition of the Impedance Tensor

A number of decomposition methods have been proposed to separate distorting effects from the underlying inductive structure in the MT impedance tensor. These aim to retrieve correct two-dimensional impedance estimates and the strike direction from galvanically distorted data. The techniques fall into two categories; those based on mathematical descriptions of the tensor with no simplifying assumptions about the underlying physical model, and those which assume a specific physical model and derive parameters to describe it. Techniques based on a mathematical description of the impedance tensor include those of Eggers (1982), Spitz (1985), La Torraca *et al.* (1986) and Yee and Paulson (1987); these methods retain all the information contained in all four complex impedance elements but their authors give no evidence for the physical significance of the parameters that they extract (Bahr, 1988). They have seldom been applied to experimental data, possibly because they do not take account of static shifts which are a serious problem in many data sets (Bahr, 1991). These methods are not discussed here.

Before introducing the physically-based decomposition methods it is useful to introduce the nomenclature of Groom and Bailey (1989) where structure is classified as either being local or regional. The local structure is considered to be inductively weak and is only responsible for galvanic distortion of the electromagnetic fields while induction occurs within the regional structure. The terms, regional and local, are defined by the spatial extent of a structure with respect to the skin depth of the penetrating signals. Regional means that the horizontal dimensions of the structure are comparable with the depth of penetration, while local means that the structure is small compared to the penetration depth of the electromagnetic signal; local structures cause DC distortion (Bahr, 1988). By this definition, a structure may be regional at high frequencies only to become local at lower ones (Groom and Bailey, 1989).

Decomposition techniques which are based on a physical model, such as those of Groom and Bailey (1989, 1991) and Bahr (1988, 1991), make simplifying assumptions about the underlying structure. In

cases where an impedance tensor is the result of the combined effects of local galvanic distortion and regional one- or two-dimensional induction, the mathematical techniques fail to take advantage of the underlying simplicity of the regional model (Groom and Bailey, 1989). Although less general than the mathematical techniques, the physical methods are still more generally applicable than the strictly two-dimensional model that underlies the Swift (1967) decomposition method and the parameters extracted from the impedance tensor are of more physical meaning. Groom and Bailey (1991) used synthetic data to make a detailed comparison between their technique and the mathematical methods. They found that, in the presence of a small scale 3-D inhomogeneity, only their decomposition retrieved correct values for the inductive strike, and only their method and that of Spitz (1985) retrieved impedance values that were not linear combinations of the principal impedances such as those retrieved by the Swift (1967) technique.

5.5 The Physical Model of Galvanic Distortion

To separate regional inductive parameters from local distorting features a physical distortion model is developed incorporating parameters describing both types of response, and the assumptions which are required in the application of this model are addressed. A description of the physical model is given below; for a rigorous treatment of the subject see Chave and Smith (1994), Habashy *et al.* (1993) and Groom and Bahr (1992). For a single, small, near surface conductivity anomaly σ_2 embedded in a media of conductivity σ_1, the effect on the measured electric field of galvanic scattering can be expressed by the equation (Bahr, 1988; Groom and Bailey, 1989; Groom and Bahr, 1992)

$$\mathbf{E_m} = \mathbf{C}\mathbf{E_r} \tag{5.6}$$

where $\mathbf{E_m}$ is the electric field component measured, $\mathbf{E_r}$ is its undistorted regional value, and $\mathbf{C}$ represents a galvanic scattering tensor. The elements of $\mathbf{C}$ are in general complex; the electric field exciting the scattering anomaly will induce a secondary electric field as well as producing a galvanic current flow (Chave and Smith, 1994). As the frequency decreases, the galvanic effects start to dominate over the inductive ones. This means that the elements of $\mathbf{C}$ become real and the measured electric field values are only affected by charge build-up in the scatterer. This assumption relies on other factors than frequency; the spatial gradient of $\mathbf{E_r}$ has to be small over the scale size of the inhomogeneity. Physically, the assumption is that the background electric field is constant over the distorting body (Groom and Bahr, 1992). Therefore, the body must be small compared to the wavelength or skin depth in the host. The distorting body must also be sufficiently removed from any other conductivity boundaries so that the spatial gradients of fields scattered by those boundaries are minimal in the vicinity of the scatterer (Groom and Bahr, 1992). The effect of $\mathbf{C}$ is that the electric fields measured are scaled linear combinations of those induced in the inductive structure (Groom and Bahr, 1992).

The anomalous currents produced by the distorting body also give rise to anomalous magnetic fields (Groom and Bahr, 1992). If the assumptions thus far made hold and the elements of $\mathbf{C}$ are real and frequency-independent, then the electric field within the scatterer will be in phase with the background electric field exciting it. It then follows that the anomalous magnetic field is also in-phase with the background electric field and can be described by a magnetic scattering matrix $\mathbf{D}$ (Groom and Bailey,

1991; Groom and Bahr, 1992),

$$\mathbf{H_m} = \mathbf{H_r} + \mathbf{DE_r}. \tag{5.7}$$

$\mathbf{H_m}$ is the measured magnetic field component and $\mathbf{H_r}$ and $\mathbf{E_r}$ are the regional magnetic and electric fields that would be measured if no distortions were present. Even though the frequency may be low enough and the structure small enough that the induction effects of the small 3-D scatterer can be ignored, there may still be a contribution to the measured magnetic field due to the galvanic scattering (Groom and Bahr, 1992). It is also clear from equation 5.7 that the effects of magnetic scattering are complex; Groom and Bailey (1991) discuss these effects and show that while the electric effects of scattering are frequency-independent, the magnetic effects are not. Combining equations 5.6 and 5.7 and taking $\mathbf{E_m} = \mathbf{Z_m H_m}$ it can be shown that the measured impedance tensor is given by (Chave and Smith, 1994; Groom and Bailey, 1991)

$$\mathbf{Z_m} = \mathbf{CZ_r}(\mathbf{I} + \mathbf{DZ_r})^{-1}. \tag{5.8}$$

When both the electric and magnetic scattering effects of a small scale conductivity anomaly are combined the full galvanic scattering tensor of equation 5.8 is complex and frequency dependent. The magnitude of the elements of $\mathbf{DZ_r} \rightarrow 0$ as $\sqrt{\omega} \rightarrow 0$ (Groom and Bailey, 1991; Chave and Smith, 1994) so that the magnetic distortion term decays with decreasing frequency. With the exception of Zhang *et al.* (1993), tensor decomposition techniques utilise this by assuming that the magnetic field distortion is small compared to that of the electric field and remove only the effects of the latter. This assumption may not hold for high frequencies at sites with strong galvanic distortion (Chave and Smith, 1994). If the effects of magnetic distortion are ignored, then for a 2-D regional structure the measured impedance elements are linear combinations of their regional values. This results in retrieval of an incorrect strike, impedance magnitudes and phases for both H and E-polarisation modes (Groom and Bahr, 1992; Chave and Smith, 1994).

5.6 The Groom and Bailey Decomposition

The decompositions of Groom and Bailey (1989) and Bahr (1988) rely on a physical model involving the superposition of a local three-dimensional structure onto a regional two-dimensional one. The model is based on the physical description of § 5.5 and makes the same assumptions. Both methods attempt to separate parameters describing local distortion and regional induction within the tensor and to retrieve accurate estimates of the static-shifted principal impedance values and the inductive strike directions. The Groom and Bailey (1989) decomposition uses a product factorisation of the telluric distortion matrix $\mathbf{C}$ into three tensor sub-operators: twist, shear and local anisotropy, and a scalar which represents the static shift factor (Groom and Bailey, 1989). These sub-operators represent different effects of galvanic distortion and allow for assimilation of the local and regional anisotropy within the decomposition (Groom and Bailey, 1989). The distortion matrix affecting magnetotelluric impedance tensors can always be factored into and described by these four sub-operators (Groom and Bailey, 1989).

The earth is assumed to have a two-dimensional regional conductivity structure and the regional electric and magnetic fields in the principal axes of the regional structure should be related to each other by a MT impedance tensor of the form

$$\mathbf{E_r} = \mathbf{Z_r}\mathbf{H_r} = \begin{pmatrix} 0 & Z_{xy} \\ Z_{yx} & 0 \end{pmatrix} \mathbf{H_r} \tag{5.9}$$

where $\mathbf{Z_r}$ is the two-dimensional regional impedance tensor relating the undistorted magnetic and electric fields. The superimposed local three-dimensional structure can lead to severe deviations of the measured fields at any point from their regional values (Groom and Bailey, 1989). Groom and Bailey (1989) make the assumption that the galvanic distortion of the magnetic field is much less severe that that of the electric field and therefore equation 5.7 can be simplified to $\mathbf{H} = \mathbf{H_r}$. This assumption is based on the fact that the magnetic field is "determined by a weighted spatial average of the telluric current density" (Groom and Bailey, 1989) and any anomalous effects should be smoothed out. The measured electric field is related to the regional electric field by equation 5.6, expressed as (Bahr, 1988; Groom and Bailey, 1989)

$$\mathbf{E_m} = \mathbf{C}\mathbf{E_r} = \begin{pmatrix} C_1 & C_2 \\ C_3 & C_4 \end{pmatrix} \mathbf{E_r}. \tag{5.10}$$

The regional electric field and local structure are considered to obey the assumptions of § 5.5 so that the elements of $\mathbf{C}$ are real, and thus four real parameters are required to describe telluric distortion; for a proof of this see Groom and Bailey (1989).

If the measured impedance tensor $\mathbf{Z_m}$ is given by the equation

$$\mathbf{E_m} = \mathbf{Z_m}\mathbf{H_m} \tag{5.11}$$

then in the measurement directions the regional and measured impedance tensors can be related to each other by the equation

$$\mathbf{Z_m} = \mathbf{R}\mathbf{C}\mathbf{Z_r}\mathbf{R}^{\mathbf{T}} \tag{5.12}$$

where $\mathbf{C}$ is the distortion tensor in the inductive regional reference frame and $\mathbf{R}$ rotates the impedance tensor from the regional axes into the measurement axes direction. There are nine parameters to determine in equation 5.12, the rotation angle, the four real elements of the distortion matrix and the magnitude and phase of the two complex impedances in the regional impedance tensor. With only eight data, the magnitude and phase of the four measured complex impedances, the decomposition expressed in equation 5.12 is non-unique.

In order to overcome this non-uniqueness Groom and Bailey (1989) suggest a more useful factorisation of $\mathbf{C}$ using a modified form of the Pauli spin matrices; see Groom and Bailey (1989) and a similar example of their usage in Spitz (1985). It is proposed that

$$\mathbf{C} = g\mathbf{TSA} \tag{5.13}$$

represents a useful factorisation of the distortion matrix (Groom and Bailey, 1989), where g is a scalar and $\mathbf{T}, \mathbf{S}$ and $\mathbf{A}$ are tensor factors defined by

$$\mathbf{T} = N_2 \begin{pmatrix} 1 & -t \\ t & 1 \end{pmatrix} \tag{5.14}$$

$$\mathbf{S} = N_1 \begin{pmatrix} 1 & e \\ e & 1 \end{pmatrix} \tag{5.15}$$

$$\mathbf{A} = N_3 \begin{pmatrix} 1+s & 0 \\ 0 & 1-s \end{pmatrix}, \tag{5.16}$$

where t, s and e are real numbers. The terms N_1, N_2 and N_3 are normalising factors defined so that $\mathbf{T}, \mathbf{S}$ and $\mathbf{A}$ individually preserve power but not isotropy when they are applied to an isotropically polarised random electric field (Groom and Bailey, 1989); they are defined as

$$N_1 = 1/\sqrt{1+e^2} \tag{5.17}$$

$$N_2 = 1/\sqrt{1+t^2} \tag{5.18}$$

$$N_3 = 1/\sqrt{1+s^2}. \tag{5.19}$$

The tensor factor $\mathbf{A}$ is the anisotropy tensor; when applied to a 2-D impedance tensor the result is given by

$$N_3 \begin{pmatrix} 1+s & 0 \\ 0 & 1-s \end{pmatrix} \begin{pmatrix} 0 & Z_{xy} \\ Z_{yx} & 0 \end{pmatrix} = N_3 \begin{pmatrix} 0 & Z_{xy} + sZ_{xy} \\ Z_{yx} - sZ_{yx} & 0 \end{pmatrix}. \tag{5.20}$$

This represents a stretching of the two field components by different factors, adding anisotropy due to local distortion to that already present from the two-dimensional regional structure (Groom and Bailey, 1989). Equation 5.20 shows that local anisotropy is only developed along the principal axes of the regional tensor and that its elements are not linearly combined; therefore, the direction of the principal impedance elements is not changed (Groom and Bailey, 1989). If the regional structure is not two-dimensional then direction is no longer conserved. Any rank two diagonal matrix and thus any anisotropy operator can be expressed in the same form as $\mathbf{A}$; therefore the distortion anisotropy and regional anisotropy are indistinguishable unless the latter is known independently (Groom and Bailey, 1989).

In order to understand the physical meaning of the other two tensor operators, it is useful to introduce the telluric vector concept of Bahr (1988, 1991). For a three-dimensional impedance tensor, the telluric vectors are defined as,

$$\mathbf{e_x} = Z_{xx}\hat{\mathbf{x}} + Z_{yx}\hat{\mathbf{y}} \tag{5.21}$$

$$\mathbf{e_y} = Z_{xy}\hat{\mathbf{x}} + Z_{yy}\hat{\mathbf{y}} \tag{5.22}$$

where $\hat{\mathbf{x}}$ and $\hat{\mathbf{y}}$ are unit vectors. $\mathbf{e_x}$ or $\mathbf{e_y}$ defines an in-phase and an out-of-phase telluric vector with

regard to the north or the east components of the magnetic field respectively (Bahr, 1988). The telluric vectors represent the magnitude and direction of an electric field induced by a single horizontal component of the magnetic field.

The Groom and Bailey (1989) shear tensor, **S**, develops anisotropy on axes which bisect the regional axes (Groom and Bailey, 1989). Equation 5.23 demonstrates the result of applying the shear tensor to a two-dimensional impedance tensor.

$$N_1 \begin{pmatrix} 1 & e \\ e & 1 \end{pmatrix} \begin{pmatrix} 0 & Z_{xy} \\ Z_{yx} & 0 \end{pmatrix} = N_1 \begin{pmatrix} eZ_{yx} & Z_{xy} \\ Z_{yx} & eZ_{xy} \end{pmatrix}. \tag{5.23}$$

Consider the effect of the shear tensor on the $\mathbf{e_x}$ telluric vector defined by column 1 of the resulting impedance tensor in equation 5.23. Before application of the shear tensor, the telluric vector was expressed as $\mathbf{e_x} = Z_{yx}\hat{\mathbf{y}}$, after shearing, it becomes $\mathbf{e_x} = eZ_{yx}\hat{\mathbf{x}} + Z_{yx}\hat{\mathbf{y}}$. A north-south component equal to the product of the east-west component and the shear e has been generated. Likewise the $\mathbf{e_y}$ telluric vector is modified from $\mathbf{e_y} = Z_{xy}\hat{\mathbf{x}}$ to $\mathbf{e_y} = Z_{xy}\hat{\mathbf{x}} + eZ_{xy}\hat{\mathbf{y}}$. The effect of this can be seen in figure 5.2. The effect of the shear tensor is to rotate the electric fields by an angle ϕ_e away from the principal axes.

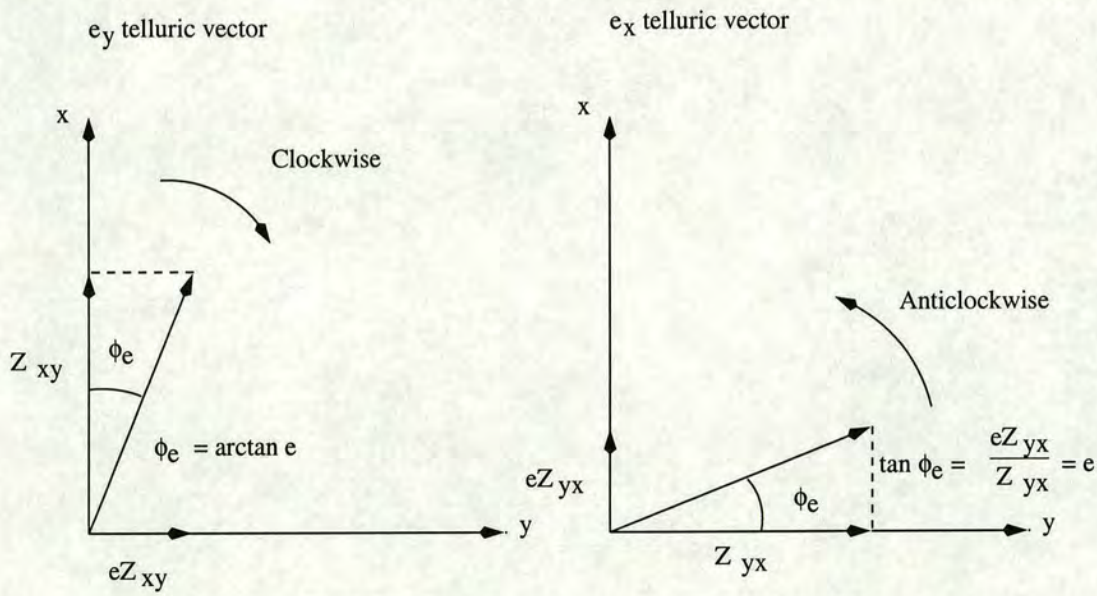

Figure 5.2. The effect of the shear tensor on a two-dimensional impedance tensor.

For the $\mathbf{e_y}$ telluric vector this rotation is clockwise and for the $\mathbf{e_x}$ telluric vector, anticlockwise. The angle ϕ_e is defined as the shear angle and is equal to $\arctan e$ (Groom and Bailey, 1989).

The twist tensor **T** is similar to the shear tensor but rotates the electric field vectors through an angle $\phi_t = \arctan t$, defined as the twist angle (Groom and Bailey, 1989). Equation 5.24 shows the effect of the twist tensor on a two-dimensional impedance tensor,

$$N_2 \begin{pmatrix} 1 & -t \\ t & 1 \end{pmatrix} \begin{pmatrix} 0 & Z_{xy} \\ Z_{yx} & 0 \end{pmatrix} = N_2 \begin{pmatrix} -tZ_{yx} & Z_{xy} \\ Z_{yx} & tZ_{xy} \end{pmatrix}. \tag{5.24}$$

The same telluric vector approach is appropriate for the explanation of the twist procedure and its

graphical representation is shown in figure 5.3. Normalisation of each of these tensors by $\mathbf{N_1}$, $\mathbf{N_2}$ and

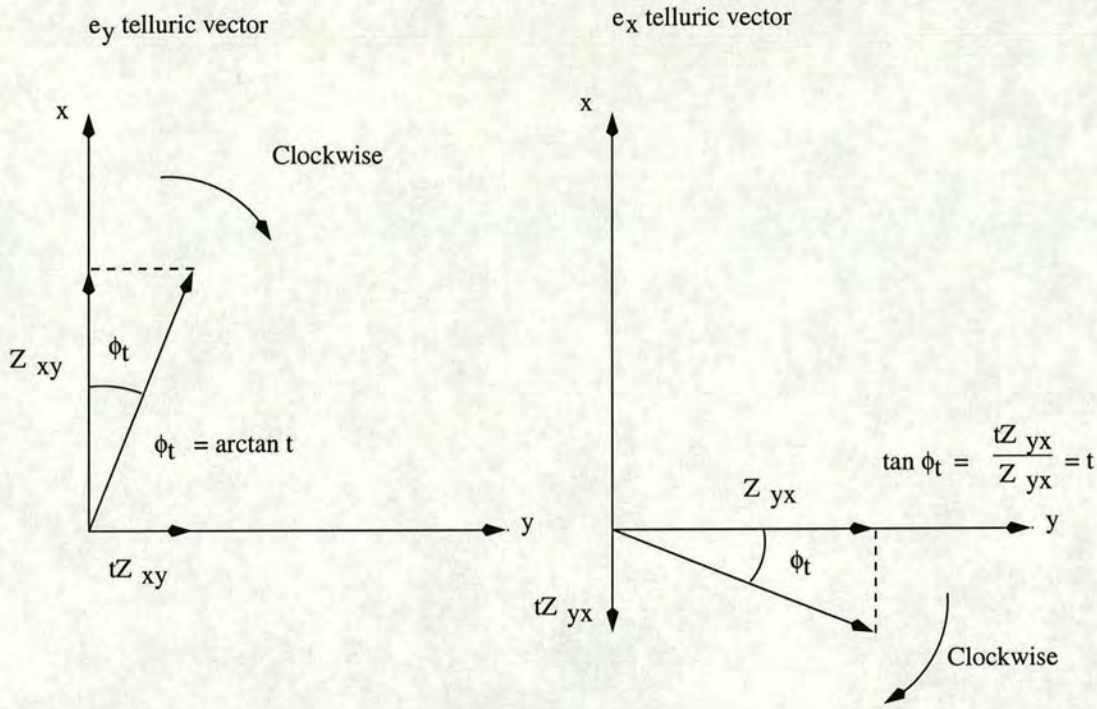

Figure 5.3. The effect of the twist tensor on a two-dimensional impedance tensor.

$\mathbf{N_3}$ leads the product of $\mathbf{A}$, $\mathbf{S}$ and $\mathbf{T}$ to differ from the distortion tensor $\mathbf{C}$. This effect is corrected by the scalar g which performs an overall scaling of the electric fields and is referred to as the 'site gain' (Groom and Bailey, 1989).

As has already been discussed, the local and regional anisotropy are indistinguishable within the regional impedance tensor without a priori information; therefore, neither the local anisotropy $\mathbf{A}$ nor the site gain can be determined from $\mathbf{Z_r}$ since $\mathbf{Z_r'} = g\mathbf{A}\mathbf{Z_r}$ is also an ideal two-dimensional impedance tensor (Groom and Bailey, 1989). Because of this fact only $\mathbf{Z_r'}$ is retrieved from the measured tensor and g and $\mathbf{A}$ are absorbed into the tensor to be determined. Thus

$$\mathbf{Z_m} = g\mathbf{RTSAZ_rR^T} \tag{5.25}$$

with g and $\mathbf{A}$ absorbed into $\mathbf{Z_r}$ to give $\mathbf{Z_r'}$ gives,

$$\mathbf{Z_m} = \mathbf{RTSZ_rR^T} \tag{5.26}$$

where the prime on $\mathbf{Z_r'}$ has been dropped since it is experimentally indistinguishable from $\mathbf{Z_r}$ (Groom and Bailey, 1989).

The advantage of this factorisation, therefore, is that the unknown parts of $\mathbf{C}$ are absorbed into the impedance tensor determined, without destroying its ideal two-dimensional form (Groom and Bailey, 1989). If the local distortion is truly frequency-independent then absorption of these two parameters into $\mathbf{Z_r}$ should not affect the shape of either the apparent resistivity or the phase curves so that they

can be determined correctly except for a static shift factor due to g and $\mathbf{A}$ (Groom and Bailey, 1989). A comparison of equation 5.26 with that for the decomposition of Swift (1967) given in equation 3.46 shows how the latter also absorbs the twist and shear tensors into the retrieved impedance tensor (Groom and Bailey, 1989). This can lead to large deviations of the tensor obtained from the two-dimensionality assumed by the model, and consequently to large errors in the strike direction and principal impedances.

Equation 5.26 has seven real parameters, the rotation angle between the measurement axes and the regional axes, the magnitude and phase of the two complex principal impedances and the twist and shear angles. These can be calculated from the measured impedance elements via a system of non-linear equations (Groom and Bailey, 1989)

$$Z_{xx} + Z_{yy} = t\sigma + e\delta \tag{5.27a}$$

$$Z_{xy} + Z_{yx} = (\delta - et\sigma)\cos 2\theta - (t\delta + e\sigma)\sin 2\theta \tag{5.27b}$$

$$Z_{yx} - Z_{xy} = -\sigma + et\delta \tag{5.27c}$$

$$Z_{xx} - Z_{yy} = -(t\delta + e\sigma)cos2\theta - (\delta - et\sigma)sin2\theta \tag{5.27d}$$

where

$$\sigma = Z_{xy} + Z_{yx} \quad \text{and} \quad \delta = Z_{xy} - Z_{yx} \tag{5.28}$$

Real data with errors and slight deviations from the ideal physical model mean that an exact solution to the decomposition is never found, so equations 5.27a to 5.27d are solved for the seven decomposition parameters using a least-squares fitting procedure (Groom and Bailey, 1989).

5.7 Methods of Assessment of the MT Impedance Tensor

Since the parameters derived from a tensor may prove unstable if it can be interpreted by a simpler model, it is important that an impedance tensor be treated in a way appropriate to the degree of structure that it describes. For instance, a one-dimensional tensor described by a two-dimensional model will have a poorly constrained strike direction since any rotation angle will result in a magnitude of zero for its diagonal elements. Therefore, techniques must be used to determine the complexity of the impedance data collected; two such techniques are described in this section.

Mohr circles can be used to represent and study the MT impedance tensor (Lilley, 1976, 1993a,b). By combining both a Cartesian diagram and a polar plot, Mohr diagrams achieve four degrees of freedom; these are the Cartesian coordinates of the centre of the circle and the length and orientation of the radius (Lilley, 1993a). A simple graphical method is thus achieved for displaying the four different values of the impedance tensor, and for assessing its dimensionality. Mohr circles can be constructed on a plot of Z'_{xy} versus Z'_{xx} for the real or imaginary part of an impedance tensor separately (Lilley, 1993a,b), where Z'_{xy} is the value of Z_{xy} after rotation of the measurement axes clockwise through an angle θ'. Such a plot is shown in figure 5.4. Taking the two parts of the complex impedance tensor separately can lead to different interpretations and care must be taken with this approach (Fischer and Masero, 1994). Lilley (1976, 1993b) shows that $\Re Z'_{xy}$ and $\Re Z'_{yx}$, where $\Re$ denotes the real part of the impedance element, are

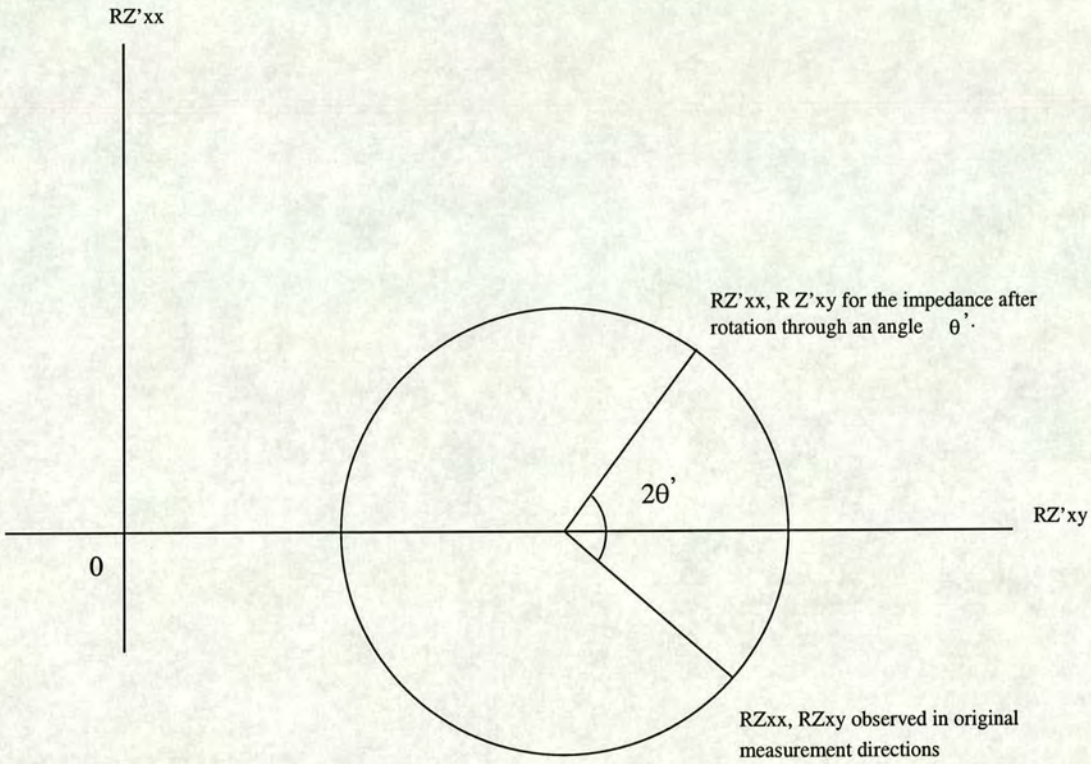

Figure 5.4. A Mohr circle for the real part of a two-dimensional impedance tensor, after Lilley (1993a).

related via the equation,

$$\Re Z'_{yx} = \Re Z'_{xy} + (\Re Z_{yx} - \Re Z_{xy}), \tag{5.29}$$

and $\Re Z'_{xx}$ and $\Re Z'_{yy}$ are related via

$$\Re Z'_{yy} = -\Re Z'_{xx} + (\Re Z_{xx} + \Re Z_{yy}). \tag{5.30}$$

The terms $(\Re Z_{yx} - \Re Z_{xy})$ and $(\Re Z_{xx} + \Re Z_{yy})$ consist of the real values of the impedance elements measured in the original observation directions and are invariant to rotation (Lilley, 1993b) so that $\Re Z'_{xy}$ and $\Re Z'_{yx}$ are linearly related, as are $\Re Z'_{xx}$ and $\Re Z'_{yy}$. As a result of these relations, axes for all four rotated tensor elements may be plotted on one diagram but only two are required for a simple analysis.

Figure 5.4 was drawn by calculating rotated values of the impedance elements for all possible angles of rotation, using equations 3.48a to 3.49d to calculate the values of the rotated impedance elements. The resulting circle has a centre point,

$$\Re Z'_{xy} = \frac{1}{2}(\Re Z_{xy} - \Re Z_{yx}) \tag{5.31}$$

$$\Re Z'_{xx} = \frac{1}{2}(\Re Z_{xx} + \Re Z_{yy}) \tag{5.32}$$

and radius

$$R = \frac{1}{2}[(\Re Z_{xx} - \Re Z_{yy})^2 + (\Re Z_{xy} + \Re Z_{yx})^2]^{\frac{1}{2}}. \tag{5.33}$$

The circle plotted takes a shape characteristic of the dimensionality of the impedance tensor. Figure 5.4 indicates a two-dimensional tensor where Z'_{xy} and Z'_{yx} are orthogonal and Z'_{xx} and Z'_{yy} are zero when the measurement axes coincide with the electrical strike and dip. This plots as a circle with its centre lying on the horizontal axes. For true two-dimensional structure, the angle of rotation to electrical strike must be the same for both the real and imaginary circles (Lilley, 1993a). In the one-dimensional case, the auxiliary impedance elements are zero and the principal elements are equal in magnitude but of opposite sign and invariant to rotation; in this case, from equation 5.33 it is clear that such a tensor will plot as a point on the horizontal axis with a radius of zero. Figure 5.5 shows a Mohr circle for a three-

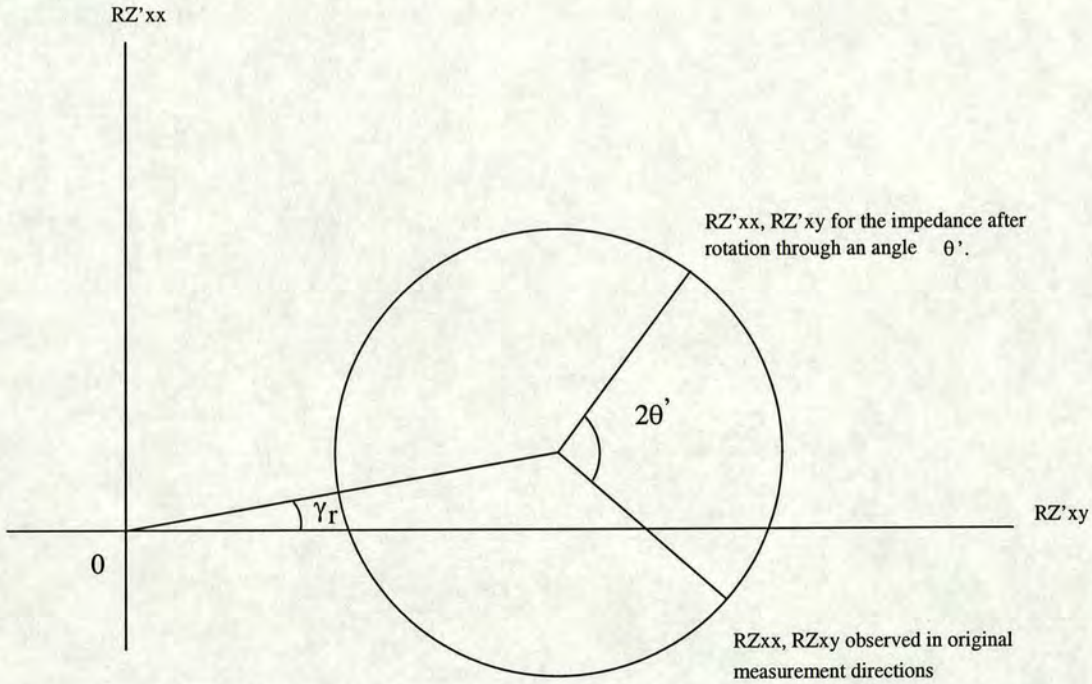

Figure 5.5. A Mohr circle for the real part of a three-dimensional impedance tensor, after Lilley (1993a).

dimensional impedance tensor; for this situation the Z'_{xy} and Z'_{yx} components are no longer orthogonal and this is shown in the diagram by the displacement of the circle centre off the horizontal axis. Lilley (1993a) represents the offset of the circle from the horizontal axes by the angle γ_r; equation 5.32 shows that this offset is directly related to the size of the auxiliary impedance elements and is therefore a measure of the degree of three-dimensionality of the tensor. The tangent of γ_r is given by

$$\tan\gamma_r = \frac{\Re Z_{xx} + \Re Z_{yy}}{\Re Z_{xy} - \Re Z_{yx}} \tag{5.34}$$

which is very similar to the skew value of Swift (1967) given in equation 4.29; γ_r therefore represents the skew of the real part of the impedance tensor graphically (Lilley, 1993a). The anisotropy of the impedance tensor is represented by the radius of the circle (Lilley, 1993a) and the tensor invariants can

also be represented on the diagram. For a discussion of MT tensor invariants and their representation by graphical means, see Szarka and Menvielle (1997), where it is shown that all seven tensor invariants can be represented using Mohr circles. Mohr circles can be plotted for impedance data at different frequencies and the change in relative size between the real and imaginary circles gives an illustration of the phase change present within the data (Lilley, 1993a). Equation 3.39 shows that the impedance and the period are related. Impedance is inversely proportional to $\sqrt{T}$; therefore, the impedance data should be multiplied by $\sqrt{T}$ to normalise them prior to display (Lilley, 1993a).

Another technique for the assessment of a measured impedance tensor was proposed by Bahr (1991) in an extension to his earlier work on tensor decomposition involving telluric vectors (Bahr, 1988). Bahr (1991) proposed a number of parameters with which to assign a measured impedance tensor to one of seven different model classes. These parameters were derived from the four modified impedances,

$$\begin{aligned} S_1 &= Z_{xx} + Z_{yy} & S_2 &= Z_{xy} + Z_{yx} \\ D_1 &= Z_{xx} - Z_{yy} & D_2 &= Z_{xy} - Z_{yx} \end{aligned} \tag{5.35}$$

They are defined in Bahr (1991) and include the conventional skew of Swift (1967)

$$k = \frac{|S_1|}{|D_2|}. \tag{5.36}$$

A rotationally invariant measure of phase difference in the impedance tensor

$$\mu = \frac{\left(|\Im\left(S_2 D_1^*\right)| + |\Im\left(D_2 S_1^*\right)|\right)^{\frac{1}{2}}}{|D_2|} \tag{5.37}$$

where D_1^* represents the complex conjugate of D_1. A rotationally invariant regional skew which describes the dimensionality of the regional structure, independent of local distortions, and the extent to which a particular data set can be interpreted with the superimposition model

$$\eta = \frac{\left(|\Im\left(S_2 D_1^*\right)| - |\Im\left(D_2 S_1^*\right)|\right)^{\frac{1}{2}}}{|D_2|}. \tag{5.38}$$

Finally, a rotationally invariant measure of two-dimensionality is defined by

$$\Sigma = \frac{\left(D_1^2 + S_2^2\right)}{D_2^2}. \tag{5.39}$$

These parameters are then used to assign an impedance tensor to one model class from a series of seven classes defined by Bahr (1991).

Class 1: the simple 2-D anomaly

Defined by $k < 0.1$ and $\Sigma > 0.1$

The low skew value implies that the tensor is either one-dimensional or is described by Swift's (1967) model. $\Sigma > 0.1$ implies that the conductivity can be considered to be 2-D and the method of Swift (1967) can be used to find the strike angle of the tensor.

For all other classes some form of tensor decomposition must be applied.

Class 2: the purely local 3-D anomaly

Defined by $\mu < 0.05$

This model class describes the case of a layered earth overlain by a three-dimensional surficial layer.

Classes 1 and 2 are special cases where the skew and phase difference measure are vanishingly small and the regional models do not deviate from one- or two-dimensionality. The remaining model classes describe cases of distorted regional models, measured by the regional skew parameter. The difference between them is merely the amount of local distortion involved.

Class 3: a regional 2-D anomaly with weak local distortion

This class includes all cases for which,

$$\phi_e - \phi_t < 5^o \quad \text{and} \quad \phi_e + \phi_t < 20^o \tag{5.40}$$

or

$$\phi_e + \phi_t < 5^o \quad \text{and} \quad \phi_e - \phi_t < 20^o. \tag{5.41}$$

These two angles, $\tan(\phi_e - \phi_t) = -Z'_{xx}/Z'_{yx}$ and $\tan(\phi_e + \phi_t) = -Z'_{yy}/Z'_{xy}$, with the tensor rotated into the regional strike direction, represent the deviation of the induced electric field from the ideal orthogonal case.

Class 4: a regional 2-D anomaly in rotated coordinates

This class refers to the case where the two skew angles, $(\phi_e - \phi_t)$ and $(\phi_e + \phi_t)$, are equal.

$$\phi_t = 0 \tag{5.42}$$

Class 5: a regional 2-D anomaly with strong local distortion

This class is characterised by $\eta < 0.3$ and larger twist and shear angles than class 3.

Class 6: a regional 2-D anomaly with strong local channelling

This class consists of cases where $\phi_e = 45^o$ and the direction of the electric field does not depend on the direction of the magnetic field, except for a sign change.

Class 7: a regional 3-D anomaly

This class includes those cases where $\eta > 0.3$, the regional conductivity distribution is not 2-D and the superimposition model is not appropriate.

5.8 Assessment of the Mana Pools Impedance Tensors

Mohr circles were plotted for all of the data collected for the Mana Pools basin so that an initial assessment of the impedance tensor's structure could be made. Figures 5.6 and 5.7 show examples of circles plotted for both the real and imaginary parts of the impedance tensor at different periods for sites 6 and 10 respectively. The radial line on each circle connects its centre and the observed point, giving an idea of the direction and magnitude of the angle that the coordinate system must be rotated through to align the tensor with the regional strike direction. The impedance values have been multiplied by

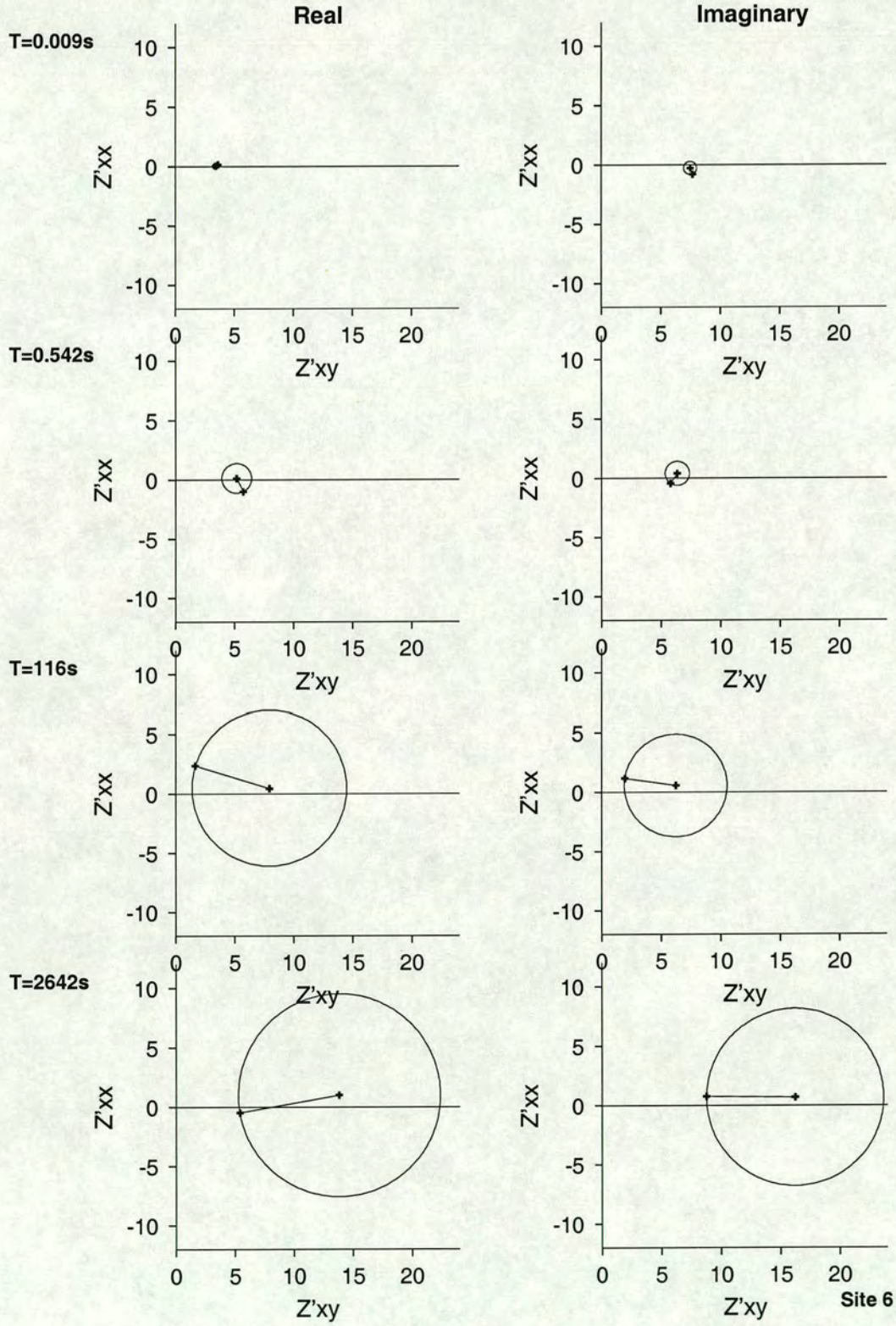

Figure 5.6. Mohr circles plotted for site 6. The axis units are m$\Omega s^{\frac{1}{2}}$.

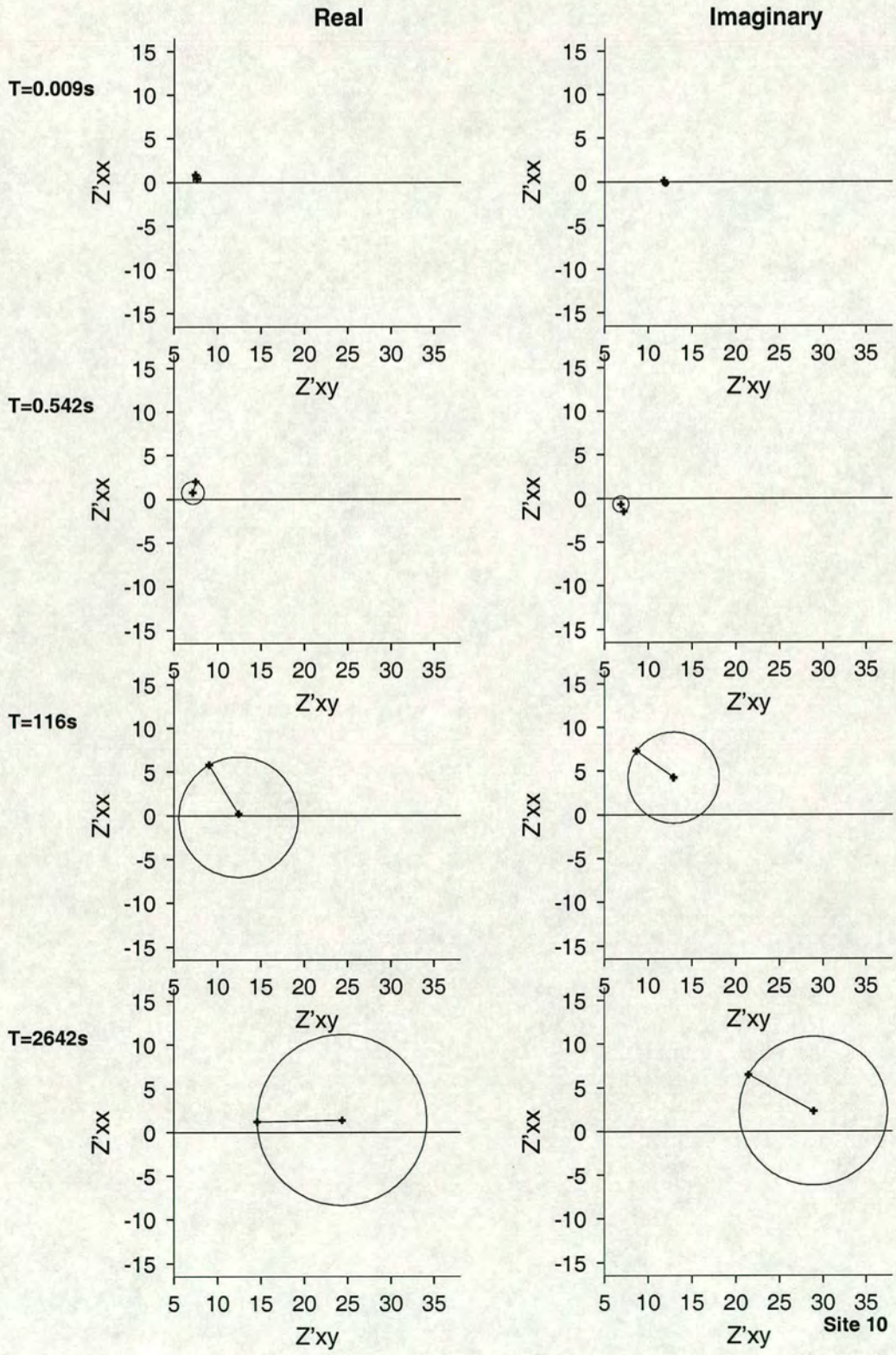

Figure 5.7. Mohr circles plotted for site 10. The axis units are $m\Omega s^{\frac{1}{2}}$.

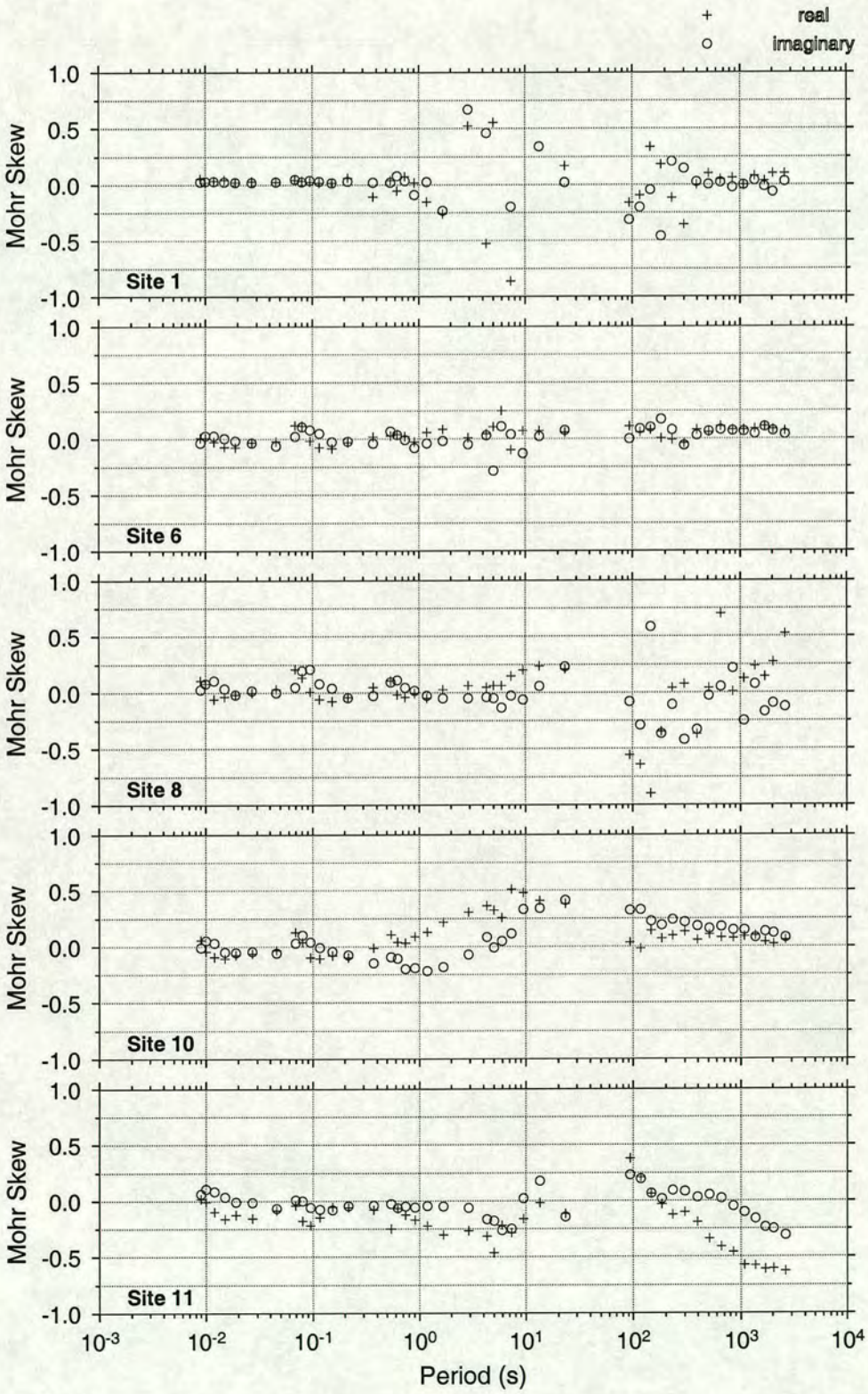

Figure 5.8. Mohr skew values calculated for all sites.

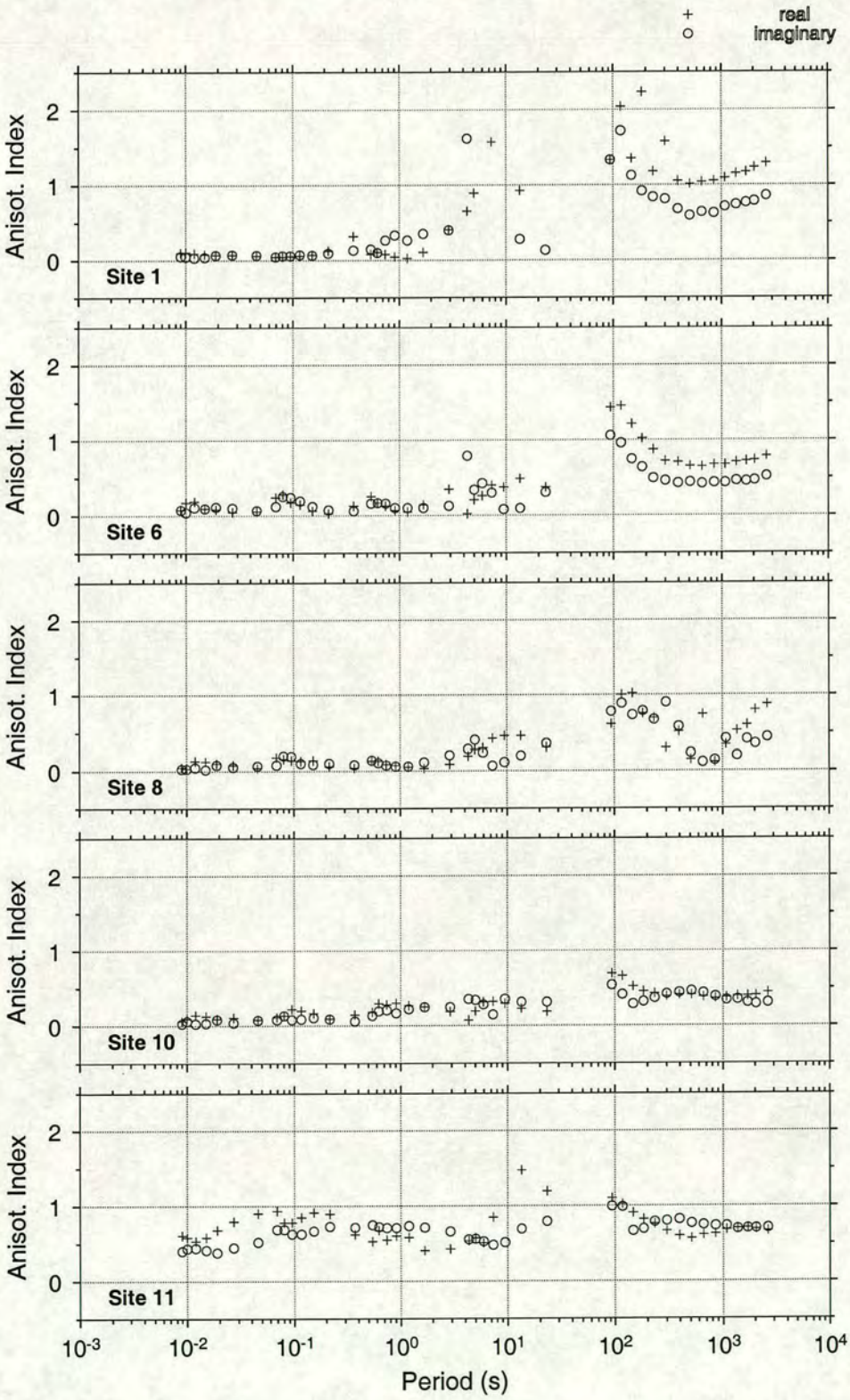

Figure 5.9. Mohr anisotropy values calculated for all sites.

$\sqrt{T}$ prior to plotting; this removes the dependence of impedance on period illustrated in equation 3.39 which might otherwise mask trends seen in the circles with changing frequency. Figures 5.8 and 5.9 show values of the impedance skew and anisotropy derived from the Mohr circles at all frequencies for all sites. The skew plotted in figure 5.8 differs from the conventional skew because it is calculated for the real and imaginary parts of the tensor separately and maintains the directional information normally lost. A positive skew for the Z_{xx}/Z_{xy} pair indicates that, in addition to the orthogonal electric field, a northward component of the magnetic field would generate a northward electric field with a magnitude dependent on the size of the skew value. A negative skew indicates an additional southward electric field component. For the Mohr circle, skew indicates three-dimensionality; differentiation between the one- and two-dimensional tensor situations cannot be made on the strength of the skew alone since both situations take a value of zero. The anisotropy index plotted in figure 5.9 is the radius of the circle normalised by the length of its tangent from the origin. This parameter gives a measure of the difference in magnitude between the two principal impedances. For the one-dimensional case it will take on a value of zero, as the principal impedances should be identical and rotationally invariant. Two- and three-dimensional tensors should be non-zero with a greater degree of anisotropy in the two-dimensional case when all the induction information is contained within the off diagonal elements. The anisotropy is also sensitive to static shifting of the data as this causes the apparent resistivity curves to split too. Together these two parameters provide a reasonable assessment of the dimensionality of the impedance tensor.

For the Mana Pools data at sites 1 to 8, consisting of the sites directly over the basin, the anisotropy values (see figure 5.9) are extremely low in the AMT period range and the skew values (figure 5.8) are also very small indicating tensors that are very close to being one-dimensional. The increase in both anisotropy and skew at these sites between 1 s and 20 s is probably due to a loss of data quality within the dead band and at the lower limits of the SPAM system's frequency range. Similar arguments of poor data quality can be made in the first half decade of the LMT data and for most of the LMT data at site 8. An increase in anisotropy is seen in the LMT data at all three sites, amplified in the real part of the tensor compared with the imaginary. The skew values remain small, with the possible exception of site 8 and this indicates a transition to a more strongly two-dimensional tensor. The separation of the real and imaginary anisotropy is indicative of a change in phase between the AMT and LMT frequency ranges, this is difficult to identify in figures 4.4 to 4.8 because of the dependence of phase on the gradient of the apparent resistivity (Kaufman and Keller, 1981, p. 108). Tensors in the entire frequency range at sites 1 to 8 are therefore two-dimensional with differing degrees of anisotropy. At site 10, the tensor also appears to be two-dimensional with a very low anisotropy up to periods of 1 s; the increase in skew over the rest of the AMT period range may indicate significant three-dimensional structure or at the least a highly distorted 2-D situation. The skew drops in the LMT period range and the anisotropy remains at a relatively similar value. This implies that the increase in anisotropy in the AMT period range is real and perhaps that the basin is slightly shallower beneath site 10. Site 11 is two-dimensional across the entire AMT period range, the skew is low but the anisotropy is non-zero. Even at short periods the anisotropy is quite high, as would be expected if the data are static shifted. Skew increases rapidly in the LMT data and the longer periods at site 11 may be three-dimensional.

Table 5.1 shows the results of the Bahr decomposition performed on the Mana Pools dataset. These results are also shown graphically in figure 5.10, the numbers tabulated and plotted respectively representing the Bahr class to which each impedance tensor at each frequency belongs. Bahr's technique

Period (s)	Site Numbers										
	1	2	3	4	5	6	7	8	9	10	11
0.8700E-02	3	3	4	3	4	3	2	3	3	4	3
0.1000E-01	2	3	3	4	3	3	3	2	2	3	5
0.1190E-01	3	4	3	3	3	5	3	3	3	4	5
0.1460E-01	3	3	3	3	2	3	3	3	3	3	5
0.1900E-01	3	3	3	7	7	3	4	2	4	3	5
0.2690E-01	3	2	3	4	3	3	4	3	3	3	5
0.4650E-01	3	3	3	3	2	3	4	3	3	3	5
0.6940E-01	2	3	3	3	3	3	3	3	3	3	5
0.8030E-01	3	3	3	3	3	5	3	3	3	3	5
0.9530E-01	2	3	3	3	4	2	3	3	3	3	5
0.1170	2	3	3	3	3	3	4	4	4	3	5
0.1517	3	3	3	3	3	3	3	3	3	3	5
0.2156	3	3	3	2	3	3	3	3	3	3	5
0.3724	3	3	3	3	4	3	5	4	3	3	5
0.5424	3	3	3	3	7	5	3	3	5	7	5
0.6275	3	3	3	3	7	3	3	3	3	7	5
0.7442	3	5	3	3	3	4	3	2	4	7	5
0.9143	3	3	3	3	3	3	2	2	3	7	5
1.185	3	3	3	4	3	4	4	2	3	7	5
1.684	5	3	6	5	5	2	3	3	3	5	5
2.909	5	4	7	7	3	5	3	4	3	5	5
4.339	7	3	-	7	3	3	5	4	3	2	5
5.020	7	5	-	7	3	3	5	1	3	5	5
5.953	-	7	-	4	3	3	5	3	1	5	5
7.314	6	7	-	7	3	3	5	3	5	5	5
9.481	-	7	-	3	3	3	7	3	3	5	7
13.47	7	7	-	3	3	2	5	3	5	5	7
23.27	1	3	-	3	5	5	3	5	5	5	7
93.09	5	-	-	-	-	1	-	1	-	5	5
116.4	5	-	-	-	-	5	-	5	-	5	2
146.3	5	-	-	-	-	5	-	5	-	5	5
182.9	5	-	-	-	-	5	-	5	-	5	5
232.7	5	-	-	-	-	5	-	4	-	5	5
301.2	6	-	-	-	-	5	-	5	-	5	5
393.8	3	-	-	-	-	5	-	1	-	7	5
512.0	3	-	-	-	-	5	-	4	-	7	5
660.6	3	-	-	-	-	5	-	5	-	7	7
853.3	3	-	-	-	-	5	-	3	-	7	5
1078.	3	-	-	-	-	5	-	5	-	7	7
1365.	3	-	-	-	-	5	-	5	-	5	5
1707.	3	-	-	-	-	5	-	5	-	5	5
2048.	3	-	-	-	-	5	-	4	-	5	5
2643.	1	-	-	-	-	5	-	5	-	5	5

Table 5.1. The Bahr distortion classes for the Mana Pools data.

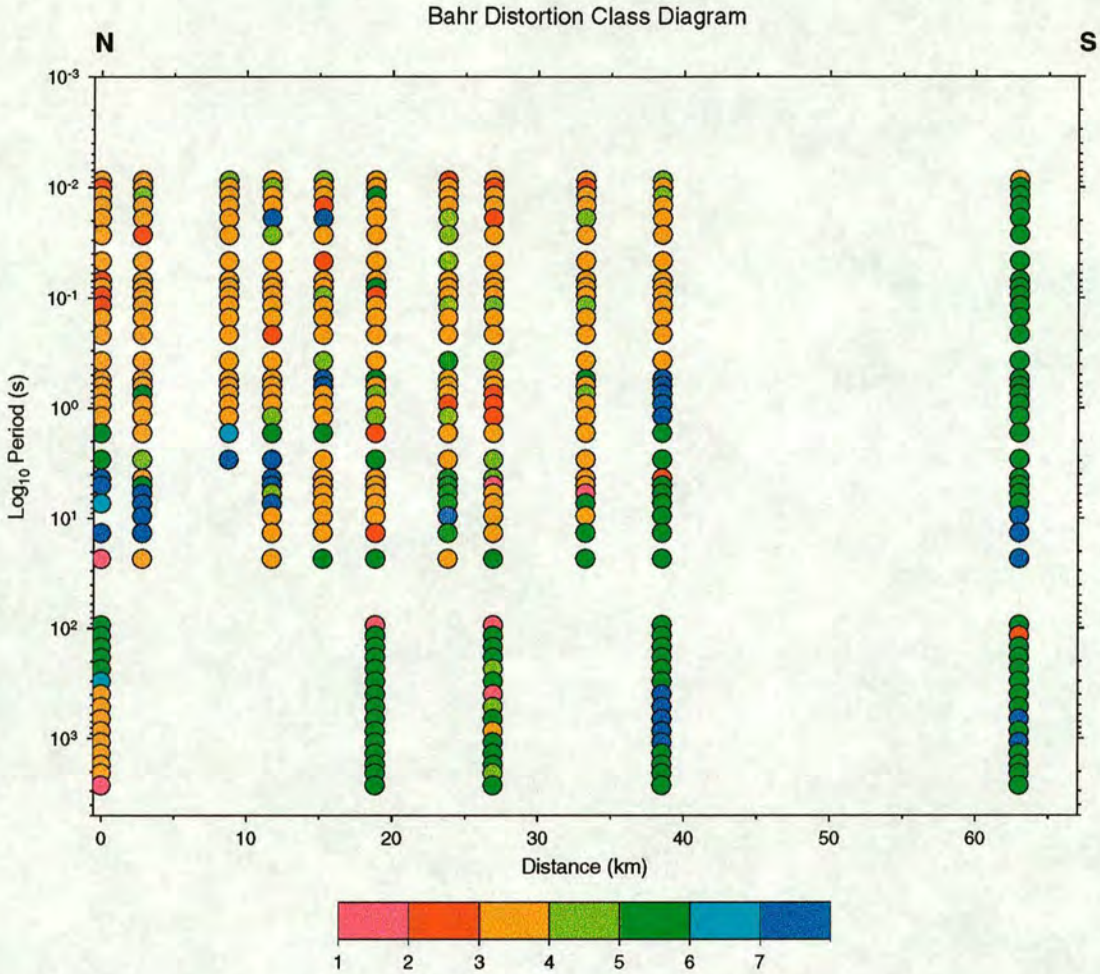

Figure 5.10. The Bahr decomposition results.

is extremely useful for categorising the structure in the impedance tensor but the uncertainties on the parameters by which this categorisation is made are usually overlooked. Using a Taylor's expansion technique suggested by Pamela Lezaeta (pers. comm., 1998) the uncertainties on the Bahr parameters in equations 5.36 to 5.39 were calculated. The partial derivatives of each parameter with respect to the real and imaginary parts of each tensor element were calculated numerically. The product of each derivative and the uncertainty in the associated impedance element were squared and summed, the uncertainty in the Bahr parameter being the square root of this value. The assumption is made that terms higher than first order in the Taylor expansion are negligible and can be discarded, this may not hold (Patrick Denny, pers. comm., 1998). Typically the values and the errors on Bahr's parameters were of the same order of magnitude. This will propagate into an uncertainty in the class that the impedance tensor belongs to and indicates that the Bahr parameters and class estimates are sensitive to uncertainties in the impedance estimates.

Several points arise from the results in table 5.1 and figure 5.10. Firstly it can be seen that very little of the data has been assigned to model class 2 which represents a layered earth with a local three-dimensional anomaly. This indicates that the dataset must be modelled two-dimensionally. Very few of the data fit within class 1, which represents a simple two-dimensional anomaly, and therefore Swift's

(1967) method for retrieving the regional strike of the anomaly may lead to unreliable results. The majority of the rest of the data fit within a distorted two-dimensional model, the only change being the degree to which the model is distorted. The data within what is believed to be the sedimentary basin are generally only weakly distorted, while that to the south and at longer periods shows stronger galvanic distortion. In both cases, as Bahr (1991) demonstrates, a decomposition such as those proposed by Bahr (1988) or Groom and Bailey (1989), which separates the regional from the local effects, must be used to retrieve the correct strike direction and impedance estimates from this dataset. There are very few significant periods of three-dimensional data, class 7. This class occur in regions where the signal to noise level is low and the data are believed to be poor in quality. Although these impedance tensors are three-dimensional and cannot be modelled two-dimensionally, the structure they describe may still be two-dimensional; while these data do not fit the model, neither do they invalidate it. As a final point it is interesting to note the increased degree of distortion evident on figure 5.10 in the AMT data at sites 10 and 11. This may reflect a galvanic charge build up on the nearby basin bounding fault, to which these two sites are closest.

5.9 Decomposition of the Mana Pools MT Tensors

The methodology for the decomposition of the Mana Pools impedance tensors is outlined using the LMT data from site 6 as an example. The LMT and AMT data are treated separately throughout the decomposition and the results combined at the end; this approach is justified because, while all possible efforts were made to locate the LMT stations at the exact sites of the earlier AMT measurements, positioning errors are bound to be present. The effect of this is likely to be a degree of variation in the local features present in the two sets of impedance tensors and consequently the distortion parameters could differ between the two.

The most important consideration in decomposing the measured impedance tensors is not to over interpret the data; each tensor should be decomposed using the simplest possible model. The model parameters derived for the more complex model classes, such as the superimposition model, become unstable if the impedance tensor already meets the requirements of a less complex model (Bahr, 1991). The initial decision of which decomposition model to fit to the data is made using the results of the Bahr model class assessment of § 5.8, displayed in table 5.1 and figure 5.10. All the impedance tensors collected and analysed in this way, with very few exceptions, belong to class 3 or higher, indicating the regional structure to be at least two-dimensional with, in the majority of cases, local distortion of varying strengths present. This gives an initial justification for applying the Groom and Bailey (1989) decomposition to the dataset.

Figure 4.5 shows plots of both the unrotated and Swift rotated (Swift, 1967) apparent resistivity and phase data for site 6; the plot of the unrotated data shows that the LMT data do not fit a one-dimensional model. Neither the two apparent resistivity or phase curves are coincident. An assessment of the fit of the data to the Swift model can be made using the parameter ϵ, the rms relative error of fit (Groom and

Bailey, 1989)

$$\epsilon^2 = \frac{\sum_{i=1}^{2}\sum_{j=1}^{2}\left|\hat{Z}_{ij} - Z_{ij}\right|^2}{\sum_{i=1}^{2}\sum_{j=1}^{2}|Z_{ij}|^2} \tag{5.43}$$

where Z_{ij} and $\hat{Z}_{ij}$ are the measured and modelled impedance tensor elements respectively. This is plotted for the Swift model of figure 4.5 in figure 5.11. The error parameter ϵ should be small compared

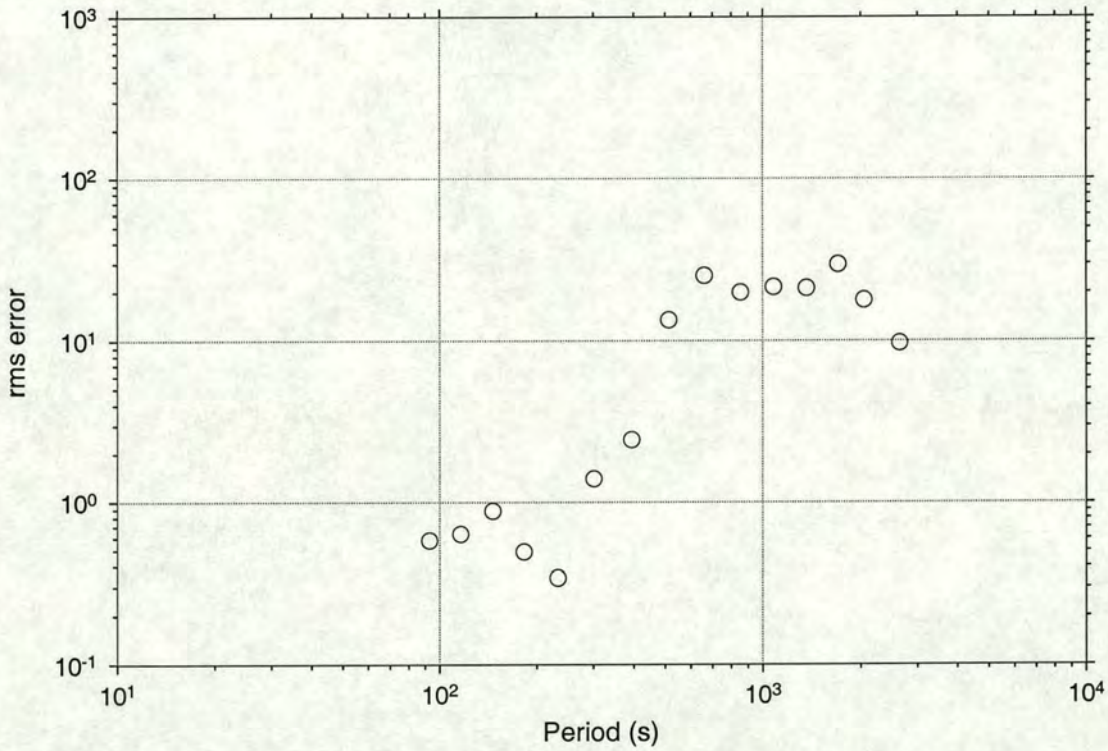

Figure 5.11. The rms relative error of fit between the model of Swift (1967) and the impedance data at site 6.

to unity and can be used to define regions where the Swift model is significantly in error. Non-zero values of ϵ may not be significant when data errors are taken into account (Groom and Bailey, 1989), but ϵ can still be used to compare the relative error of fit between different decomposition types. The shape of the curve in figure 5.11 reflects a change in error structure due to the increase in coherency discussed in the previous chapter at periods above approximately 400 s in the LMT data. At periods shorter than 400 s, the error bars on the model parameters are so large that the calculated rms values seem low. A look at the period range from 400 s to 3000 s where the data are better constrained shows that the relative mismatch of the two-dimensional model to the data is actually a factor of 10 and above.

Figure 5.12 shows the results of the Groom and Bailey (1989) decomposition for site 6 with all the parameters allowed to vary freely. The error bars on the parameters are not centred around the parameter estimates, and in some cases do not even coincide with them. This is because the value of a parameter represents the value calculated from the mean impedance tensor while the error bars represent the spread

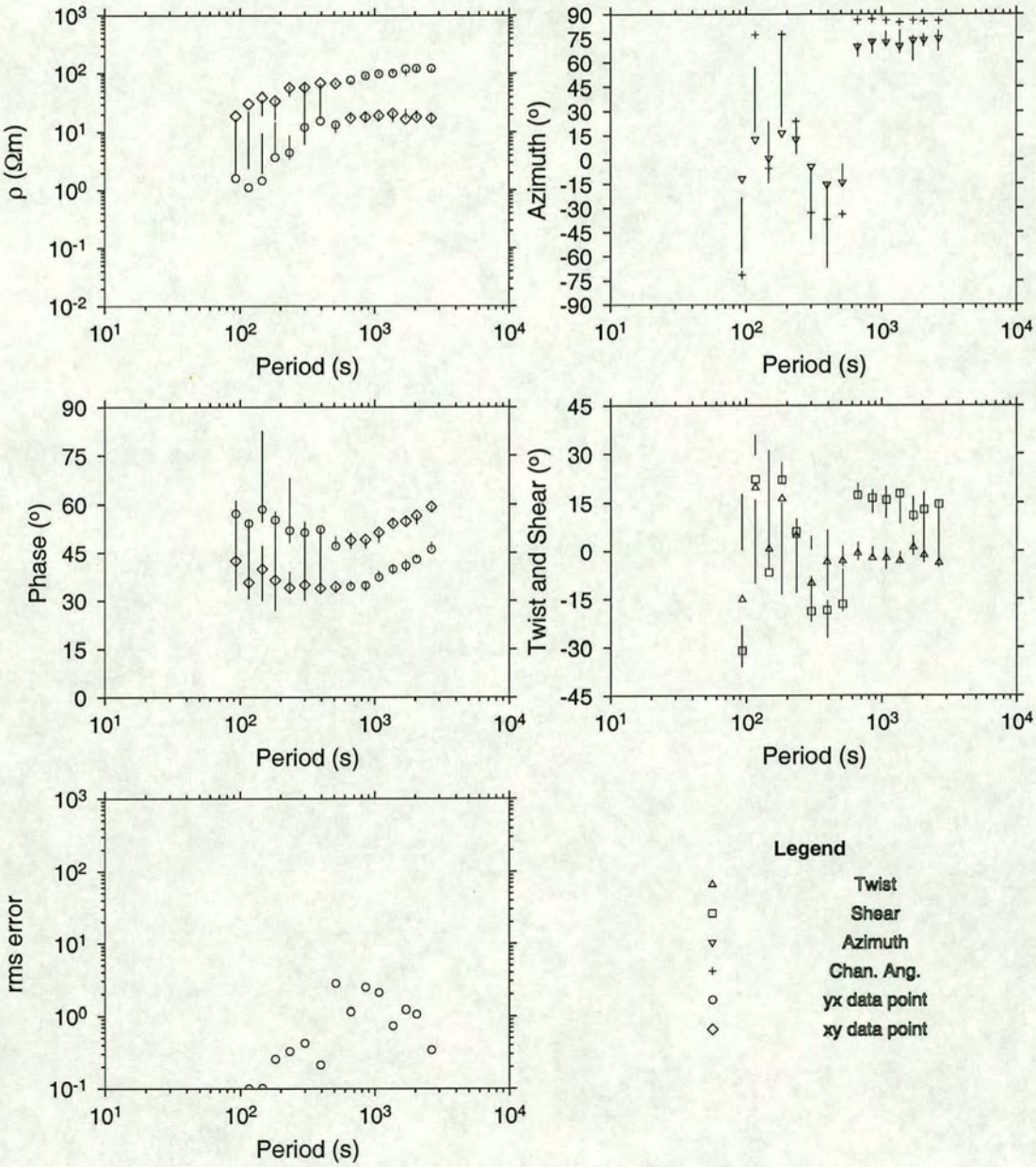

Figure 5.12. The data from the unconstrained Groom and Bailey (1989) decomposition for site 6. The swapping of the apparent resistivity and phase curves below 400 s is caused by instability due to noise on the shorter period data.

of the parameter calculated from each individual impedance estimate that constitutes the mean. The parameters are non-linear functions of the data and thus noise can bias a parameter estimate such that the error bars will not be symmetric about the mean estimate. When the noise bias is sufficiently strong the error bars will not include the mean estimate (Groom and Bailey, 1991). The first consideration from figure 5.12 is whether the Groom and Bailey superimposition model is adequate to describe the data or if there are significant deviations from it, for example through three-dimensional induction. There are two ways in which deviations from the ideal distortion model can be detected (Groom and Bailey, 1989). The error parameter ϵ can be used to look at the fit of the distortion model to the data. Comparing the value of ϵ calculated for the distortion model in figure 5.12 and that for the purely two-dimensional model of Swift in figure 5.11, the distortion model clearly fits the data an order of magnitude better than the two-dimensional model. The rms values are again even lower below 400 s reflecting the difference in error structure above and below this period.

The second indicator supporting the distortion model is the frequency independence of the twist parameter across the period range from 400 s upwards. For the distortion model to be realistic across a range of frequencies, the twist and shear should be approximately frequency-independent across those frequencies (Groom and Bailey, 1989). The shear parameter is also relatively stable in a slightly narrower period range. The different appearance of the twist and shear below 400 s is again caused by instability due to the poor data quality at shorter periods. A local channelling angle is also plotted on figure 5.12; this is defined as (Groom and Bailey, 1989)

$$\theta_l = \theta + \phi_t + \phi_e, \tag{5.44}$$

where θ is the regional inductive strike and ϕ_t and ϕ_e are the twist and shear angles respectively. The local channelling angle θ_l is the strike of the local distortion structure with the usual 90° ambiguity (Groom and Bailey, 1989). Conventional two-dimensional decompositions often rotate data to the local channelling angle rather than the regional one (Groom and Bailey, 1989, 1991). This is the case with the data from site 6. Comparing the local and regional strike in figure 5.12 and the rotation angle in figure 4.5, it is clear that the Swift model rotates the data in the LMT period range into the direction of the local distorting strike while the regional strike is actually c.15° farther west of north. The apparent resistivity and phase values retrieved by the two decomposition models are very similar because the local strike is close to the regional one. The Swift method however, derives parameters for an arbitrary co-ordinate system and the apparent resistivity and phases will not correspond to the correct values for the E- and H-polarisations but be linear combinations of the two.

A final test of the applicability of the distortion model to the LMT data from site 6 is made by testing whether the distortion parameters are really frequency-independent and whether the variations in them are due to noise or slight inadequacies in the model (Groom and Bailey, 1989). If the distortion parameters are truly frequency-independent then fixing them should not significantly affect the fit of the distortion model and the model is probably valid (Groom and Bailey, 1989). To decide on what constraints to impose, contour plots are constructed of twist, shear and model misfit for all possible regional azimuths; figure 5.13 is such a plot for site 6. It is clear from figure 5.13 that the regional azimuth can be constrained to approximately 68 to 73° for all periods longer than 400 s. Above 400 s the impedance estimates are so poorly constrained that they can be fit within their uncertainties at any regional azimuth. The contour plot of twist angle also shows this to be constant between -6 and 6° over

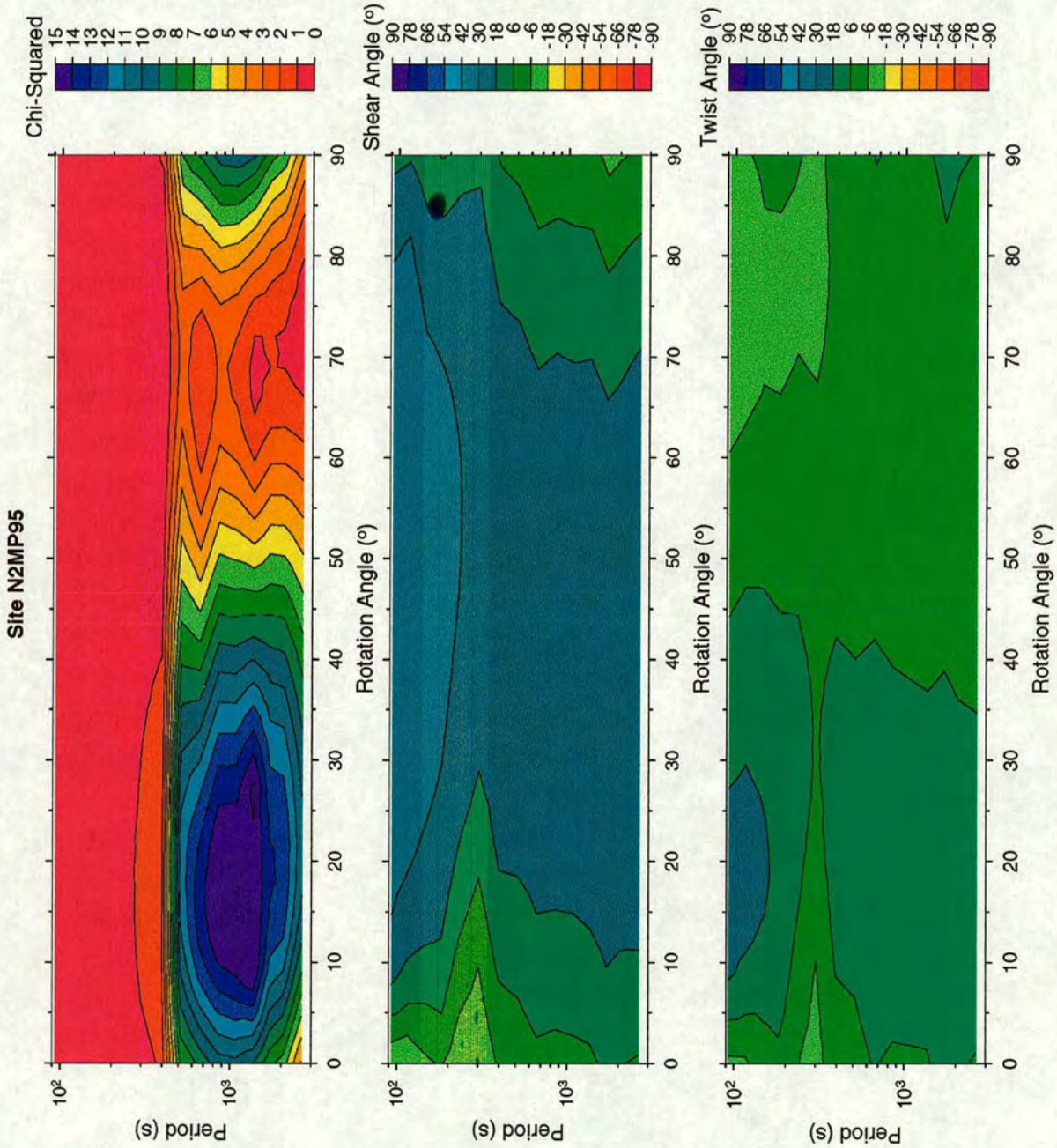

Figure 5.13. A contour plot of the model misfit, twist and shear angles at site 6 for a variety of regional azimuths.

this period range and the shear can be constrained to between 6 and 18°. The final constraints applied were a 68-73° azimuth, twist -4-0° and shear 13-19°; the parameters retrieved for the constrained decomposition are shown in figure 5.14. If N is the number of frequencies of data then the Groom and Bailey decomposition uses 7N parameters in total. By constraining the regional azimuth and the twist and shear we reduce this to 4N + 3 parameters (Groom and Bailey, 1989) which is less than the 5N parameters of Swift's two-dimensional model, but the fit is still an order of magnitude better. Constraining the decomposition has not significantly increased the misfit in figure 5.14. The error on the impedance estimates is identical to the unconstrained case at all but the four shortest periods where the data is too poor to constrain the data properly. The distortion parameters for the constrained model are all approximately frequency-independent and the apparent resistivity and phase curves are relatively smooth indicating the distortion model to be valid for this section of the data at this site.

A final comparison of the fit of the distortion model and the Swift model to the data can be gained from a look at the fits of the modelled tensor estimates to each component of the measured impedance tensor. Figure 5.15 shows the fit of the decomposed tensor from the Swift model to the data and figure 5.16 shows the fit of the Groom and Bailey tensor. These two plots show that the distortion model fits the auxiliary impedance elements considerably better.

The approach outlined in this section was used in the analysis of all the impedance tensors in the Mana pools dataset. The appropriateness of the Groom and Bailey model has been assessed by comparing its error of fit with that of the simpler two-dimensional model of Swift (1967) and by assessment of the frequency independence of the distortion parameters. The intention is to fit the tensor with the simplest possible model. If the distortion model is considered appropriate then its validity is checked by attempting to constrain the distortion parameters over a certain frequency range; this should result in no significant increase in the error of fit to the data. The frequency dependence of the terms regional and local mean that the distortion parameters may vary in different sections of the frequency range. In attempting to constrain these parameters, sections of data of at the least one decade are sought over which they are constant. The constrained distortion model is considered to be valid provided it has a misfit lower than a model requiring fewer parameters and not significantly greater than that for the unconstrained distortion model, the distortion parameters are frequency-independent over a frequency range of at least one decade and the apparent resistivity and phase curves are smoothly varying and consistent with those at neighbouring sites (Groom and Bailey, 1989).

The results of the constrained Groom and Bailey decomposition for those sites with data in both the LMT and AMT period range are shown in figures 5.17 to 5.21. In all cases the relative error of fit between the data and the model impedance estimates was smaller for the Groom and Bailey distortion model than for the Swift model, typically by an order of magnitude. This is true throughout the entire period range. The Groom and Bailey decomposition gives a good fit to each element of the measured impedance tensor at all sites, the only exception to this being the AMT frequency range at site 11. Site 11 shows the effect of strong distortion, the twist and shear are both large, c.-15° and c.30° respectively for the AMT frequencies, and figure 5.10 shows that the tensors at this site generally belong to class 5 and above. The fit of the model elements to the measured Z_{xy} and Z_{yy} components is slightly worse for frequencies above 0.04 Hz; this may indicate magnetic galvanic distortion of H_y at high frequencies caused by a strong distorting feature. This produces a magnetic field out of phase with the primary magnetic field (Groom and Bailey, 1989) whose major effect on the decomposition is

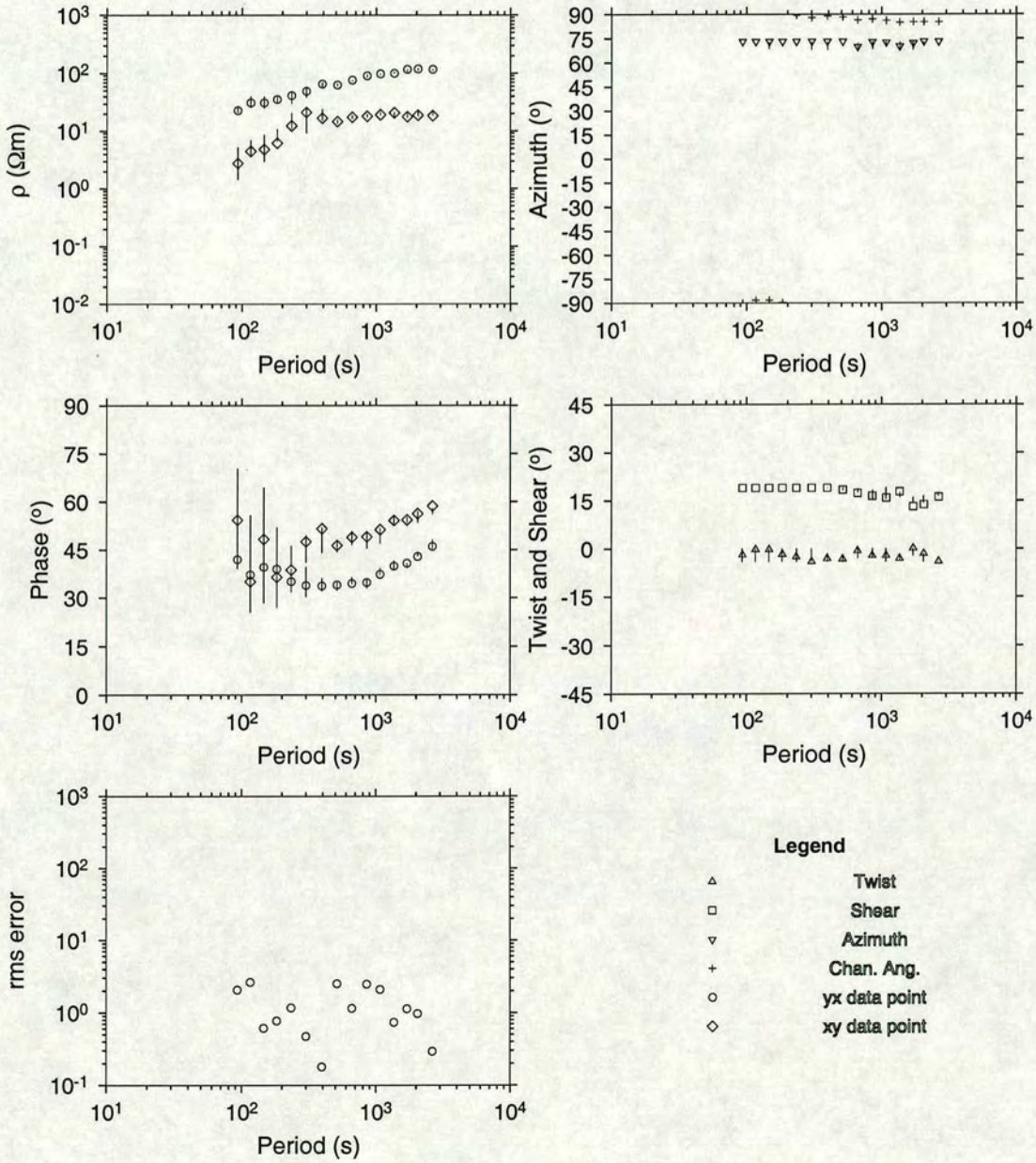

Figure 5.14. The results from the constrained Groom and Bailey (1989) decomposition for site 6.

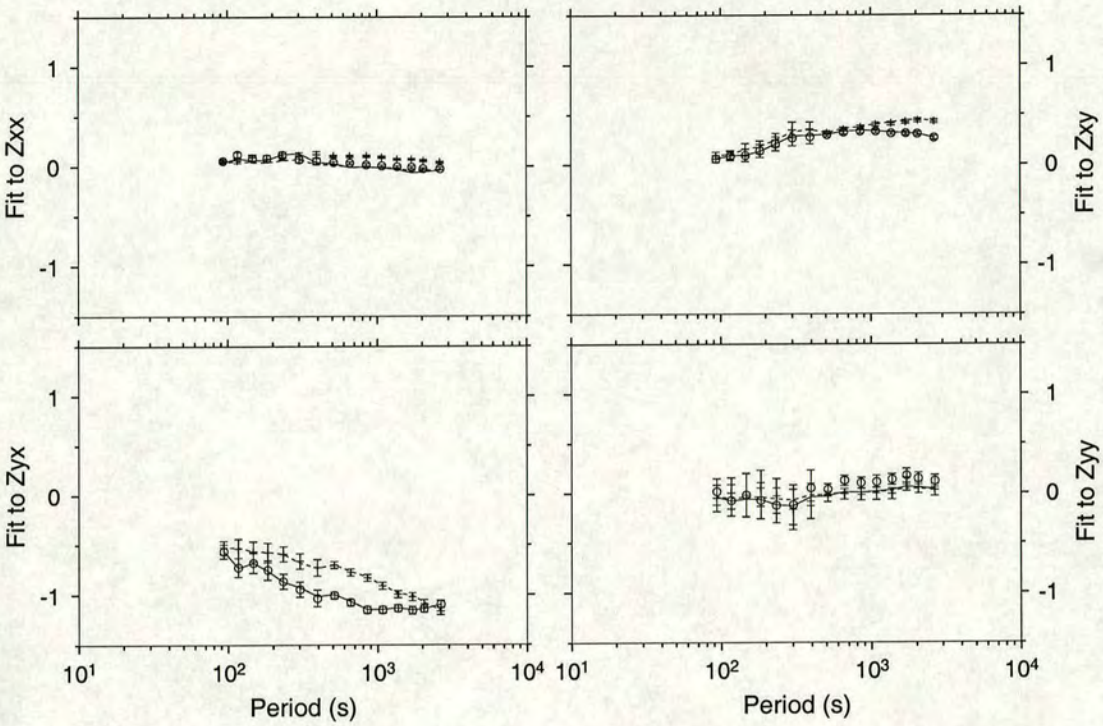

Figure 5.15. Fit of the Swift (1967) model tensor to the data. Real data are circles, imaginary are crosses, the real model fit is a solid line and the imaginary is dashed.

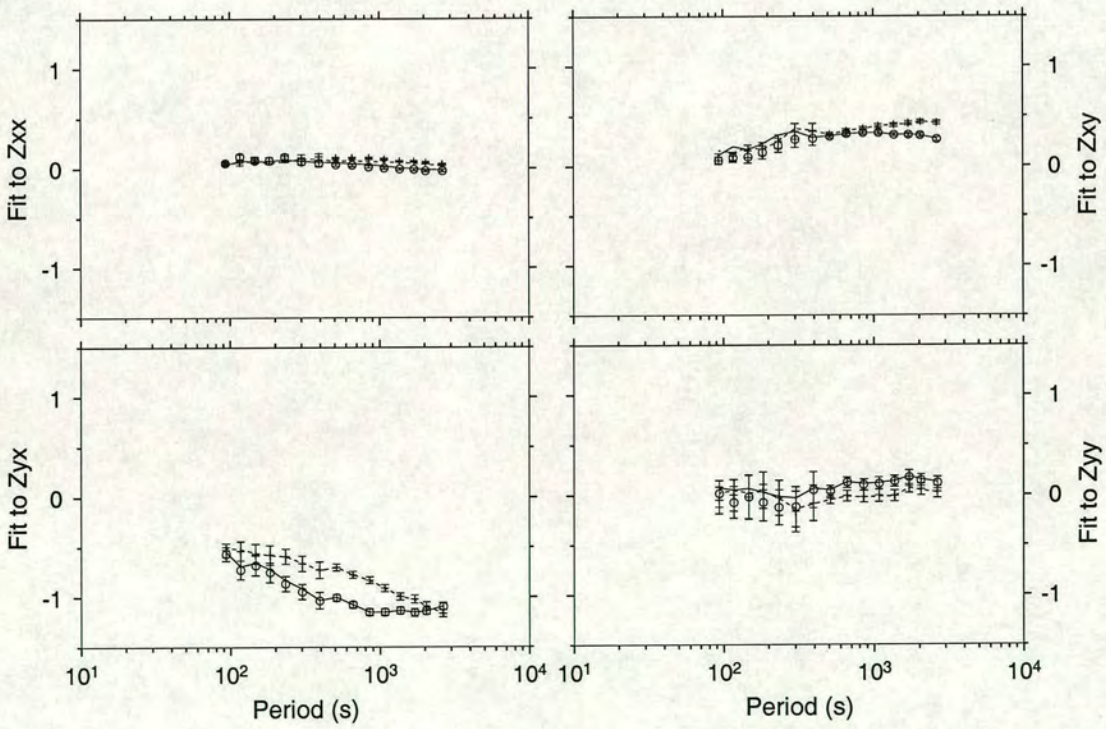

Figure 5.16. Fit of the Groom and Bailey (1989) model tensor to the data. Real data are circles, imaginary are crosses, the real model fit is a solid line and the imaginary is dashed.

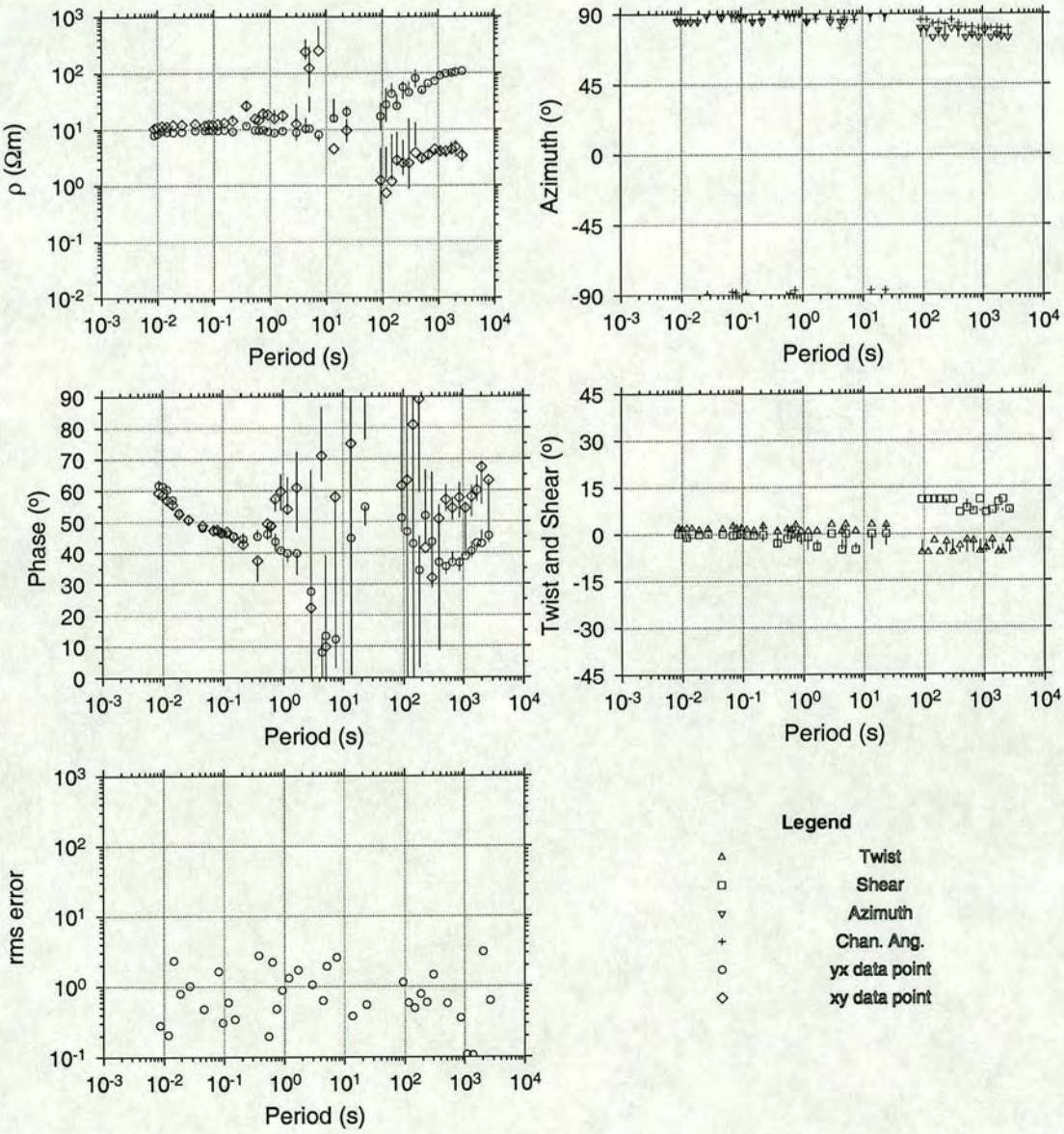

Figure 5.17. The results of the constrained Groom and Bailey (1989) decomposition for site 1.

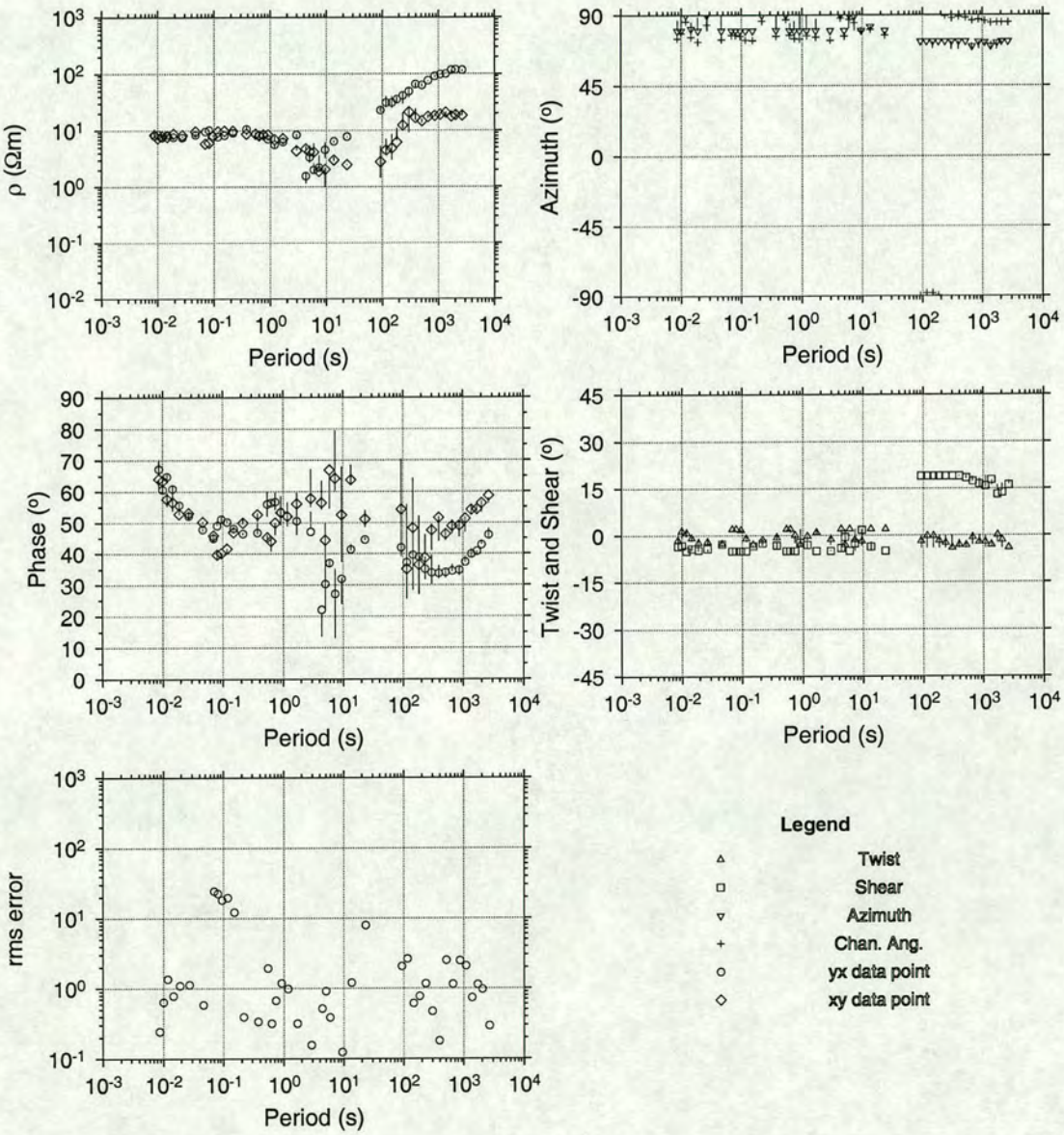

Figure 5.18. The results of the constrained Groom and Bailey (1989) decomposition for site 6.

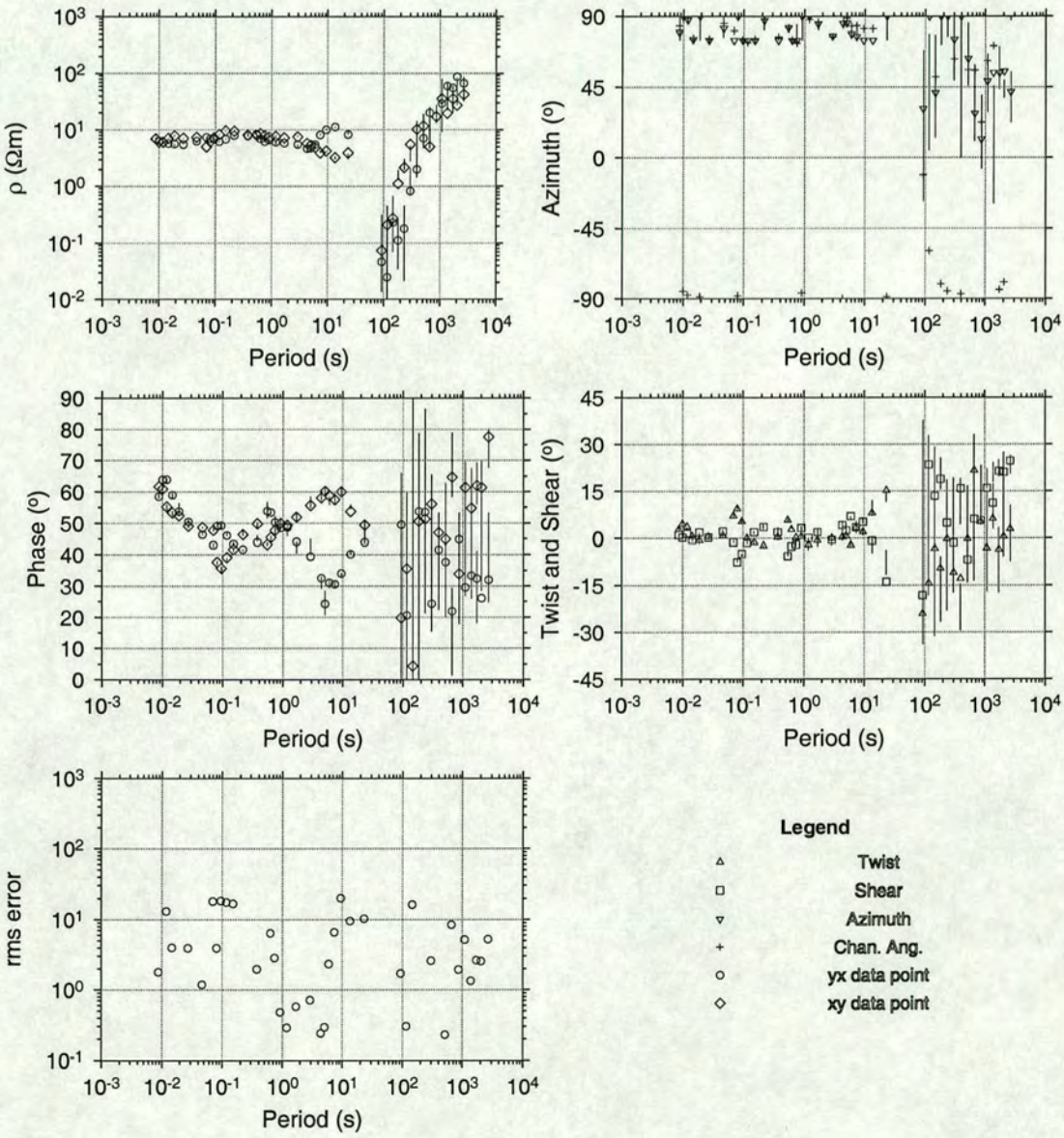

Figure 5.19. The results of the constrained Groom and Bailey (1989) decomposition for site 8. The drop in the LMT apparent resistivity curves and noise on all the LMT parameters is due to the poor quality of the LMT data at this site.

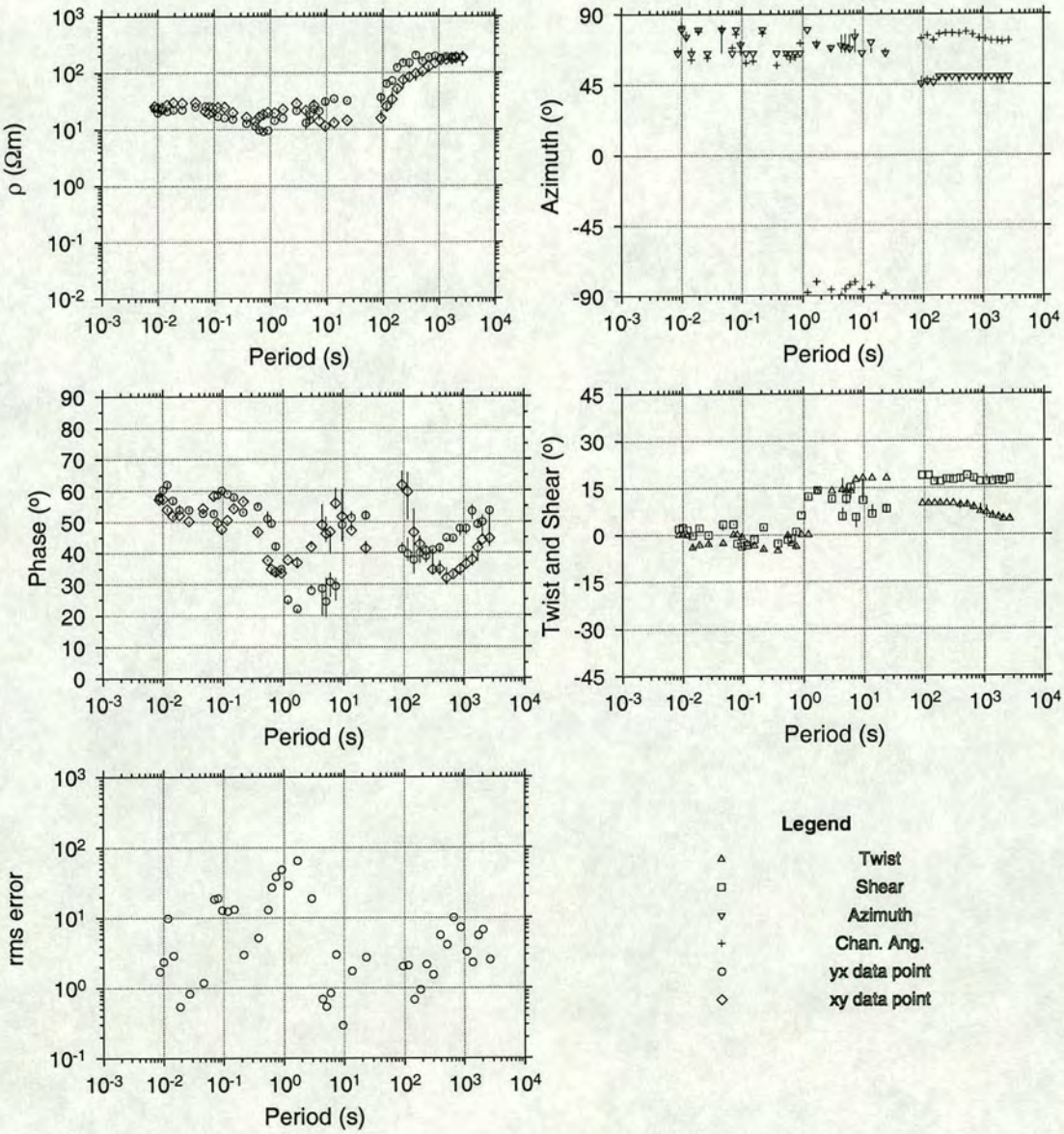

Figure 5.20. The results of the constrained Groom and Bailey (1989) decomposition for site 10.

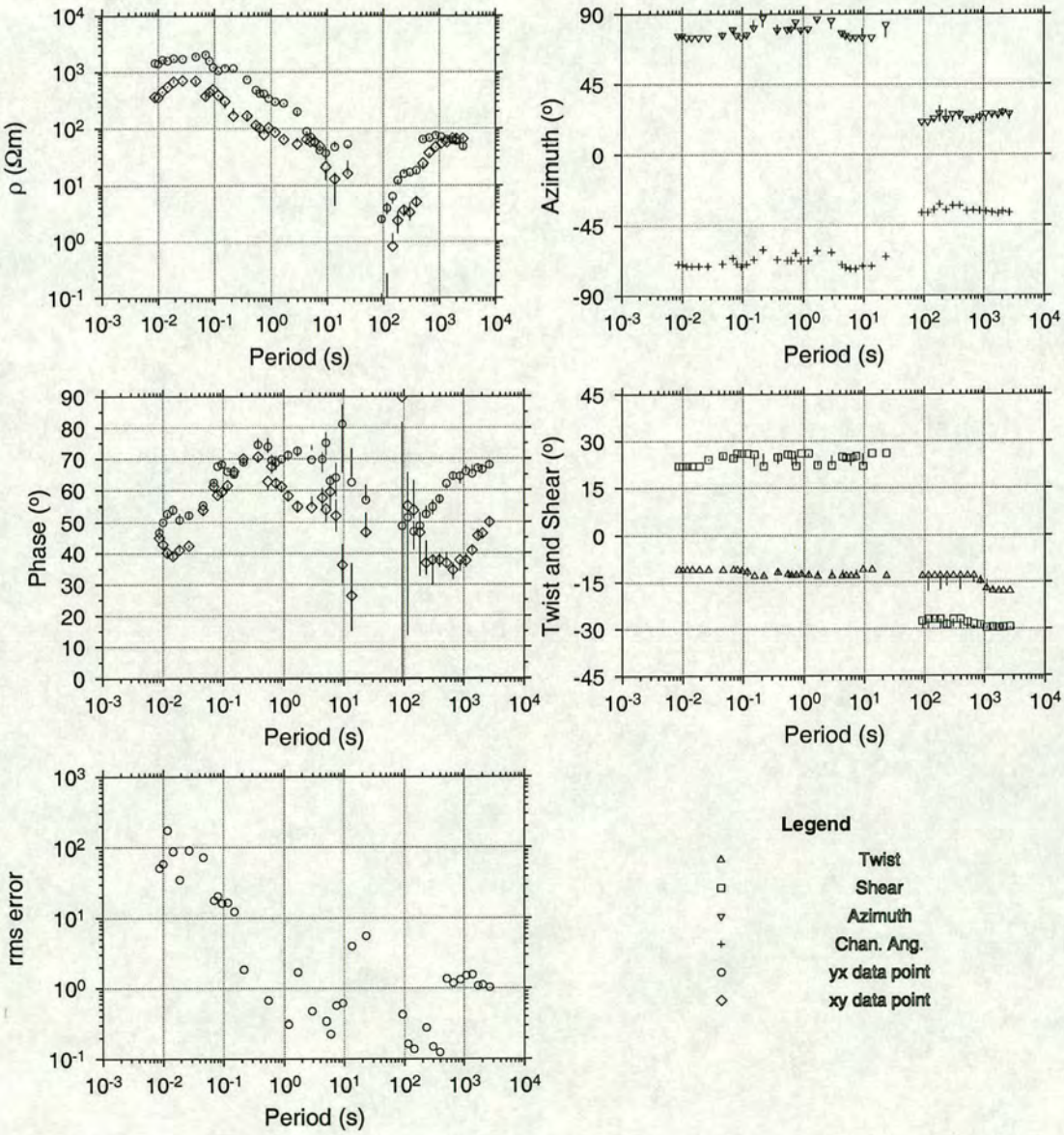

Figure 5.21. The results of the constrained Groom and Bailey (1989) decomposition for site 11.

to alter the phases of the regional impedance (Groom and Bailey, 1989; Groom and Bahr, 1992). This may partially explain the complex and markedly rough appearance of the phase curves at site 11. The effects of magnetic distortion are not seen in the tensors at any other sites. There are also problems in the apparent resistivity curves at site 11, which appear to be static shifted multiples of each other in the AMT period range, and there is also an offset in the LMT apparent resistivity at about 400 s. This period again marks the transition from noisy data to better constrained data and clearly the impedances at this site between 100 s and 400 s are not sufficiently constrained to be meaningful.

Frequency independence of the distortion parameters is diagnostic of a valid distortion model and this is achieved very satisfactorily for the LMT data at all sites barring site 8 where the data were too poor to justify the application of constraints. Twist and shear are relatively consistent in the LMT period range between sites within the valley; no significant change occurs until site 11. The twist within the valley is very small, with a slight increase at site 10, but the shear is close to 15° indicating a strong distortion, in agreement with the results of the Bahr distortion classification. The regional azimuth is seen to vary from approximately east-west to north of east as the sites are traversed from a north to south direction. Within the valley the local distortion strike and hence the direction in which the electric field is polarised (Groom and Bailey, 1989) is consistently closer to east-west than the regional strike, the former is the direction to which the data are rotated in the Swift decomposition results of § 4.9. The distortion parameters are significantly different between the AMT and LMT datasets as expected. Problems were encountered with the decomposition of the AMT data collected with the SPAM system; the data from SPAM are collected in four overlapping frequency bands. These overlap at periods of approximately 6×10^{-2}, 5×10^{-1} and 4 s. The data at these periods outlie the general trend slightly and this affects the decomposition. Evidence of this can be seen in the values of twist and phase in figure 5.18. Anomalously high twist values can be seen at the first two of these band overlaps and also at c.8×10^{-3} s where the highest frequency band begins. Corresponding jumps in the phase curve can also be seen in the same figure and also for site 8 in figure 5.19 where the shear is also affected. The effects of this problem are seen in the contour plots of model misfit by rotation angle where no rotation angle is found which fits the data at the affected periods. This is a problem with the data and not an indication of the inappropriate nature of the model; clearly the data at the extremities of each frequency band are more erratic than that for the band in general. This feature of the data must be considered when studying the shape of the parameter curves and the variability of the misfit of the model to the data. To stop this problem from affecting the decomposition too much the distortion parameters are not constrained as rigidly as those of the LMT data and effort is concentrated on achieving a smooth regional azimuth estimate while allowing small deviations in the magnitude of twist and shear.

The misfit of the LMT data increases from north to south within the valley, indicating an increasing amount of three-dimensional induction. This may be due to the increasing proximity of the escarpment and a shallowing of the basin to the south. The sediments in the valley often tend to be good gatherers of current and therefore at longer periods, where the valley is no longer long or straight enough to be approximated two-dimensionally, strong 3-D current channelling effects can be encountered (Groom and Bahr, 1992). A similar effect can be expected as the distance to the edge of the valley decreases. That a low misfit is achieved for the long periods at site 1 is not consistent with this. The problem can be explained if the greater basin depth in the north makes the skin depth of the EM signals small enough for the Zambia escarpment, just over 10 km to the north not to affect the data. The implication is that

the shallowing of the basin to the south is the dominant factor responsible for the increasing misfit of the model at longer periods. The local strike direction is extremely consistent within the LMT data in the valley, lying approximately east-west. The northward rotation of the local strike seen at site 11 in both data sets is indicative of current channelling into the valley. Site 11 is on the resistive side of the Zambezi escarpment and the electric field becomes distorted as the current deviates northward to flow into the more conductive valley, altering the local strike and increasing the magnitude of the distortion parameters.

Figure 5.20 shows an increase in the distortion parameters in the period range 1 to 30 s; this is not seen in the AMT frequency range for any of the other sites. The significant difference between site 10 and the other sites is its proximity to the Zambezi escarpment. The increase in distortion observed is related to a vertical discontinuity or a resistivity gradient and may represent either an increase in resistivity as the craton is approached or a significantly smaller sedimentary thickness. Following the discussion above, the latter hypothesis is more likely. This change occurs at a period of approximately 2 s and an approximate skin depth calculation at this period gives a value of c.3 km. This may represent an approximate depth to basement estimate at this site.

Within the AMT data, the regional and local strike tend to be parallel and the distortion parameters are very small; this indicates that the electric fields in this frequency range experience very little distortion within the valley. The increase in the distortion parameters in the LMT data represents a rotation of the regional strike by a small angle northward. The regional structure of the AMT data is now local to the LMT data and leads to distortion of the electric field with a local strike direction near parallel to that of the regional AMT strike. Although the difference between the local and regional strike directions are generally small, the plots of § 4.9 indicate that the Swift decomposition generally rotates the data to the local strike direction. This strike represents the direction of electric field polarisation due to current channelling rather than the inductive strike and gives principal impedance estimates which are linear combinations of their correct regional values. The results of the Groom and Bailey decomposition are believed to be better estimates of the correct regional strike and impedances.

5.10 Magnetotelluric Pseudosections

Table 5.2 shows the constraints placed on the regional azimuth in the Groom and Bailey decomposition of § 5.9. The regional azimuth bounds are used to choose a strike direction to which the data are decomposed before two-dimensional modelling; an azimuth of 80° is selected as this is consistent with the bulk of the AMT data and still very close to the azimuth constraints at sites 1 and 7. It is also close to the upper azimuth bounds on the LMT data within the valley, noting that the LMT data at site 8 are left unconstrained. The deviation from the correct azimuth bounds for the LMT data at sites 10 and 11 is extreme and models derived from data decomposed at this strike direction may be significantly in error at these two sites; however, it is the resistivity structure within the valley that is of prime interest in this study.

Figures 5.22 to 5.25 are pseudosections of the Mana Pools apparent resistivity and phase data after the decomposition to 80°. The geological strike of the Zambezi valley is known to be east-west and the measured xy mode is defined as the H-polarisation and yx as the E-polarisation. Figures 5.22 to 5.25

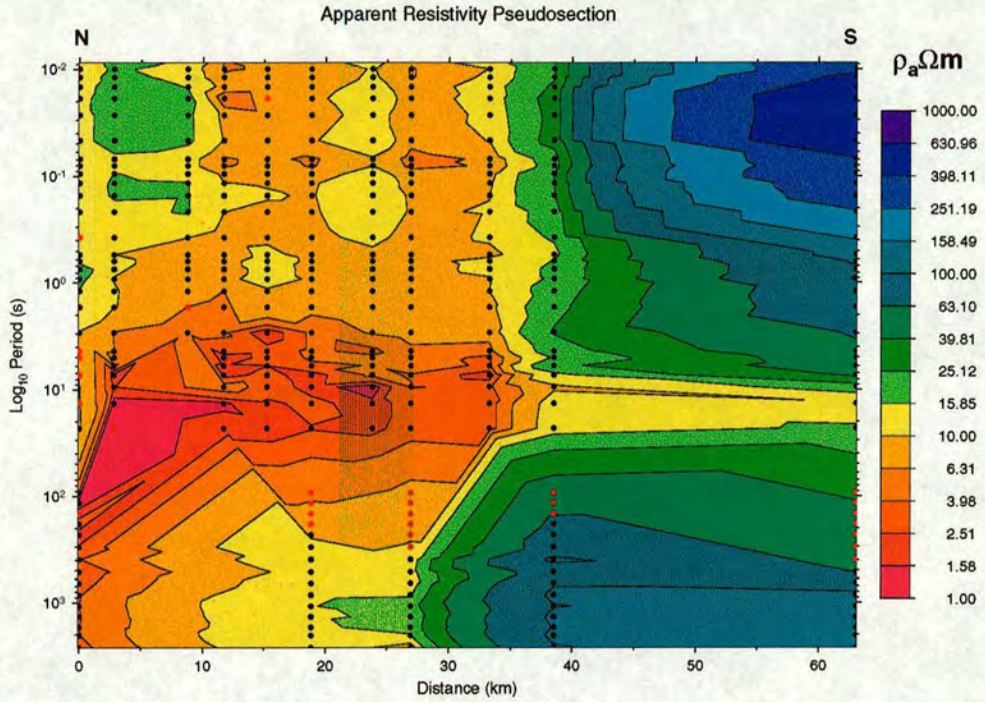

Figure 5.22. The H-polarisation apparent resistivity pseudosection. Circles mark data points; black are included in the contouring and red are excluded.

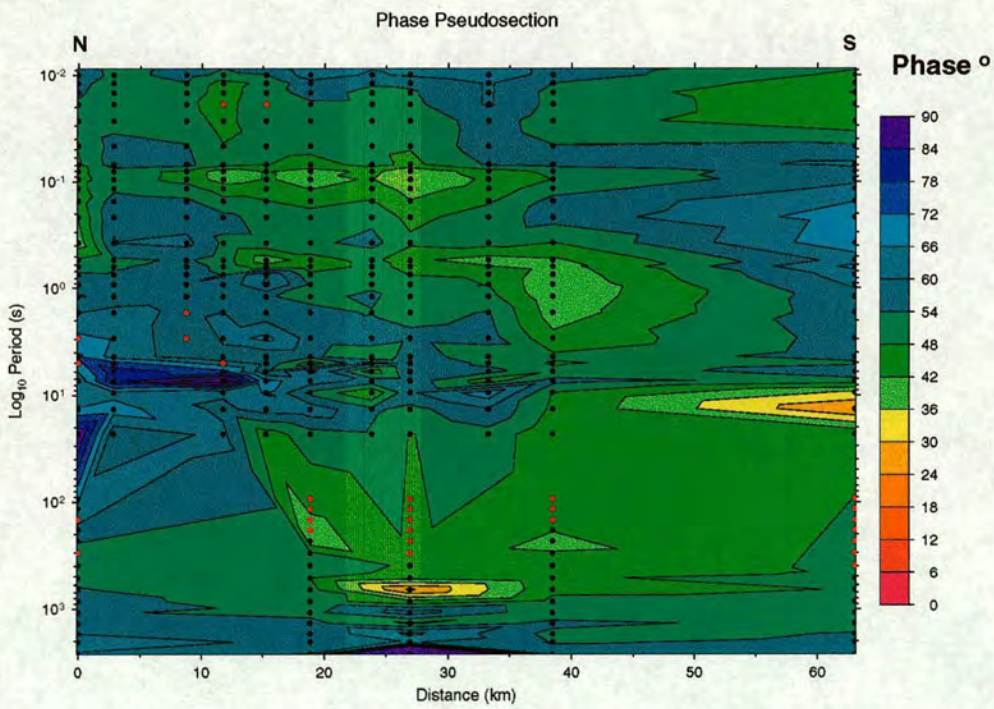

Figure 5.23. The H-polarisation phase pseudosection. Circles mark data points; black are included in the contouring and red are excluded.

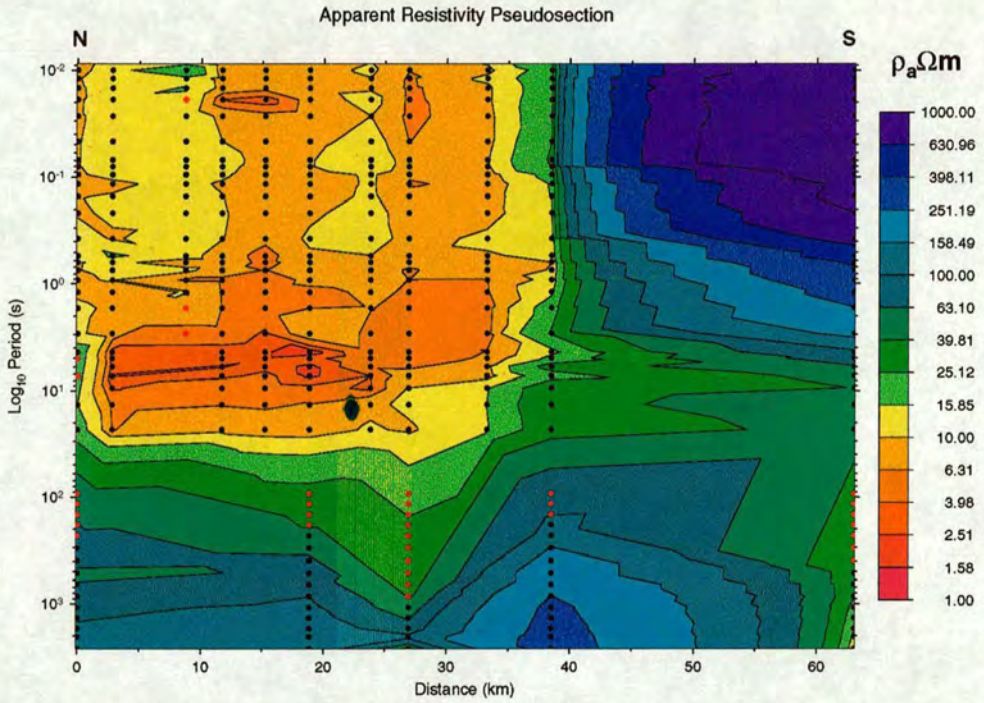

Figure 5.24. The E-polarisation apparent resistivity pseudosection. Circles mark data points; black are included in the contouring and red are excluded.

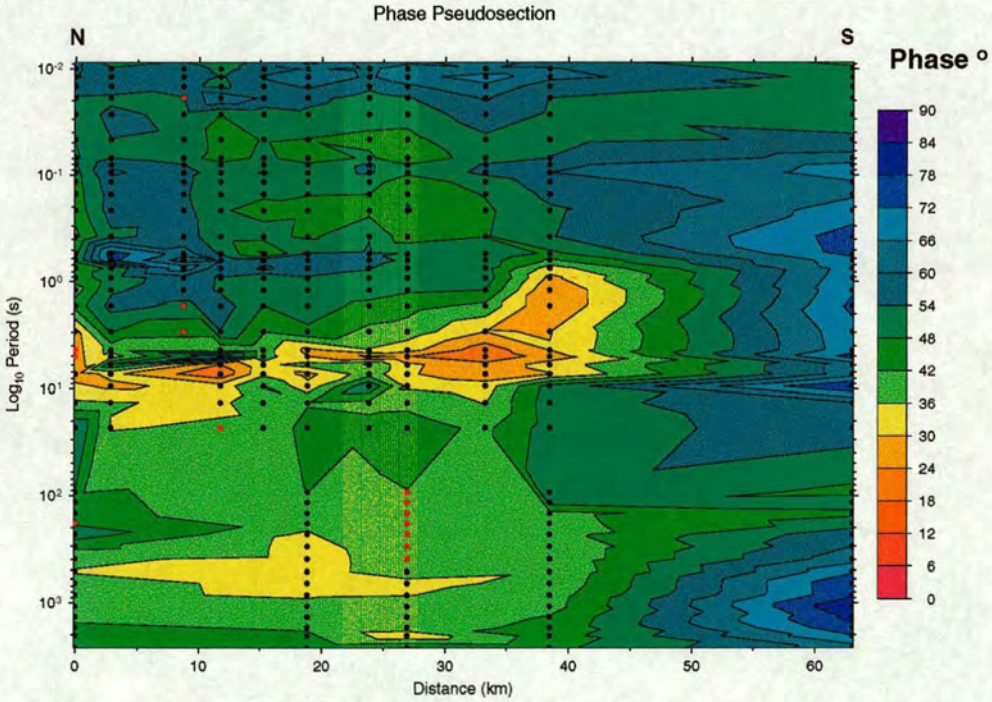

Figure 5.25. The E-polarisation phase pseudosection. Circles mark data points; black are included in the contouring and red are excluded.

Site	Regional Azimuth Bounds			
	AMT		LMT	
	Lower (^{o})	Upper (^{o})	Lower (^{o})	Upper (^{o})
1	85	90	75	81
2	80	90	-	-
3	80	90	-	-
4	80	90	-	-
5	80	90	-	-
6	80	90	68	73
7	85	90	-	-
8	75	90	free	free
9	80	90	-	-
10	65	80	45	50
11	75	90	21	28

Table 5.2. Constraints on the regional strike direction from the Groom and Bailey (1989) decomposition.

are useful as they give a first indication of the two-dimensional resistivity structure beneath the profile; horizontal position is plotted along the horizontal axes and the $\log_{10}$ period on the vertical axes gives a pseudo-depth scale. The circles plotted on the pseudosections represent the frequencies for each site at which impedance data are available; black circles represent data that are contoured and red represents data rejected. The data not used is important as it has implications for the spatial variation in model resolution. Data have not been rejected on a strictly coherency based measure but rather on the degree to which they outlie their neighbours. Apparent resistivity data have been rejected where a jump of in excess of one decade in resistivity occurs between two adjacent points and phase data have been rejected when they are found to lie in an incorrect quadrant. Many of these data can be included in the subsequent modelling where they will be weighted by their associated errors; they are eliminated here since the pseudosections plot only the value of a parameter and take no account of its associated error. Some AMT data within the dead band and at the extremities of the instrument's dynamic range are plotted. These data may be of poor quality due to their low coherency (see figures 4.4 to 4.8 of § 4.9) but are not in conflict with the trend of the rest of the data and so are included here. In comparison, the period range between 93 s and 400 s for the LMT data where the impedance estimates are both of low coherence and generally biased downwards (figures 5.17 to 5.21) are rejected in most cases for the apparent resistivity pseudosections as they significantly outlie neighbouring data. Not all the data are poor across the entirety of this period range and the biasing effects are not seen as strongly in the phase data, therefore not all of the phase data are rejected.

The ramifications that this has for subsequent modelling are more in the interpretation than in the strategy. Clearly, the rejected data in figures 5.22 to 5.25, marked with red circles, indicate a region of approximately two decades in frequency on which there will be very little constraint. The pseudosections indicate that the regions either side of this gap may be significantly different but the position of the transition may be difficult to determine; its position on figure 5.24 is determined only by a small number of data points and must be considered to be an artifact of a smooth contour transition rather than a definite, well determined boundary.

Not withstanding these reservations, there is much that can be deduced from the pseudosections. The plots of E-polarisation mode can give an idea of the continuity of features within the geoelectric section while the H-polarisation mode, where the electric field flows normal to strike, picks out lateral discontinuities. The accompanying phase plots convey the same information; in a layered medium a transition from one medium to a more conductive one with increasing period will see a rise in phase while a transition to a more resistive medium will see a drop in phase. It is clear from figures 5.22 and 5.24 that there is a transition from a good conductor to a poor one moving from north to south at site 10. This feature may initially seem an artifact of the high resistivity of site 11 and its large separation from site 10, but is in fact also seen in the data collected at site 10. Little can be deduced about the resistivity structure between these two sites as they are too widely separated to give adequate spatial resolution. Site 11 is also believed to be statically shifted and the high magnitude of the resistivity at site 11 may be doubted. The phase is unaffected by static shift but the pseudosections are difficult to interpret; at site 11 they show an increase in phase over the first two decades of data indicating that the surface is relatively more resistive than the underlying layers but this cannot really provide any answers to the problem. A modelling strategy to correct for this static shift will be used in the next chapter. The major boundary between the conductor and the resistor near site 10 is likely to mark the position of the Zambezi escarpment and should be well constrained because of its proximity to that sounding site.

The other main feature of the pseudosections is the termination of the conductive structure in the E-polarisation mode on figures 5.24 and 5.25. An increase in resistivity is seen from less than 10 Ωm to over 250 Ωm between 10 s and 1000 s with an accompanying decrease in phase. The exact location of the boundary marking this change is unsure due to the gap in the data. The decrease in phase marking this transition occurs at shorter periods at site 10, approximately 1 s, and this is accompanied by higher resistivity values at this site than at neighbouring ones and may indicate either cratonic material or a shallowing of the basin adjacent to the escarpment.

With the low resistivity within the basin and the site spacing used, the spatial resolution of the AMT data means that resolution of structure within the conductor is unlikely. The large separation of site 10 from site 11 will probably not impair detection of the boundary between the basin and the Zimbabwe craton but allows no determination of the intervening structure. Figures 5.24 and 5.25 show that the LMT data are sufficient to resolve the structure beneath the basin conductor but the transition may occur within the frequency range where the data are unreliable.

5.11 Summary

Analysis of the measured impedance tensors using Mohr circles shows the majority of the Mana Pools data to be close to two-dimensional. However, this is a generalisation as the skew of the data, though small, is non-zero over the entire frequency range. Application of the Bahr technique for assessment of the impedance tensor, in terms of its structural dimensionality and the degree of distortion present, indicates the overwhelming majority of the data to be of a galvanically distorted two-dimensional form. The degree of this distortion varies within the data; within the valley, the AMT data are only weakly distorted while those at longer periods are more strongly so. This may be due to a change in regional azimuth at longer periods. The data at all frequencies at site 11 are strongly distorted due to current

channelling into the valley to the north.

To analyse the distorted tensors, the Groom and Bailey (1989) decomposition was applied to the entire dataset to try to separate the local distortion effects from the regional inductive structure and retrieve accurate estimates of both the regional strike direction and the principal impedances. This technique provided impedance estimates with a better fit to the data than those obtained using the Swift (1967) method. The estimated regional strike directions recovered are relatively consistent for the AMT data and run approximately east-west although this deviates increasingly to north of east traversing the sites from north to south. The LMT regional strike is more variable but in a systematic manner, rotating northward from east-west as the sites are traversed north to south. This deviation from an east-west regional strike is much larger in the LMT data; all the AMT data has a regional strike within at least 10° of east-west while the LMT data rotates from within 10° of east-west at site 1, to 20° east of north at site 11. The local and regional strike directions are often found to be quite close but, where they differ significantly, the Swift model is seen to favour rotation to an angle nearer that of the local strike direction. This would result in a mixing of the regional impedances in the estimated tensor and clearly shows the superiority of the parameters retrieved in the Groom and Bailey decomposition.

Errors in relocating the AMT sites occupied in 1987, estimated to be at least 500 m, were expected to lead to different local conditions and variation in the distortion parameters between the data in the two separate period ranges. The observation is found to be true but the cause may be different; the distortion parameters are remarkably consistent site to site within each dataset. This implies that small errors in location may have little effect. The difference between the two datasets is due to the consistency of the local strike within the valley coupled with a variation in the regional strike between the two datasets. The variation in twist and shear between AMT and LMT represents the distortion of the regional electric fields caused by the change in regional strike. The AMT data have very little distortion so the two strike estimates are near parallel but, for the LMT data, the regional structure from the AMT period range now causes a distortion with a local strike parallel to the regional strike at the higher frequencies. While the local strike direction for the two datasets is similar, this does not mean that the static effects of the local structure need be the same; the quantity of charge built up on boundaries and resistivity gradients local to each site may be very different. Therefore the static shifting of a site such as site 11, which combines data from different frequencies collected under different local conditions, may vary within the different frequency bands. Here the errors in site relocation become important.

The results of the decomposition allow a further assessment of data quality to be made. At some sites within the AMT data there are small discontinuities in the phase curves which correspond to the ends of the overlapping frequency bands in which SPAM records data. The Groom and Bailey distortion parameters deviate from their smooth frequency-independent values at these frequencies and there is a high misfit to the distortion model for any rotation angle. This does not appear to be a three-dimensional effect but an artifact of the data inaccuracies at the extremity of each recording band. These data obviously need to be down weighted during modelling. At the long period end of the AMT data, the coherency is poor across the dead band and up to the end of the instrument frequency range. The data are also poor up to approximately 400 s in the LMT range; this gives a data gap of at least one and a half decades between the well constrained data from each dataset. This must be taken into account during the interpretation of models subsequently derived.

The data are decomposed at a regional strike angle of 80° prior to two-dimensional modelling. This

angle agrees with the majority of the AMT data and is close to the upper limit for the regional strike of the LMT data within the basin. It is also in good agreement with the strike of the Zambezi mobile belt which runs east-west along this section of the Zimbabwe border and also contains the Lower Zambezi basin (see chapter 2). The strikes at LMT periods from sites 10 and 11 deviate significantly from this value and two-dimensional models derived with this strike angle may be significantly in error for these regions of the data. The pseudosections plotted for the data, decomposed at this angle, give a resistivity or phase pseudo-depth section for the E-polarisation and H-polarisation data. They show three main features, a basin conductor, a more resistive basement layer and a resistive escarpment. The spatial resolution is unlikely to be sufficient to resolve structure within these features except at the highest frequencies. The proximity of the escarpment to site 10 should mean that it can be accurately located but the transition from the conductive basin to the resistive basement occurs within the data gap between the LMT and AMT surveys and may be difficult to resolve. The problem of static shift at site 11 remains to be addressed but an attempt will be made to solve it using a modelling strategy at the beginning of the next chapter.

Chapter 6

Modelling of the Mana Pools MT Data

6.1 Introduction

This chapter introduces the techniques used to model the Mana Pools MT data and discusses the models of the resistivity structure obtained with them. Chapter 5 showed the data to be two-dimensional and the modelling concentrates mainly on the use of two-dimensional inverse techniques. Due to the imprecision in the data and its availability at only a finite number of frequencies, the MT inverse problem is non-unique. To overcome this non-uniqueness, RRI (Smith and Booker, 1991), a minimum structure algorithm, is used to model the data. This type of inversion routine seeks models that are extreme in the sense that they are maximally smooth. This is achieved by simultaneous minimisation of the model misfit and the model roughness and means that the model only contains structure which is required by the data.

The one-dimensional D^+ modelling technique (Parker, 1980; Parker and Whaler, 1981) is used to determine the penetration depth of the data and the related ρ^+ technique (Parker and Booker, 1996) is used to assess the data consistency and place bounds on the apparent resistivity and phase where the data coherency is poor. The models obtained are compared to one-dimensional models of the Mana Pools AMT data derived by Whaler and Zengeni (1993).

6.2 One-Dimensional Modelling Techniques

Parker (1980) investigated the existence and construction of solutions to the inverse problem of electromagnetic induction in a one-dimensional earth. The data to be modelled usually consist of a set of estimates of either the MT complex impedance or admittance, available only as imprecise values at a finite number of frequencies. The inducing source field is assumed to be a uniform and horizontal magnetic field with periodic time behaviour of the form $e^{i\omega t}$. The conductivity σ varies only with depth and the resistivity model exists between $z = h$ at the surface and a perfect conductor at the base, $z = 0$. The electric field $\mathbf{E}(z, \omega)$ is horizontal and perpendicular to the magnetic field $\mathbf{H}(z, \omega)$ with boundary conditions $\mathbf{E}(0, \omega) = 0$ and $\partial\mathbf{E}/\partial z|_o = \mathbf{E}'_o \neq 0$. Neglecting displacement currents, measurements

of the electric and magnetic fields taken as a function of frequency at the surface can be related by a complex admittance $\mathbf{c}(\omega)$ (Weidelt, 1972; Parker, 1980), similar to the MT impedance $\mathbf{Z}(\omega)$, where

$$\mathbf{c}(\omega) = \frac{\mathbf{E}(h,\omega)}{i\omega\mu_o\mathbf{H}(h,\omega)} = \frac{\mathbf{E}(h,\omega)}{\partial\mathbf{E}/\partial z|_h}. \tag{6.1}$$

Parker (1980) showed that for a very large space of conductivity functions, the complex admittance $\mathbf{c}(\omega)$ can always be expressed as (Parker, 1980; Parker and Whaler, 1981),

$$\mathbf{c}(\omega) = b_0 + \int_0^\infty \frac{\Omega^2 - i\omega\lambda}{\lambda + i\omega} db(\lambda) \tag{6.2}$$

where b is a real, bounded nondecreasing function and Ω is an arbitrary real constant which is used to retain consistent dimensions. Parker (1980) further shows that with inexact data, there is a unique conductivity structure, consisting of a finite number of discontinuities, which gives the optimal fit of a one-dimensional model to the data. This class of model, termed a D^+ model, consists of a finite comb of positive delta functions (Parker, 1980). Parker (1980) and Parker and Whaler (1981) show that the D^+ solution can be represented by an expression equivalent to equation 6.2 where,

$$\mathbf{c}(\omega) = a_0 + \int_0^\infty \frac{da(\lambda)}{\lambda + i\omega} \tag{6.3}$$

and a has the same properties as b. Parker and Whaler (1981) go on to apply this technique and calculate D^+ models for real data. For the fit to be adequate to support the assumption of one-dimensionality, Parker and Whaler set a criterion of $\chi^2 < M + 2\sqrt{2M}$ for M independent data. The admittance data are complex and two independent data are thus obtained at each frequency. For data with normally distributed errors, this χ^2 limit means that models are accepted for which χ^2 lies within two standard deviations of its expected value M (Parker and Whaler, 1981). If no D^+ model is found to fit the data within this χ^2 limit then it can be concluded that the data are incompatible with the assumption of one-dimensionality.

The D^+ technique has a further important application; the assessment of the limiting depth below which the conductivity structure cannot be determined from the available data. Parker (1982) finds this limiting depth by using the properties of electrical shielding. If a thin perfectly conducting layer exists at a depth $H < h$ then the conductivity below this depth has no effect on the measured admittance estimates $\mathbf{c}(\omega)$. If the complex admittance data can be fitted with a model incorporating such a layer then it follows that the conductivity structure below H is completely arbitrary as it has no effect on the fit of the model. Parker (1982) adds a perfectly conducting delta function to the calculation of the D^+ model. This conductor is gradually raised until the χ^2 misfit of the model exceeds the limit set by Parker and Whaler (1981), at which depth the conductor lies at the penetration limit of the data.

The D^+ and related ρ^+ algorithms are the only one-dimensional modelling techniques applied to the Mana Pools data. The dataset was shown to be two-dimensional in chapter 5 and no attempt is made to fit the data with a one-dimensional model. The D^+ method is used to provide information about the one-dimensional penetration limit of the data.

6.3 Two-Dimensional Modelling Techniques

A central problem in data inversion is that the data themselves are imprecise and only available for a finite number of frequencies. This makes the inversion process non-unique and, for MT data, an infinite number of resistivity distributions exist which fit the data. Due to this inherent non-uniqueness, the parameterisation and the type of model sought present a problem. The solution of a least squares inversion for a set of model parameters defined by a priori geological knowledge are closely dependent on the parameterisation employed (Constable *et al.*, 1987). For instance, the layer depths and resistivities of a one-dimensional model may be significantly different depending on whether a three or five layer model is sought. In such circumstance there is no guarantee that structure within the model is required by the data rather than being an artifact of the style of parameterisation (deGroot Hedlin and Constable, 1990). As an alternative approach to the problem, the model can be over-parameterised and divided into more blocks than there are degrees of freedom in the data, the resistivity being sought for each block. This can also be problematic as it can lead to large oscillations in the resistivity structure which are physically unrealistic and in extreme cases (deGroot Hedlin and Constable, 1990) tends towards the D^+ model of Parker (1980).

One approach to the inversion of MT data is to seek a model that deviates from the simplest model possible only where structure is required to fit the data. This approach is taken by the Occam inversion method (Constable *et al.*, 1987; deGroot Hedlin and Constable, 1990). The algorithm seeks to overcome the difficulties of the under- and over-parameterised approaches by seeking models that are extreme in the sense of having the minimum possible structure (deGroot Hedlin and Constable, 1990). This approach is based upon the tenet known as Occam's razor (deGroot Hedlin and Constable, 1990; Constable *et al.*, 1987); "a simple solution is preferable to one which is unnecessarily complicated." At each step of the two-dimensional Occam inversion, an over-parameterised model is inverted and the smoothest model sought for a specified value of misfit (deGroot Hedlin and Constable, 1990). The advantages of this are twofold; firstly, the resistivity structure obtained is minimal, giving merely structure that is required by the data - the implication is that the earth structure is at least as rough as the model (deGroot Hedlin and Constable, 1990). Secondly, an idea of the resolution of the data is gained, since more complex models of the same misfit cannot be distinguished from the smoothest one.

Occam's 2-D inversion over-parameterises the model as a series of rectangular prisms each of a constant resistivity (deGroot Hedlin and Constable, 1990). This grid extends laterally until it becomes a series of uniform layers and continues vertically with the block size increasing on a logarithmic scale, terminating with a set of prisms which are elongated with depth. This grid is called the regularisation mesh (deGroot Hedlin and Constable, 1990). The size of the resistivity blocks are determined from a resistivity estimate based on the results of a one-dimensional inversion of the E-polarisation data. Each block is made much smaller than the resolution length of the data so that the location of their boundaries has no effect on the resistivity structure retrieved (deGroot Hedlin and Constable, 1990). The forward calculations are made using the forward code of Wannamaker *et al.* (1987) on a finite element mesh consisting of a rectangular array of nodes. This mesh must at least contain the nodes of the regularisation mesh and in general can be much finer to maintain the accuracy of the forward calculations (deGroot Hedlin and Constable, 1990). The finite element grid and mesh remain constant between iterations (deGroot Hedlin and Constable, 1990) and the model response is calculated for a set of logarithmically-spaced

frequencies.

As the model grid is terminated both laterally and vertically by uniform resistivity blocks, rather than blocks of a constant resistivity gradient, first derivative smoothing is used to suppress model structure not required to fit the data. This is achieved by minimising the model roughness, which for a 2D structure with a strike parallel to the x direction is defined by (deGroot Hedlin and Constable, 1990),

$$R_1 = ||\partial_y \mathbf{m}||^2 + ||\partial_z \mathbf{m}||^2. \tag{6.4}$$

Here $\mathbf{m}$ is the vector of model parameters, ∂_y is a roughening matrix (deGroot Hedlin and Constable, 1990) which differences the model parameters of laterally-adjacent prisms and ∂_z is a vertical roughening matrix that differences the model parameters of vertically-adjacent prisms. The width of the finite element mesh prisms is controlled by the need to have a fine grid at the surface and their width remains constant with depth. The vertical extent of the prisms, however, increases with depth to mirror the decrease in resolution power (deGroot Hedlin and Constable, 1990). This in effect corresponds to an increase in the penalty for vertical roughness at depth. The penalty for lateral roughness is therefore also increased. The lateral smoothing measure is weighted by a factor v_i/h so that,

$$\frac{v_i}{h} m_2 - \frac{v_i}{h} m_1 \tag{6.5}$$

is the first difference between two laterally adjacent mesh blocks of resistivity m_1 and m_2 where v_i is the vertical extent of the grid block i, and h is its horizontal width. Roughness is penalised more heavily at depth to stop the vertical extension of structure to excessive depth through the increase in size of the regularisation mesh blocks (deGroot Hedlin and Constable, 1990).

If the data are defined as $d_j, j = 1, 2...M$, and are of known variance σ_j, a model can be constructed with a misfit to the data quantified by a standard least squares two-norm measure:

$$\chi^2 = ||\mathbf{Wd} - \mathbf{W}F[\mathbf{m}]||^2 \tag{6.6}$$

where $F[\mathbf{m}]$ are the non-linear forward functionals relating the discrete model parameters $\mathbf{m}$ to the data $\mathbf{d}$ (deGroot Hedlin and Constable, 1990). $\mathbf{W}$ is a diagonal weighting matrix defined by

$$\mathbf{W} = diag\{1/\sigma_1, 1/\sigma_2, \cdots 1/\sigma_M\}. \tag{6.7}$$

From this point the smoothest possible model is sought subject to the condition that it fit the data with some prescribed tolerance. If the assumptions of statistically independent, zero mean Gaussian errors are made then χ^2 has an expected value of M, the number of independent data (deGroot Hedlin and Constable, 1990).

The minimisation problem is solved using a Lagrange multiplier μ^{-1} and minimisation of the function (deGroot Hedlin and Constable, 1990),

$$U[\mathbf{m}] = ||\partial_y \mathbf{m}||^2 + ||\partial_z \mathbf{m}||^2 + \mu^{-1}\{||\mathbf{Wd} - \mathbf{W}F(\mathbf{m})||^2 - X_*^2\}, \tag{6.8}$$

U is minimised at all points where the gradient with respect to the model is zero. To overcome the

non-linearity of the forward functionals $F[\mathbf{m}]$ the problem is first linearised and then solved iteratively. For a starting model $\mathbf{m_1}$ the Taylor expansion of the forward functional truncated to only first order terms is given by (deGroot Hedlin and Constable, 1990).

$$F[\mathbf{m_1} + \Delta] = F[\mathbf{m_1}] + \mathbf{J_1}\Delta, \tag{6.9}$$

where $\mathbf{J_1}$ is the Jacobean matrix, an $M \times N$ matrix of Frechet derivatives of $F[\mathbf{m_1}]$ and

$$\Delta = \mathbf{m_2} - \mathbf{m_1} \tag{6.10}$$

is a small perturbation about a starting model. Substituting back into equation 6.8 we get (deGroot Hedlin and Constable, 1990),

$$U = ||\partial_y \mathbf{m_2}||^2 + ||\partial_z \mathbf{m_2}||^2 + \mu^{-1}\{||\mathbf{W}\hat{\mathbf{d}}_1 - \mathbf{W}\mathbf{J_1}\mathbf{m_2}||^2 - X_*^2\}, \tag{6.11}$$

where,

$$\hat{\mathbf{d}}_1 = \mathbf{d} - F[\mathbf{m_1}] + \mathbf{J_1}\mathbf{m_1}. \tag{6.12}$$

U is linear about $\mathbf{m_2}$ (deGroot Hedlin and Constable, 1990). Differentiating with respect to $\mathbf{m_2}$ to find the model which minimises U gives an iterative expression,

$$\mathbf{m}_{i+1} = [\mu(\partial_y^T \partial_y + \partial_z^T \partial_z) + (\mathbf{W}\mathbf{J}_i)^T \mathbf{W}\mathbf{J}_i]^{-1} (\mathbf{W}\mathbf{J}_i)^T \mathbf{W}\hat{\mathbf{d}}_1. \tag{6.13}$$

The Lagrange multiplier μ is sought at each iteration. The details of how this is done and the implementation of a scheme to solve equation 6.13 are given in Constable *et al.* (1987).

The difficulty with standard two-dimensional inversions such as the Occam method is that they require large amounts of computer time. A much faster method for two-dimensional inversion of MT data, the rapid relaxation inverse (RRI) technique, was proposed by Smith and Booker (1991). Conventional 2D techniques run multiple forward solutions to calculate the Jacobean matrix. A solution technique is then used to predict the resistivity perturbations which will best improve the fit to the data. The RRI technique optimises its iteration time over a standard technique by reducing the number of forward model calculations required. The crucial assumption allowing this is that the lateral gradients of the magnetic and electric fields can be approximated by those from the previous iteration. This allows the decoupling of the equations for each horizontal coordinate, allowing the improved resistivity profile to be sought separately beneath each site (Smith and Booker, 1991). The set of resistivity perturbations for each site is calculated via a problem that is very similar to the one-dimensional inverse problem (Smith and Booker, 1991). These separate profiles of the resistivity structure are interpolated to generate a new two-dimensional resistivity structure from which two-dimensional field values can be calculated for use in the next iteration. The only forward solution required is the final one, to calculate the data residuals and the two-dimensional field values. This is solved efficiently using an iterative scheme starting from the field values of the previous model which are expected to be a reasonably good approximation to the new values. This reduction in the number of forward steps required is the reason for RRI's relatively short run time.

The theory behind the RRI algorithm is demonstrated for the E-polarisation where the electric field is parallel to the geoelectric strike. Smith and Booker (1991) make the assumptions of a good isotropic conductor and no ferromagnetism. Displacement currents are ignored and a harmonic time dependence of $e^{-i\omega t}$ is assumed for the magnetic and electric fields. Under these assumptions Maxwell's equations reduce to,

$$\nabla \times \mathbf{H} = \sigma \mathbf{E} \qquad \nabla \times \mathbf{E} = i\omega\mu_o \mathbf{H} \tag{6.14}$$

where $\mathbf{E}$ and $\mathbf{H}$ are the electric and magnetic fields, σ is the conductivity and μ_o is the magnetic permeability of free space. For a two-dimensional resistivity structure in a right handed co-ordinate system where x is parallel to geoelectrical strike, these equations become

$$\nabla^2 E_x = -i\omega\mu_o\sigma(y,z)E_x \tag{6.15}$$

$$\frac{\partial E_x}{\partial z} = i\omega\mu_o H_y. \tag{6.16}$$

To solve the inverse problem, it is necessary to determine the sensitivity of the data to changes in the conductivity. Smith and Booker (1991) do this using a perturbation analysis. Equation 6.15 can be re-expressed as,

$$\frac{1}{E}\frac{\partial^2 E}{\partial z^2} + \left\{\frac{1}{E}\frac{\partial^2 E}{\partial y^2}\right\} + i\omega\mu_o\sigma = 0 \tag{6.17}$$

where the variables and subscripts on the field components have been dropped for simplicity. The term in the braces $\{\}$ involves the lateral gradient of the electric field. If it were discarded then equation 6.17 would be exactly the same as the induction equation for a one-dimensional earth (Smith and Booker, 1991). The data are defined as the surface values of the variable V which is closely related to the MT impedance,

$$V = \frac{1}{E}\frac{\partial E}{\partial z} = i\omega\mu_o\frac{H_y}{E_x}. \tag{6.18}$$

It can be shown from this definition that

$$\frac{1}{E}\left(\frac{\partial^2 E}{\partial z^2}\right) = \frac{\partial V}{\partial z} + V^2 \tag{6.19}$$

and it therefore follows that equation 6.17 can be written as,

$$\frac{\partial V}{\partial z} + V^2 + \left\{\frac{1}{E}\frac{\partial^2 E}{\partial y^2}\right\} + i\omega\mu_o\sigma = 0. \tag{6.20}$$

Again the lateral gradients of the field are confined to the terms within the braces $\{\}$. Equation 6.20 is satisfied for data V_o by an initial two-dimensional conductivity distribution σ_o with associated electric field values E_o. A small perturbation can then be made, $\delta\sigma$, to the conductivity structure σ_o so that $\sigma = \sigma_o + \delta\sigma$, causing the modelled data values to change correspondingly, $V = V_o + \delta V$. Using the justification that vertical field gradients are generally larger than horizontal gradients due to the skin

depth effect, Smith and Booker (1991) make the approximation

$$\frac{1}{E}\frac{\partial^2 E}{\partial y^2} = \frac{1}{E_o}\frac{\partial^2 E_o}{\partial y^2}. \tag{6.21}$$

Substituting these expressions into equation 6.20, subtracting the zeroth-order equation and neglecting second-order terms gives a first-order linear differential equation relating the perturbation in the conductivity structure to that in the data, where (Smith and Booker, 1991)

$$\frac{\partial}{\partial z}\delta V + 2V_o\delta V + i\omega\mu_o\delta\sigma = 0. \tag{6.22}$$

This can be made an exact differential using an integrating factor (Smith and Booker, 1991). Combining the definition of V with vertical integration at each site, y_i, gives the complex expression (Smith and Booker, 1991)

$$\delta V(y_i, 0) = \frac{i\omega\mu_o}{E_o^2(y_i, 0)}\int E_o^2(y_i, z)\delta\sigma(z)dz. \tag{6.23}$$

Integration is performed from the surface down to a depth large enough for the electric field to have effectively decayed to zero.

Smith and Booker (1991) redefine the data as

$$d_{xy} = \ln\left(-i\omega\mu_o\left[\frac{H_y}{E_x}\right]^2\right) = \ln\left(\frac{V^2}{-i\omega\mu_o}\right) \tag{6.24}$$

for the purpose that,

$$\Re[d_{xy}] = -\ln\rho_a \qquad \text{and,} \qquad \Im[d_{xy}] = 3\pi/2 - 2\phi$$

where ρ_a and ϕ are the apparent resistivity and phase more commonly used in MT inversion. Differentiating equation 6.24 gives (Smith and Booker, 1991)

$$\delta d_{xy} = \frac{2}{V(y_i, 0)}\delta V = \int \frac{2\sigma_o(z)E_o^2(y_i, z)}{E_o(y_i, 0)H_o(y_i, 0)}\delta(\ln\sigma)dz \tag{6.25}$$

where $H_o(y_i, 0)$ is calculated from $E_o(y_i, 0)$ using equation 6.16.

The expression for the residual on the left side of equations 6.23 or 6.25 represents the misfit of the model response calculated from σ_o to the measured data at each frequency, the choice of equation depending on the way the data are defined; usually equation 6.25 will be used. This equation can then be used to invert for a conductivity perturbation directly beneath each site. Smith and Booker (1991) call these site inversions "pseudo-1D" because the "pseudo-Frechet" derivatives only differ from one-dimensional Frechet derivatives because the field used to compute them, $E_o(y_i, z)$ must obey the two-dimensional equation 6.15 with $\sigma = \sigma_o(y, z)$.

An iterative cycle of the RRI program therefore consists of an initial guess at the conductivity distribution $\sigma_o(y, z)$. The two-dimensional field values are then calculated from equation 6.15 using an iterative procedure. These field values are then used to calculate the pseudo-Frechet derivatives beneath each

site and the residuals between the model conductivity estimates and the data at each frequency for each site. Equation 6.23 or 6.25 is then inverted, coupled with a smoothness criteria designed to discriminate against superfluous structure within the model. The results of this inversion are used to update $\sigma_o(y, z)$ with usually only a percentage of the calculated conductivity perturbation. The conductivity structures beneath the sites are then interpolated across the whole model to produce a new two-dimensional conductivity structure $\sigma(y, z)$. Equation 6.15 is again solved iteratively for the new field estimates, a new set of data residuals is calculated and the new field values are passed to the subsequent iteration until convergence is achieved.

Exactly the same approach is used with the H-polarisation. The pseudo-Frechet derivatives for the two modes may be inverted separately from each other or combined in a joint inversion of both modes of data (Smith and Booker, 1991). RRI uses a first derivative smoothing measure like Occam and the resistivity models obtained possess minimum structure.

6.4 D^+ Penetration Analysis of the Mana Pools Data

A study of the Mana Pools dataset was made using the D^+ modelling technique discussed in § 6.2. As was shown in chapter 5, the Mana Pools data are two-dimensional. At no site did the data satisfy the condition of Parker and Whaler (1981) required for an acceptable D^+ model. Table 6.1 shows the results of the penetration depth analysis performed on the Mana Pools dataset, where the depth was

Site Number	E-Polarisation		H-Polarisation	
	Longest Period used (sec)	Penetration depth limit (km)	Longest Period used (sec)	Penetration depth limit (km)
1	2642.6	200	2642.6	32
2	13.5	7	13.5	2
3	2.9	2	2.9	2
4	23.3	11	23.3	3
5	23.3	9	23.3	5
6	2642.6	270	2642.6	60
7	23.3	9	23.3	5
8	2642.6	50	2642.6	54
9	23.3	14	23.3	5
10	2642.6	310	2642.6	150
11	2642.6	53	2642.6	130

Table 6.1. The maximum depth of penetration for the E-pol and H-pol responses calculated using the D^+ method of Parker and Whaler (1981).

deduced by raising the delta function until the model misfit exceeds that achieved for the D^+ model by two standard deviations. This was performed separately for the E- and H-polarisation data decomposed at an 80° strike angle.

The results in table 6.1 show two main features: firstly, the difference in penetration depths between the E- and H-polarisation. Except for site 11 on the craton the E-polarisation has a much greater penetration depth. This is due to the higher resistivity of this mode at longer periods in the AMT data and at all

periods in the LMT data. The second feature is the increased penetration depth of the LMT data relative to the AMT due to the much longer periods used in the LMT survey. These results can be used to determine the degree of reliance to be placed on different regions of the models obtained. It is to be remembered that the penetration depth results in table 6.1 are for a one-dimensional model which is inadequate for this dataset and they should be treated with a degree of caution.

6.5 Two-Dimensional Modelling of the Mana Pools MT Data

During two-dimensional modelling of the Mana Pools MT data, the Occam2d algorithm proved to be very unstable and model convergence was never satisfactorily achieved. Consequently, all the two-dimensional modelling is done solely using RRI. The data are inverted on a grid conforming to the guidelines given by Booker (1997). Horizontal grid nodes were laid out as uniformly as possible; this maximises the accuracy in the two-dimensional field calculations (Booker, 1997). Initially nodes are placed beneath each site and then the gaps between sites are filled with nodes at a constant spacing of 1 km to keep the grid even. Outside the profile, the horizontal node spacing is increased by a constant factor of 1.5 and the grid padded out to a distance which is comparable with the total depth of the model (Booker, 1997). The vertical grid is constructed with a node at a depth of zero, the node spacing of the first three layers below the earth-air interface is constant and equal to the thickness of the first air layer. These air layers are required in the calculation of the E-polarisation response and their spacing increases by a factor of five, upwards to a height of 100 km (Booker, 1997). With the vertical grid accuracy in the 2D field calculations is again maximised on a grid that is as uniform as possible. The grid on which the Mana Pools data is inverted has an upper earth layer 10 m thick. This is one fifth of the skin depth for the lowest resistivity at the highest frequency. After the first five nodes, the node spacing increases by a factor of 1.10 downward until a depth of two skin depths of the highest resistivity at the lowest frequency is reached. This gave a total grid depth of approximately 600 km consisting of 71 nodes vertically and 93 laterally.

Prior to inversion, the E- and H-polarisation data are weighted by their associated errors so that undue weight is not given to poor data, this tends to emphasise sub-bands of the data with low errors. A relative error floor was employed to raise any datum error smaller than 2%; this spreads the data weighting more evenly over the full bandwidth allowing a more global fit to the data (Booker, 1997). The error bars obtained from the decomposition of Groom and Bailey (1989) are in the form of upper and lower bounds on the apparent resistivity and phase parameters. Ideally the modelling code weights each datum using standard deviation values but no formulation for calculating the error bars on the decomposed parameters exists. Instead, the modelling code is given errors equal to the larger of the two parameter bounds on each datum. This is not the only possible method for generating a set of error bars. The data could simply be rotated to 80° and a set of standard deviations calculated but there is no guarantee that the error calculations will give similar results. It was decided to keep the type of error bar used consistent with the type of data being modelled. The data are inverted using a number of least squares iterations and then subsequently applying Huber weights so that poorly-fitting data are downweighted according to Huber's M-estimate (Huber, 1981) which down-weights data that misfits the model by more than 1.5 standard errors. Redescending weights are then employed which downweight large outliers more severely. Finally, as many smoothing iterations are made as the total number of iterations previously

completed (Booker, 1997), the misfit and the data weights are fixed at the values achieved in prior iterations while RRI tries to reduce the roughness of the model (Booker, 1997).

As Livelybrooks *et al.* (1993) discuss, joint inversion of the E-polarisation and H-polarisation data can often result in a model with a resistivity structure dominated by structure derived from the H-polarisation response. Structure that is only resolvable by the E-polarisation data is swamped. The reason for this lies in the form of the H-polarisation apparent resistivity curve (Livelybrooks *et al.*, 1993). This mode may fluctuate more rapidly than the E-polarisation apparent resistivity as it tends to encounter and be influenced by more lateral resistivity contrasts. This makes joint inversion of the two modes difficult as models may sacrifice the regional fit to the E-polarisation data for a better fit to the more locally variable H-polarisation (Livelybrooks *et al.*, 1993). This is a general problem in magnetotelluric inversion. A further consideration in inverting this particular dataset is the effect on the model of the difference in the periods of data available at different sites and of the differences in recording equipment used in the two surveys. One of the advantages of RRI is the ability to vary the χ^2 misfit goal between sites. This allows variation in how tightly the data are fit at each site; the facility is used here to try to balance the inversion of sites with data for the entire frequency band and those with only AMT data. Each site is fit to the higher χ^2 misfit value achieved during separate inversions of the E-polarisation and H-Polarisation data. In this way, the fit to the two modes is even and the model does not fit any site more tightly than is justified.

In overcoming the modelling problems outlined, the data are inverted in a 4 stage procedure similar to that laid out by Livelybrooks *et al.* (1993). The first step is a one-dimensional inversion; the H-polarisation apparent resistivities are averaged over all sites for each frequency in turn and a one-dimensional inversion is sought for these data to generate a starting model for step 2. In Step 2, this starting model is used and an inversion sought to fit the E-polarisation data solely, revealing structure that has little or no response in the H-polarisation data (Livelybrooks *et al.*, 1993). The misfit of the model to the E-polarisation data achieved at each site is recorded. The third step uses the one-dimensional starting model from step 1 and an inversion is performed to fit the H-polarisation data giving the best fit to the data from this mode. Again the model misfit achieved at each site is recorded. The final step uses the result of step 2 as a starting model and inverts both modes; the χ^2 misfit goal at each site is set to the higher of the two values achieved for that site in steps 2 and 3. The resistivity structure obtained should contain H-polarisation structure and also maintain the E-polarisation structure from step 2.

Prior to inversion of the data, each data point is assessed and extreme outliers and data of low coherency rejected. The cut-off threshold for data acceptance is a coherency of 80%. This affects a large proportion of the data in the frequency range c.1 to 0.01 Hz, comprising the data lying in the MT dead band and at the long period extremity of the AMT data, and also the first half decade of the LMT data which appear to be downward biased. The resistivity structure derived from the E-polarisation data is shown in figure 6.1; this model converged to an rms misfit of 1.07 in 47 iterations. This misfit value is expressed in terms of standard deviations, as are all such subsequent rms values. Figure 6.2 shows the resistivity structure resulting from the inversion of only the H-polarisation data; convergence to an rms misfit of 1.31 was achieved in 55 iterations. The resistivity structure obtained when both modes were inverted simultaneously is shown in figure 6.3; an rms misfit to the data of 1.71 was achieved after 46 iterations. The skin depth estimates plotted for each frequency datum are calculated under the assumption of an

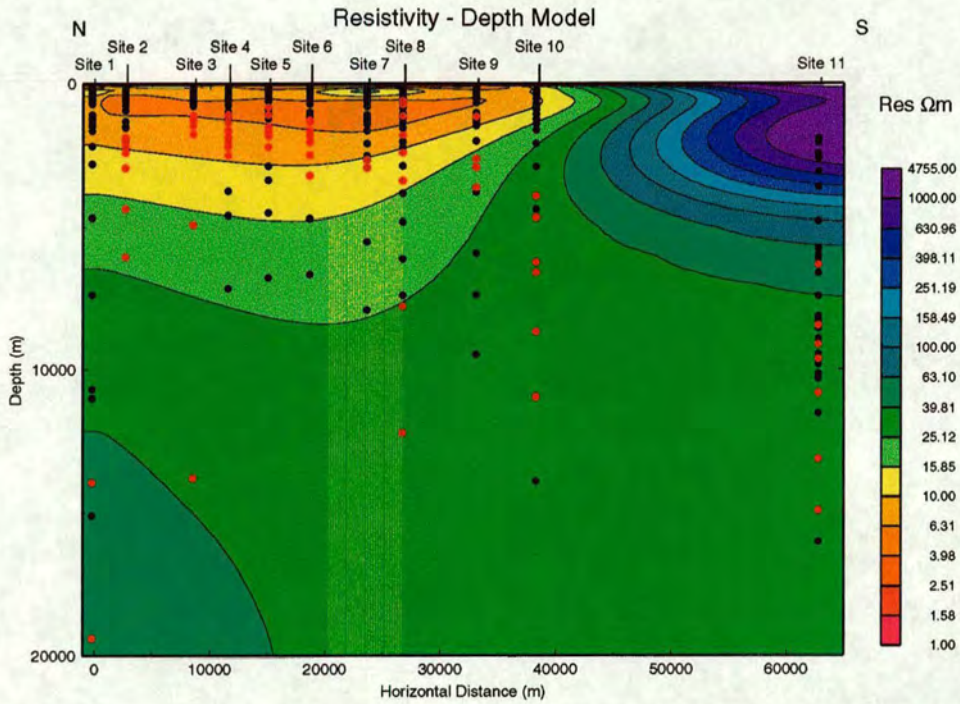

Figure 6.1. The resistivity structure of the Mana Pools basin derived solely from the E-polarisation data. Circles represent data points plotted at one skin depth. Black points are data included in the inversion and red points are downweighted because of poor coherency.

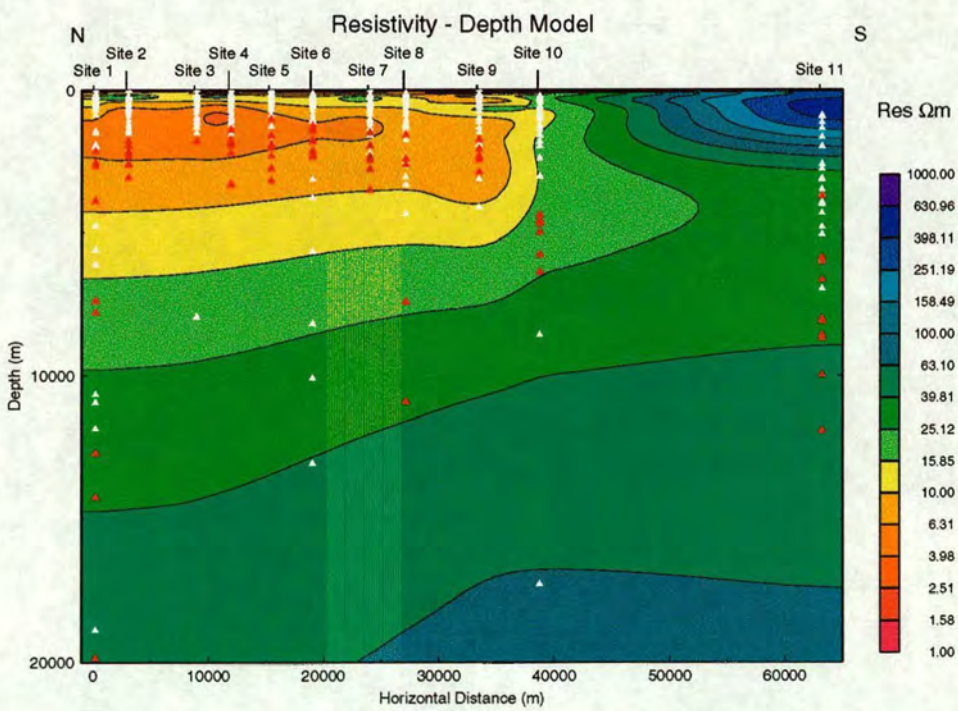

Figure 6.2. The resistivity structure of the Mana Pools basin derived solely from the H-polarisation data. Triangles represent data points plotted at one skin depth. White points are data included in the inversion and red points are downweighted because of poor coherency.

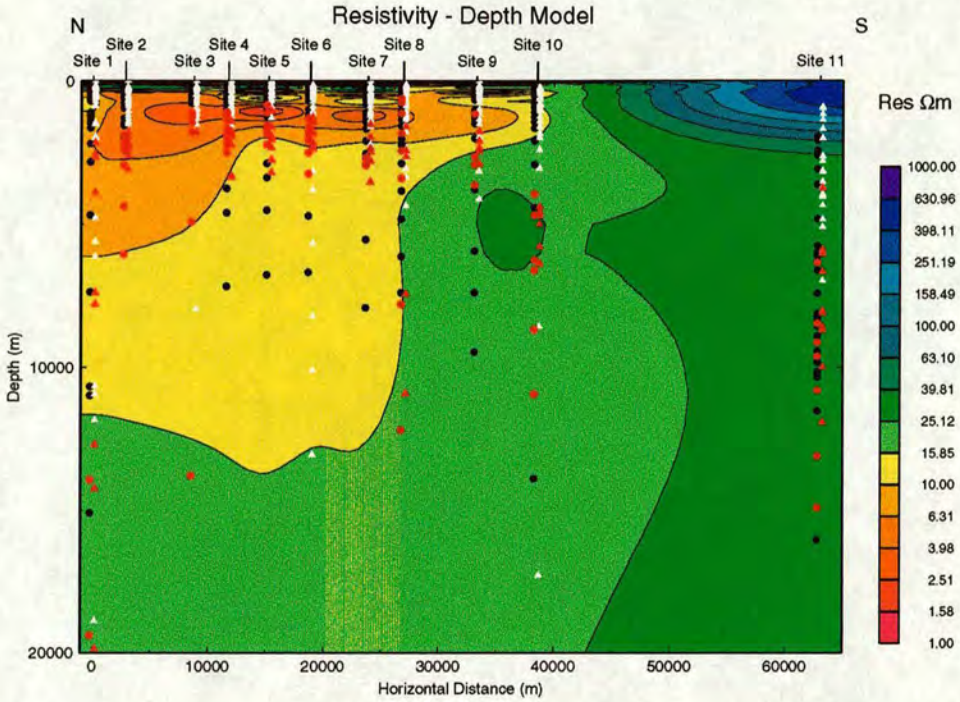

Figure 6.3. The resistivity structure of the Mana Pools basin derived from the H-polarisation and E-polarisation data. Triangles represent H-polarisation data points plotted at one skin depth and circles represent E-polarisation data, also at one skin depth. The colours of the triangles and circles have the same meanings as in figures 6.1 and 6.2.

overlying layer of homogeneous resistivity, equal to the apparent resistivity at that frequency.

There are three main points to be noted from the three models shown in figures 6.1 to 6.3. Each model shows a conductive structure down to a depth of between 5 and 10 km, this is in good agreement spatially with the position of the basin defined by the seismic (Hiller and Buttkus, 1996) and gravity data (Orpen *et al.*, 1989). Secondly, the surface layer at site 11, on the craton, is resistive to a maximum depth of 5 km and thirdly, beneath this is a layer of relatively uniform resistivity below both the craton and the basin. This third observation is less certain than the previous two. There are reliable LMT data penetrating to below 25 km but the depth range from approximately 8 to 20 km is beyond the penetration depth of most of the AMT data and badly affected by low coherency at the LMT sites. Therefore the amount of data constraining the structure in this region is small and the uniformity of resistivity may be solely a feature of the smoothing process. How does the model compare with that of Whaler and Zengeni (1993)? These authors, using one-dimensional models, observed a three layer basin structure, illustrated in figure 2.10. This resistivity section comprised an approximately 10 km section consisting of a 1 km thick 1 Ωm conductor overlying a 5 Ωm unit which extends to 2 km depth and itself overlies an extremely good conductor of resistivity down to less than 1 Ωm which reaches a depth of between 6 and 10 km. This kind of layering is not seen in the model shown in figure 6.3 and is therefore not required by the data. What is seen is a more extreme layering in the first 500 m comprising an alternation of resistive and conductive layers. This kind of 'oscillation' may represent the effects of the model overfitting slight variations in the extreme high frequency part of the data rather than genuine earth structure. Such oscillation is also observed at other artificial jumps in the data such as occur

within the dead band and justifies the rejection of those data on the coherency criteria used here. This type of behaviour becomes important when considering the possible existence of a conductive feature in the basement beneath the basin. There is reasonable agreement between the estimates of the depth-to-basement given by Whaler and Zengeni (1993) and that shown by the model in figure 6.3. Whaler and Zengeni (1993) state that there is a contrast between the resistivity at site 11 and that in the basin at all depths. As has already been highlighted this is not seen at depth in figure 6.3. While this may be due to a lack of data at depth it is also due to the contrast between a stitched one-dimensional model and a smooth two-dimensional minimum structure model and also the effects of a static shift of the data at site 11. Lateral smoothing of the two-dimensional model by RRI will suppress the effect of the static shift. The structure within the basin itself is also difficult to compare. The layering seen by Whaler and Zengeni (1993) is not seen in figure 6.3. Again this may have more to do with the contrasting modelling techniques than any significant structural differences.

It was mentioned above with reference to the high frequency variability of the AMT data that artificial jumps in the data can lead to artificial structure within the model. The plots of the decomposed data shown in chapter 5 commonly show a drop in the phase of the data across the dead band; this ties in well at most sites, though not all, with the observed drop in coherency. Beyond the dead band the phase is seen to climb again towards the end of the AMT frequency range. A similar pattern is also seen for the noisy portion of the LMT data at some sites. The effect of this on the model is to introduce a resistor and a deeper conductor in the model at a depth which approximately corresponds to the frequency gap between the two datasets. This deeper conductor then remains as a permanent feature. By rejecting the poorer coherency data the phase varies more smoothly and these structures are not present in the final model. Such deep conductive structures have been modelled or observed at basement depths in other Pan African mobile belts by other authors, for instance beneath the Lower Zambezi basin by Losecke *et al.* (1988), also using MT data, and in a zone extending from the Damara orogenic belt in Namibia to the Zambezi mobile belt of Zimbabwe using DC resistivity and GDS array techniques by authors including De Beer *et al.* (1975, 1976, 1982a); Van Zijl and De Beer (1983); see chapter 2. Such a deep conductive structure cannot be justified for the Mana Pools basin on the basis of the MT data modelled here. The existence of such a feature relies on the inclusion in the inversion process of poor quality data.

The near-surface resistivity at site 11 is much higher than in any other part of the model. Figures 6.4 to 6.7 show the fit of the model in figure 6.3 to the data. A circle is plotted for each frequency at every site and coloured according to the misfit of the model to the data at that frequency. White circles represent data points whose misfit is positive and larger than the maximum value on the scale and black circles, points whose misfit is negative and smaller than the lowest value. While the model fits the AMT data well, the magnitude of the E-polarisation apparent resistivity is consistently underestimated for the LMT data while that of the H-polarisation is overestimated. Attempts to overcome this by forcing RRI to place structure at depth failed. The E-polarisation resistivity at site 11 is also underestimated by this model, probably due to static shifting of the data at this site. RRI provides a facility for estimating the static shift as a parameter at each site. This method is not employed, as the parameter is assessed using data from the neighbouring sites; the geoelectrical structure at site 11 is expected to differ from that for all the other sites on the profile, invalidating such an approach. As an alternative, a further inversion was performed using the same method as outlined for the model shown in figure 6.3. This time the

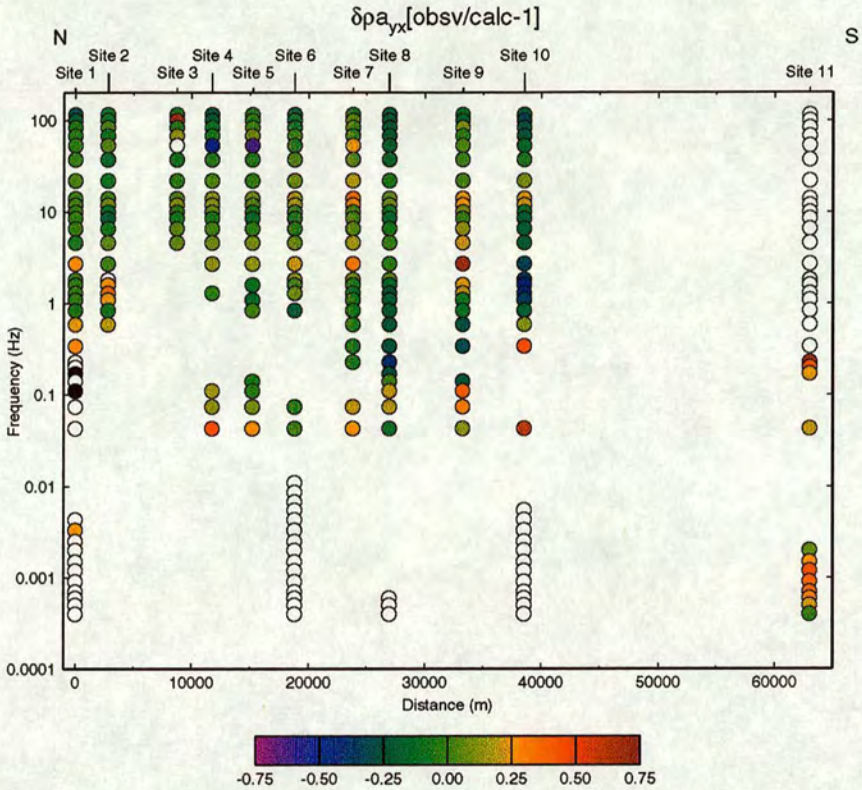

Figure 6.4. The fit of the model of figure 6.3 to the E-polarisation apparent resistivity data.

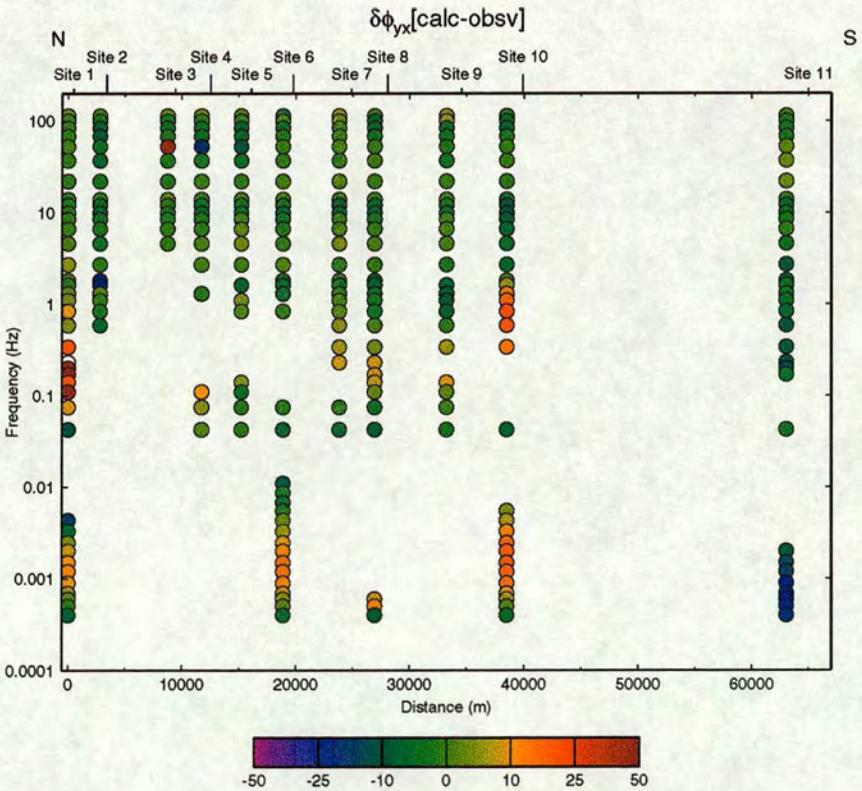

Figure 6.5. The fit of the model of figure 6.3 to the E-polarisation phase data.

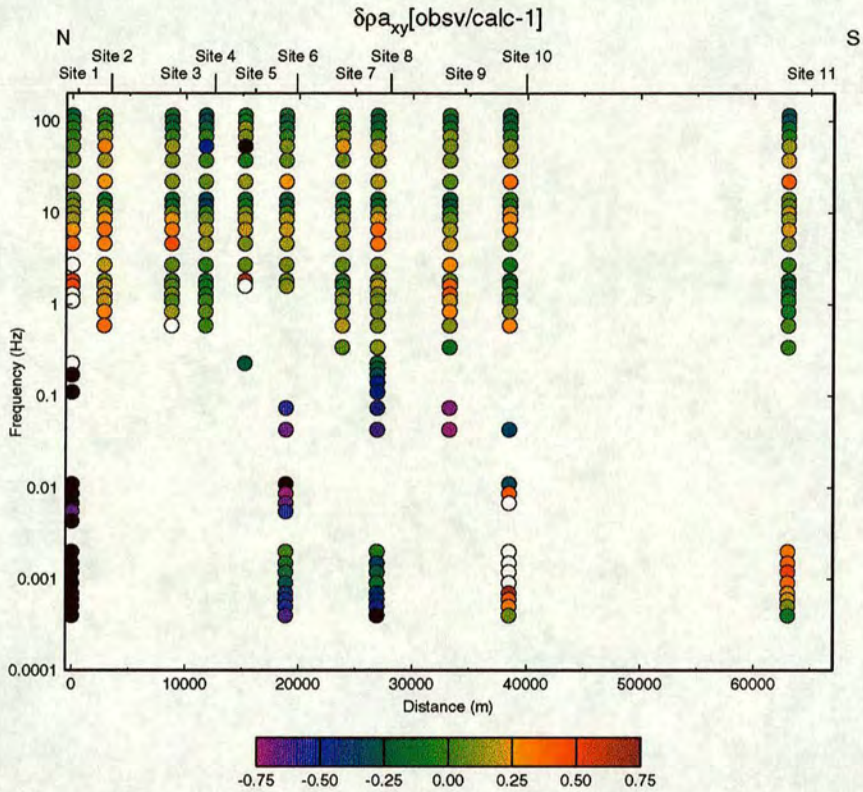

Figure 6.6. The fit of the model of figure 6.3 to the H-polarisation apparent resistivity data.

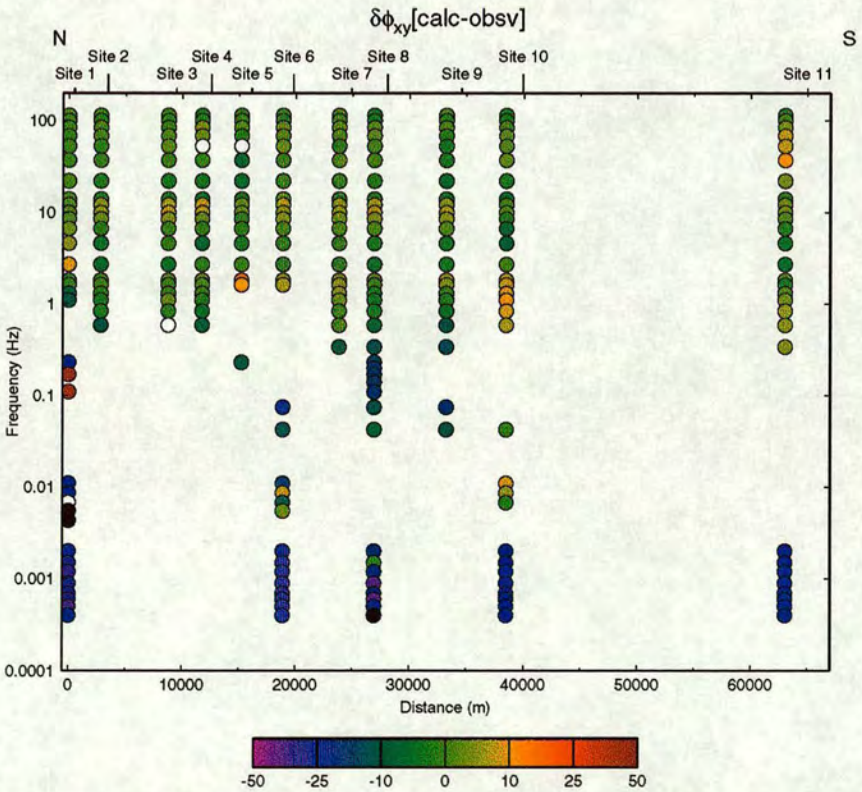

Figure 6.7. The fit of the model of figure 6.3 to the H-polarisation phase data.

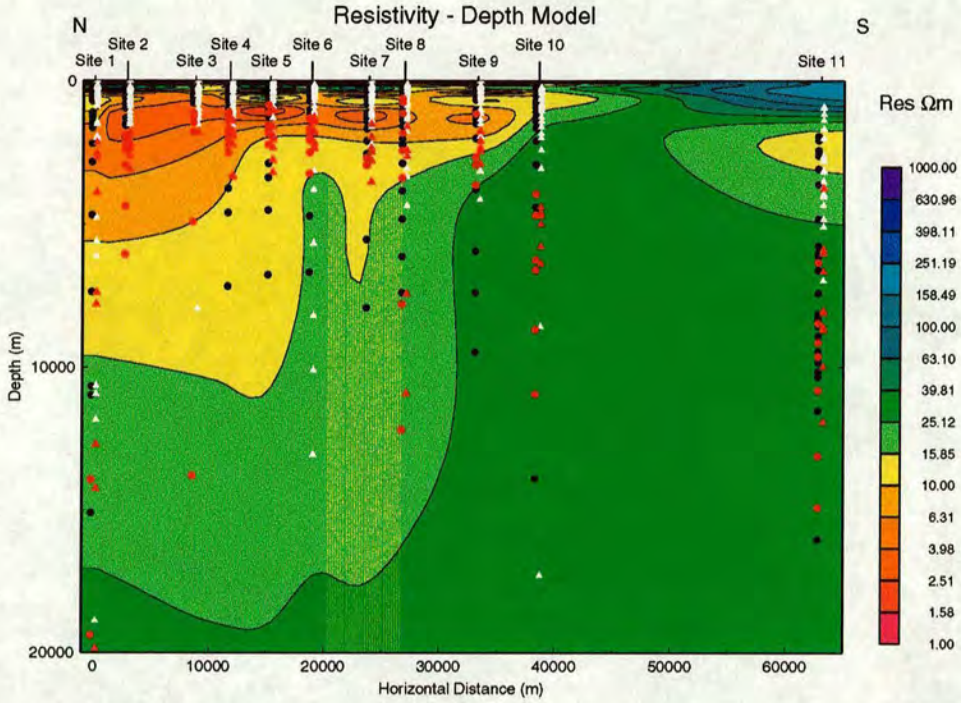

Figure 6.8. The resistivity structure of the Mana Pools basin derived from the H-polarisation and E-polarisation data. Fitting the phase data only at site 11, the symbols have the same meanings as in figure 6.3.

apparent resistivity data for site 11 are not used in the inversion. The resistivity structure is sought, together with estimates of the apparent resistivity curves for site 11 obtained from the phase data at that site and the data at adjacent sites. The resistivity structure obtained is shown in figure 6.8, the model converging to an rms misfit of 1.58 in 47 iterations. This improvement in fit over the model of figure 6.3 is due mainly to an improvement in the fit at site 10 but the fit to the data is also seen to improve at all of the LMT sites. Comparison of the models of figure 6.3 and 6.8 shows them to be broadly similar. The latter has a slightly lower surface resistivity at site 11 and also a thin more conductive region at about 2 km beneath the same site, which is not seen in the former model. The model obtained without the resistivity data from site 11 also shows a more clearly defined narrowing of the conductive layering towards the escarpment and site 10. A general observation can be made that, within the valley, increases in resistivity occur closer to the surface than they do in figure 6.3. This is primarily seen in the raising of the yellow layer associated with the basin to above 10 km and a slight increase in the resistivity beneath the basin at a depth of approximately 17 km. This small increase in resistivity beneath the basin probably accounts for the slight improvement in fit of the model in figure 6.8 to the sites with LMT data. The misfit to the LMT resistivity is smaller in this case but still significant.

Figure 6.9 shows a plot of the apparent resistivity and phase data from site 11 with the fit of the model of figure 6.8 to the phase data and the associated apparent resistivity estimates. There is a good fit between the model and the phase data in terms of the shape of the two curves and a reasonable fit to the phase magnitude for the H-polarisation mode within the AMT frequency band. The degree of static shift is expected to be different between the LMT and AMT data and this is seen to be so. Remembering that no attempt is made to fit the poor quality data within the dead band and at periods up to approximately

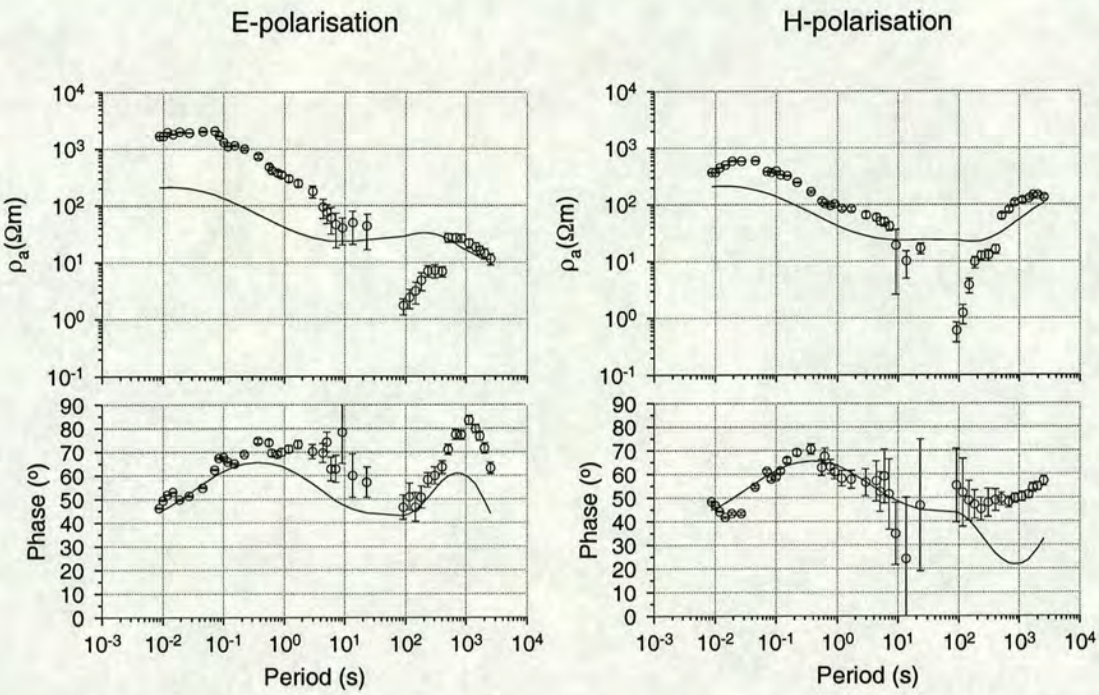

Figure 6.9. Fit to the data from site 11 for the model shown in figure 6.8. Circles represent data points decomposed at a strike angle of 80° and the lines represent the response of the model.

400 s, both LMT and AMT apparent resistivities are seen to be underestimated by the model. This underestimation is greater in the AMT data and for the E-polarisation but is shown to be approximately frequency-independent for each dataset and for both polarisations. The inference to be drawn from this is that the high resistivity near surface at site 11 has shifted the data to a higher resistivity. To overcome this, all further modelling will be performed using only the phase data at site 11.

To improve the fit to the MT data and in particular to the LMT data, the available a priori structural information can be incorporated into the inversion process. The most important piece of information within the survey area is the existence of the fault separating the sedimentary basin from the Zimbabwe craton to the south. This can be included in the RRI inversion procedure by allowing a discontinuity in the smoothness matrix at the position of the escarpment; this will allow a resistivity jump across the fault without any resulting penalization of the model due to the departure from smooth behaviour. The escarpment reaches the surface between sites 10 and 11 but its subsurface nature is ambiguous. Neither Bosum and Geipel (1988) nor Zhou (1988), within their interpretations of the potential field data, discuss the nature of the escarpment fault within the Mana Pools basin. Zhou (1988) does however include it in the gravity model as a vertical discontinuity to a depth of 20 km. Orpen *et al.* (1989) uses both of these surveys and argues that the Mzarabani fault reaches at least 10 km depth in the Lower Zambezi basin and is steeply dipping. The steep gradient in the isolines of the Bouguer gravity anomaly map shown in figure 2.6 support this. The most recent information is the seismic work done by Hiller and Buttkus (1996). Their interpretation of the basin structure is shown in figure 2.11 and shows the escarpment fault in the Mana Pools basin to a depth of at least 7 km with a steep dip to the north.

For the purposes of modelling the Mana Pools MT dataset, it was decided to assume the escarpment fault to be vertical. This assumption does not represent a great departure from the information available

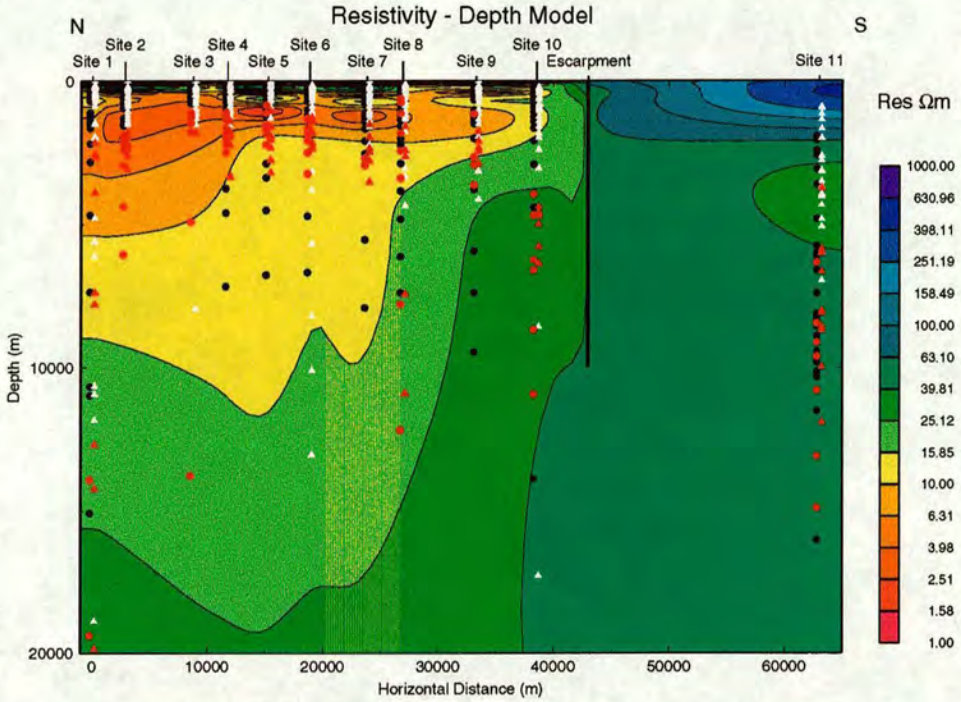

Figure 6.10. The resistivity structure of the Mana Pools basin derived with an escarpment fault extending to 10 km depth.

from other techniques and is easier to implement within the limits of the software. The depth to which the discontinuity was implemented was varied in order to test the effect on the final model. It was found that varying the depth of the fault from between 10 km to the entire depth of the model affected the model misfit very little. What was observed was that terminating the fault closer to the surface caused the structure north of it to be comparatively more resistive than for a model with a fault extending to a greater depth. In all cases the resistivity south of the fault in what is expected to be cratonic material, is slightly higher. Figure 6.10 shows a plot of the resistivity structure obtained from an inversion implementing an escarpment fault to a depth of 10 km. The model converged to an rms misfit of 1.39 in 48 iterations. This depth limit was chosen because it can be supported by the seismic data, and for much greater depths the horizontal position starts to become inaccurate due to the slight northward dip of the fault apparent in figure 2.11. This model still shows a systematic misfit to the LMT data at all the basin sites; the improvement in the misfit may only be due to the extra freedom given to the model by allowing a break in the roughness matrix.

The increasing separation between the E- and H-polarisation LMT apparent resistivity data as the sites are traversed from south to north is similar to the behaviour of the MT data of Losecke *et al.* (1988) for the Lower Zambezi basin as the proximity to the southern escarpment fault increases. It is this aspect of the behaviour of the LMT data that the models have been unable to replicate. A second escarpment exists in Zambia bounding the northern edge of the Mana Pools basin. This lies approximately 10 km to the north of site 1 in the MT survey and is represented at the surface by a rapid topographic height increase of over 600 m. This feature was introduced into the model as a vertical fault separating the basin from a region with a resistivity of 2000 Ωm. This is an arbitrarily chosen value which is of the same order of magnitude as that used by Losecke *et al.* (1988) in the Lower Zambezi basin and

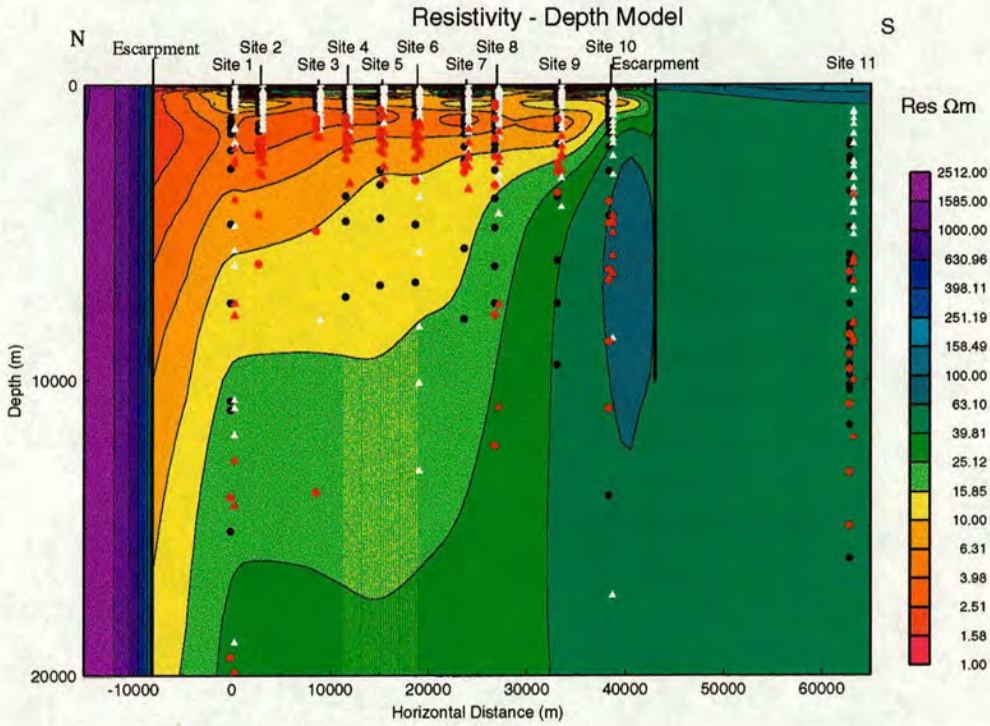

Figure 6.11. The resistivity structure of the Mana Pools basin derived with the addition of a second escarpment fault. The region plotted north of site 1 has been extended to show the position of the northern escarpment.

deemed large enough to produce the desired separation in the two apparent resistivity curves. The model obtained is plotted in figure 6.11 and has an rms misfit to the data of 1.26 after 52 iterations. Again the improvement in misfit may be a consequence of the addition of another break in the roughness matrix but as figures 6.12 to 6.15 show, the fit to the data is better across the LMT period range than in previous models. The northern escarpment was represented as a vertical fault extending for the full depth of the model; attempts were made to vary the depth at which the fault terminated but these resulted in instabilities within the modelling procedure and were in all cases unsuccessful. Figures 6.16 to 6.20 show the comparative fits to the data of the models shown in figure 6.10 and 6.11. It can be seen that for the sites overlying the basin and shown in figures 6.16 to 6.18 the model in figure 6.11 (solid) fits the data from both modes much better than that for the model in figure 6.10 (dashed) with the exception of the E-polarisation phase data. The important observation is that while the exact magnitude of the apparent resistivity data is not matched, the fit to the shape and trend of the data is much better with the second escarpment fault added. Attempts were made to fit the data more accurately by varying the magnitude of the resistivity of the northern escarpment. As the resistivity was increased the fit to the E-polarisation apparent resistivity data improved but the fit to the phase data deteriorated. The opposite effect was found when the resistivity of the escarpment was decreased. An escarpment resistivity of 2000 Ωm offers a compromise in which both responses are fit to a reasonable degree.

Figures 6.19 and 6.20 show the fit of the one and two escarpment models to the data from sites 10 and 11. Remembering that to overcome the static shift problem, the apparent resistivity data from site 11 are not inverted, the pattern of the fit of the two models is similar to that in figures 6.16 to 6.18 with difficulty

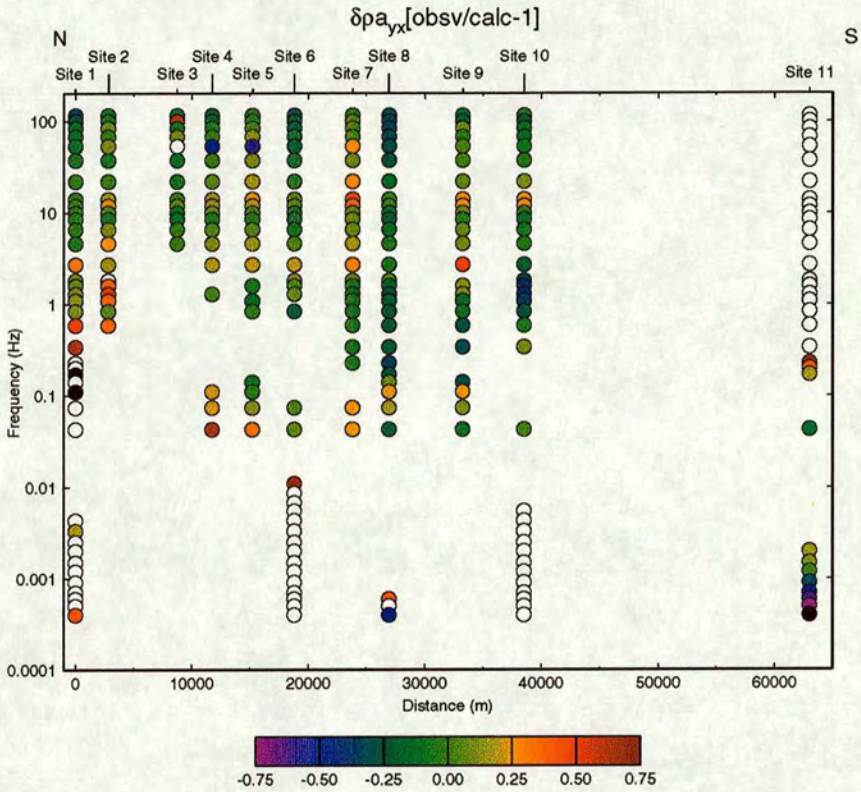

Figure 6.12. The fit of the model of figure 6.11 to the E-polarisation apparent resistivity data.

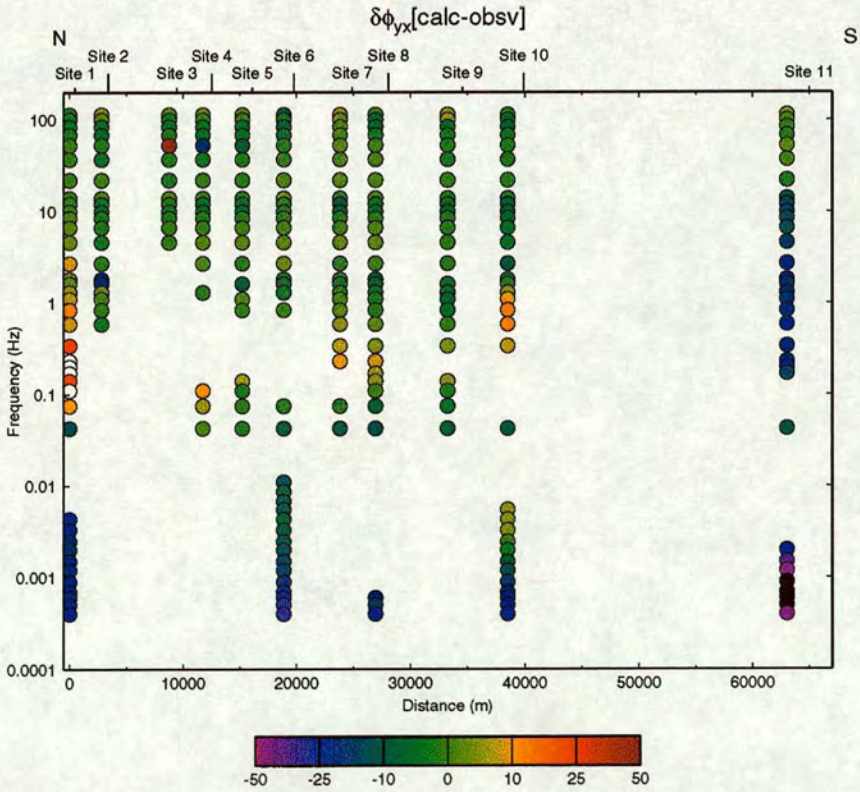

Figure 6.13. The fit of the model of figure 6.11 to the E-polarisation phase data.

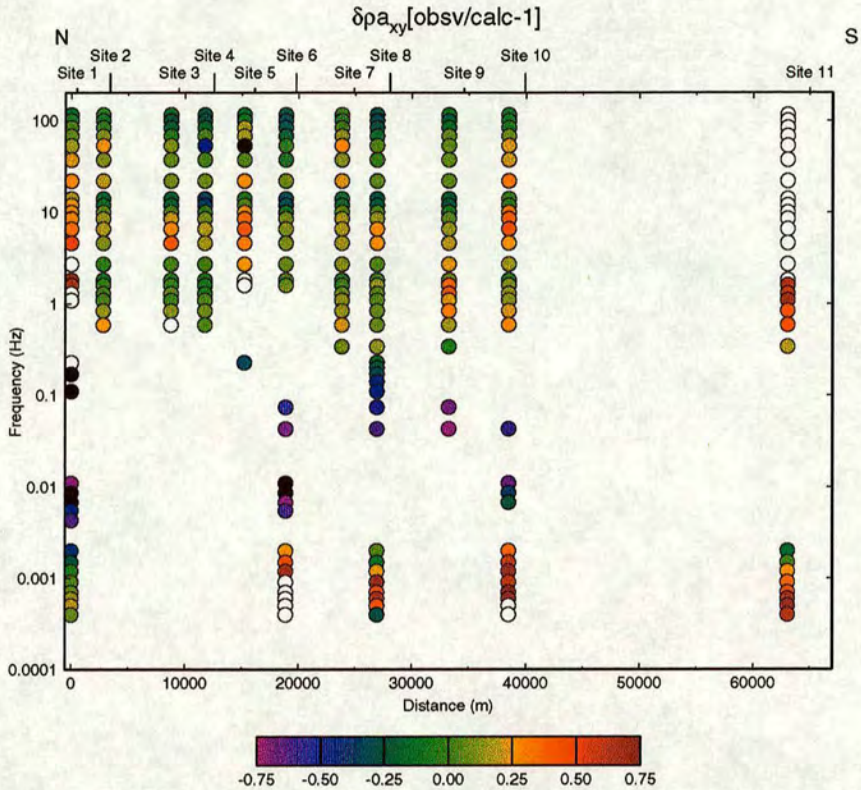

Figure 6.14. The fit of the model of figure 6.11 to the H-polarisation apparent resistivity data.

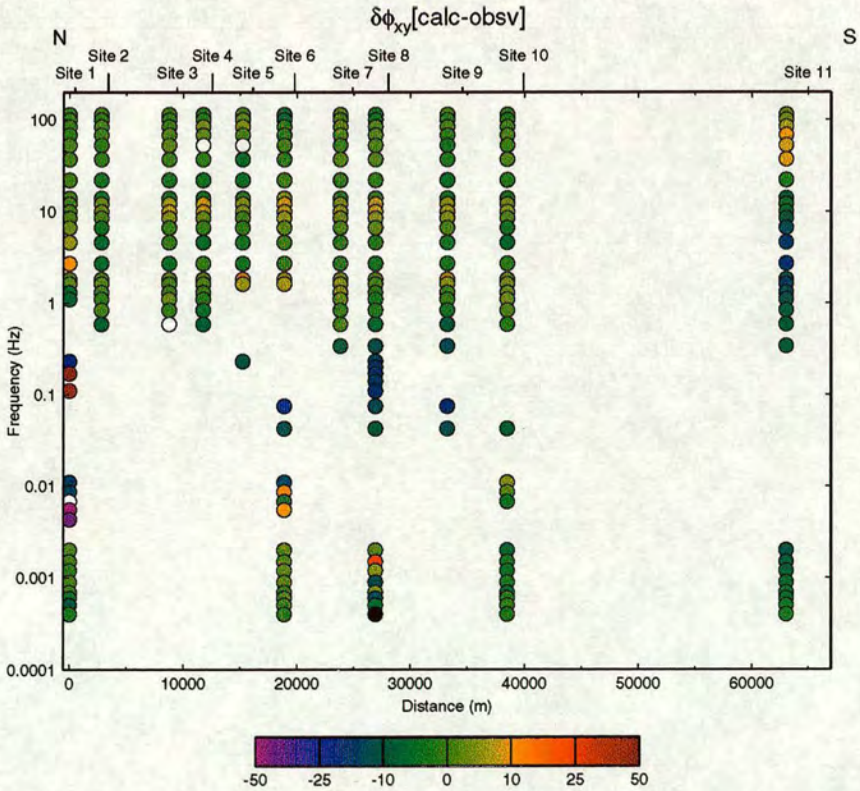

Figure 6.15. The fit of the model of figure 6.11 to the H-polarisation phase data.

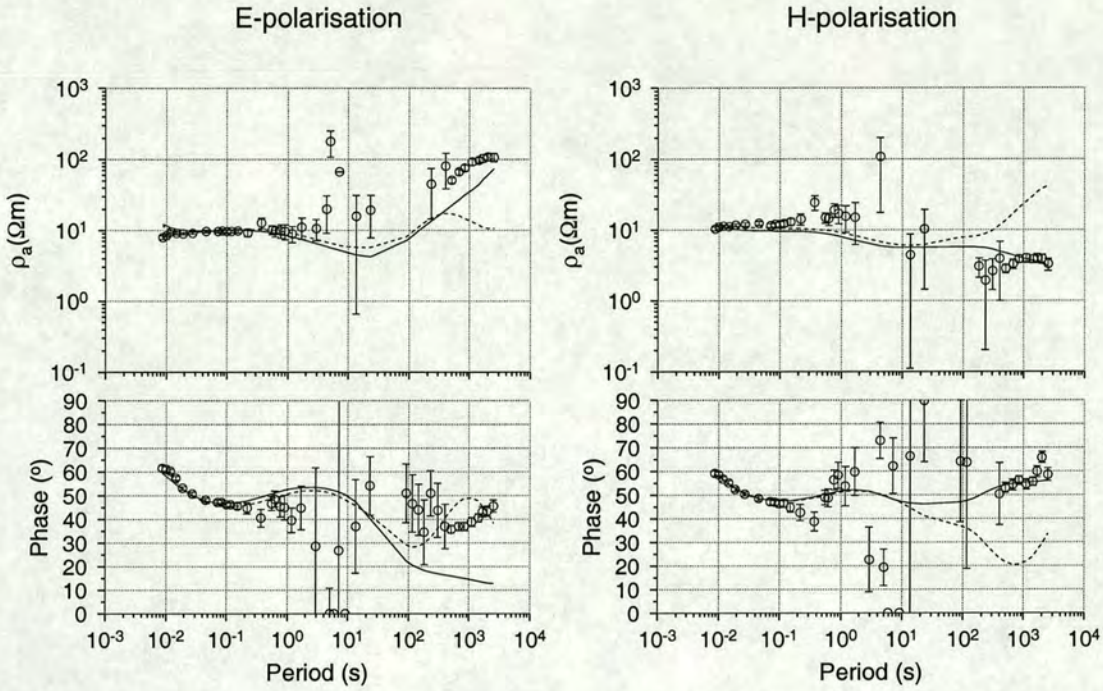

Figure 6.16. The fit of the models to the data from site 1. The solid line is the forward response of the model from figure 6.11, the dashed, that of the model of figure 6.10.

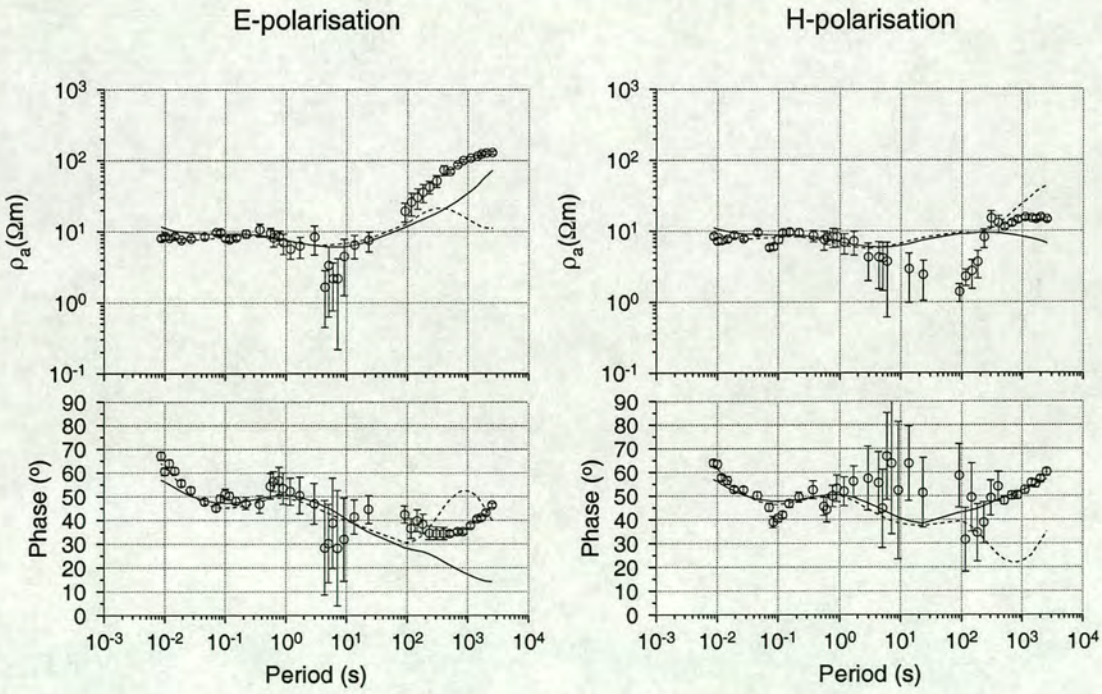

Figure 6.17. The fit of the models to the data from site 6. The solid line is the forward response of the model from figure 6.11, the dashed, that of the model of figure 6.10.

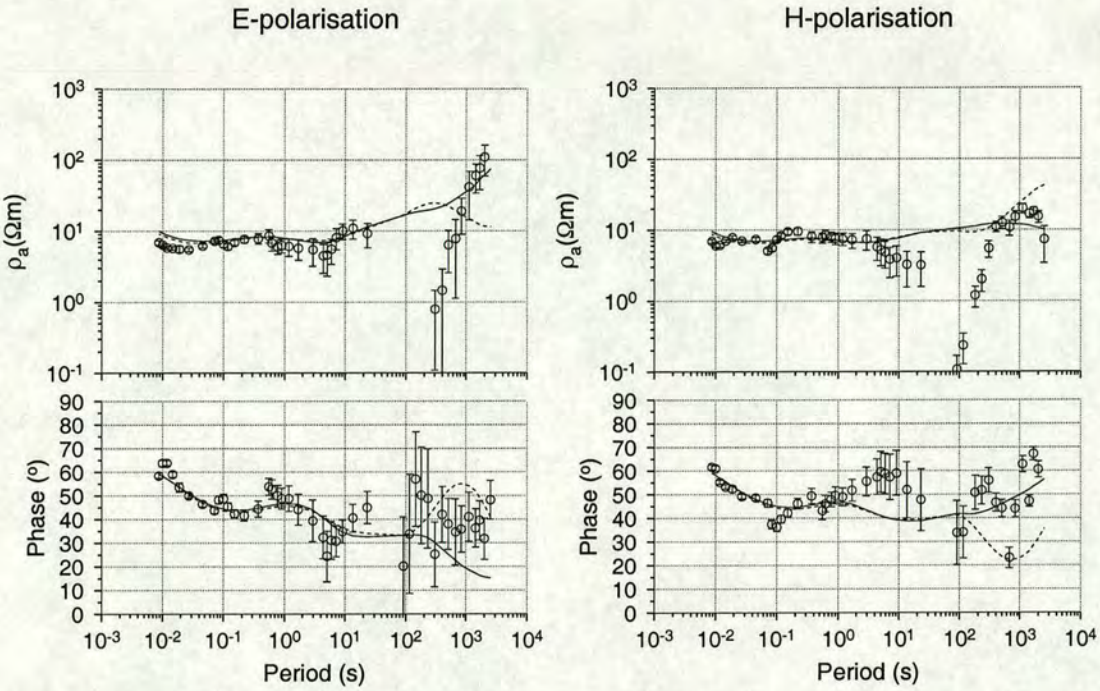

Figure 6.18. The fit of the models to the data from site 8. The solid line is the forward response of the model from figure 6.11, the dashed, that of the model of figure 6.10.

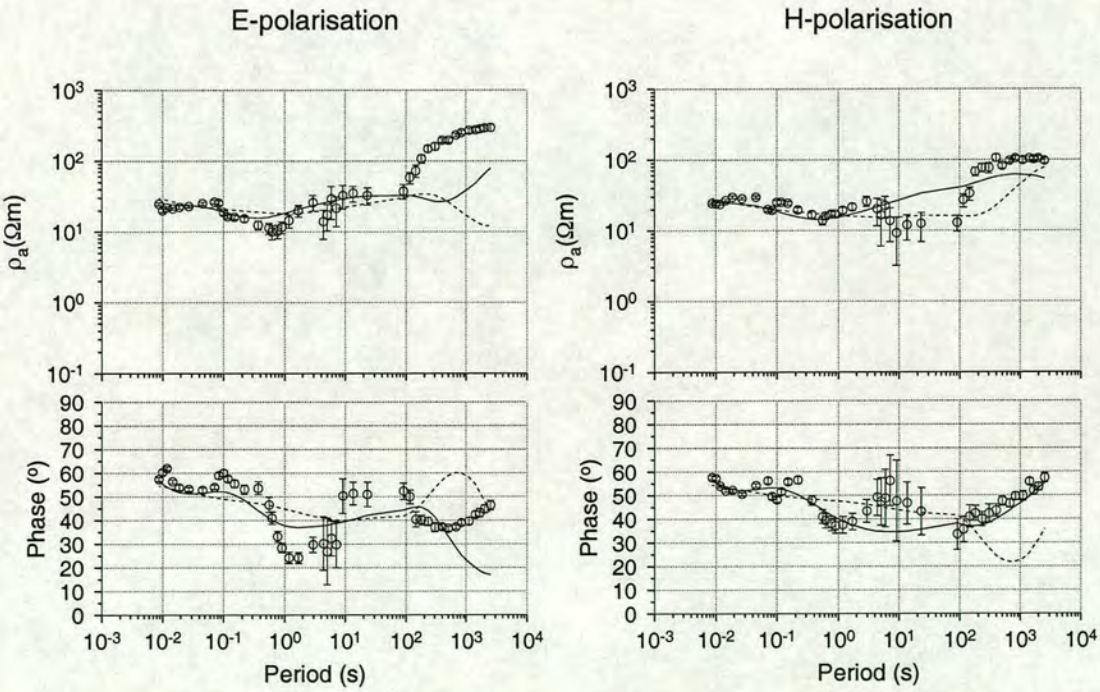

Figure 6.19. The fit of the model to the data from site 10. The solid line is the forward response of the model from figure 6.11, the dashed, that of the model of figure 6.10.

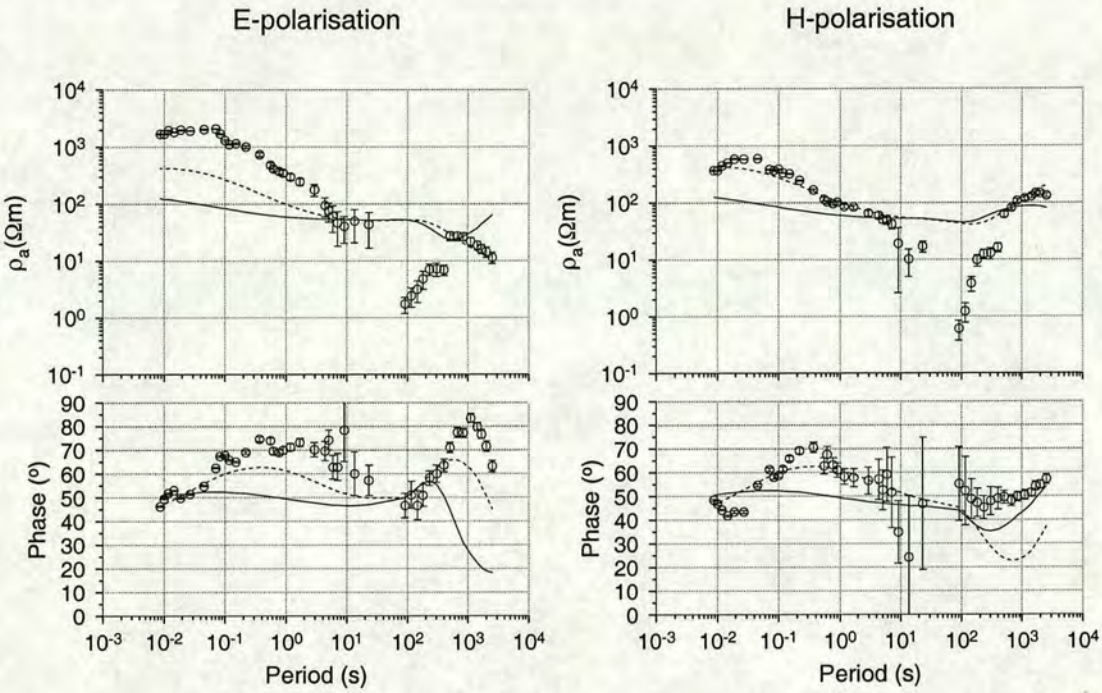

Figure 6.20. Plots of the model fits to the data from site 11. The solid line is the forward response of the model from figure 6.11, the dashed, that of the model of figure 6.10.

being experienced in fitting both the E-polarisation phase and apparent resistivity data. The discrepancy between the models and the data at these two sites is also due to the difference between the 80° data decomposition angle and their preferred strike direction derived from the Groom and Bailey (1989) decomposition. It can be seen in figure 6.20 that the frequency independence of the shift between the model apparent resistivity curve and the data for site 11 is lost for the model with two escarpments and the fit to the phase data is particularly poor. Clearly the model must be interpreted cautiously for sites 10 and 11 but, in spite of these difficulties, there are still observations that can be made from figure 6.11. The Mana Pools basin deepens from south to north until it encounters the northern escarpment which the data require to have a large resistivity contrast with the basin. The southern escarpment fault seems to represent a smaller resistivity change and its effect on the data is much less pronounced. This southern fault appears to dip steeply to the north which is in agreement with the interpretation of the seismic data by Hiller and Buttkus (1996). Site 11 on the craton has a high resistivity near-surface zone but at depths over 2km the difference in resistivity between the cratonic material and the basement beneath the basin is small. As already discussed this differs from the observation of Whaler and Zengeni (1993) but, if genuine, may be due to the combination of their use of stitched one-dimensional models and the static shift present at site 11. The structure of the geoelectric section is in good agreement with that of the seismic method (Hiller and Buttkus, 1996) and also supports the interpretation of the Mana Pools basin by Orpen *et al.* (1989) as a half graben-like basin with an asymmetric cross-profile and a depocentre offset to the northwest.

Figure 6.21 shows the Parkinson convention induction arrows for the LMT data and the induction arrows calculated from the model in figure 6.11. The RRI model is purely two-dimensional and the H-polarisation has no vertical magnetic field component (see equation 3.38) therefore the model induction

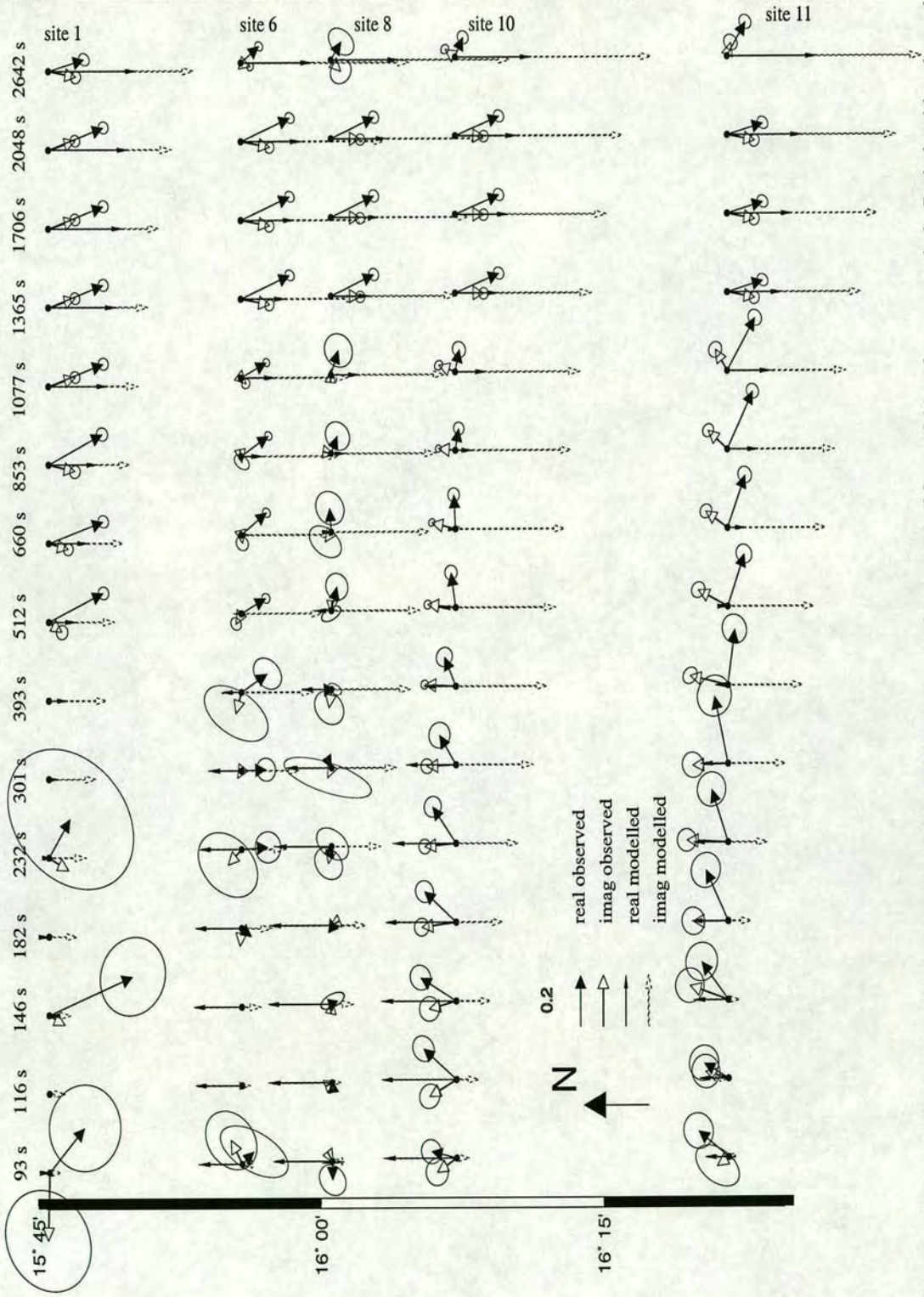

Figure 6.21. The LMT induction arrows (Parkinson convention) and the response of the model of figure 6.11 at the same periods. Periods with only model arrows are periods at which the data has been rejected due to large uncertainties.

vectors will have a north-south component solely, this makes the real and modelled data difficult to compare. The model shows a trend from anti-parallel real and imaginary induction arrows to parallel southward pointing arrows with increasing period. This transition occurs at 393 s at site 1, 660 s at site 11 and 853 s at intervening sites. Physically this represents the transition from an inductive anomaly at a depth comparable to the skin depth to one which is small in comparison, indicating that the inductors at shorter periods are small compared to the skin depth of the dataset as a whole. The real arrows rotate from pointing north at short periods at all sites except site 1, to south at longer periods, this may be due to the increasing influence of the resistive northern craton in Zambia, the same feature may also be the reason for the increase in arrow size at longer periods. If this hypothesis is correct then it is surprising that the Zambia craton should still have an effect on the data as distant as site 11. The very small induction arrows at the shorter periods at site 1 may be due to attenuation of the fields in this, the deepest part of the basin. Within the limits of a purely two-dimensional model these induction arrows replicate the relative orientations of the induction arrows reasonably but their actual magnitudes are often overestimated at longer periods. The small amount of available data for the magnetic field transfer functions precludes any serious attempts to model them and the interpretations offered here are speculative.

The available information from the potential field methods was also used in an attempt to constrain the MT inversions. This data consisted of the estimate of a 5 km depth to basement from the gravity survey of the Zambezi valley (Orpen *et al.*, 1989) and the observation of two magnetic horizons at a depth of 0.8 and 3 to 4 km during the aeromagnetic survey of Bosum (1985). The Mana Pools data were reinverted, this time allowing horizontal discontinuities within the model at these depths to test the effect on the resulting resistivity model. The different constraints were found to have very little effect on the misfit of the resistivity model to the data but caused some differences in the appearance of the model structure at depths close to that of the discontinuity. The imposition of any of the constraints achieved a slight reduction in the model misfit, however the small size and consistency of this reduction implies that it is a result of the increased freedom of the model due to the break placed in the roughness matrix. The upper of the two horizons seen in the aeromagnetic survey (Bosum and Geipel, 1988) is clearly unresolvable by the MT data. Inclusion of this boundary causes no improvement in the model misfit at all. Its depth appears to coincide with a transition from a resistor to a more conductive layer but this, as previously discussed, may merely represent fluctuations in the resistivity model from the overfitting of scatter in the data at high frequencies. The nature of the AMT data in this region of the model makes it difficult to ascertain whether the upper magnetic horizon corresponds to a genuine change in resistivity.

A horizontal discontinuity was variously placed at 5 km, the depth to basement estimate from the gravity data (Orpen *et al.*, 1989), 4 km, the depth to the lower magnetic horizon (Bosum, 1985), and 6 and 7 km, which are close to the depth of the seismically defined basement, to see what effect each of these had on the MT model. The results of these inversions were models with a slight improvement in fit over that shown in figure 6.11; this can again be attributed to the extra freedom achieved by breaking the roughness matrix. No clear pattern was seen during the variation in depth of this lower boundary indicating that the resistivity structure is relatively insensitive to the potential field boundaries. The consistent behaviour of the rms misfit indicates that either the MT data are insensitive to the position of the lower boundary of the basin or that this boundary does not correspond to a sudden change in resistivity. One of the features of the models obtained when including a lower horizontal boundary is

that that boundary is only apparent in the northern section of the resulting resistivity profile. Earlier models such as that shown in figure 6.11 indicate that the lower boundary of the basin deepens to the north and it may not be possible to model it adequately using a horizontal feature. In the southern section of the model the discontinuity may underlie the basin-basement interface; it is not required and is merely smoothed across by RRI. The results of the attempts to constrain the inversion indicate that addition of a horizontal discontinuity at varying depths neither adds to nor detracts from the fit from the model to the data. Such a feature is not required by the MT data and it can be concluded that these features in the interpretation of the potential field data are not accompanied by major changes in resistivity.

6.6 Sensitivity Analysis of the MT Model

The models in § 6.5 show a conductor in the upper 5 km of the Mana Pools basin. To test the sensitivity of the data to this feature, an analysis is made of the behaviour of the model when the resistivity of this region is constrained. It is insufficient merely to alter the resistivity of such a zone and demonstrate that the forward response of the altered model fails to fit the data (Park *et al.*, 1996). In such cases an alternative resistivity distribution may compensate for the constrained region, giving a model which fits the data equally well. To make an adequate analysis requires an inversion to be performed with the desired region constrained to a different resistivity value, thus allowing a search to be made for a different model. If the data can be fit equally well by a different resistivity distribution then the resistivity of the fixed region is not robust.

One of the drawbacks of the RRI modelling technique is that it lacks focus (Schnegg, 1996). This is seen primarily in the vertical elongation of structure evident in the models of figures 6.3, 6.8 and 6.10 and has important consequences for the sensitivity analysis. If the vertical extent of the Mana Pools conductor is exaggerated by RRI then it may be thinner than it appears in the models. To take account of this, only the region with resistivity lower than 6 Ωm, at the centre of the conductive layer, is constrained. The constrained region lies between 500 m and 3500 m beneath sites 2 to 8 and thins towards the south. This region of the starting model was fixed to different resistivities ranging from 0.1 to 15 Ωm and step 4 of the inversion process repeated to search for a new model to fit the data; the constrained region was included in the model roughness measure. The procedure is also repeated for models allowing a horizontal break in the roughness matrix at the top and bottom of the constrained layer. Each inversion involves 20 least squares and 20 smoothing iterations; iterations with robust weights were only used after 10 successful non-robust steps. The robust iterations only converge properly if the number of outliers is approximately 20% or lower (Booker, 1997). This criterion cannot be met without a good starting model which is unlikely to be obtained from only a small number of successful non-robust steps. Difficulties in achieving convergence of the inversion process were experienced. To overcome this, the minimum χ^2 reduction on the first iteration was increased from the default value of 0.7 to 0.8 of the initial misfit, this allows RRI to seek a smaller initial improvement to the model. The maximum amount of the new model to use at each iteration was also lowered from the default of 0.7 to 0.25, this parameter controls the amount of the calculated resistivity perturbation added to the initial model. These two alterations slow convergence but are designed to reduce the number of failed iterations. Lowering the χ^2 reduction parameter only affects the first iteration; subsequent reduction goals are set internally

by RRI (Booker, 1997).

As can be seen from table 6.2, even with the additional measures taken the inversion fails to converge when constraints are put on the resistivity of the conductor. This failure appears to be due to a failure

Constrained ρ of the Conductor in Ωm	Number of Successful Iterations		rms fit
	Non Robust	Smoothing	
0.1	4	0	8.011
0.3	2	0	6.178
0.5	4	0	5.113
1.0	8	0	3.866
3.0	1	0	4.657
5.0	2	0	4.134
10.0	2	0	4.134
15.0	3	0	3.415

Table 6.2. The performance of the inversion routine with the Mana Pools conductor constrained to a fixed resistivity value.

to reduce the model roughness sufficiently for the model to pass the combined misfit and smoothness measure. Insight into the behaviour of the model is gained from figure 6.22 which shows the resistivity - depth profile for site 6 at each iteration during inversion with the conductor fixed at 0.3 Ωm. The red line in figure 6.22 is the initial starting model. The first iteration then fails because the success criterion, which is a weighted sum of the model misfit and the model roughness, increases. Iterations 2 and 3 are successful; subsequent iterations fail before progress stalls and RRI attempts to smooth the model, smoothing iterations 7 to 9 also fail. Superimposed onto this figure in black is the model profile from the unconstrained inversion of figure 6.11. It can be seen that the oscillation in the profile between 30 and 1000 m for the unconstrained model is mirrored in a less pronounced manner in the constrained iterations. The exact reason for the model behaviour is uncertain but the two successful iterations, 2 and 3, in yellow, increase the model roughness and develop features seen in the unconstrained curve. After the failure of iteration 4 subsequent iterations try to reduce the roughness; this is seen between 100 and 700 m where the development of features seen in the unconstrained curve is suppressed. The suppression of the conductive jump seen at 400 m in the unconstrained profile suggests a reason for the model's behaviour. This feature may be missing from the model to compensate for the effect of the constrained conductor below. The removal of such features needed by the data prevents reduction of the χ^2 misfit. The model tries to maintain convergence by reducing the model roughness to compensate for the high χ^2, this leads to the reduction in resistivity variation of later iterations. The same behaviour is seen with other constraints placed on the resistivity of the conductive zone.

While a complete picture of a two-dimensional inversion cannot be gained from a study of just the resistivity depth profiles, addition of a constrained layer across such a large section of the model should decrease the lateral roughness rather than increasing it. The process outlined may not be an accurate description of the mechanism of failure but the outcome is still the same. Addition of the extra constraint stops convergence as the inversion attempts to compensate for it by introducing structure that is inconsistent with the data. Subsequent discrimination against real model structure occurs in an attempt to reduce the model roughness and compensate for the high misfit.

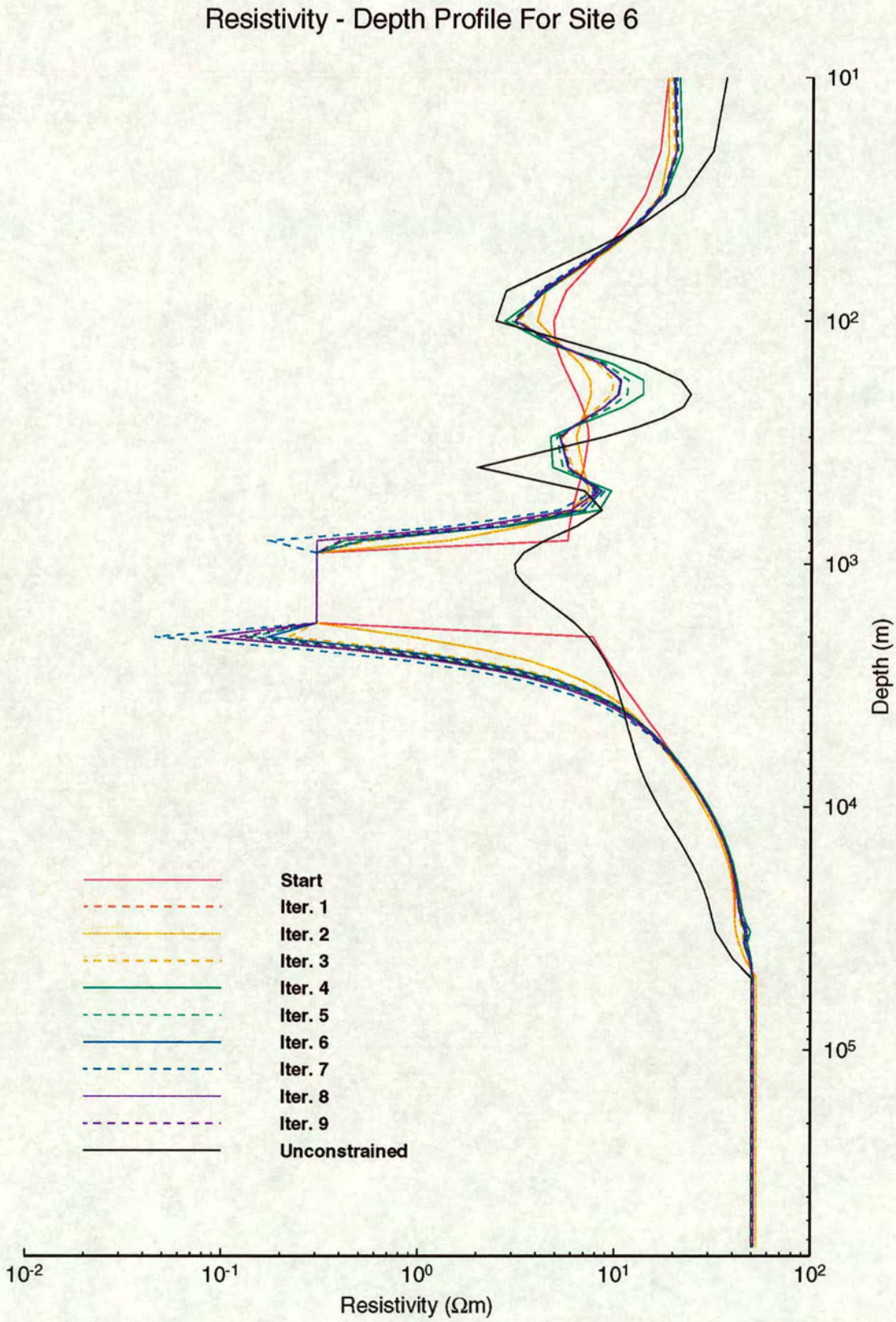

Figure 6.22. The resistivity-depth profile at site 6 during the nine iterations of the RRI inversion routine with the conductive zone constrained to a resistivity of 0.3 Ωm.

If horizontal breaks in the model roughness matrix are allowed at the boundaries of the constrained zone, the results obtained are identical. This indicates that these sharp changes in resistivity are not the major features in the roughness matrix or the reason why the inversions do not converge. It is the structure needed to compensate for the constrained resistivity that is important. Further tests explore the possibility that a different model can be found if the conductance of the constrained zone is kept constant by varying its thickness. The thickness of constrained material was varied from between 500 and 3000 m but none of the models converged. To test if the failure to converge was due to the starting models, the constraints were added earlier in the inversion process. The same constrained region was included within the one-dimensional starting model for step 2 to generate a starting model for step 4. Again the model did not converge, so each site was constrained individually to increase the amount of freedom available during the inversion process. The model again failed to converge and the algorithm failed after only one or two successful non-robust steps. The behaviour of the model in this case supported the description of the failure process previously given. Due to the high misfit of the one-dimensional starting model to the E-polarisation data, the first non-robust step easily improves the misfit of the model. Subsequent steps fail because the model roughness cannot be reduced sufficiently to compensate for structure which is not required by the data but is required to compensate for the constraint applied.

Constraining the resistivity of the Mana Pools conductor results in the formation of compensatory structure preventing the models from converging. This is in itself evidence that the feature is robust. The failure to converge does however limit the information obtained about the response of the model to constraining the conductive zone. This is instead gained by calculating the forward response of the model in figure 6.11 with the resistivity of the conductor constrained. The disadvantages of this approach were discussed at the beginning of this section but the results obtained are still informative. The model of figure 6.11 with the conductor constrained to a fixed resistivity was gridded according to the guidelines of Booker (1997) and the forward response calculated using the code of Wannamaker *et al.* (1987). The response of the constrained model for several different constraints is shown for the data from site 6 in figure 6.23. The rms misfit of each model to the data is calculated and tabulated in table 6.3 together

Constrained ρ of the conductor in Ωm	rms misfits	
	site 6	model
unconstrained	5.53	3.16
0.1	12.85	10.10
1	7.45	5.88
10	9.15	7.12
100	10.28	9.52

Table 6.3. The rms misfit to the data for the Mana Pools resistivity section of figure 6.11 with the conductor constrained to a fixed resistivity.

with the rms misfit achieved for the last non-robust step of the model in figure 6.11. Site 6 is chosen as a demonstration because the effects of fixing the resistivity can be seen particularly clearly at this site. The largest model and site misfits are seen for the conductor fixed to 0.1 or 100 Ωm. For both E- and H-polarisations the model with the 0.1 Ωm conductor underestimates the apparent resistivities at periods longer than 100 s by more than an order of magnitude. The corresponding phase estimates

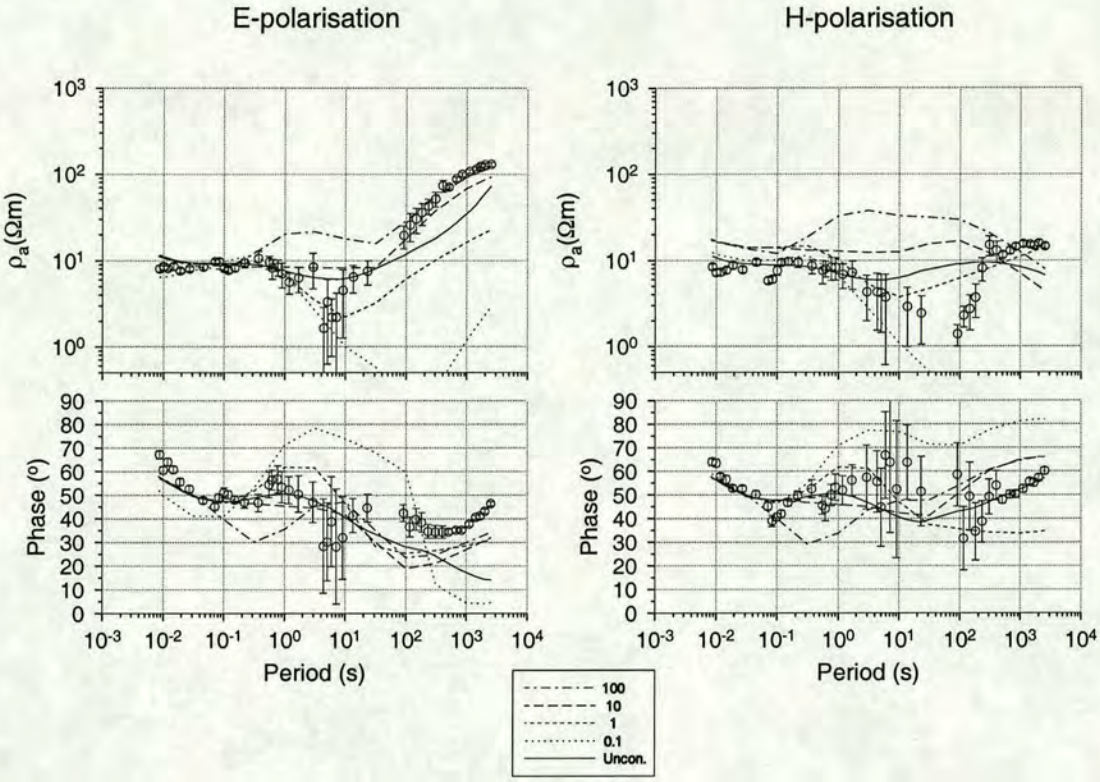

Figure 6.23. The forward response of the Mana Pools resistivity section of figure 6.11 with the conductive zone constrained to different resistivity values. The legend gives the resistivity of the region replacing the conductor in Ωm.

are too high for both modes across most of the period range above 0.1 s but drop sharply from 100 s for the E-polarisation. The model with a 100 Ωm conductor overestimates the apparent resistivity of both modes in the period range from 0.1 s to 40 s and up to 200 s for the H-polarisation mode. The fit to the longest periods of the E-polarisation apparent resistivity curve is better than that for any of the other models but the trend in the H-polarisation data is not replicated. The phase response of this model outlies the phase data for both modes at most periods. The misfit to the data of these two models is more than three times larger than that of the unconstrained model. The model containing a 1 Ωm conductor has an rms misfit of 5.88, the closest of any of the constrained models to the 3.16 of the unconstrained model (table 6.3). The fit to the apparent resistivity data in figure 6.23 is very similar to that of the unconstrained model over large parts of the period range but there is an underestimate in the E-polarisation apparent resistivity at periods longer than 10 s. The H-polarisation apparent resistivity is overestimated at periods shorter than 1 s. The trends in the phase data of both modes are replicated but with a considerably greater misfit than in the unconstrained case. The model with a 10 Ωm conductor improves the fit to the E-polarisation apparent resistivity for periods longer than 10 s but considerably degrades the fit to the H-polarisation apparent resistivity. The model only passes through the error bars of points between 300 and 600 s. The fit of this model to the phase data is also an improvement and, for the E-polarisation data, is comparable to that of the unconstrained model. For the H-polarisation phase, the fit of the model is the best of any of the four constrained models but is considerably poorer than that of the unconstrained model for periods longer than 20 s. This model has an rms misfit to the

data of 7.12, considerably lower than that of the 0.1 and 100 Ωm models but significantly greater than the 1 Ωm model (table 6.3).

Constraining a smaller region of the conductor has little effect on the misfit of those models where the constraint involves a decrease in the resistivity of the constrained zone compared to the unconstrained model. Where the constraint increases the resistivity the misfit of the model is reduced. For instance, if the constraint region is reduced to that with a resistivity less than 4 Ωm in the unconstrained model and now fixed at 100 Ωm the misfit of the model is reduced to 7.08 from 9.52 (table 6.3). An explanation of this observation becomes apparent if the conductance is considered rather than the resistivity. At site 6 there is 2 km of constrained material; for the model with the 0.1 Ωm conductor, this gives a conductivity-thickness product of 20,000 S and for the 100 Ωm model, 20 S. If the constrained region of the model is reduced to that with unconstrained resistivities less than 4 Ωm, then the thickness of constrained material below site 6 is only 700 m. If this material is constrained to 0.1 Ωm then the misfit to the data is still large, but if it is constrained to 100 Ωm then the misfit is reduced. This indicates that the model is not sensitive to thinner layers of resistive material within the conductor.

In summary, the conductor is a robust feature of a smooth model since its absence causes the formation of compensatory structure which the RRI algorithm cannot remove. This structure increases the misfit of the model and real structure is suppressed as the algorithm tries to compensate by decreasing the model roughness. The forward modelling studies show how the response of the model changes with different constraints on the conductive region and give an idea, irrespective of smoothness, of how the fit to the data is affected. It is clear from these models that the misfit is minimised when the conductor is constrained to a value close to that obtained in the unconstrained model, i.e. close to 1 Ωm. Varying the thickness of the constrained region indicates that the model is more sensitive to the conductance of the region than its resistivity. It is therefore possible that resistive igneous units exist within the conductor and are not detected by the MT data.

The maximum depth of sensitivity of the two-dimensional model was also assessed using a method outlined in Park *et al.* (1996). A large contrasting resistivity of 1000 Ωm was placed at depth and then gradually raised until the inversion became unstable. This harsh condition was chosen rather than making a direct comparison of the change in the misfit to the data because the effect of the deep body will first be seen in the LMT data. The fit of the model is generally poorer to the LMT data and the effect of the deep resistor therefore harder to judge. The deep resistor underlies the entire profile and was placed at the depth of the deepest grid node, this was raised a node at a time and no difference in the model misfit was observed at any of the sites until the resistor was raised to a depth of 50.6 km. The next deepest node is at 42.1 km and with the resistor raised to this depth the inversion stalls after 5 non-robust iterations. It is therefore concluded that the maximum depth of sensitivity is between 42 and 50 km. This is close to the 1-D penetration depth of the H-polarisation across much of the basin in § 6.4, surprisingly no increase in the depth of sensitivity is seen on the craton.

6.7 Rhoplus Study of the Mana Pools Data

The D^+ technique of Parker and Whaler (1981) was described in § 6.2 and can be used to test the assumption of one-dimensionality for a dataset consisting of the real and imaginary parts of the MT

complex admittance. This presents a practical difficulty as MT data are usually expressed as apparent resistivity and impedance phase. These two quantities are related to the complex admittance; the apparent resistivity is related to the magnitude of the complex admittance and the impedance phase to the complex admittance phase. The conversion from apparent resistivity and phase to real and imaginary parts of the complex admittance is not however straightforward. This is because of the relationship between the uncertainties in the apparent resistivity and phase data and those of the real and imaginary parts of the complex admittance (Parker and Booker, 1996). During the time series analysis the phase estimates are found to be less robust than the apparent resistivity to problems encountered with the equipment and during processing. This is often seen as larger error bars on the phase data than the apparent resistivity data and missing phase data points. The consequence is that, while the uncertainties in the apparent resistivity and phase can usually be taken as uncorrelated, this is unlikely to be true for the real and imaginary parts of the complex admittance itself (Parker and Booker, 1996). Reconstruction of the complex admittance often gives a well constrained magnitude estimate because of the small uncertainty in the apparent resistivity data. However, large phase errors will propagate into the process giving estimates of the real and imaginary parts whose associated errors are also very large (Parker and Booker, 1996). This is obviously a barrier on the use of the D^+ technique. To remedy the problem, Parker and Booker (1996) developed a very similar technique for investigating the consistency of one-dimensional systems starting from the apparent resistivity and phase data rather than the complex admittance; this technique is called ρ^+.

Parker and Booker (1996) show that there is an integral representation for one-dimensional MT apparent resistivity and phase similar to that for the complex admittance. The inverse problem of finding a one-dimensional model to fit the MT data can be solved using the same technique as Parker and Whaler (1981) used for the complex admittance. It was found that the one-dimensional resistivity model required to minimise the χ^2 statistic for noisy apparent resistivity and phase data was also a series of delta functions (Parker and Booker, 1996). The applications of the ρ^+ technique are manifold; while one-dimensionality holds for only a select number of problems, the work of Weidelt and Kaikkonen (1994) shows that this condition often holds for the H-polarisation data in a two-dimensional case. The ρ^+ technique can be used to determine whether one-dimensionality is a reasonable assumption, confirm whether two-dimensional data are compatible with the H-polarisation, check the mutual consistency of apparent resistivity and phase data, and set acceptable bounds on missing data points.

To apply this technique to real apparent resistivity and phase data, Parker and Booker (1996) derived an integral representation similar to that for the complex admittance given by Weidelt (1972) and used by Parker (1980). Parker (1980) showed that the MT response of any one-dimensional conductivity profile could be matched equally well at a finite number of frequencies by the response of a series of delta functions. Parker and Booker (1996) use an expression for the admittance of this system at radian frequency ω as the starting point for their work,

$$c(\omega) = a_o + \sum_{n=1}^{N} \frac{a_n}{\lambda_n + i\omega} \tag{6.26}$$

where c is the admittance and $\lambda_n \geq 0$ and $a_n > 0$ are real constants. The apparent resistivity ρ_a and

impedance phase ϕ are related to the admittance by,

$$\rho_a = \mu_o \omega |c|^2 \tag{6.27}$$

and,

$$c = |c| e^{i(\phi - \pi/2)} \tag{6.28}$$

In order to be able to treat these two quantities separately rather than as the real and imaginary parts of the admittance, Parker and Booker (1996) take the natural log of the admittance.

$$G(\omega) = \ln c(\omega) = \ln |c(\omega)| + i(\phi(\omega) - \pi/2) \tag{6.29}$$

$$= \frac{1}{2} \ln(\rho_a(\omega)/\mu_o \omega) + i(\phi(\omega) - \pi/2) \tag{6.30}$$

From equations 6.29 and 6.30 it can be seen that the real and imaginary parts of G are related to the measured apparent resistivity and phase. From this separation Parker and Booker (1996) derive an integral representation for G where,

$$G(\omega) = \ln a_o + \int_0^\infty \frac{\mu(\lambda)}{\lambda + i\omega} d\lambda. \tag{6.31}$$

Equation 6.31 is valid for the case where an insulator lies close to the surface; a similar expression is also derived for the case where a conductor is adjacent to the surface.

To apply this representation to practical data, a quadratic programming approach is taken. A weighted 2-norm measure is examined to assess the agreement between the model responses and the observed data; this measure is χ^2 distributed if the noise on the measurements is normally distributed (Parker and Booker, 1996). This minimisation problem is solved in a similar way to that described by Parker and Whaler (1981) for the solution of the D^+ problem.

The ρ^+ code was used to check the consistency of the H-polarisation of the Mana Pools MT data. The code did not become available until June 1997, after the modelling was completed, so this test was made subsequently. The contribution of the ρ^+ study is to test the assumption that the apparent resistivity data are downward biased across the dead band and at the extremes of the instrument recording ranges. The methodology used is adapted from that of Parker and Booker (1996) and is demonstrated using site 8 as an example. In the first step, a 1-D model is sought to fit all of both the apparent resistivity and phase data, except for points of coherency lower than 80% which were excluded during modelling. The minimum χ^2 is calculated for the fit of the one-dimensional model to the data, if this misfit is lower than the criteria of Parker and Whaler (1981) (see § 6.2) for an acceptable 1-D model, 95% confidence bounds are calculated on each of the ρ_a and ϕ data points. This is done using a quadratic programming approach. For instance, if only apparent resistivity data are known, an example bounding problem may involve calculating, at a particular frequency, the largest and smallest value of the phase which is consistent with the apparent resistivity data. This corresponds to finding the maximum and minimum values of the imaginary part of $G(\omega)$ at the frequency in question, under the constraint of achieving an adequate misfit. This problem is solved by minimising the model misfit by taking a series of trial values for the unknown phase. The bounds on the phase datum are then calculated by allowing the phase value to vary and recalculating the minimum misfit of the model for each value. This gives a set

of models with different phase values and different χ^2 misfits. These models can be used to construct a curve of misfit as a function of phase, this curve will intersect the acceptable misfit value at two points, the upper and lower phase bounds. This method is used to calculate bounds at any frequency, on either the apparent resistivity or phase, which are consistent with a finite collection of measurements (Parker and Booker, 1996). Step 1 attempts to estimate the 95% confidence bounds for both the apparent resistivity and phase data together. For the Mana Pools data the χ^2 misfit in all cases was higher than the acceptable value of Parker and Whaler (1981), indicating that the H-polarisation data are incompatible with the assumption of one-dimensionality. For site 8 the minimum possible χ^2 was 463.9 which is greater than that of 92.8 which would be necessary for the model to adequately fit the data and for the confidence limits to be calculated. It is concluded that the H-polarisation data from site 8 fail the one-dimensionality test.

This failure may not indicate that the data are multidimensional; an inconsistency between the apparent resistivity and phase data or within one of the response curves may be responsible for the high calculated misfit. To examine why the data failed this test, a second model is sought using only the apparent resistivity data to bound both the ρ_a and ϕ data using the methodology described above. This is step 2 and shows whether the apparent resistivity curve alone is compatible with the assumption of one-dimensionality and highlights any outliers within the apparent resistivity data. For site 8, the minimum possible χ^2 misfit of the model to the apparent resistivity data alone was 39.4, well below the acceptable value of 51.0. Therefore the H-polarisation apparent resistivity data are compatible with the assumption of one-dimensionality. Calculation of the 95 % bounds allows outliers beyond these bounds to be isolated within the ρ_a curve and a third model, step 3, is sought with these outliers rejected. For site 8, the ρ_a data at 7.1×10^{-2}, 8.3×10^{-2} and 2632 s were rejected for step 3, giving a χ^2 misfit of 14.5; this model is shown in figure 6.24. Reducing the minimum χ^2 misfit to the data means that a greater range of apparent resistivity values at each frequency is permitted before the misfit of the model exceeds the satisfactory level. This is seen in wider confidence limits and gives a stronger test of an excluded datum's incompatibility with the rest of the data (Parker and Booker, 1996). The data excluded after step 2 still lie outside their 95% bounds and are thus rejected confidently. The final step using the apparent resistivity data is to repeat step 3 while also rejecting any ρ_a data which cause a systematic misfit of the model to the phase data; this is step 4. Step 4 was only necessary at site 1 where it was found that the phase model derived from the ρ_a data did not fit the trend in the phase data at the highest frequencies. An examination of the model residuals indicated that the phase curve was being biased by the two highest frequency ρ_a data points. This is due to the high frequency fit of the model being unduly controlled by these two points because of their very low estimated errors. Step 3 or 4 gives the best fitting model to both the H-polarisation phase and apparent resistivity data derived from the apparent resistivity data alone.

Steps 5 to 7 are a repeat of steps 2 to 4 but using only the phase data to bound both the apparent resistivity and phase curves. In step 5 one well determined ρ_a datum is included in the inversion of the phase data to scale the magnitude of the ρ_a curve (Parker and Booker, 1996); for site 8, the apparent resistivity datum at 1.7 s was included with the phase data and inverted. The χ^2 misfit of the step 5 model to the data was 403.0, way above the 47.4 required if the one-dimensionality assumption is to be considered valid. Additional phase outliers, beyond the 95% confidence bounds, were found at 666, 1075, 1695 and 2632 s. The failure of the model to achieve the desired misfit in step 5 is due

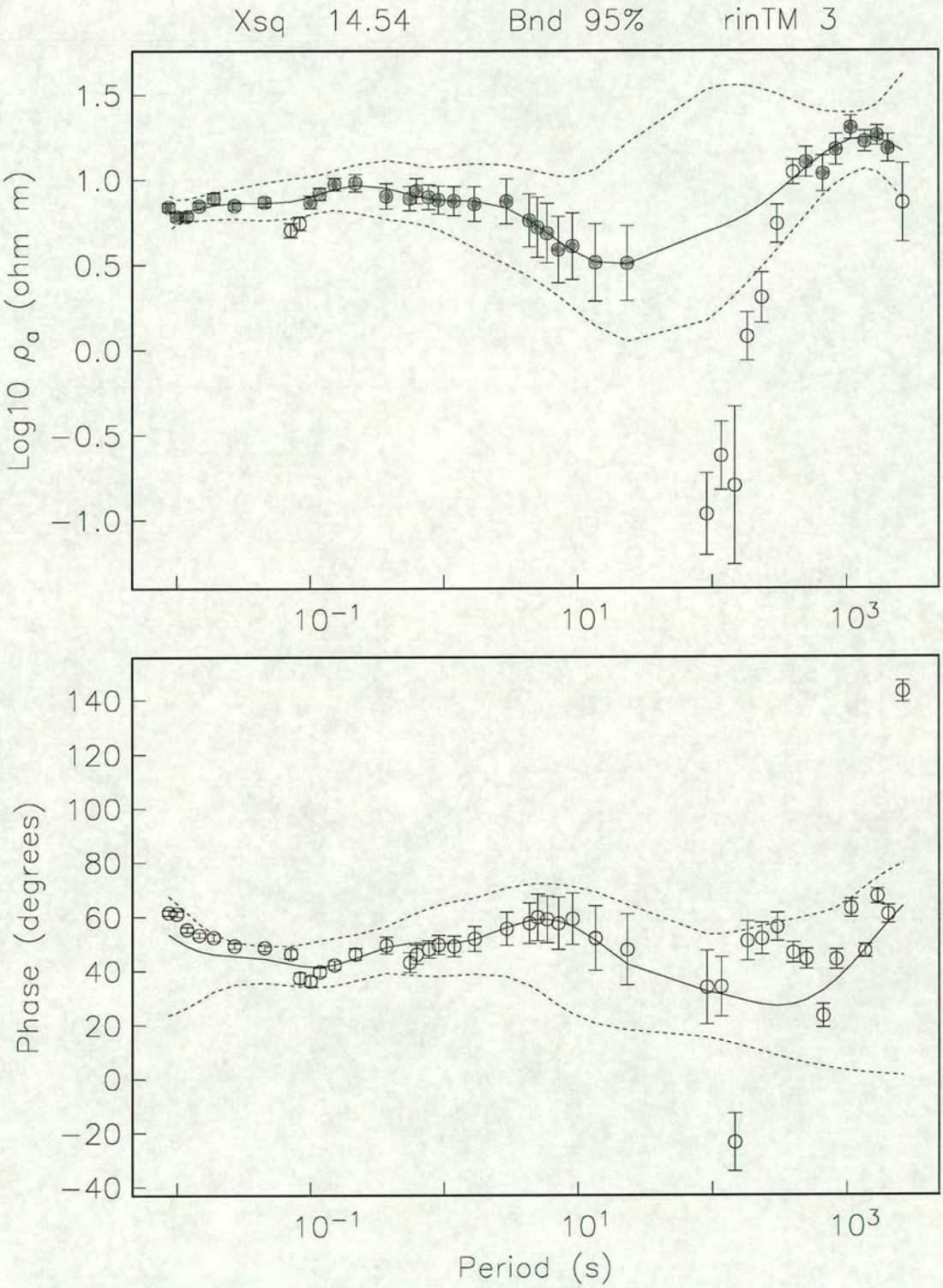

Figure 6.24. The ρ^+ model for the H-polarisation ρ_a data from site 8. The solid line represents the ρ^+ model, the dotted lines are upper and lower 95% confidence limits; hollow circles represent excluded data. Low coherency data are excluded and also data at periods rejected after step 2 (see text).

to these outliers, particularly the erroneous datum at 2632 s. Step 6 is an inversion of just the phase data excluding these outlying periods from step 5, the model has a χ^2 misfit of 34.4 to the data and is shown in figure 6.25; the H-polarisation phase data alone are consistent with the assumption of one-dimensionality. Figure 6.25 shows how the ρ_a at periods longer than 400 s are underestimated by the model derived from the phase data; because of the huge range of values possible within the confidence limits this discrepancy does not seem significant. The difficulty in constraining the ρ_a curve is due to the small number of phase data at these periods which are of sufficient quality to be included in the inversion. Step 7 repeats step 6 with the additional rejection of phase data that cause a systematic misfit of the model to the apparent resistivity data. This step was not required for the data from any of the Mana Pools sites. Having selected the ρ_a and ϕ data to reject, step 8 is a repeat of step 1 and both ρ_a and ϕ data are used to try to bound both curves; for site 8 this was successful: a χ^2 misfit of 70.5 was achieved, just below the acceptable figure of 84.8. Site 8 now passes the ρ^+ test and the H-polarisation data are consistent with the assumed one-dimensionality. As a final step, any of the rejected data that lie within the 95% confidence limits are reincluded, and any data outside the new bounds rejected. For site 8, this resulted in a final model with a χ^2 misfit to the data of 54.9, which is shown in figure 6.26. The final model shows outliers within the data from site 8 and regions which are inconsistent with the rest of the data. Figure 6.26 supports the assumption that the apparent resistivity data at site 8 are downward biased at the short period end of the LMT period range.

The results of the ρ^+ modelling at the three sites within the valley with LMT data, sites 1, 6 and 8 were consistent: all three sites initially failed to achieve the χ^2 misfit level required to justify the one-dimensional modelling assumption, as they did in § 6.4. In all three cases, the phase and apparent resistivity curves pass the criterion individually; this indicates some degree of incompatibility between the two responses. In the case of the valley sites, the incompatibility appears to be due to outlying data points with underestimated error bars. Once erroneous data have been determined and rejected during separate modelling of the two responses, the new models determined from both responses satisfy the assumption of one-dimensionality. There is no evidence of actual incompatibility between the two responses except for the shortest periods at site 1 where the apparent resistivity data at 8.7×10^{-3} and 1.0×10^{-2} s cause an underestimate of the model phase response. This problem is overcome by rejecting these two data. The fit of the model in figure 6.25 to the apparent resistivity data at periods longer than 400 s may suggest that there is some static bias between the AMT and LMT sections of the apparent resistivity curve, resulting perhaps from an instrument calibration error or a wrongly determined filter correction during processing. This possibility is raised because the problem is seen consistently at all three of the valley sites; two reasons lead to the rejection of this theory. Firstly, the 95% confidence limits in each case are similar to those in figure 6.25 and allow for a huge range of resistivities in this period range. Secondly, in all cases a model with a misfit to the data sufficiently low to be consistent with a one-dimensional model can be derived from simultaneous inversion of both modes simply excluding a few points. This suggests that the apparent shift between the AMT and LMT apparent resistivity curves merely indicates that the phase data alone are insufficient to constrain the model in the LMT period range, rather than pointing to a systematic bias between the data collected with two different sets of instruments.

Site 10 behaved in a similar way to the sites within the valley. This is surprising as it is very close to the escarpment fault and did not behave in a straightforward two-dimensional manner in chapter 5. Initially

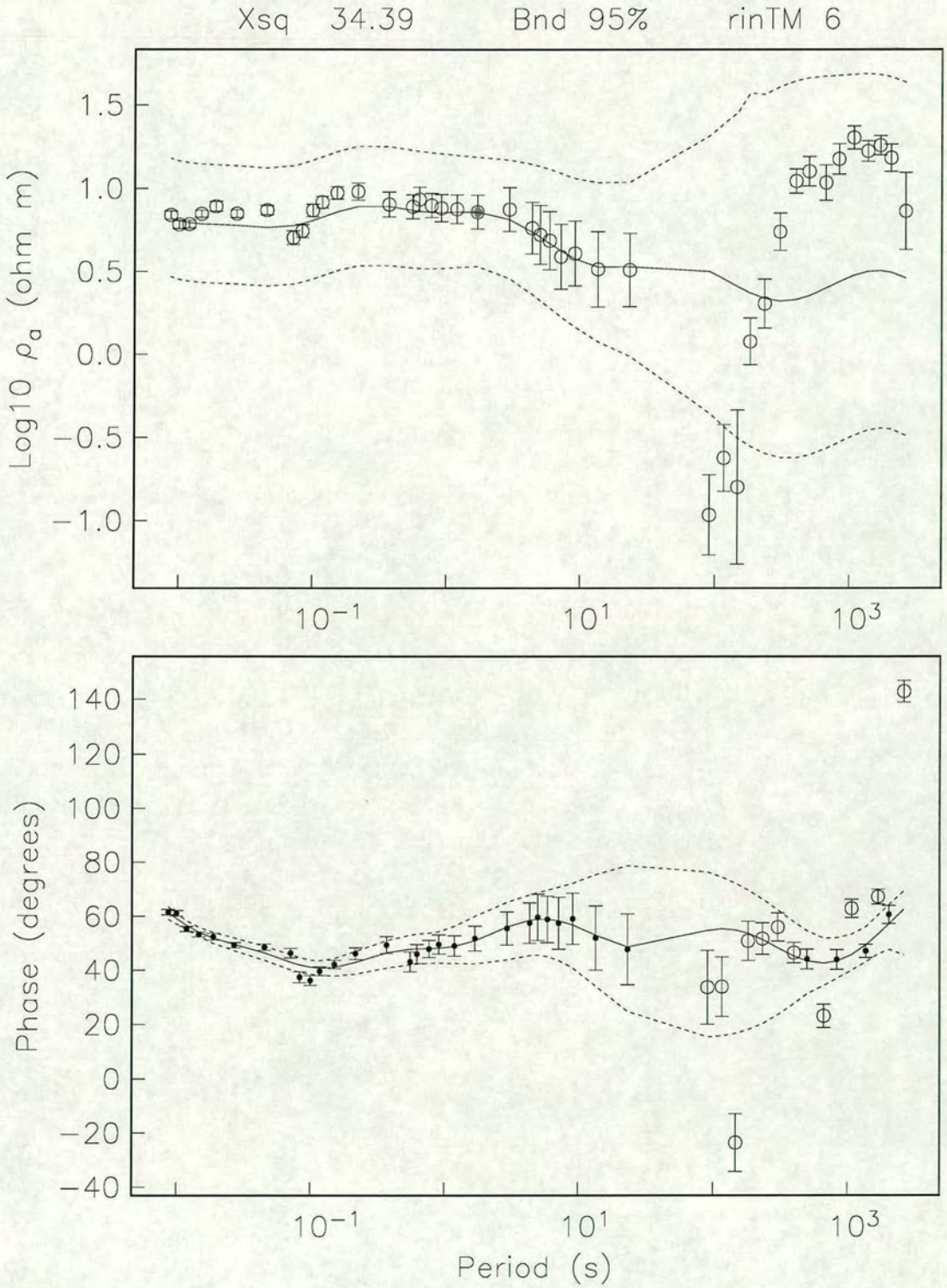

Figure 6.25. The ρ^+ model for the H-polarisation phase data from site 8. The solid line represents the ρ^+ model, the dotted lines are upper and lower 95% confidence limits; hollow circles represent excluded data. Low coherency data are excluded and also data at periods rejected after step 5 (see text).

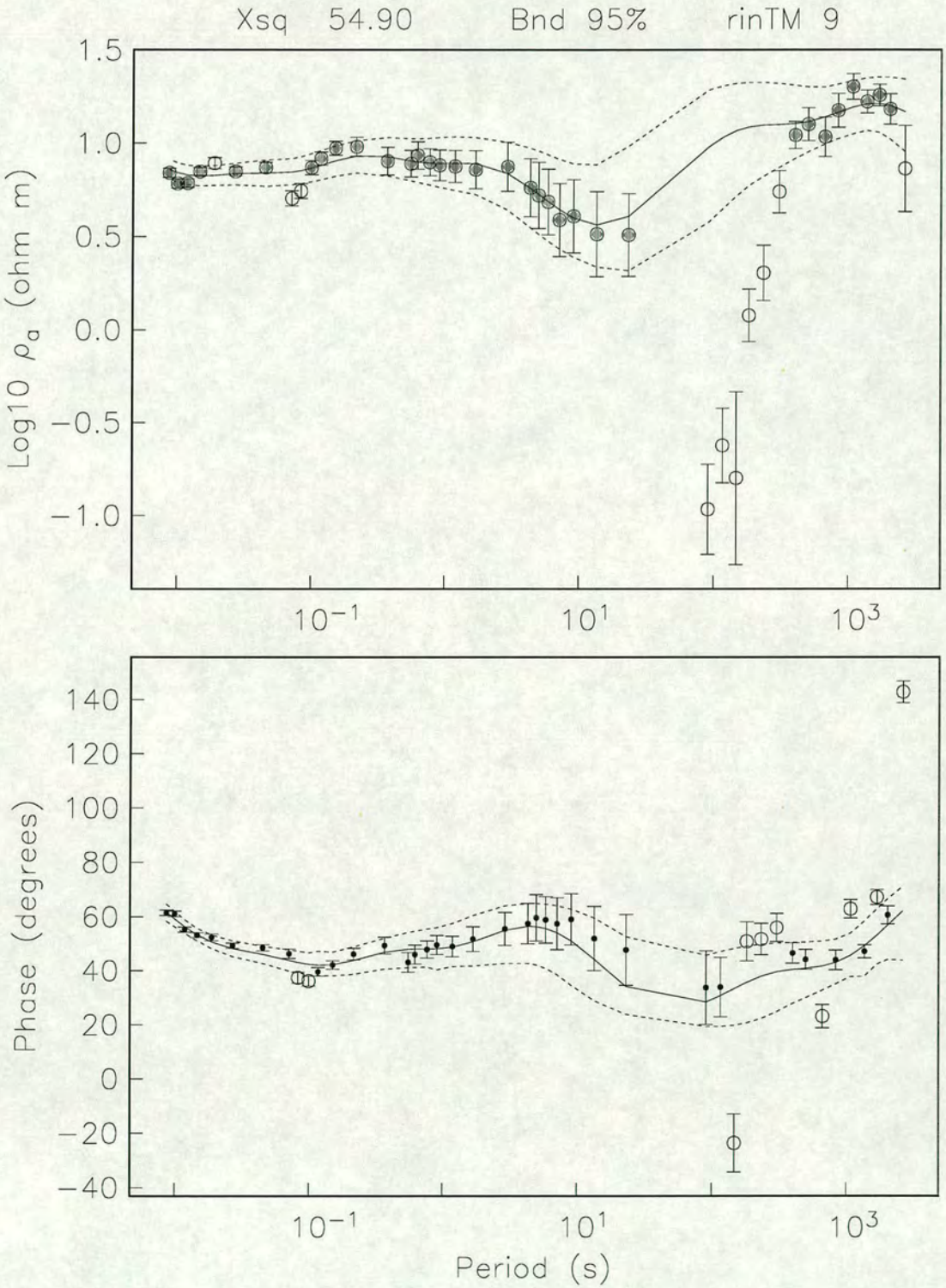

Figure 6.26. The ρ^+ model for the H-polarisation ρ_a and phase data from site 8. The solid line represents the ρ^+ model, the dotted lines are upper and lower 95% confidence limits; hollow circles represent excluded data.

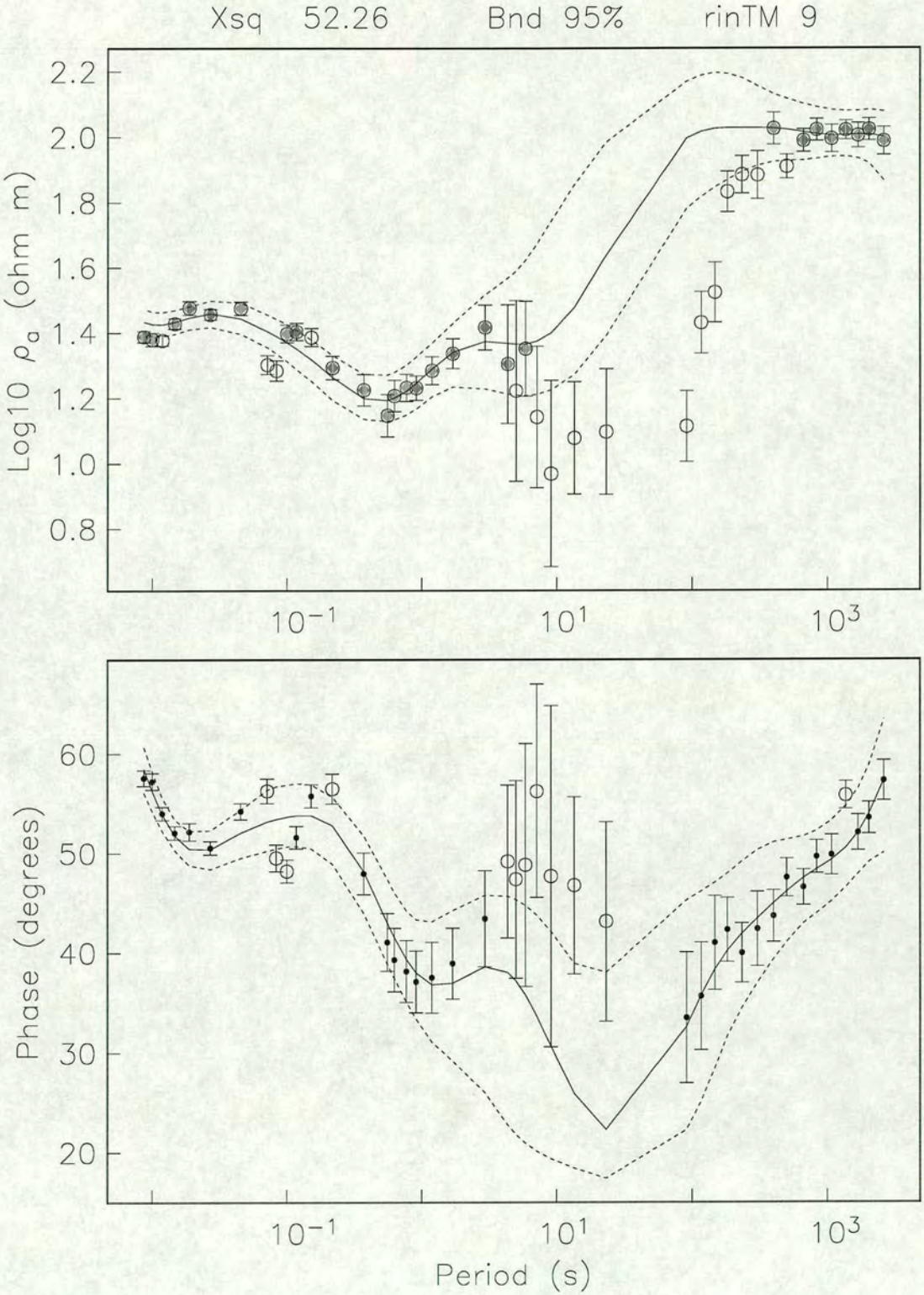

Figure 6.27. The ρ^+ model for the H-polarisation ρ_a and phase data from site 10. The solid line represents the ρ^+ model, the dotted lines are upper and lower 95% confidence limits; hollow circles represent excluded data.

in step 1, the H-polarisation data fail to achieve a low enough misfit to pass the one-dimensionality test. With the elimination of a few outliers, both modes pass separately and, having identified the outliers and rejected them, the data from both responses together achieve a χ^2 misfit of 52.3 which is sufficient to pass the one-dimensionality test. The model and confidence limits obtained are shown in figure 6.27 and again support the theory that the data at the long period end of the AMT recording range and the high frequency end of the LMT range are inconsistent with the rest of the data. The apparent resistivity data are downward biased in these regions and the phase data are too high in this section of the AMT curve.

Site 11 is incompatible with the modelling assumption; it has a χ^2 misfit of 477.0 and neither the ρ_a nor ϕ data pass the one-dimensionality test individually. This would seem to indicate that the H-polarisation data from site 11 cannot be modelled one-dimensionally and that three-dimensional effects are present in the data. The determination of different strike directions for the AMT and LMT data in chapter 5 support this suggestion. The presence of a static shift of the data at site 11 is also suspected which may contribute to the difficulty in fitting the data with a one-dimensional model. To test this, a gain is arbitrarily applied to the LMT section of the data, calculated by taking the median ratio of the low-frequency ρ_a to the predicted D^+ response and then using this factor to adjust the low-frequency apparent resistivity values (Parker and Booker, 1996). This resulted in a model with a χ^2 misfit to the data of 471.4, very similar to that when no shift is applied. This indicates that the majority of the misfit is caused by the dimensionality of the data and not by a static shift problem.

6.8 Summary

The existing model for the AMT data from the Mana Pools basin, derived by Whaler and Zengeni (1993), is only of limited use. The modelling techniques that were employed were one-dimensional and the two-dimensional basin section was constructed by stitching these one-dimensional models together. A full two-dimensional resistivity section has been derived in this chapter for the combined AMT and LMT datasets using the RRI minimum structure routine (Smith and Booker, 1991). Combining the AMT dataset with the recently collected and more sparse LMT dataset presents the challenge of finding a modelling approach which ensures a uniform treatment of the entire set. Some sites have data over a considerably larger frequency range than others. The results of the D^+ penetration analysis show the difficulties involved by the contrast in the penetration depths between sites that are augmented by the LMT frequencies and those that have solely AMT data. This problem has been overcome by the use of different misfit goals at different sites. In all cases, preliminary inversions of both the E- and H-polarisation mode separately are used to determine these goals.

The coherency information obtained from processing of the data was used in the modelling. A coherency threshold of 80% was selected and data of a lower coherency were downweighted during the inversion process. This affects a large amount of data, comprising the extreme low frequency end of the AMT data, data within the dead band and points up to 400 s for the LMT data. The appearance of both the apparent resistivity and phase curves within this region suggests that they are downward biased to some degree. Use of the ρ^+ technique (Parker and Booker, 1996) to assess the consistency of and the bounds on the H-polarisation data supports this assumption. The models obtained from inversion

of the E- and H-polarisation data, both separately and together, are very similar and show three main features. There is a low resistivity body, down to 2 Ωm in approximately the upper 5 km of the valley, terminating at between 5 and 10 km depth. Secondly, the cratonic material at the surface of site 11 is the most resistive material in the model with a resistivity of approximately 100 Ωm in the upper 2 km. Thirdly, the resistivity of the model at depths below 10 km is remarkably consistent between the craton and the valley. It is also remarkably low at between 20 and 40 Ωm.

It is clear from the apparent resistivity curves at site 11 that the data on the craton have been static shifted to higher resistivities. This is confirmed by an inversion of the entire dataset excluding the apparent resistivity data from the affected site. The phase data at site 11 and the data from the adjacent sites predict model apparent resistivity curves which are frequency-independent shifts of the measured data. The static shift problem is overcome by rejecting the apparent resistivity data at site 11 in subsequent inversions. The affect this has on the model is limited - the resistivity structure is little changed except for a lowering of the near surface resistivity on the craton - but the fit of the model to the data from site 10 is considerably improved. The fit to the AMT data is uniformly good for the apparent resistivity and phase response of both modes but there is a significant misfit to the LMT data. The degree of separation between the E- and H-polarisation apparent resistivity curves at long periods is not replicated. To try to overcome this problem, a priori information about the geological structure in the profile area is included in the model. Within the profile this involves including the escarpment fault between sites 10 and 11. The fault is implemented as a 10 km deep break in the roughness matrix; this allows a jump in resistivity between sites 10 and 11 without incurring a penalty due to increased roughness. The effect of this is minimal and neither the fit of the model nor the structure of the craton were significantly altered. With the apparent resistivity data excluded at site 11 and no other sites to the south of the fault, the resistivity of the craton is controlled by the data from the sites to the north of the fault. The large distance between sites 10 and 11 may contribute to the relatively low resistivity inferred for the craton but the lack of separation in the apparent resistivity curves at site 10 prevent it from being too high.

The low resistivity contrast between the Zimbabwe craton in the southern section of the model and the valley, means that the charge built up on the fault is small. Due to this, the effect on the model response in the valley to the north is also small and the craton does not improve the fit to the LMT data. The degree of separation between the two LMT apparent resistivity curves within the basin increases as the sites are traversed from south to north. This is the reverse of the situation in the Lower Zambezi basin (Losecke *et al.*, 1988), where the separation in the curves increases from north to south as the resistive southern craton is approached. The Mana Pools basin is bounded, within Zambia, to the north by a second escarpment; this feature was added to the model and given a resistivity of 2000Ωm. This model matched the trend of the LMT curves much more closely but still showed a significant mismatch to the magnitudes of the apparent resistivities. Increasing the resistivity of the Zimbabwe craton can improve this, but leads to a worsening in the fit to the E-polarisation phase data suggesting that there is some kind of mismatch between the apparent resistivity and phase responses. It can be concluded from this model and the appearance of the data curves that a resistive escarpment to the north is required to achieve an adequate fit to the LMT data.

The conclusions that can be drawn from the resistivity section presented here agree well with the geological evidence and the potential field data presented by Orpen *et al.* (1989), and also the seismic results of Hiller and Buttkus (1996). The conductor in the upper 5 km of the valley in the new MT

model can be identified with the basin using both the seismic data and the depth to basement estimate for the gravity data. The new MT model shows the depth to basement within the Mana Pools basin is approximately 7 km, with a deepening from south to north giving an asymmetric cross profile and depocentre adjacent to the northern margin. This agrees with the interpretation of Orpen *et al.* (1989) and the interpretation of the seismic data by Hiller and Buttkus (1996); the deepening of the basin adjacent to the Zimbabwe craton in the seismic interpretation is not however seen in the MT model. The large resistivity contrast across the northern escarpment suggests that it is likely to represent a faulted contact. The appearance of the resistivity sections is consistent with the suggestion of Orpen *et al.* (1989) that the basin is a half graben in origin. The resistivity of the basin conductor drops as low as 2 Ωm which is reasonable for a sedimentary succession. An examination of the sensitivity of the data to this conductor shows it to be a robust feature of the model but cannot exclude the possibility that it contains thin resistive layers. The possibility of thin basalt layers within the sedimentary pile such as is postulated for the neighbouring Lower Zambezi basin (Losecke *et al.*, 1988) can therefore not be ruled out.

There are quite a number of differences between the new model and that of Whaler and Zengeni (1993), who observed a layered resistivity structure within the basin and a contrast at all depths between the resistivity on the Zimbabwe craton and the basin to the north. The models here show no similar layering except for a number of very thin layers within the upper 500 m of the model which may represent over fitting of slight data variations at high frequencies. That RRI reveals no layering within the basin suggests that the features reported by Whaler and Zengeni within the basin are not required by the data. There is only a small resistivity contrast in the new models, between the resistivity on the Zimbabwe craton and that in the basin to the north except for the upper 2 to 3 km. These differences between the two models arise from Whaler and Zengeni's use of a stitched one-dimensional modelling approach and the use here of a two-dimensional minimum structure algorithm. The RRI technique removes extraneous resistivity variation within the basin and also between the craton and the sites to the north. While the basin-craton contrast observed by Whaler and Zengeni is partially the result of an uncorrected static shift at site 11, the minimal contrast seen in the new models may be due to the small amount of data in the depth range between approximately 8 and 20 km and the smoothing action of the algorithm. The contrast in resistivity between the northern craton and the Zimbabwe craton, due to the low resistivity of the Zimbabwe craton, is also difficult. The contrasting resistivities are required by the data but the reason for the Zimbabwe craton's low resistivity is unknown.

Inclusion of the boundaries defined by the gravity and aeromagnetic methods as discontinuities in the smoothing matrix made little difference to the model and clearly the potential field data boundaries do not correspond to a major change in resistivity. The estimate of the depth to basement of 5 km from the gravity data is a little lower than that predicted by the MT data and does not take account of the dip in the basement to the north which is seen in the latter. Similarly, the lower magnetic horizon at 4 km lies within the basin, it was not required and simply smoothed across by RRI. The upper magnetic horizon at 0.8 km is very close to the region of the model where there are near surface resistivity fluctuations. It is therefore difficult to tell whether the upper magnetic horizon corresponds to a jump in resistivity, but the minimal effect its inclusion has on the model makes it unlikely. Losecke *et al.* (1988) detected an extremely good conductor at depth beneath the Lower Zambezi basin during an MT survey carried out there, and various other authors, including De Beer *et al.* (1975, 1976, 1982a) and Van Zijl and De Beer

(1983), have detected a zone of enhanced conductivity at crustal depths extending between the Zambezi mobile belt and the Damara orogen to the west. Although the resistivity beneath the Mana Pools basin is extremely low for basement rock, such a localised conductor as described by those authors is not seen beneath the Mana Pools basin. There is an appropriate drop in resistivity across the dead band and at the high frequency end of the LMT data which would correspond to the depth of such a feature. This section of the data has very low coherency and the ρ^+ study shows it to be downward biased and inconsistent with the rest of the data. It is therefore rejected; its inclusion would put a similar conductor to that seen by Losecke *et al.* at depth beneath the Mana Pools basin but the data quality is far too poor to support this. Clearly, such a feature could exist in this region of missing data, but the bounds on the resistivity curves suggested by the ρ^+ method make it unlikely.

Chapter 7

Comparison of the MT Data and the Mobil Seismic Data

7.1 Introduction

This chapter introduces the MT data collected by the BGR in the Lower Zambezi basin. The BGR data were modelled by Losecke *et al.* (1988) using a combination of one-dimensional inversion and two-dimensional forward modelling techniques. This model is here compared to one obtained using the two-dimensional minimum structure RRI technique (Smith and Booker, 1991), to determine whether it exhibits structure not required by the data. Both the resistivity sections obtained from modelling the MT data from the Lower Zambezi and Mana Pools basins are compared to structural cross sections of the two basins derived from seismic reflection data acquired for Mobil (Hiller and Buttkus, 1996). The correspondence, or otherwise, between the resistivity layers and the seismic horizons is then used to aid in the interpretation of the MT resistivity sections.

7.2 Comparison of the MT and Seismic Models for the Mana Pools Basin

Structural interpretations (Hiller and Buttkus, 1996) of the reflection seismic data collected by Mobil in the basins of the Zambezi valley were presented in figure 2.11. For the Mana Pools basin, these data were collected along two lines, the first trending southeast to northwest in the southern portion of the basin, and the second, southwest to northeast in the northern section. These two lines are located considerably to the west of the profile along which the MT data were collected, outside the national park; their respective locations are shown on figure 7.1. A comparison was made between the models obtained from these two data sets to assess whether the structural interpretation of the seismic data and the resistivity section derived from the MT data were consistent. A joint study of the two datasets may yield a more comprehensive interpretation of the observed resistivity structure.

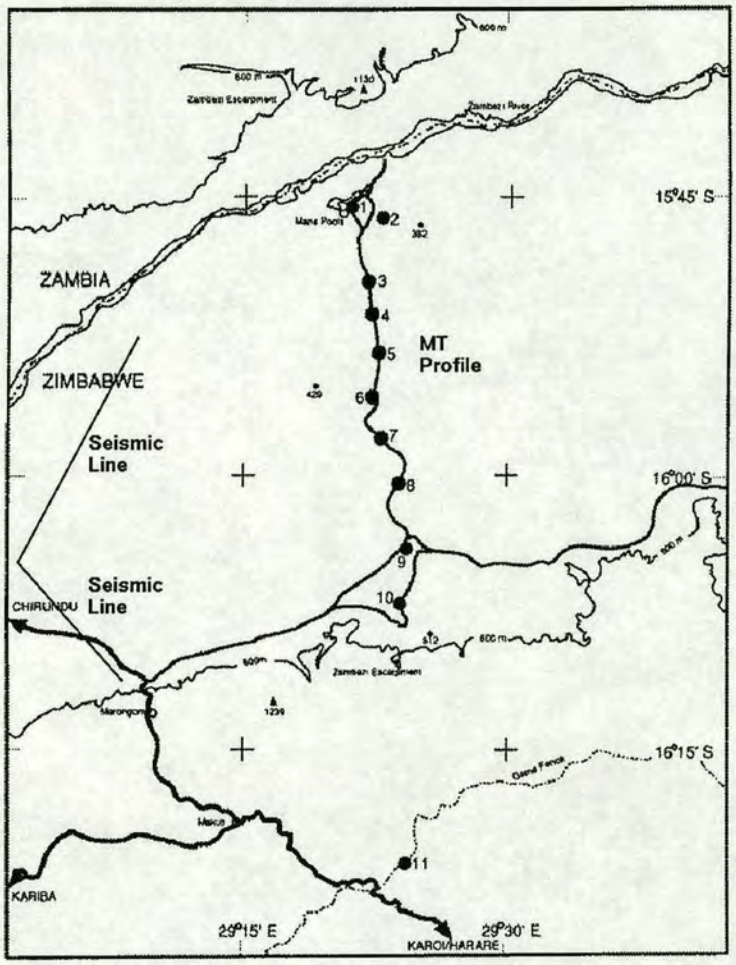

Figure 7.1. The location of the Mobil seismic lines in the Mana Pools basin in relation to the MT profile.

To make this comparison, the difference in location of the two profiles had first to be overcome. It was assumed that the Mana Pools basin was two-dimensional with an east-west strike direction, approximately perpendicular to the MT profile. Therefore a line parallel to that of the MT data would show structure identical to that beneath the MT profile itself; this assumption seems reasonable in view of the regional azimuth directions and dimensionality parameters determined in chapter 5. The profile was constructed by projecting the structure, shown in figure 2.11, from the two seismic lines onto a line parallel to the MT profile and will be referred to as the seismic model. This line occupies a section of the basin which, in terms of its north-south position relative to the basin boundaries, is similar to that covered by sites 1 to 10 of the MT profile. This seismic model was placed beneath the first ten sites of the MT profile and a resistivity block model constructed from its structure, each rectangular block being assigned a resistivity appropriate to the analogous region of the MT resistivity section. Each stratigraphic layer of the seismic model was assigned a single resistivity, where necessary an averaged resistivity for a layer was estimated or the more abundant of two values selected; each assigned resistivity is therefore only an estimated value for that region. The block model derived from the seismic

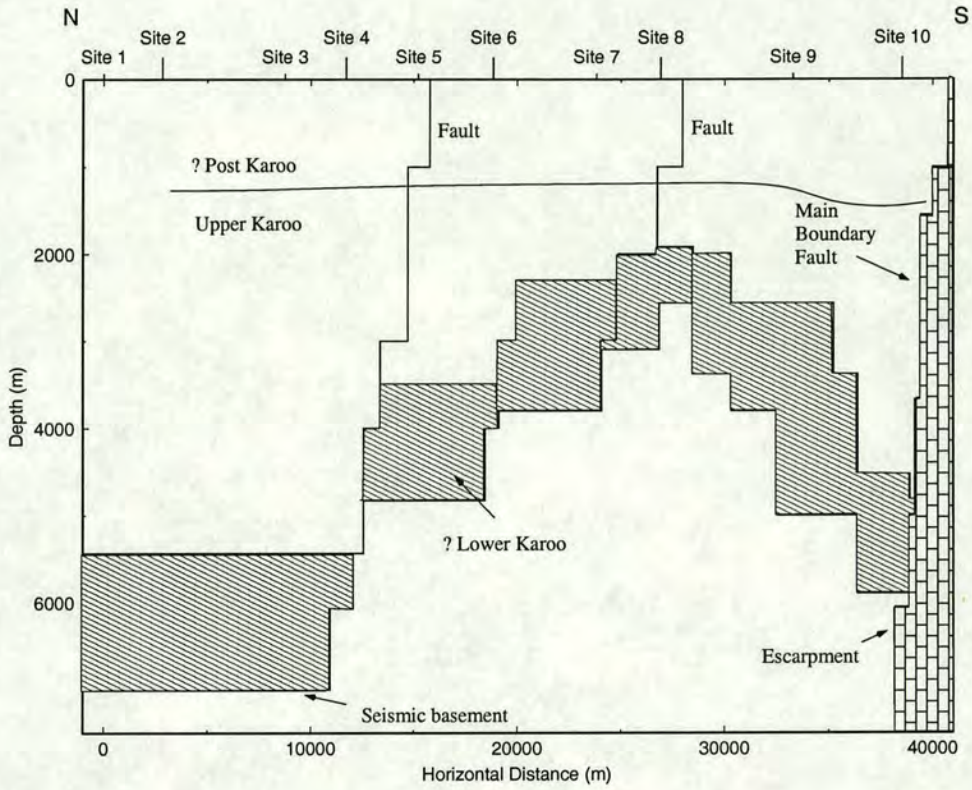

Figure 7.2. The block model reproduced from the seismic structure of figure 2.11 and used to forward model the MT data.

structure is shown in figure 7.2; the depths of boundaries have been calculated from the two-way time section shown in figure 2.11 using the time-depth relationships given in Hiller and Buttkus (1996).

Figure 7.2 shows the tentative stratigraphic interpretations given by Hiller and Buttkus (1996). As these authors state, the lack of suitable outcrop makes the identification of seismic reflectors uncertain within the Mana Pools basin. With the exception of the seismic basement, the identifications given for each horizon are not definite. Figure 7.3 shows the seismic structure projected onto the MT model of figure 6.11. From figure 7.3 it is clear that some regions of the resistivity model are in better agreement with the seismic boundaries than others. For instance, it is clear that the good conductor lies almost exclusively within what is defined as the upper Karoo layer in figure 7.2 and that the escarpment fault coincides with the resistive region in the resistivity model. However, the boundary between the Lower Karoo and the seismic basement below does not correspond to any obvious trend in the resistivity model. South of the escarpment, the resistivity was set to 100 Ωm and the resistivity of the Upper Karoo layer is averaged out and fixed at 5 Ωm. The majority of the Lower Karoo layer lies within the 10 to 15 Ωm region and was fixed at 10 Ωm while the layer below was given the slightly higher value of 20 Ωm. The resistivity within the post Karoo layer is very variable, this variation is averaged out and a resistivity of 10 Ωm assigned to the layer; this model is referred to as *M1*. The resistivity structure was gridded according to the guidelines given in Booker (1997) and forward modelled using the two-dimensional modelling code of Wannamaker *et al.* (1987).

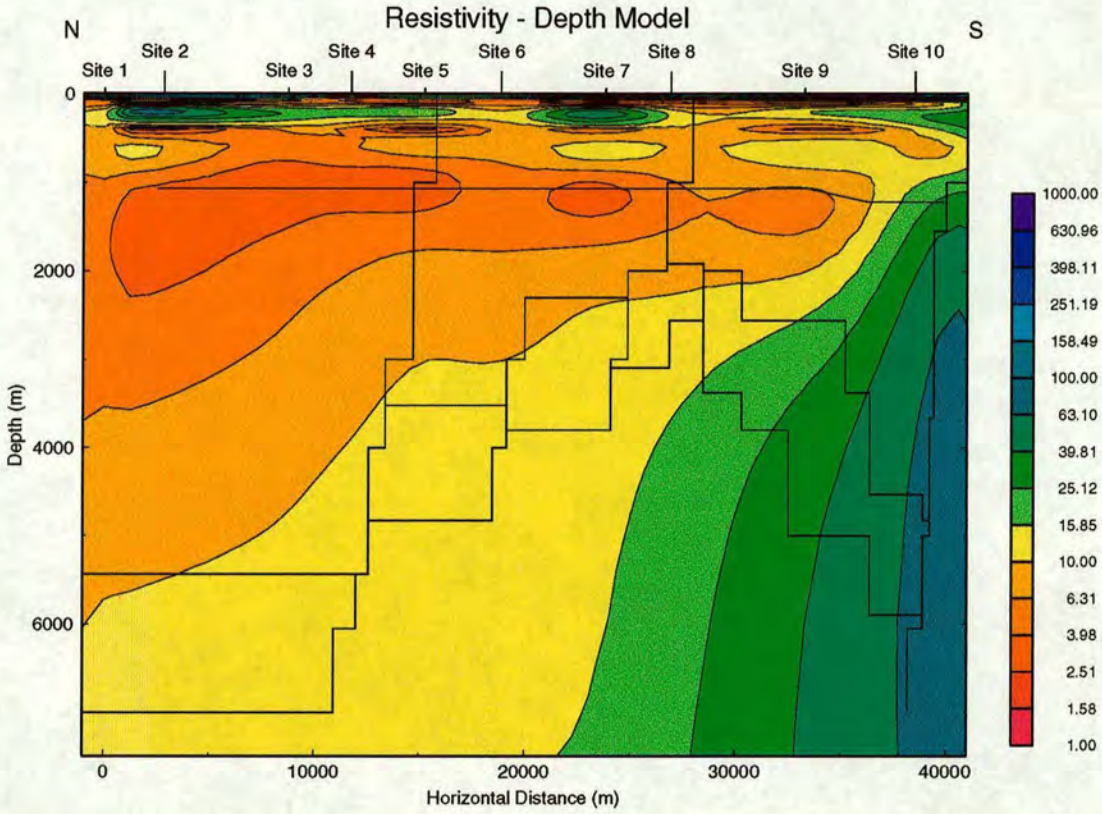

Figure 7.3. The boundaries of the block model shown in figure 7.2, overlain on the resistivity-depth section from the inversion of the Mana Pools MT data.

Model *M1* was forward modelled, initially without an escarpment fault to the north of the basin and then again with a fault identical to that used in the RRI modelling of chapter 6. The fault was placed approximately 10 km to the north of site 1 and marks the transition to a 2000 Ωm craton. This is more than an order of magnitude greater than the resistivity used to model the southern escarpment, which is based on the resistivity of that region in figure 7.3. Again, it was found that a resistive northern escarpment was required to generate the observed separation in the E- and H-polarisation apparent resistivity curves. A quantitative estimate of the fit of the seismic model to the data was obtained using the same method as is used in RRI to assess the model fit. The mathematics for this are given in appendix A. A direct comparison of the misfit of the resistivity model from figure 6.11 and that derived from the seismic structure cannot be made, as the former is weighted by the data weights calculated during robust iterations. Instead, the misfit of the seismic model must be compared to that of the resistivity model after the last non-robust iteration. This comparison gives an rms misfit of 3.22 for the RRI model and 6.30 for the seismic model, *M1*.

Figures 7.4 to 7.6 show the fit to the MT data for three of the sites on the MT profile of both the RRI model of figure 6.11 and model *M1* derived from the seismic structure shown in figure 7.2. At sites 4 and 6, shown in figures 7.4 and 7.5, the fit of model *M1* is comparable to that of the RRI model. The fit of the former model is, however, much poorer than that of the latter at site 10 in figure 7.6. This seems to be mainly due to an overestimate of the near surface resistivity at this site and is due to modelling the escarpment as a single resistivity block which extends to the surface; the RRI model indicates that

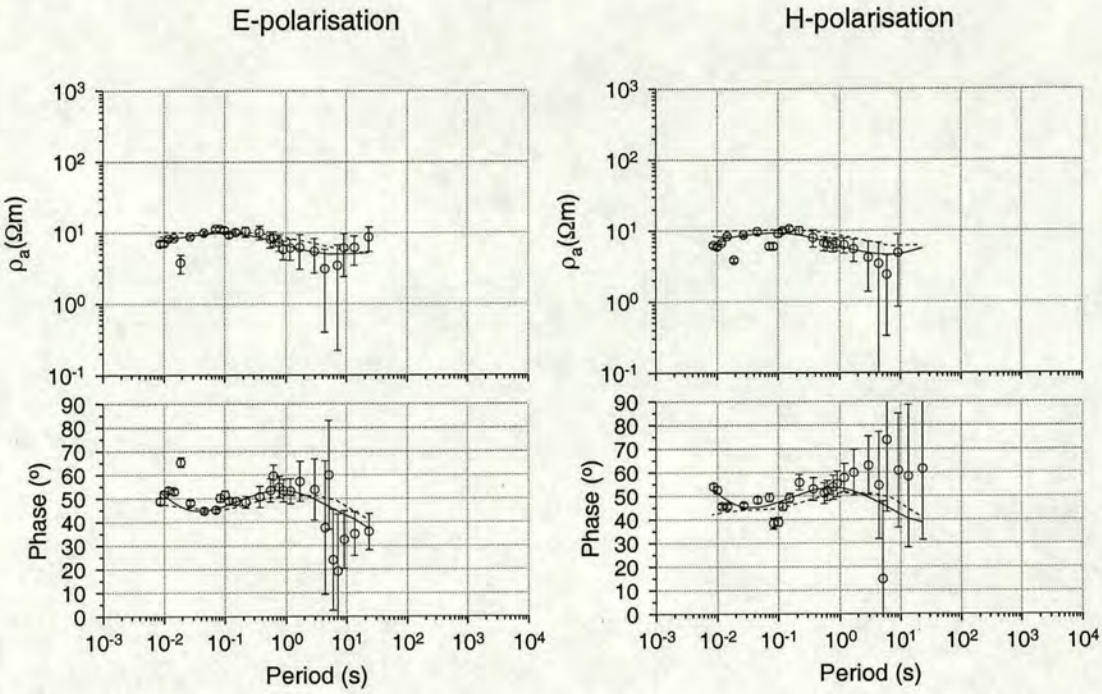

Figure 7.4. The fit of the seismic model *M1* and the MT model to the MT data from site 4. The solid line represents the forward response of the MT model and the dotted line is that of *M1*.

the escarpment resistivity starts to increase at just over 1 km depth at site 10. All of the figures show the fit of *M1* to the phase data to be poorer than that of the RRI model at the highest frequencies. This arises from a difficulty in modelling the near surface structure. Extending the Upper Karoo layer to the surface lead to an underestimation of the resistivity at the highest frequencies for all sites within the basin, but a fixed resistivity Post Karoo layer is also inadequate. The problem cannot be overcome without introducing resistivity variations within the Post Karoo layer itself. This would be reasonable as the region within the resistivity model of figure 6.11 to which this top layer corresponds shows an alternating resistor, conductor, resistor with increasing depth, which is not always consistent between adjacent sites. This structure may originate from an attempt to achieve too close a fit to slight data variations in the upper kilometre of the model and may represent structure required only to fit the data rather than real earth structure; alternatively, it may represent natural variability in the near surface resistivity. The Post Karoo layer does appear within the seismic structure and attempts to fit the MT data without it are unsuccessful, therefore the latter hypothesis is more probable.

Figure 7.5 shows the fit of both models to the data from site 6. There is good agreement between the two for the apparent resistivity data although the fit of *M1* to the H-polarisation data is slightly poorer at longer periods. The fit to the phase data is again reasonably similar with the exception of the poorer fit of the seismic model at higher frequencies and some slight differences, in particular a worsening of the fit to the H-polarisation data at longer periods. This degrading of the fit of the seismic model to the H-polarisation data at long periods is seen at all the LMT sites and is possibly because the seismic model is only resolved to a depth of 7 km whereas the LMT data contain information from much greater depths. Interestingly, the difference in fit of the two models to the data is much smaller for the E-polarisation mode and the fit of *M1* to the phase data from this mode is slightly better at longer

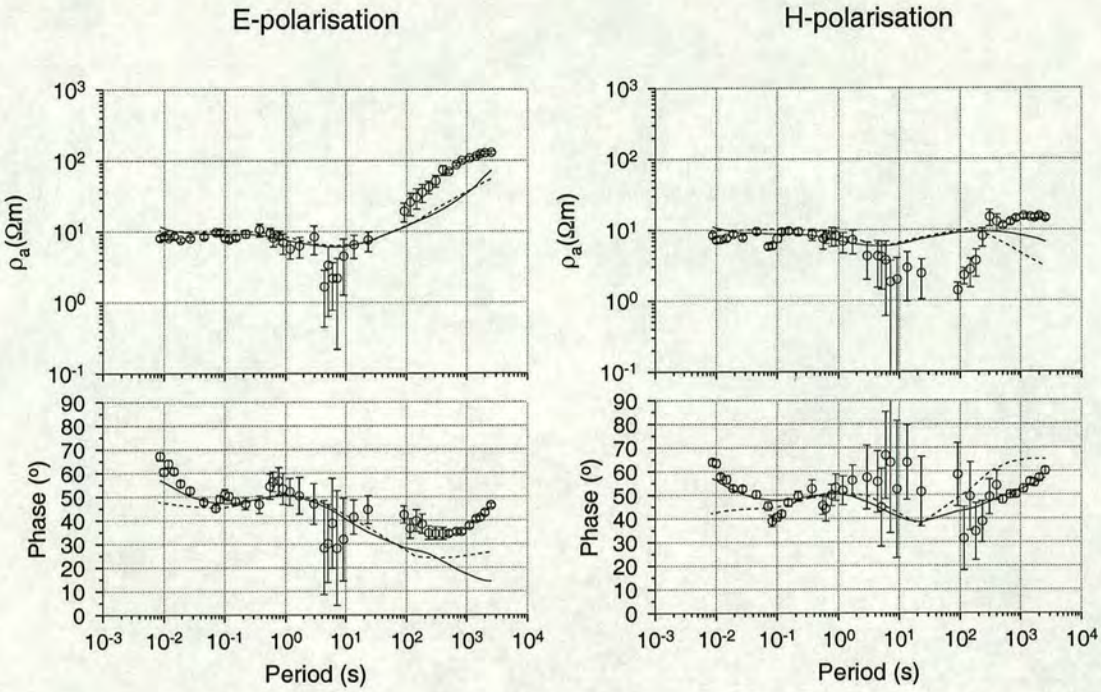

Figure 7.5. The fit of *M1* and the MT model to the MT data from site 6. The solid line represents the forward response of the MT model and the dotted line is that of *M1*.

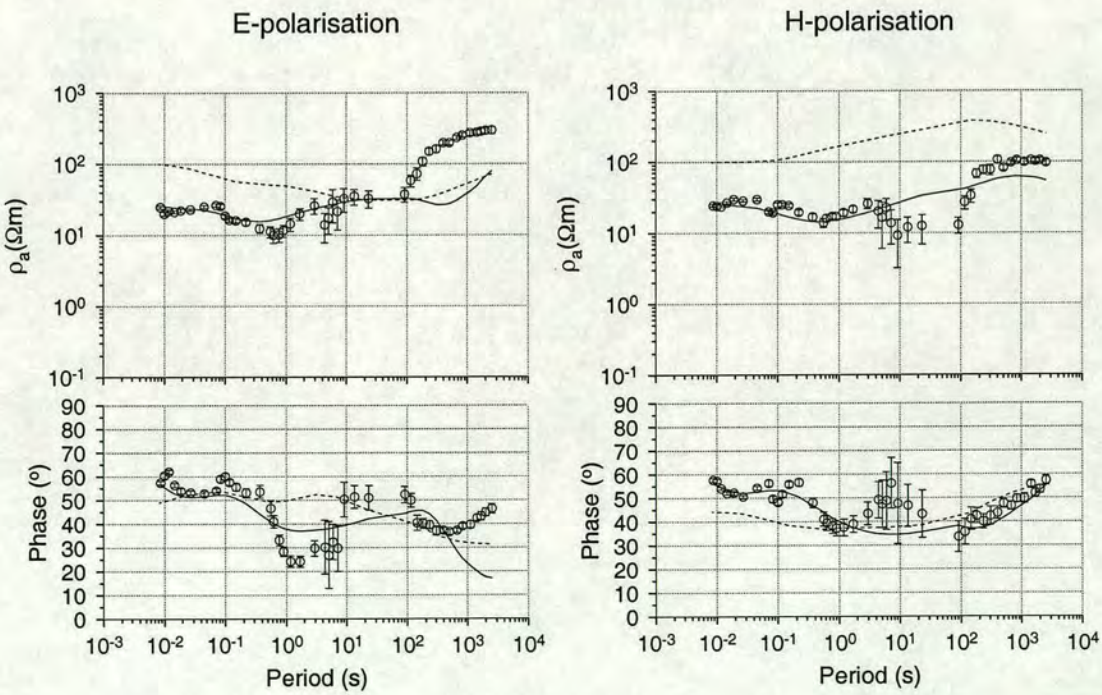

Figure 7.6. The fit of *M1* and the MT model to the MT data from site 10. The solid line represents the forward response of the MT model and the dotted line is that of *M1*.

periods. The similarity in the fit of the RRI and seismic models to the MT data in figures 7.4 and 7.5 is typical for all of the first nine sites.

The fit of *M1* to the data from site 10 in figure 7.6 is much poorer, this is due to the difficulties encountered in modelling the escarpment block. Of particular interest is the contrast in resistivity of the northern and southern escarpments, 2000 Ωm and 100 Ωm respectively, used here during the modelling process. This contrast results from the fact that the separation of the E- and H-polarisation apparent resistivity curves at longer periods decreases as the sites are traversed from north to south. This fact precludes too high a charge build up on the southern escarpment fault; increasing the resistivity of the southern block leads to an increase in charge on the fault which causes the H-polarisation mode at the southern basin sites to drop further than is required by the data. The data curves for site 10 in figure 7.6 and the resistivity model in figure 7.3 both indicate a low resistivity at this site close to the surface, approximately 20 Ωm with a resistivity increase with depth. A model, *M2*, which moves the resistive escarpment block to the depth of the base of the Post Karoo layer, approximately 1500 m and continues the 10 Ωm Post Karoo to the south can accommodate a resistivity of 2000 Ωm for the southern craton and also achieve a better fit to the data. The rms misfit of this model is 5.98 and the improvement comes from a better fit to the long period H-polarisation data while the fit to the E-polarisation data remains relatively unchanged. Physically, the extension of the Post Karoo layer into the escarpment allows an escape route for currents trapped within the valley, lowering the charge build up on the escarpment fault. The main feature to recommend model *M2* is the improvement in the fit to the data at site 10, but this is outweighed by associated problems. While a continuation of the Post Karoo layer through site 10 is consistent with the data at that site, it is hard to justify at site 11. There is no evidence for such a low resistivity feature beneath site 11 in figure 6.11 and it is hard to imagine such a layer being continuous across the topographic boundary presented by the 600 m Zambezi escarpment and then on into the craton to the south. Continuing the Post Karoo upper layer beneath site 10 and then bounding it to the south with a 100 Ωm layer is in better agreement with the resistivity section in figure 6.11 and the data from site 11, assuming some degree of static shift occurs there. This model, *M3*, gives an rms misfit to the data of 6.20, very similar to the model whose response was plotted in figures 7.4 to 7.6. The improvement in misfit for this model comes mainly from a much better fit to the data from site 10, shown in figure 7.7. The fit at the other sites is very similar to those for *M1*, with the high resistivity escarpment extending to the surface, except for a slight deterioration in the fit to the H-polarisation data at longer periods.

In terms of their overall fit to the data, these two models, *M1* and *M3*, are indistinguishable and suggest that the southern escarpment can be modelled using a variety of resistivities. While the fit to the sites within the basin is better in the earlier model, the improvement in fit at site 10 is obviously an advantage of the latter. The contrasting resistivity of the northern and southern escarpments is an interesting problem. All the available evidence supports the Mana Pools basin being a half graben structure with a depocentre in the northern portion. This implies that the southern escarpment section of the basin was the hinge and would have experienced a different style of fracturing and tectonic disturbance to that of the northern escarpment. This may account for a contrast in resistivity to the north and south of the basin.

Returning to the *M1* model, much of the discrepancy between its misfit of 6.30 and the 3.22 misfit of the RRI model to the data can be accounted for by the constraint of maintaining constant resistivity layers.

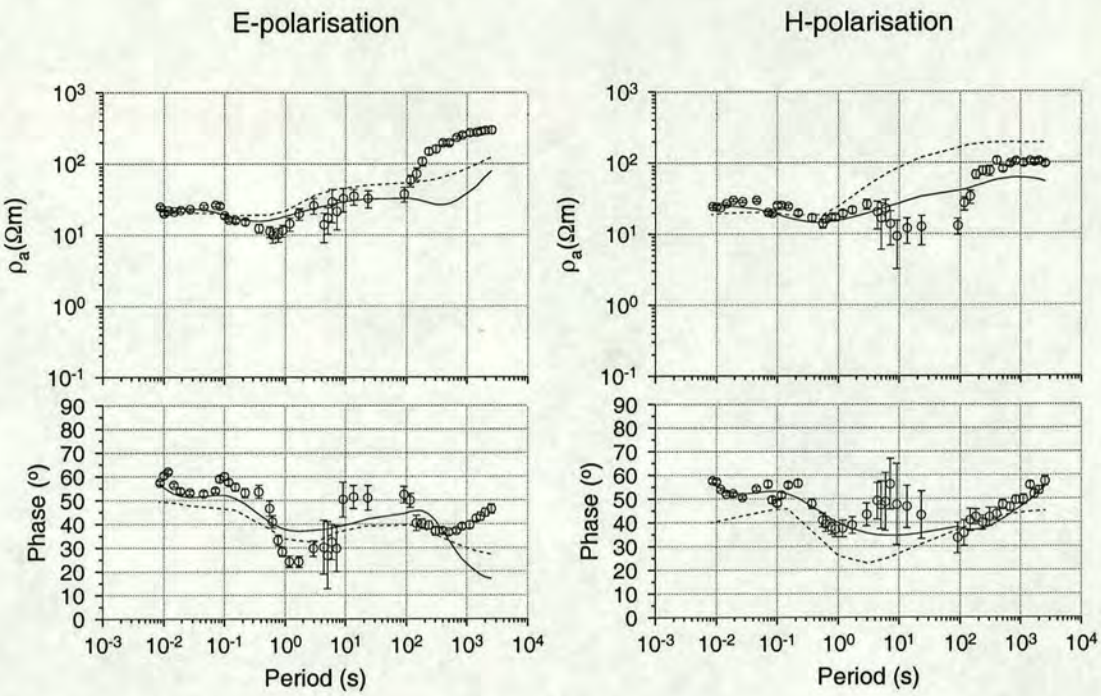

Figure 7.7. The fit of *M3* and the MT model to the MT data from site 10. The solid line represents the forward response of the MT model and the dotted line is that of *M3*.

This is particularly true for the Post Karoo layer, which shows the most variability in the resistivity-depth sections and which controls the fit to the high frequency data with their lower error bars. As an example of the improvement of fit to the high frequency data that can be achieved by allowing some resistivity variation in the Post Karoo layer, we look at the case of sites 2 and 3. The resistivity section in figure 7.3 indicates that there is a small amount of higher resistivity material beneath these two sites, extending to a depth of 500 m. This was added to the 10 Ωm Post Karoo layer of *M1* and the forward response of the new model, *M4*, recalculated; figures 7.8 and 7.9 show the response of both *M1* and *M4*. *M1* with the constant resistivity layer is represented as a solid line and the dotted line is *M4* incorporating the resistor in the Post Karoo beneath sites 2 and 3. The fit to the high frequency section of all four responses at each site is improved, though the improvement is most noticeable in the E-polarisation responses. The rms misfit of the model at site 2 improves from 8.74 to 4.14 and that for site 3 from 5.05 to 2.72, the overall model rms is improved to 5.81. These small variations in resistivity of the surface layer are clearly important; by allowing for them beneath the rest of the profile, the misfit of the seismic model could almost certainly be brought down to a value close to that of the RRI model.

The forward response was calculated for a further model with exactly the same resistivities as *M1* except that both the Lower Karoo layer and the region beneath, the seismic basement, were set to 20 Ωm. The fit of this final model did not deviate significantly from that of *M1* and indicates that the MT data do not require a differentiation to be made between these two layers, and that such a differentiation is not justified on the basis of the MT data alone. The conclusion from the overall assessment of the response of the seismic model is that the structure present is compatible with that shown by the RRI model, and that the resistivity structure can be as well described by a number of resistivity layers. The near surface, Post Karoo, layer of 10 Ωm is required to fit the data but its identification as a single

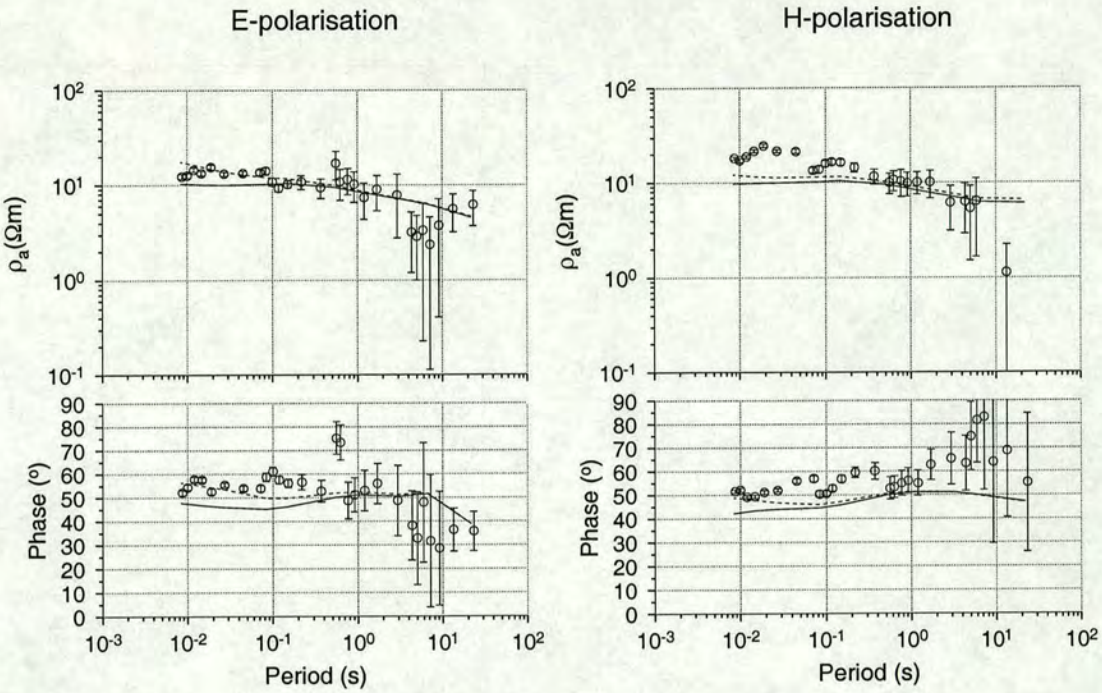

Figure 7.8. The fit of *M1* and *M4* to the MT data from site 2. The solid line represents the forward response of *M1* and the dotted line that of *M4*.

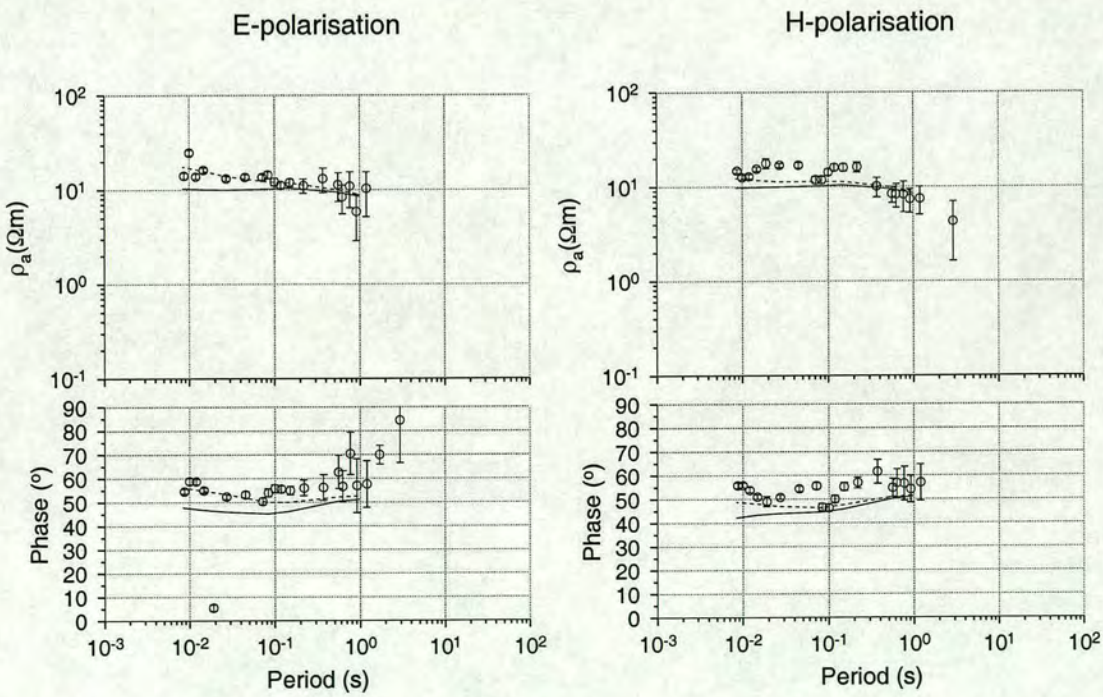

Figure 7.9. The fit of *M1* and *M4* to the MT data from site 3. The solid line represents the forward response of *M1* and the dotted line that of *M4*.

stratigraphic unit cannot be either supported or dismissed on the evidence of the RRI model. To fit the data well, this layer has to be laterally varying, which is reasonable for the resistivity of a surface layer. The good conductor above 5 km can be represented as a 5 Ωm layer confined to the Upper Karoo. Beneath this are the Lower Karoo and the seismic basement which in terms of resistivity can be treated as one unit with no significant degradation in the model; the resistivity of 20 Ωm for the seismic basement is remarkably low. The fit of the seismic model cannot be improved significantly without allowing a degree of resistivity variation within the Post Karoo layer and allowing the region south of the escarpment to decrease in resistivity towards the surface.

7.3 Two-Dimensional Modelling of The BGR MT Data

The data collected in the Lower Zambezi basin by the BGR were introduced in section 2.7. The data along a single north-south profile from this dataset were made available to me by the ZGS and the University of Zimbabwe; the location of this profile relative to the Mana Pools profile is shown in figure 7.10. The BGR survey was undertaken to determine whether the northern Zambezi valley in

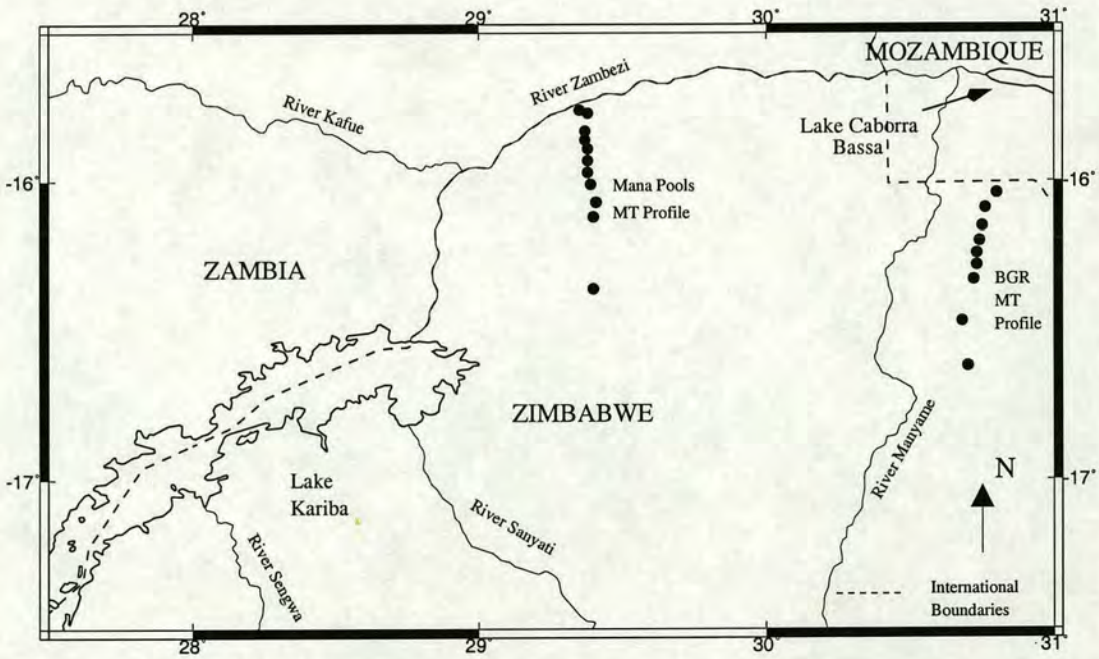

Figure 7.10. The relative locations of the Mana Pools and BGR MT profiles.

Zimbabwe was sufficiently prospective for hydrocarbons to justify further exploration. The aims were to gain a regional picture of the Lower Zambezi basin and to delineate its gross structure. The main question to be answered was the depth to basement within the basin and thus the consequent sedimentary thickness. This question arose from the results of an aeromagnetic survey of the Zambezi valley, re-interpreted by Bosum and Geipel (1988), which revealed two magnetic horizons, one at a depth of approximately 2 km, the other at approximately 10 km. It was expected that one of these two horizons would correspond to the sediment-basement interface.

Losecke *et al.* (1988) interpreted the BGR MT data using one-dimensional inverse modelling techniques and two-dimensional forward modelling. Their two-dimensional model for the resistivity distribution of the MT profile modelled here was shown in figure 2.8. Losecke *et al.* (1988) interpreted the model as a three layer structure with conductive non-metamorphic sediments to 4 km depth overlying a resistive layer to depths of between 4 and 10 km with a very good conductor beneath, which they claimed extends to depths of more than 30 km. In interpreting the geoelectric model, Losecke *et al.* also made use of the gravity data from the Zambezi valley modelled by Zhou (1988) and the aeromagnetic data re-interpreted by Bosum and Geipel (1988). These two potential field methods support the interpretation of layer one as consisting of good conducting non-metamorphic sediments, the gravity data shows a corresponding region of low density, 2200 - 2300kgm^{-3} (Losecke *et al.*, 1988) and the upper magnetic horizon can be interpreted as the base of this conductivity layer. The resistive zone underlying this upper layer is more difficult to interpret. Losecke *et al.* offer two possible hypotheses, either the resistor represents the upper part of the crystalline basement or it consists of consolidated sediments with intercalated basalt sills. The MT, gravity and magnetic data cannot distinguish between these two hypotheses (Losecke *et al.*, 1988). The later seismic survey of the Zambezi valley interpreted by Hiller and Buttkus (1996) helps separate these two interpretations by determining the sedimentary thickness of the Lower Zambezi basin to be 11.6 km; clearly the resistor cannot therefore be interpreted as crystalline basement. This also aids interpretation of the aeromagnetic data. While Losecke *et al.* (1988), using the work of Bosum and Geipel (1988), interpret the lower magnetic horizon as marking the transition to "old crystalline basement", the upper horizon can either represent a transition to basement rock again, with the lower horizon marking a change in magnetisation, or it could mark magnetic layers within the sediments. Clearly, the latter explanation has to be favoured in light of the later seismic work. The consequence of this interpretation would be that neither the MT nor magnetic data can detect the base of the consolidated sedimentary layer unless the lower magnetic horizon is interpreted as the basement interface. The lower horizon is approximately coincident with the boundary between the resistive MT layer and the deeper conductor below and would imply phenomenally low resistivities down to 0.2 Ωm for the basement rocks. Identification of the lower magnetic horizon with the basement interface is problematic; Bosum and Geipel (1988) identify the region between the two magnetic horizons, identified with the resistor, as a region of magnetic minerals underneath a non-magnetic cover. The second magnetic horizon represents a change in magnetisation; this horizon lies close to the basement depth of 11.6 km determined seismically (Hiller and Buttkus, 1996) but is slightly shallower at 10 km. There are three possible interpretations of this lower magnetic horizon; it may represent a change in magnetisation at the sediment-basement interface, a change in magnetisation internal to the sedimentary layer or thirdly it may represent the Curie surface beyond which magnetisation is lost. The third explanation is discussed in detail by Losecke *et al.* (1988); if it is correct then the aeromagnetic data does not detect the basement interface either.

The resistivity model was derived by Losecke *et al.* (1988) using assumptions including an identical resistivity distribution within the cratonic block north of the Zambezi graben as that in the Zimbabwe craton bordering it to the south. This is different to what was found for the Mana Pools basin in chapter 6 but the mode of formation is believed to be different for the Lower Zambezi basin (Orpen *et al.*, 1989). Much of the Lower Zambezi basin falls within Mozambique and therefore there are no data. The northern section of the graben within Mozambique is therefore modelled using a continuation of the resistivities calculated for the sites closest to the Mozambique border. Clearly from the preceding

discussion, the interpretation of the Lower Zambezi MT data is not straight forward although some of the ambiguity has been removed with the help of the seismic data. Comparison of this geoelectric model with that of Whaler and Zengeni (1993) for the Mana Pools basin has also proved difficult. This section aims to make a minimum structure two-dimensional inversion of the BGR data profile using RRI (Smith and Booker, 1991) to assess whether all the structure within the forward model of Losecke *et al.* (1988) is necessary to model the data. This model should aid in answering the questions that arise from discussion of the Losecke *et al.* model. Namely, does a minimum structure model require a three layer basin? Does the layer 3 conductor extend to the depths claimed at such high resistivity? Do the magnetic horizons correspond to conductivity boundaries within the model or are the magnetic properties independent of the resistivity? Finally, do the modelling assumptions of Losecke *et al.* affect the structure of the model obtained?

Only the principal impedance elements for a constant strike direction of 0°, were available for modelling. This regional azimuth agrees with the findings of Losecke *et al.* (1988), which showed an average deviation of only 9° from an east-west electrical strike along the profile. Frequencies common to all the sites were selected for inversion; this covered a range from 2.5 Hz down to 0.48×10^{-3} Hz or 2050 s and the model was gridded according to the guidelines of Booker (1997) laid out in § 6.5. None of the data in this frequency range were rejected as coherency information was not provided and there were no clear outliers at any of the survey sites. The data were two-dimensionally modelled using the RRI method of Smith and Booker (1991) and the methodology described in § 6.5. The conductivity depth section obtained from the E-polarisation data alone is shown in figure 7.11 and has an rms misfit to the data of 1.07 after 55 successful iterations. That for the H-polarisation data is shown in figure 7.12 and has an rms misfit to the data of 1.04 achieved after 33 iterations.

The resistivity structures seen in figures 7.11 and 7.12 are very different. The structure derived from the E-polarisation data is more reminiscent of the model of Losecke *et al.* (1988). A thin layer of approximately 2 to 10 Ωm appears in the upper two kilometres of the model with a resistive unit below, which tapers and dies out northward. Spatially, this resistor occupies approximately the same region as the resistive zone 2 of Losecke *et al.* (1988) but it does not span the entire survey and has a considerably lower resistivity (with a maximum of approximately 100 Ωm compared to 3000 Ωm for the earlier model). Beneath this layer and rising close to the surface in the north is an extremely good conductor with resistivities as low as 0.5 Ωm. Spatially and in terms of resistivity, this conductor is in very good agreement with that observed by Losecke *et al.*. To the south, at sites 8 and 9 which lie on the Zimbabwe craton, the resistivity is much higher at all depths reaching figures of approximately 2×10^4 Ωm, an order of magnitude higher than in Losecke *et al.*'s model. The black circles plotted on figure 7.11 show the E-polarisation data plotted at a single skin depth to give a guide to the penetration depth of the data. The calculation method assumes an overlying homogeneous layer of resistivity equal to the apparent resistivity at the frequency of calculation. In view of the extremely low apparent resistivities at long periods at some of the sites in the Lower Zambezi profile, this may give conservative estimates of skin depth. Different values would be achieved with other techniques such as averaging the apparent resistivity in some way down to the frequency of calculation. Bearing this in mind, figure 7.11 shows a decrease in the amount of information returned from below 20 km at the northern end of the profile. On the basis of these calculations and in agreement with Losecke *et al.*, the base of the conductive zone is not seen; the conductor's claimed extension to 30 km depth may be feasible but on the basis of the skin

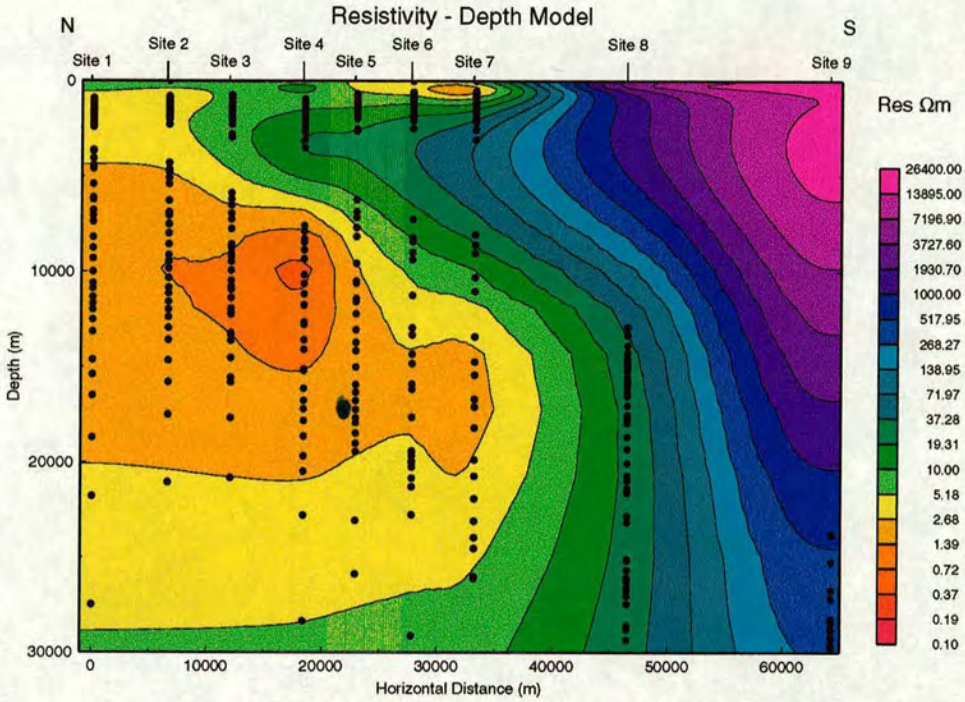

Figure 7.11. The resistivity structure of the Lower Zambezi basin modelled from E-polarisation data only. The circles represent the E-polarisation data points plotted at one skin depth.

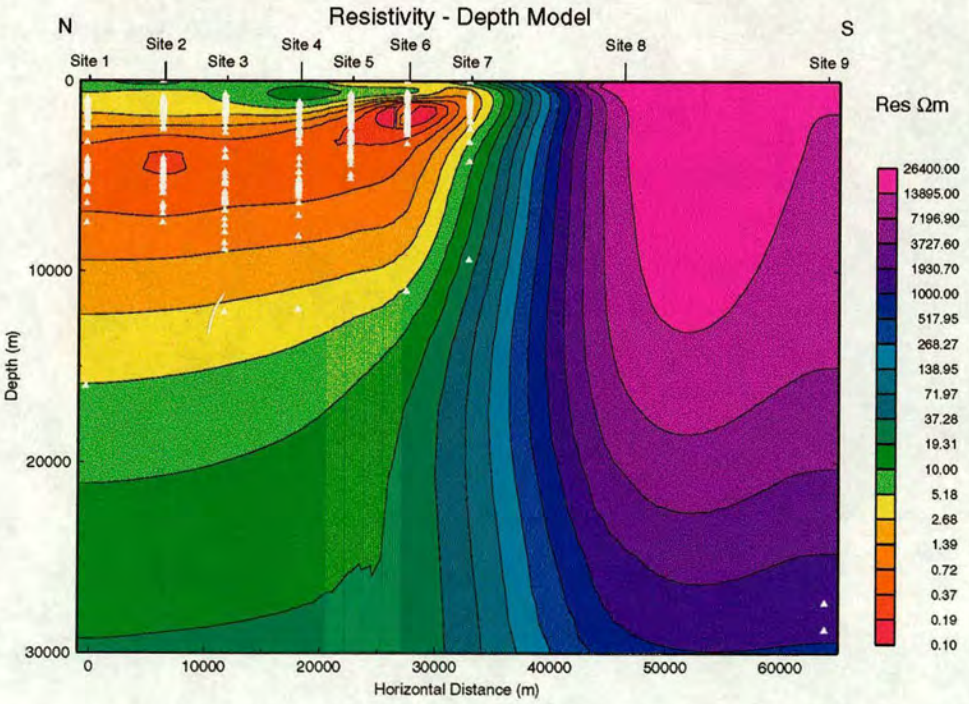

Figure 7.12. The resistivity structure of the Lower Zambezi basin modelled from H-polarisation data only. The triangles represent the H-polarisation data points plotted at one skin depth.

depth calculation presented here seems optimistic.

The resistivity structure shown in figure 7.12 derived from the H-polarisation data alone is very different from that shown in figure 7.11. Figure 7.12 again shows an approximately 2 km thick near surface conductor of resistivity 2 to 10 Ωm but beneath this there is no resistive layer, instead an extremely good conductor with resistivities down to 0.1 Ωm. Below 10 km, the resistivity increases slowly. To the south there is a rapid rise in resistivity between sites 7 and 8, and the two sites on the craton again have an extremely high resistivity. Superficially, the structure of figure 7.12 is very similar to the interpretation of the seismic data by Hiller and Buttkus (1996) given in figure 2.11, with a Post Karoo layer extending from the surface to approximately 2 km depth and an Upper Karoo layer coinciding with the conductor here and extending to 11 km depth with a southern boundary fault dipping to the north. This similarity may be misleading though, as the triangles representing single skin depth estimates on figure 7.12 do not extend to the base of the conductor and only the upper 10 km is constrained. Clearly, all structure within the basin and beneath this depth is merely speculative. The high surface resisistivity on the craton to the south increases the depth of penetration at sites 8 and 9 and the skin depth estimates are much greater; two triangles can be seen close to 30 km on figure 7.12.

The resistivity structure derived from the unconstrained data from both modes is plotted in figure 7.13; this model achieved an rms misfit to the data of 1.460 in 27 iterations. The resistivity structure shows

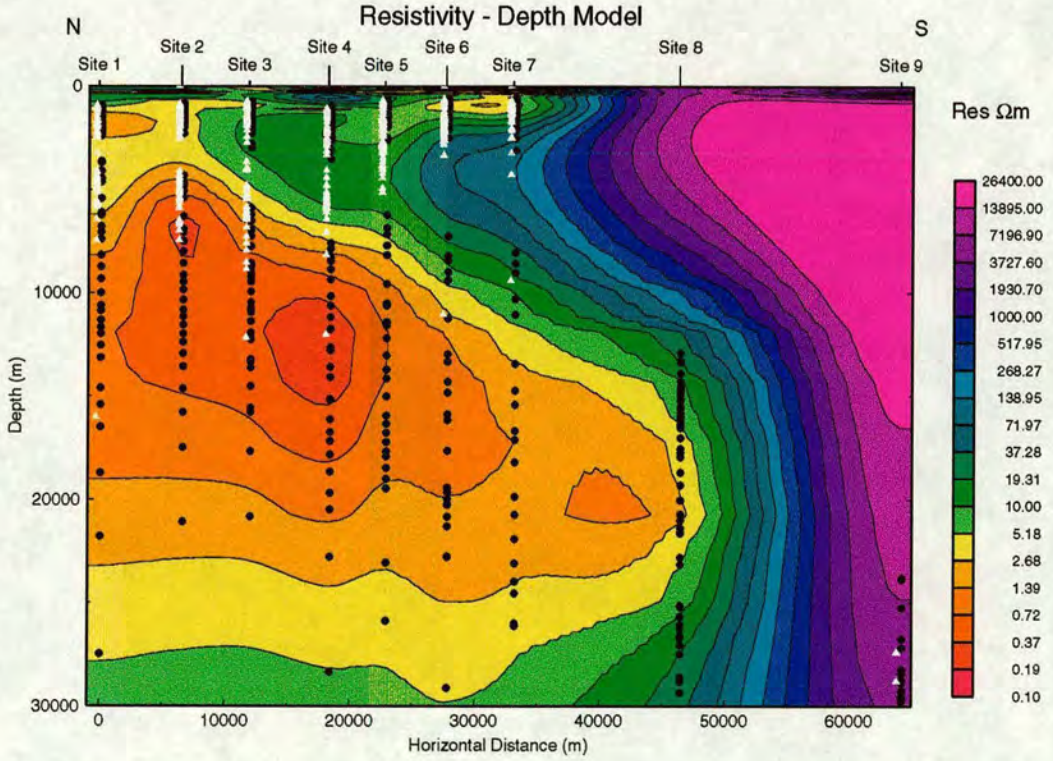

Figure 7.13. The resistivity structure of the Lower Zambezi basin modelled from both polarisations with no constraints applied. The circles and triangles have the same meanings as in figures 7.11 and 7.12.

most of the features of the E-polarisation structure plotted in figure 7.11. The upper conductive layer is quite indistinct and varies in resistivity between approximately 2.5 Ωm and 50 Ωm just beneath site 4,

typically it has a resistivity of 10 Ωm and lies in the upper 2 km of the model. Beneath this is a resistive layer very similar to that seen in figure 7.11. It thins to the north and dies out, not underlying sites 1 or 2. Underlying this is the very good conductor, its upper surface dipping to the south of the basin and approaching the surface to the north; the resistivity of this layer is as low as 0.2 Ωm. The escarpment to the south is again much more resistive, approaching $2 \times 10^4 \Omega$m. The final model is dominated by E-polarisation structure; there is very little evidence of the conductor between 1 and 10 km in figure 7.12 in the model of figure 7.13. This is difficult to explain. At depths below 10 km within the basin, there is effectively no H-polarisation resolution which explains the similarity of figure 7.13 at depth to that for E-polarisation data alone. It may be that the greater resolution of the E-polarisation mode at depth leads to domination over the H-polarisation mode and of the joint model even at depths where the H-polarisation resolution is good. The transition in figure 7.13 of the deep conductor to higher resistivities at depths below 20 km is unlikely to be meaningful; at this depth it is not likely to be well resolved if at all. The rather diffuse nature of the resistivity structure may result from a combination of two effects: the tendency of RRI to vertically smear structure, as described by Schnegg (1996) and the fact that it is almost entirely resolved by E-polarisation data which gives a more smoothed response than the H-polarisation. We could therefore speculate that the conductor is confined to a narrower vertical zone.

The structure of the unconstrained model is in reasonable agreement with that of Losecke *et al.* (1988). The seeking of a minimum structure model restricts the continuity of layering, removing the resistive zone in the north of the section, but all three of the layers in the Losecke *et al.* model are present. No

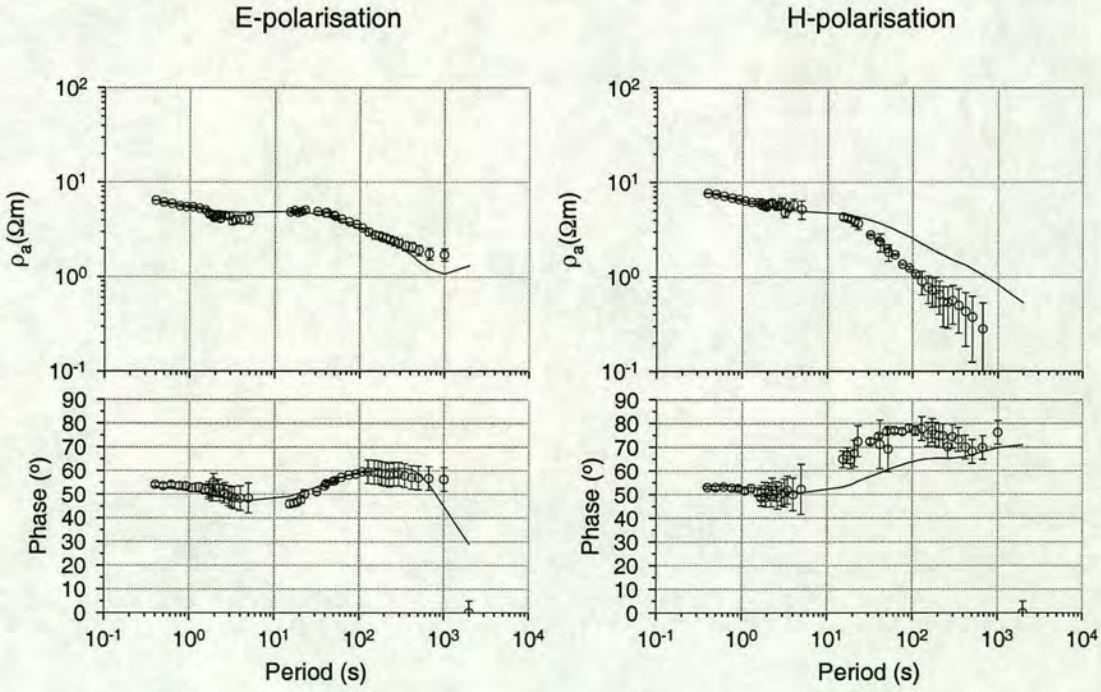

Figure 7.14. The fit of the unconstrained model of figure 7.13 to the data from site 2.

associated misfit for the modelling of the Lower Zambezi basin data was given by Losecke *et al.* so it is difficult to compare the misfit of the RRI model here with their model. Instead, plots of the misfit of the RRI model to the BGR data were made and compared with equivalent plots in the report by Losecke

et al., not reproduced here. One such plot for site 2 is given in figure 7.14 with the model response plotted as a solid line and the data plotted with their associated error estimates. The misfit plots for the two models are almost indistinguishable at all sites. Typically, the fit is better in both cases to the E-polarisation than the H-polarisation data; this is seen mainly at the longer periods as in figure 7.14. From this comparison, the model of figure 7.13 appears to be as good as that of Losecke *et al.*.

A problem with both the inversion of the H-polarisation mode alone and the joint inversion was the small number of successful iterations achieved. This was brought about by a failure of both models to smooth successfully; neither achieved more than three smoothing iterations. The cause of this and many of the other failed iterations seemed to be a difficulty in achieving a smooth fit to sites 7 and 8, particularly site 8. This is probably due to the huge jump in conductivity across the basin bounding escarpment between these two sites. Neither the RRI model presented here nor the forward model of

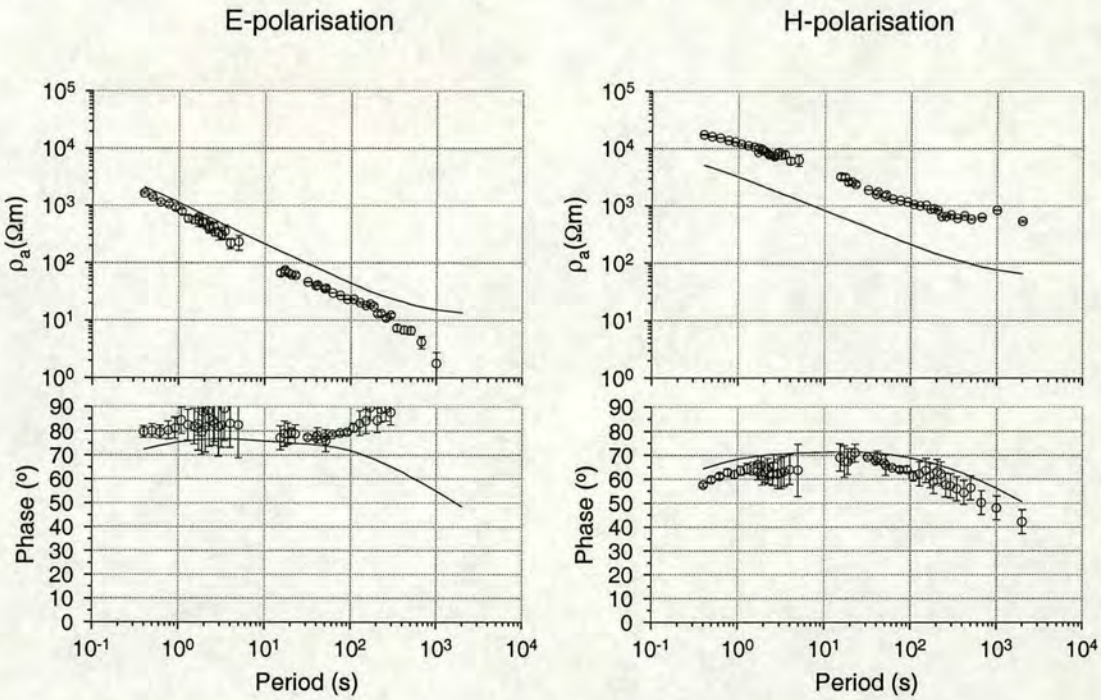

Figure 7.15. The fit of the unconstrained model of figure 7.13 to the data from site 8.

Losecke *et al.* achieved a good fit to the data from site 8 and both models misfit the data at this site in a very similar way. The misfit of the RRI model to the data from site 8 is shown in figure 7.15. Unlike most of the other sites in the profile, the E- and H-polarisation apparent resistivity curves do not converge at high frequencies. This may indicate that the data here are static shifted, a not unreasonable assumption in view of the extremely high surface resistivities seemingly encountered. Plots of site 9, not shown here, indicate that it may also be static shifted to a lesser degree. If this hypothesis is correct, then it would account for the difficulty in fitting sites 7 and 8; the H-polarisation mode is not able to vary both quickly and smoothly enough to fit both sites. A second possibility is that the model requires a break in the roughness matrix between sites 7 and 8 to simulate the escarpment fault separating the cratonic sites from those within the valley; both hypotheses were tested.

To test for the effects of static shift, the BGR data were inverted with only the phase data from site 8

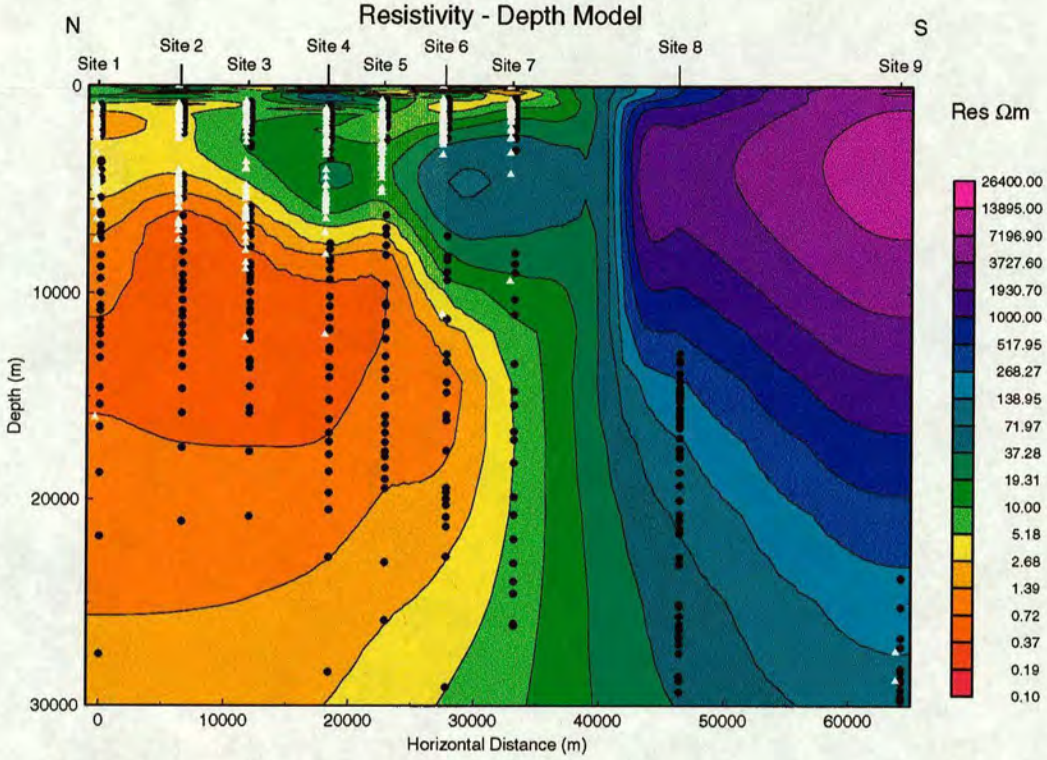

Figure 7.16. The resistivity structure of the Lower Zambezi basin modelled with an escarpment fault between sites 7 and 8 and assuming the apparent resistivity curves at site 8 are static shifted.

included, and the magnitude of the apparent resistivity being set by the data from the neighbouring sites. The inversion achieved an rms misfit of 1.307 in 58 iterations, including 29 successful smoothing iterations and the model apparent resistivity curves at site 8 were frequency-independent shifts of the observed data curves. The model with all the data included, assuming no static shift at any of the sites but employing a break in the roughness matrix to 10 km depth between sites 7 and 8 converged to an rms misfit of 1.278 in 50 iterations with 25 successful smoothing iterations. The exact location of the escarpment fault is not known, so it was placed equidistant from sites 7 and 8 and the 10 km depth extent was chosen from the location of the basin bounding fault in the interpretation of the seismic data by Hiller and Buttkus (1996), shown in figure 2.11. Both solutions to the smoothing problem succeed and give models with very similar misfits and very similar resistivity-depth sections, apart from a decrease in the near surface resistivity at site 8 in the case where the apparent resistivity data at that site is omitted. Neither solution to the problem merits preferential acceptance and so they are combined. It is known from the seismic data that there is a major escarpment fault bounding the Lower Zambezi basin to the south, and the appearance of the apparent resistivity curves at site 8 together with the frequency-independent shift predicted by the models is consistent with the assumption of a static shift problem. The data were modelled omitting the apparent resistivity at site 8 and including an escarpment fault to 10 km depth between sites 7 and 8; the resistivity structure obtained is shown in figure 7.16. The model achieved an rms misfit of 1.15 after 50 iterations; in its general features, it differs very little from that previously discussed and plotted in figure 7.13. The decrease in the rms misfit is due to the improvement in the fit to site 8 from a mean squared misfit of 5.64 to 1.21 for the model in figure 7.16. This is obviously due to omitting the apparent resistivity data and achieving a closer fit to the phase

data, and by the break in the roughness matrix across the escarpment which allows extra freedom in the smoothing process.

Figures 7.17 to 7.20 show the fit of the model plotted in figure 7.16 to the observed data. The fit is very much as would be expected considering that the final model bears far more similarity to the E-polarisation data model than that of the H-polarisation data. For the E-polarisation data in figures 7.17 and 7.18, the fit to both apparent resistivity and phase data within the basin is extremely good. The fit to the data on the escarpment at sites 8 and 9 is poorer, remembering that the apparent resistivity data from site 8 was not fitted during modelling. We see that the magnitude of the apparent resistivity data at site 9 is underestimated, particularly at longer periods. This is mirrored by an overestimate of the phase at long periods at the same site. Contrastingly, the phase data at site 8 are underestimated, meaning that the model at this site is too resistive. Clearly, although the basin sites are fit very evenly and closely, the model is still finding it difficult to fit the sharp change in resistivity encountered moving onto the craton. The fit of the model to the H-polarisation data in figures 7.19 and 7.20 is quite different. The fit to the apparent resistivity data within the basin is quite good for frequencies down to 0.1 Hz; this represents skin depths of between 1.2 and 3.5 km where the geoelectric structure of the two modes in figures 7.11 and 7.12 appears similar. At frequencies lower than this, the apparent resistivity is overestimated by the model. This represents the region of the geoelectric structure that is a resistor in the E-polarisation model of figure 7.11 and a conductor in the H-polarisation model of figure 7.12 and occupies depths of 2 to 10 km. The same phenomenon is observed in the fit to the H-polarisation phase data. Clearly, it is very difficult to fit the two modes simultaneously, and the final model is dominated by the structure derived from the E-polarisation data. This is quite unusual as H-polarisation structure often dominates E-polarisation structure in joint inversions (Livelybrooks *et al.*, 1993); a possible explanation may be that the H-polarisation errors are greater than for the E-polarisation (Losecke *et al.*, 1988) and a more balanced inversion may be achieved by relaxing the fit to the E-polarisation data slightly.

The modelling assumption employed by Losecke *et al.* (1988) during forward modelling were also tested. Namely, the extension of the vertical resistivity structure at site 1 northward to a second basin bounding escarpment in Mozambique with a resistivity structure identical to that bounding the basin to the south. The lateral extension of the vertical resistivity structure from site 1 was generated automatically by RRI and the second escarpment fault was placed to the north of the basin in the initial starting model, juxtaposing a craton to the north with an identical resistivity-depth structure as that used by Losecke *et al.* and reproduced in figure 2.8. Inversion for a model employing these constraints produced an identical rms value as that for the model plotted in figure 7.16 in exactly the same number of iterations. There were no significant differences in the resistivity structure derived except for a slight decrease in resistivity at the centre of the deep conductor between 12 and 13 km. Clearly, the assumed resistivity structure to the north of the profile under which Losecke *et al.* modelled the data has no bearing on the RRI model obtained beneath the actual data sites. Models were also obtained allowing horizontal discontinuities at the depths of the two aeromagnetic horizons, both singly and together. These models produced very small improvements of misfit, within the level expected from the extra degree of freedom given to the model by breaking the roughness matrix. The resistivity depth sections were very similar to that in figure 7.16; the imposed discontinuities made virtually no difference to the model and their presence was hard to detect. It is clear from this that the magnetic horizons do not correspond to a change in the resistivity properties of the basin and their interpretation is not aided by

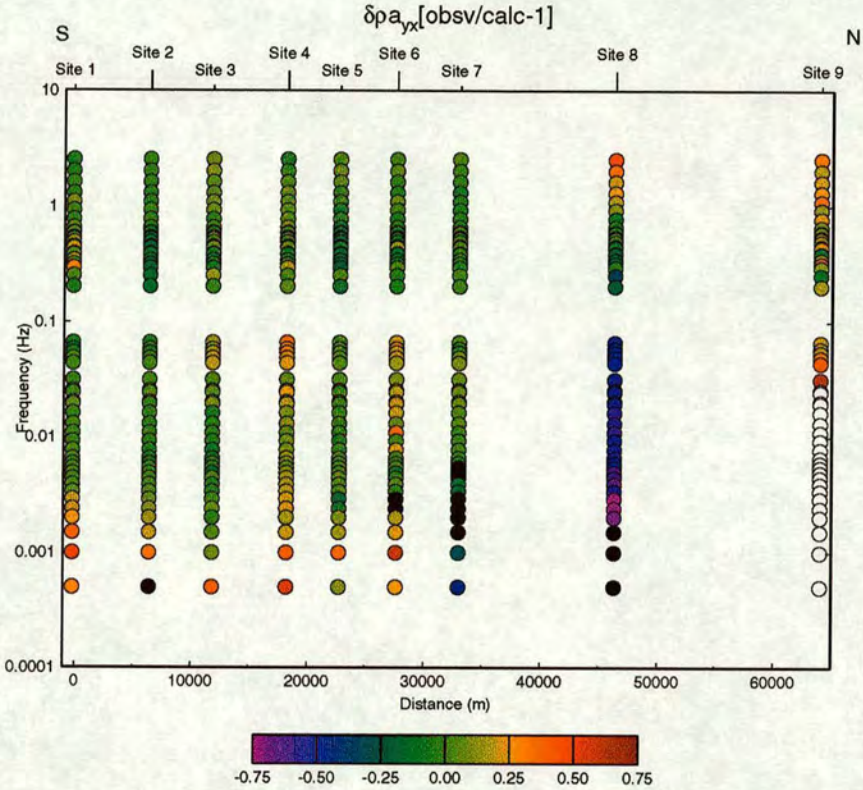

Figure 7.17. The fit of the model plotted in figure 7.16 to the E-polarisation apparent resistivity data.

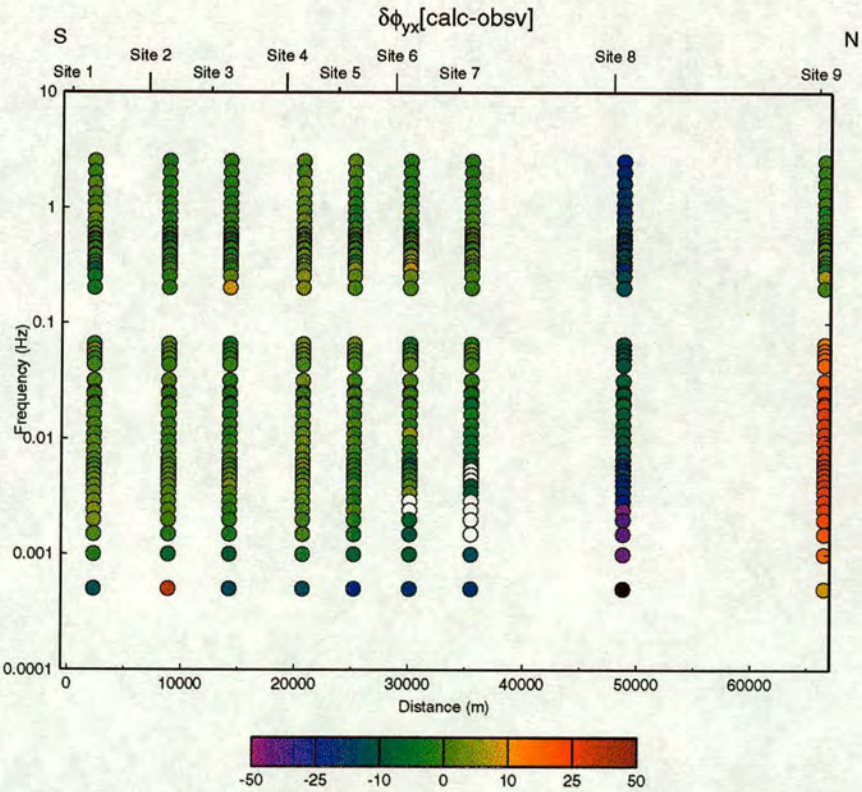

Figure 7.18. The fit of the model plotted in figure 7.16 to the E-polarisation phase data.

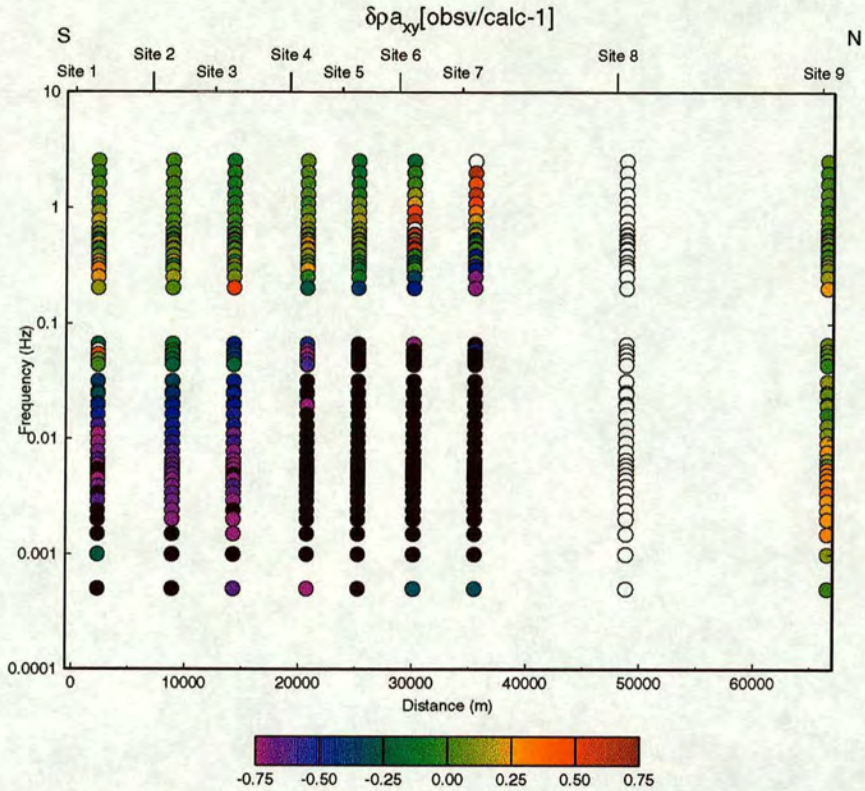

Figure 7.19. The fit of the model plotted in figure 7.16 to the H-polarisation apparent resistivity data.

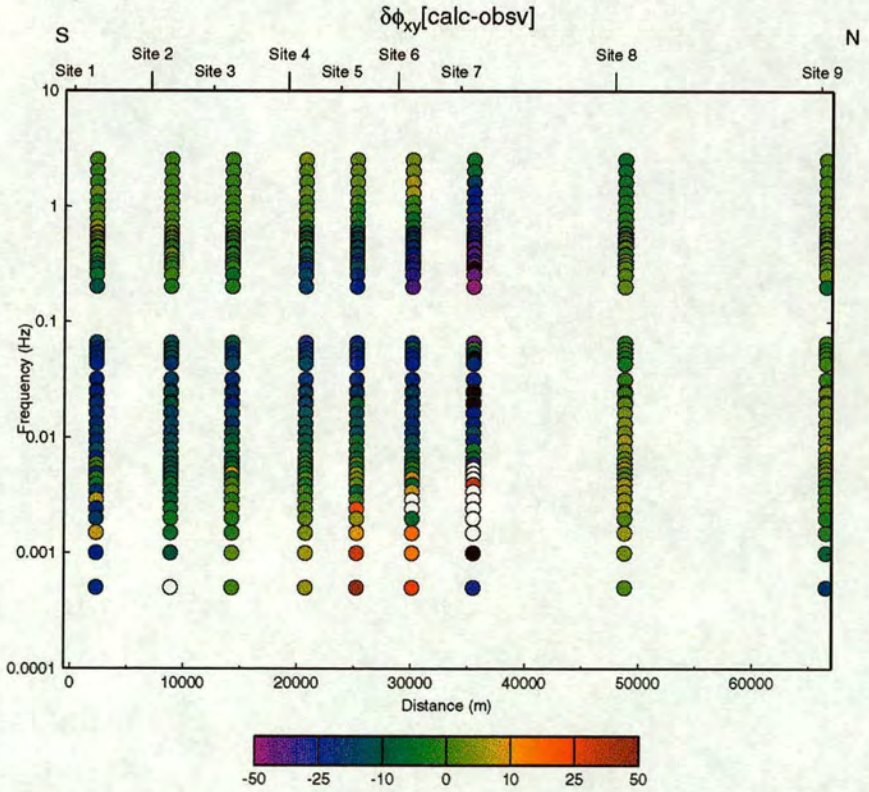

Figure 7.20. The fit of the model plotted in figure 7.16 to the H-polarisation phase data.

combining them with the MT data.

7.4 Comparison of the MT and Seismic Models for the Lower Zambezi Basin

The interpretation of the seismic data collected in the Lower Zambezi basin (Hiller and Buttkus, 1996) was shown in figure 2.11; that interpretation is here compared to the model of the resistivity-depth section obtained from the RRI inversion and given in figure 7.16. The purpose behind this comparison, as with the Mana Pools basin, is to determine whether the MT data can be interpreted within the structural bounds of the stratigraphic features determined from the seismic data. A further assessment is also made of the sensitivity of the MT data to the resistivity below the seismic basement interface at 11.6km (Hiller and Buttkus, 1996).

The seismic data were collected in Zimbabwe along a profile running from 16.41^{o}S and 30.90^{o}E northward to 15.99^{o}S and 30.90^{o}E on the Mozambique border, a line approximately parallel and 0.10^o east of sites 1 to 8 in the MT profile of the BGR. The assumption is again made, based upon the calculations of Losecke *et al.* (1988), that the basin is two-dimensional with an approximately east-west strike, so that the structure beneath the seismic line is equivalent to that beneath the MT profile. The structural interpretation of Hiller and Buttkus (1996) for the Lower Zambezi basin in figure 2.11 was converted into a model consisting of layer boundaries at different depths and projected beneath the MT profile. It is referred to as the seismic model and shown in figure 7.21. The depth to each boundary in this model is calculated from the two-way times given in figure 2.11 and the time-depth relations of Hiller and Buttkus (1996). The lithological identifications given in figure 7.21 are much better constrained than those for the Mana Pools basin (Hiller and Buttkus, 1996) and each of the individual layers is assigned a resistivity based on the corresponding region of the resistivity-depth model.

Figure 7.22 shows the boundaries of the seismic model overlying the resistivity-depth section obtained from the inversion of the Lower Zambezi MT data. As can be seen from this figure, it is extremely difficult in this case to designate a single resistivity to each layer in the seismic model. The variation in resistivity within the Post Karoo layer encompasses a range of approximately 2-50 Ωm, but the majority of the layer is between 2 Ωm and 10 Ωm; an average value of 5 Ωm was selected for modelling. The Upper Karoo layer is much more difficult to model. It seems to consist of two features; a resistor stretching northward from the craton close to 4 km depth, and a conductor at a depth of 6 to 9 km. This gives a resistivity variation internal to this layer of approximately 100 Ωm to 0.2 Ωm. For the first model, *L1*, a resistivity of 1 Ωm was selected for the entire layer. Spatially, a majority of the layer has a resistivity lower than 10 Ωm and the conductor at depth is of such a low resistivity that it was chosen as the dominant feature. The Lower Karoo consists entirely of this conductive feature and was also assigned a resistivity of 1 Ωm. The structural interpretation of Hiller and Buttkus (1996) indicates a joint treatment should be made of the escarpment material and the seismic basement beneath the Lower Karoo. The resistivity model of figure 7.22 does not allow for this. Instead, a distinction is made between the regions to the north and south of the basin bounding fault; the exact location of this fault is unknown and so is placed midway between sites 7 and 8 in both the MT and seismic models; the seismic model shows it dipping steeply to the north. The material to the south of this

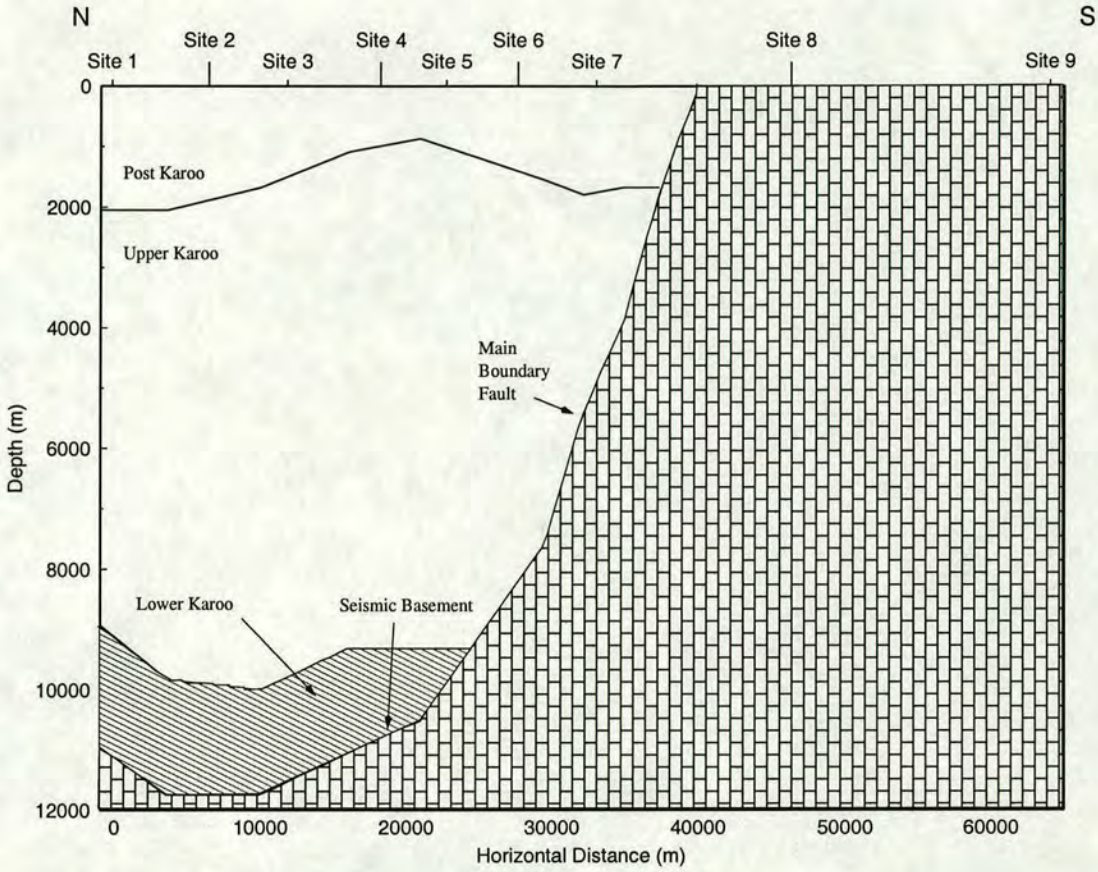

Figure 7.21. The stratigraphic model of the Lower Zambezi MT profile reproduced from the interpretation of the seismic data by Hiller and Buttkus (1996).

fault on the resistivity section is considered to be escarpment material and is assigned a resistivity of 1000 Ωm, that to the north is considered to be seismic basement and given a resistivity of 2 Ωm. This is an average value determined from the variable resistivity values encountered within this layer. Each layer in the Lower Zambezi basin is slightly less resistive than its equivalent in the Mana Pools basin. The resistivities of the Post, Upper and Lower Karoo in the Mana Pools basin are 5, 1 and 1 Ωm respectively. These differences are small and are unlikely to be significant; the resistivities selected for each layer are already averaged estimates. A bigger contrast is seen between the basements and bounding escarpments of the two basins. The Mana Pools basin has a 20 Ωm, very conductive, basement but the Lower Zambezi basement has an even lower resistivity of 2 Ωm. The contrast between the Mana Pools and Lower Zambezi escarpments is 100 to 1000 Ωm. As has already been discussed the Mana Pools southern escarpment has a remarkably low resistivity. The resistivity structure of model *L1* was gridded according to the guidelines given in Booker (1997) and forward modelled using the two-dimensional modelling code of Wannamaker *et al.* (1987).

The fits of the model *L1* to the data from sites 1 and 6 are shown in figures 7.23 and 7.24 respectively as dashed lines, with the fit of the MT model of figure 7.16 for comparison shown as a solid line. The seismic model has an rms misfit of 16.32 and the RRI model a misfit of 4.18 after the last non-robust step. As has been discussed in § 7.3, the RRI model has a better fit to the E-polarisation than the

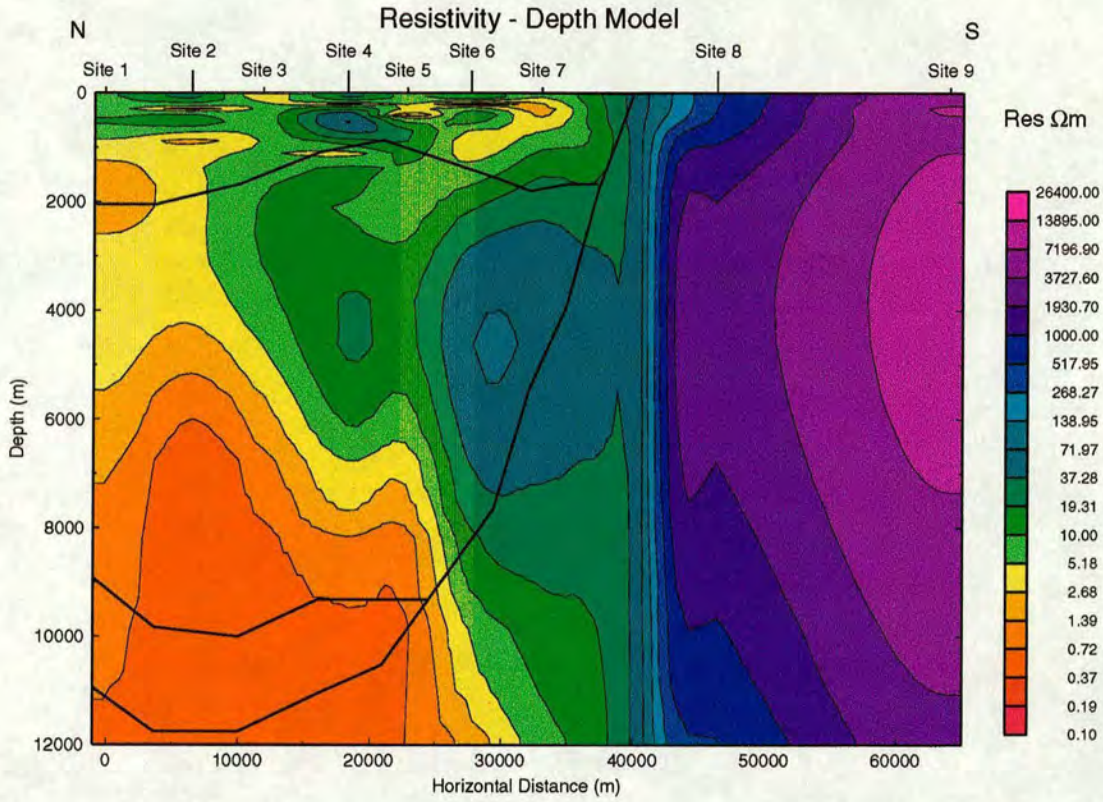

Figure 7.22. The boundaries of the stratigraphic model shown in figure 7.21, overlain on the resistivity section from the inversion of the Lower Zambezi MT data.

H-polarisation data and this is also true for the seismic model, the rms misfits to the E-polarisation mode are 19.30 and 5.60 for magnitude and phase data respectively and for the H-polarisation, 24.94 and 6.31. However, while the fit to the H-polarisation data is worse, the shapes of the E-polarisation curves, particularly in figure 7.24, are not reproduced at all by the *L1* model. In figure 7.24, there is a slight overestimate of the surface resistivity of the E-polarisation data; this is seen in the model response at the highest frequencies and is a minor problem. Far more seriously, from approximately 2 s, the apparent resistivity of the model response begins to drop as the Upper Karoo conductor is reached. The resistivity then climbs again slightly from 100 s to 2000 s due to the effect of the resistive craton at these longer periods. This behaviour is exactly the opposite to that seen in the data; the behaviour of the E-polarisation phase response shows the same characteristics. It is clear that to model the E-polarisation data more accurately, a resistive feature is needed within the Upper Karoo sediments with a response from periods as short as 2 s; this resistive feature was seen in figure 7.22. The effect of this is less marked in figure 7.23, indicating that the resistive feature has a less strong effect here which is consistent with the tapering of the feature. This resistive feature required by the E-polarisation data and seen in the RRI model does not correspond to any structural change in the seismic stratigraphic section, implying that a model based on the seismic data alone is not sufficient to explain the MT data. The *L1* model used thus far and plotted in figure 7.21 corresponds more closely to the resistivity section obtained from inversion of just the H-polarisation data which was plotted in figure 7.12, so addition of a resistive feature with a response in the required period range will cause a deterioration of the fit to the H-polarisation data.

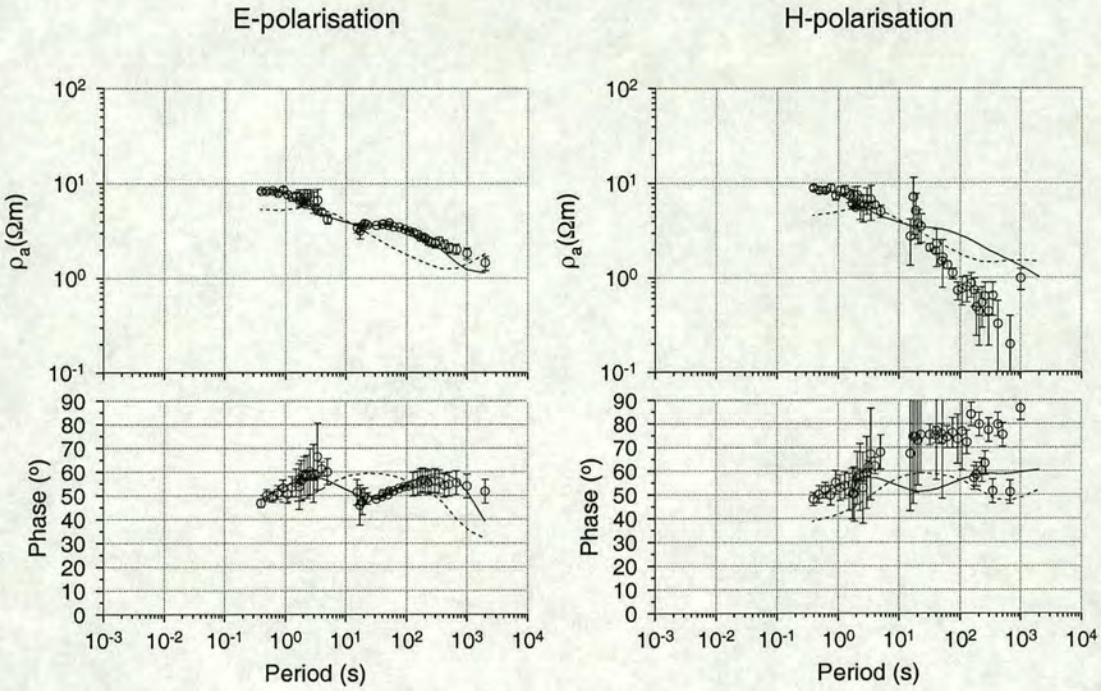

Figure 7.23. The fit of *L1* and the MT model to the MT data from site 1. The solid line represents the forward response of the MT model and the dotted line is that of *L1*.

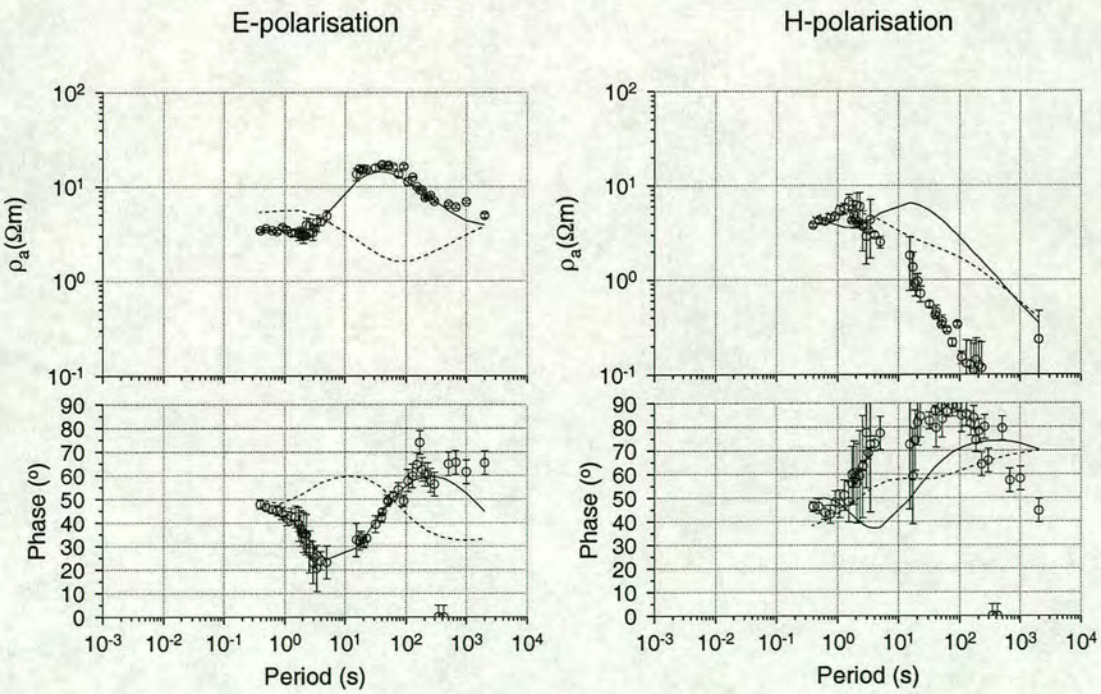

Figure 7.24. The fit of *L1* and the MT model to the MT data from site 6. The solid line represents the forward response of the MT model and the dotted line is that of *L1*.

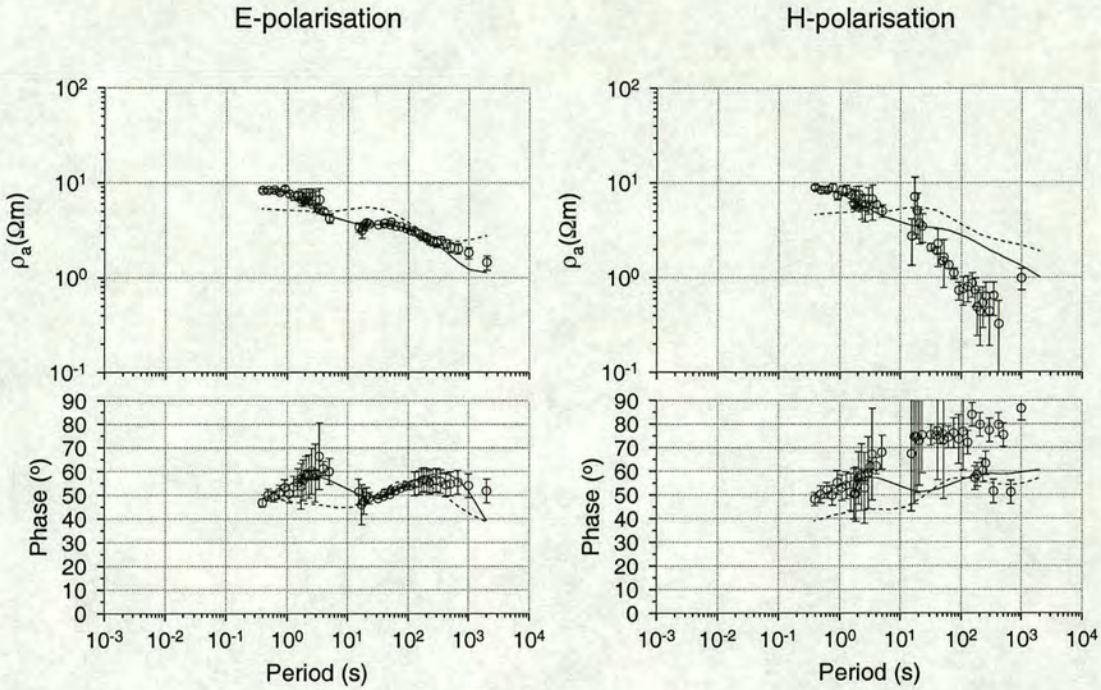

Figure 7.25. The fit of *L2* and the MT model to the MT data from site 1. The solid line represents the forward response of the MT model and the dotted line is that of *L2*.

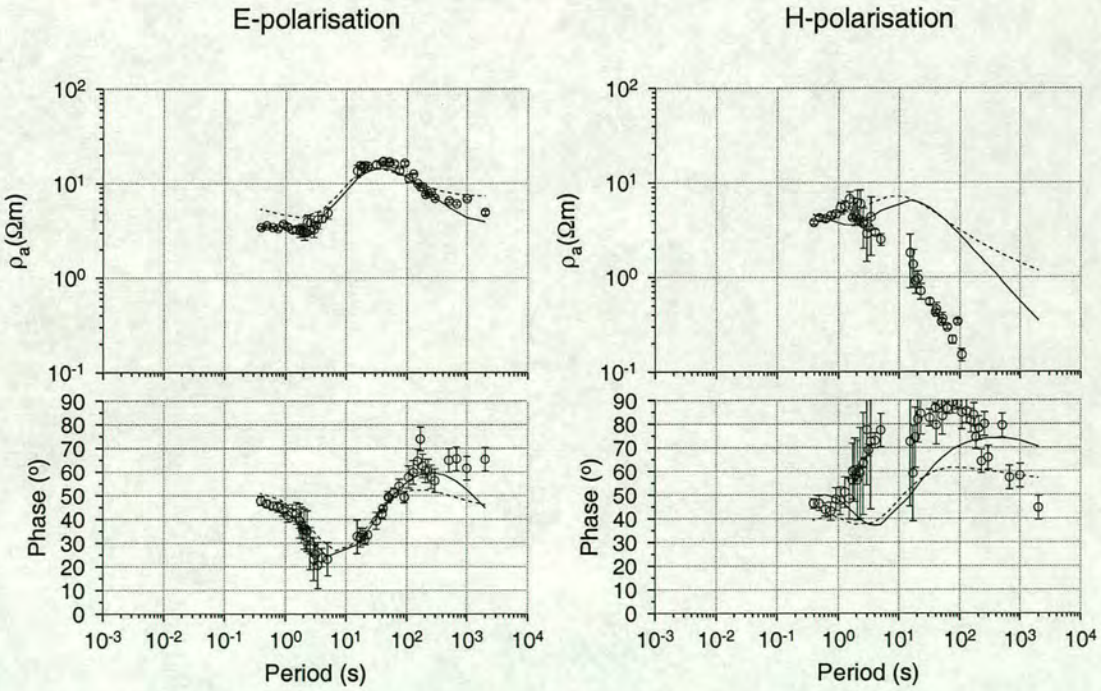

Figure 7.26. The fit of *L2* and the MT model to the MT data from site 6. The solid line represents the forward response of the MT model and the dotted line is that of *L2*.

A second model, *L2*, was constructed; this model was identical to *L1* except that it incorporated the resistive feature seen in the Upper Karoo on figure 7.22. Figures 7.25 and 7.26 show the fit of seismic model *L2* to the data at sites 1 and 6 respectively. The response of *L2* is shown as a dotted line and compared with the fit of the RRI model, the solid line. A comparison of figures 7.24 and 7.26 shows the improvement of fit to the E-polarisation data in the latter, achieved with *L2*. The improvement at site 1 is not so dramatic and can only be seen in the comparison of the fit to the E-polarisation phase between figures 7.23 and 7.25. The resistive feature improving the fit at site 6 is not present beneath sites 1 and 2 and therefore its introduction makes a much smaller difference to the improvement in fit of *L2* to the data. The improvement in fit to the E-polarisation data of *L2* over *L1* is replicated at all the sites underlain by the resistive body introduced. While the fit of *L2* to the E-polarisation data is an improvement, the actual misfit of the model, 18.66, is worse than that of *L1*. The misfit consists of an rms misfit of 36.65 and 4.09 to the H-polarisation magnitude and phase data and 8.39 and 5.85 to the E-polarisation magnitude and phase. The considerable improvement in the fit to the E-polarisation data is outweighed by the worsening of the fit to the H-polarisation; this is due to the increased misfit of *L2* over *L1* for the longer period apparent resistivity data.

It again seems that the two data polarisations cannot be simultaneously modelled. The steadily dropping apparent resistivity seen at all the basin sites for the H-polarisation mode and the resistivity-depth section resulting from the inversion of just the data from that mode in figure 7.12 indicate that a good fit would only be obtained with a low resistivity to approximately 10 km depth, the approximate penetration limit of the data. This is similar to the model first described in this section which failed to fit the trend of the E-polarisation data. There is an obvious choice here of which mode to fit and both the RRI algorithm and Losecke *et al.* (1988) choose to fit the E-polarisation. This may be because the greater penetration of the E-polarisation mode gives the resistivity curves more structure as seen in, for instance, figure 7.24. Here the H-polarisation curve encounters extremely low resistivities and tails off at long periods and the E-polarisation curve shows a distinct rise then fall. Fitting the E-polarisation data preferentially would appear to give a lower overall misfit to the data than fitting the H-polarisation data.

To fit the data accurately would require the introduction of variability within the layering defined by the seismic data; this has already been shown by the inclusion of a resistor within the Upper Karoo layer in order to improve the fit to the E-polarisation data. To further improve the fit, variations within the other layers must also be introduced; for instance, the data indicate that the Post Karoo cover requires an increase in resistivity towards the north. This can also be seen in figure 7.22, and in the model of Losecke *et al.* (1988) plotted in figure 2.8. We do not introduce such a feature since the aim here is not to produce a forward model which fits all of the MT data accurately; this has already been done by Losecke *et al.*. Rather, the aim is to show that the structure of the seismic model alone cannot fit the MT data without the addition of extra structure such as the resistor in the Upper Karoo for which there is no support from the seismic data. Attempts were made to achieve a better fit to the MT data than that given by *L2* but it proved impossible to improve the fit of the seismic model to the data significantly without resorting to incorporating all the features of the RRI model.

In summary, what Losecke *et al.* and the RRI inversion did was to fit preferentially the features that were required by the E-polarisation mode. This section shows again that, although the main one of these features, the resistor within the Upper Karoo layer, has no expression in the seismic data, it is required

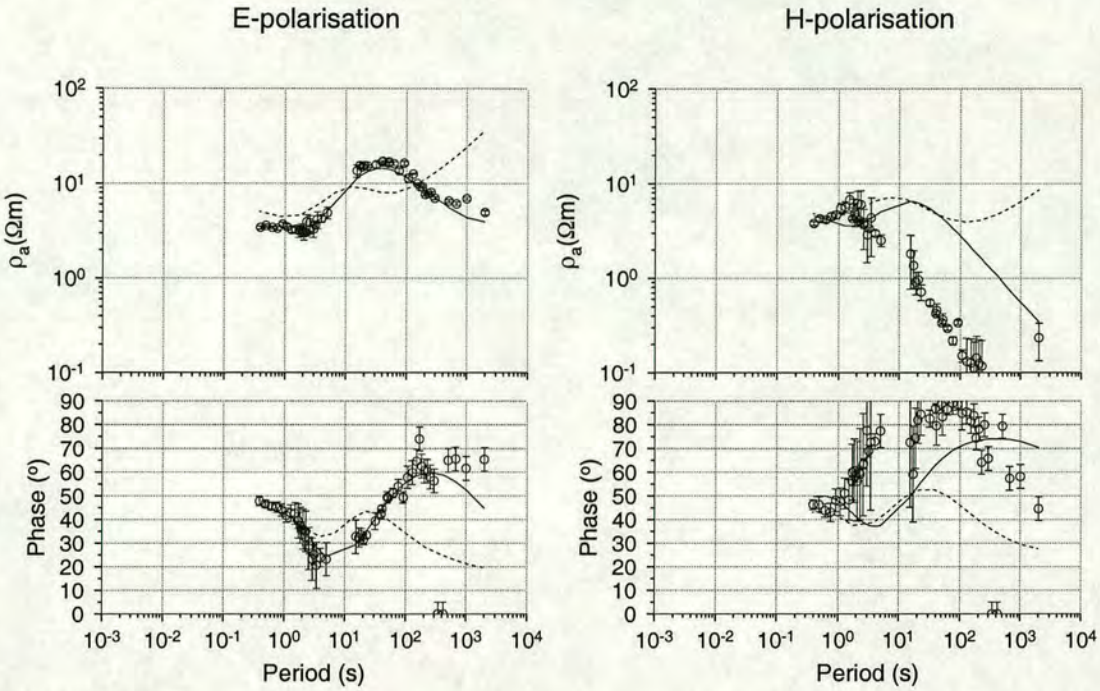

Figure 7.27. The fit of *L3* and the MT model to the MT data from site 6. The solid line represents the forward response of the MT model and the dotted line is that of *L3*.

to model the E-polarisation MT data. The findings of this section do not imply that the seismic model and MT model are incompatible; what they do say is that the MT data requires variability of resistivity within the seismic layering due to features with no seismic expression.

To assess the sensitivity of the MT data to the basement resistivity below 11 km a model, *L3*, was constructed identical to *L2* but increasing the basement resistivity to 1000 Ωm, the same as on the escarpment. Model *L3* had an rms of 23.08, with a misfit of 18.97 and 7.62 to the E-polarisation magnitude and phase data, and 40.86 and 6.61 to the H-polarisation data. The fit of the model to the data from site 6 is shown in figure 7.27; both modes are affected by the increased resistivity at depth, the E-polarisation from approximately 20 s and the H-polarisation from approximately 100 s. For the sites to the north, as the depth to the seismic basement increases the effect seen in the H-polarisation response becomes smaller. Increasing the basement resistivity causes a smaller relative increase in misfit to the H-polarisation data than to the E-polarisation data because fewer periods are affected due to the former's lower penetration depths. It can be concluded that, in the south of the basin, both modes are sensitive to the resistivity of the seismic basement, while only the E-polarisation mode remains sensitive to it in the north. Therefore the low values of basement resistivity detected in the RRI models and that of Losecke *et al.* are definitely required, and the seismic impedance contrast at the basement interface is not coupled with a resistivity contrast.

7.5 Summary

When modelling the BGR MT data from the Lower Zambezi basin, Losecke *et al.* (1988) used pre-existing gravity data (Zhou, 1988) and aeromagnetic data (Bosum and Geipel, 1988) and attempted to produce an interpretation of the MT model consistent with all three. This proved very difficult. More than one hypothesis could explain both the structure of the MT model and the two magnetic horizons revealed by the aeromagnetic data; these hypotheses were indistinguishable with the data available. Later problems were also encountered by Whaler and Zengeni (1993) in their efforts to compare the resistivity structures of the Lower Zambezi and Mana Pools basins.

The acquisition of seismic data (Hiller and Buttkus, 1996) by Mobil from both basins has helped to remove some of the ambiguity in the interpretation of the resistivity model of the Lower Zambezi basin proposed by Losecke *et al.* (1988) and reproduced in figure 2.8. The zone terminology of Losecke *et al.* will be used throughout this discussion. With the aid of the seismic data, Losecke *et al.*'s three zone model can be interpreted as a conductive non-metamorphic sedimentary layer, zone 1, overlying a resistive layer of consolidated sediments and intercalated basalt sills, zone 2. Beneath this is an extremely good conductor with resistivities as low as 0.2 Ωm extending into the seismic basement, zone 3. The seismic data also affect the interpretation of the aeromagnetic data horizons. The upper magnetic horizon at 2 km depth marks the transition from a non-magnetic cover layer to a region containing magnetic minerals (Bosum and Geipel, 1988). This can be interpreted as the transition to a region with magnetic layers within the sediments which is consistent with the hypothesis of a sedimentary layer containing intercalated basalt sills (Bosum and Geipel, 1988). The lower magnetic horizon at 10 km depth is still problematical. It lies close to the basement interface at 11.6 km (Hiller and Buttkus, 1996) and Losecke *et al.* give three possibilities for its interpretation. It may represent: a change in magnetisation at the sediment-basement interface, a change in magnetisation internal to the sedimentary layer, or the Curie surface. These three hypotheses are still indistinguishable but, unless the first hypothesis is correct, the magnetic data cannot see the sediment-basement interface.

Losecke *et al.* (1988) obtained their resistivity model through a combination of one-dimensional inverse modelling and two-dimensional forward modelling techniques. In this chapter, the MT data from one of the BGR profiles were modelled using the minimum structure RRI algorithm of Smith and Booker (1991) to assess whether all the structure present in the model of Losecke *et al.* is actually required to fit the data. Using the information from Hiller and Buttkus's interpretation of the seismic data, the RRI model incorporated an escarpment fault between sites 7 and 8. Its location is not definite and was fixed arbitrarily, midway between these two sites and extended to a depth of 10 km, approximately the estimated depth of the basin (Hiller and Buttkus, 1996). The apparent resistivity data from site 8 were not included in the inversion; the curves from this site were judged to be static shifted due to the extremely high surface resistivity. The model curves predicted both by Losecke *et al.* and here using the RRI algorithm are approximately frequency-independent shifts of the data curves and support this assumption. These two steps were taken to overcome the problem of fitting the H-polarisation data between sites 7 and 8. The rapid change in resistivity between the basin and the craton causes the inversion process to fail due to the difficulty in fitting smoothly the rapid jump in the H-polarisation response between these two sites. The resistivity-depth model obtained with RRI is shown in figure 7.16 and has an rms misfit to the data of 1.15. It is broadly in agreement with the model of Losecke *et al.*

in figure 2.8. All three of the latter's resistive zones are present in the former although less distinct, due to smoothing and discrimination against resistivity jumps at the zone boundaries. Spatially, the agreement between the two models is very good; the upper conductor, zone 1 in Losecke *et al.*'s model is slightly indistinct and more difficult to identify in the northern section of the basin but there is a good agreement on the location of the resistive zone 2 between the two models. This resistive zone tapers and dies out to the north and is not present north of site 3; its resistivity is much lower in the RRI model with a maximum of approximately 100 Ωm, compared with 3000 Ωm in Losecke *et al.*'s model. There is again excellent agreement between the two models on both the position and resistivity of the conductor beneath zone 2. This region extends close to the surface in the northern part of the profile and has a minimum resistivity of approximately 0.5 Ωm; its lower boundary is unresolved. The resistivity-structure of the RRI model is also found to be independent of the modelling assumptions of Losecke *et al.*, the northern escarpment in Mozambique is too far from the MT sites to have an effect on the model obtained from the data in this period range.

A quantitative comparison of the two models of the resistivity structure in the Lower Zambezi basin is not possible, as Losecke *et al.* provided no quantitative information on the misfit of their model to the data. Plots comparing the response of the two models to the data suggest that they are comparable and fit the data equally well; they also appear to misfit certain sections of the data in the same way. Most noticeably, both models preferentially fit the E-polarisation data at sites within the basin; as seen in figures 7.17 to 7.20. This is probably because of both the greater penetration depth of the E-polarisation mode and the greater degree of structure in the E-polarisation curves. This leads to a misfit to the H-polarisation data at long periods, corresponding to a depth of approximately 10 km. At most sites, this is shallower than the basement interface and means that the basement structure below 10 km is resolved by E-polarisation data only, accounting for the model's lack of structure at depth. Inversions of the E-polarisation and H-polarisation data alone, shown in figures 7.11 and 7.12, indicate the structure required by the two modes to be incompatible in the first 10 km. The descending apparent resistivity curves of the H-polarisation mode require a very good conductor while a corresponding upturn in the E-polarisation curves requires a resistive layer in order for a good fit to be achieved.

Some of the features of the resistivity model of figure 7.16 need further comment. The most striking feature is the extremely low resistivity body at depths greater than the seismic basement. The results from forward modelling the seismic structure confirm that the top of the seismic basement is resolved by the E-polarisation data. This demonstrates that the extremely low resistivities of zone 3 are genuine and that this conductor is within basement material. Losecke *et al.* (1988) claim that this region extends to depths of greater than 30 km; this is plausible but may be stretching the resolution limit of the data. The estimates of a single skin depth shown in figure 7.16, as has been discussed, are on the conservative side but suggest that the quantity of data resolving the structure below 20 km within the basin is very small, as low as 6 data points for sites 1 to 3. It therefore seems reasonable to suggest that the basin structure below 20 km cannot be relied upon. The craton region south of site 8 is extremely resistive, comparable to the value of 2000 Ωm used to model the escarpment north of the Mana Pools basin and emphasises how low the resistivity of the craton south of Mana Pools is. These differences between the two basins may support the suggestion of Orpen *et al.* (1989) that they are of different tectonic origin, the Lower Zambezi being a pull-apart basin and Mana Pools a half-graben, the latter suggestion is supported by the modelling of chapter 6. The resistivity contrast between the two escarpments bordering the Mana

Pools basin may be due to its half-graben nature. The depocentre is offset to the north, adjacent to the more resistive escarpment (Orpen *et al.*, 1989), while the resistivity of the southern escarpment may have been lowered through tectonic disturbance assuming, as Orpen *et al.* do, that it acted as a hinge for the graben. This cannot be compared to the situation in the Lower Zambezi basin without a constraint on the resistivity of the escarpment to the north. A final comment on the resistivity model of figure 7.16 is that, while the resistive zone 2 is incompatible with modelling the H-polarisation data, it appears to be required by RRI in order to fit the E-polarisation and is retained throughout smoothing. It can therefore be concluded that this resistor in the sedimentary fill is a real feature and required to model the MT data.

Inversions of the data were attempted while employing breaks in the roughness matrix to simulate the two magnetic horizons. Neither modelling the magnetic horizons singly or together affected the data. The resistivity models obtained did not show significantly better fits to the data nor was there any evidence of the presence of resistivity discontinuities within the resistivity-depth section. Clearly, the changes in magnetisation resulting in the two magnetic horizons are not mirrored by a change in resistivity. This does not lead to a problem of interpretation for the upper magnetic horizon. If resistive zone 2 contains sediments with intercalated basalt sills but lies at a slightly greater depth than the upper magnetic horizon, then it seems reasonable that the basalt may also be present higher up, at the magnetic horizon. If the basalt is initially thin or adequately conductive then no increase in resistivity need be seen until more massive units are encountered at the depth of zone 2. This would mean that the start of resistive zone 2 and the upper magnetic horizon are not coincident. This is an attractive hypothesis and plausible within the constraints of the data. It would also explain why the resistivity model is unaffected by the imposition of a smoothing discontinuity at the depth of the upper magnetic horizon. A discontinuity placed at the depth of the lower magnetic horizon also leaves the resistivity model unaffected. This horizon lies close to the basement depth defined by the seismic data and may correspond to a change in magnetisation across that interface. It can be seen from the resistivity model that the resistivity does not vary between the base of the sediments and the seismic basement, making it reasonable that a break in the roughness matrix at this depth would not affect the model. However, the possibilities that the lower magnetic horizon could also represent the Curie surface or a change in magnetisation internal to a layer (Bosum and Geipel, 1988; Losecke *et al.*, 1988) are also plausible and the modelling results cannot distinguish between them.

Efforts to model the Mana Pools MT data using boundaries defined by the seismic structure were very successful. Retaining the lithological identifications of Hiller and Buttkus (1996), in spite of their uncertainties, a good fit to the MT data could be achieved with a model consisting of a 10 Ωm Post Karoo layer overlying a 5 Ωm Upper Karoo feature with a 10 Ωm Lower Karoo horizon and a 20 Ωm seismic basement beneath. The craton region to the south had a fixed resistivity of 100 Ωm and that to the north 2000 Ωm; the rms misfit of this model, *M1*, is 6.30, comparable to the 3.22 of the RRI model prior to the start of robust iteration. The low resistivity of the craton region to the south was examined more closely; the higher than average resistivities at depths of 4 to 7 km beneath the sites from 7 southward to the escarpment suggested that the resistivity contrast across the boundary was being smoothed and that the resistivity of the craton could be higher. The difficulty with implementing this is that, at long periods, the separation of the E- and H-polarisation apparent resistivity curves decreases to the south due to a rise in the H-polarisation apparent resistivity. Increasing the resistivity

of the southern craton leads to an increased charge build up on the fault causing the model response to underestimate the H-polarisation apparent resistivity. This problem can be overcome by placing a 20 Ωm extension to the Post Karoo layer at the surface, beneath site 10, and extending down to a depth of 1500 m. This not only produces a model, *M2*, with a better fit to the data from site 10 but also a lower rms misfit of 5.98, mainly due to an improvement in the fit to the longer period H-polarisation data. The low resistivity region at site 10 acts as a channel, giving the currents trapped within the valley a route to escape and lowering the amount of charge built up on the escarpment fault. The problem with this model is that it is hard to see how such a continuous layer could exist. It would have to extend from the basin southwards through an escarpment with nearly 1 km topographic relief and onto the craton to the south. It is also difficult to find any evidence for this low resistivity layer beneath site 11. Another model identical to *M2* but with an added 100 Ωm block bounding the Post Karoo layer to the south, *M3*, gave a misfit to the data of 6.20. Bounding the conductive Post Karoo layer in this way is in better agreement with the results of the RRI modelling and, providing some degree of static shift is assumed, the data from site 11. The misfits of models *M1* and *M3* are similar but the latter has a better fit to the data from site 10 while the former has a better fit to the data from the sites within the basin, due primarily to a closer fit to the longer period H-polarisation data. The two models are difficult to separate but the RRI model shows that a similar fit to that of *M3* can be achieved for the data from site 10 with a southern escarpment resistivity of only 100 Ωm, equal to that employed by *M1*. Because of this and the lack of evidence for the continuity of a conductive layer far into the craton, the resistivity structure of model *M1* with a 100 Ωm southern craton is preferred. This does, however, present a marked contrast to the values of 10000 - 100000 Ωm obtained by Blohm *et al.* (1977) from resistivity soundings on the Zimbabwe craton.

A better fit to the Mana Pools MT data could be achieved but this would mean introducing internal layer resistivity variations which were without expression in the seismic data. The misfit of the model *M1* was sufficiently low that it offered a valid but simpler interpretation of the data than the RRI model. The data require the Post Karoo layer; models where the Upper Karoo layer of 5 Ωm extended to the surface misfit the data to a high degree at high frequencies. The corresponding region of the RRI model covering the first 1500 m is very convoluted, showing a number of thin conductive and resistive layers which are not consistent between sites; this may be due to overfitting of small data variations at high frequencies. The seismic model shows that this region can be modelled as a single 10 Ωm layer but the nature of the RRI model makes it difficult to tell whether it is really a single unit. Beneath the Post Karoo layer, the Mana Pools conductor can be modelled as a 5 Ωm Upper Karoo layer extending to 5.5 km depth, with basement lows adjacent to the north and south faulted boundaries, the deeper one in the north. This unit is made up of a series of grits, sandstones and arkose units (Hiller and Buttkus, 1996) for which such a resistivity is not unreasonable given the correct physical conditions. The Lower Karoo layer below, constituting more sandstone and arenite rocks (Hiller and Buttkus, 1996; MOBIL, 1993) is indistinguishable from the seismic basement of 20 Ωm below. This is an extremely low resistivity for basement rock and very different from the cratonic material to the north which is modelled with a resistivity of 2000 Ωm. This implies either a change in material beneath the basin compared to the craton or some degree of tectonic alteration of the basement due to extensive fracturing and/or chemical alteration. That some degree of faulting of the basement beneath the Mana Pools basin has occurred is known by the presence of a faulted basement high separating the two basin depocentres (Hiller and Buttkus, 1996).

Fitting the Lower Zambezi MT data using only the structure of the seismic model proved far more difficult and no reasonable fit was achieved. As was found while modelling the MT data using RRI, it is only possible to accurately fit one data polarisation at a time. Attempts to model both polarisations using the seismic structure failed and the lowest rms misfit achieved was 16.32, considerably higher than the 4.18 achieved by RRI. The main discrepancy between the two modes is the resistivity of the Upper Karoo layer. The E-polarisation curves require a resistor in the Upper Karoo, as seen in both the model of Losecke *et al.* (1988) and the RRI model in § 7.3. This feature conflicts with the requirements of the H-polarisation data and there is no evidence for it in the seismic interpretation of Hiller and Buttkus (1996). The difference in the two modes for the Upper Karoo layer suggests a layer exhibiting macroscopic anisotropy such as that described by Kellett *et al.* (1992). A quantitative analysis of this is not possible as the full impedance tensors are not available but the data curves support such a theory. Azimuthal anisotropy can be modelled by a layer of repeated conductive and resistive vertical dykes (Kellett *et al.*, 1992). If these dykes strike north-south, then the H-polarisation response would be dominated by the conducting sediments separating them, giving a low overall resistivity. The E-polarisation mode would encounter alternating good and bad conducting layers and would overall be more resistive. This interpretation is supported by the separation also seen in the two phase curves (Kellett *et al.*, 1992). For a macro anisotropic model the phase shift should persist at nearby sites (K. Bahr, pers. comm., 1998). Only data from the nine sites along the profile are available but the phase shift between the two modes is observed at all of the sites within the basin. This is an attractive hypothesis, and it agrees well with Losecke *et al.*'s interpretation of zone 2 as a layer of sediments and intercalated sills. If the intercalations are thin dykes instead of sills then this can also explain why they are not seen on the seismic data. Failure to fit the MT data within the limitations of the seismic structure does not imply that the seismic model is incompatible with the MT data, just that extra features, not present in the seismic data, are required. An anisotropic Upper Karoo layer could conveniently explain the discrepancy. The structure resolved by the seismic data is closer to the H-polarisation resistivity structure, which is unaffected by intercalated dykes, but the MT inversions are dominated by the E-polarisation which are affected.

Notwithstanding the failure to adequately model the Lower Zambezi MT data, the seismic models can still be useful in comparing the resistivity structure between the two basins. There are considerable similarities; both have a near surface Post Karoo layer of similar and quite variable resistivity. This is probably due to natural variability in the resistivity of the near surface more than scatter in the data, although the latter may be a contributory factor. The depth extent of this layer is similar in both cases, between 1 and 2 km. Below this, the Upper Karoo layer in both basins contains a good conductor of similar resistivity. The resistive feature present in the upper portion of the southern half of the Lower Zambezi basin which is not seen in Mana Pools may be a feature of anisotropy within the Upper Karoo due to intercalated basalt dykes. This layer extends to depths of 10 km in the Lower Zambezi and 5.5 km in Mana Pools and corresponds approximately to the magnetic layer between the two magnetic horizons in each basin. Clearly, both basins could contain intercalated basalts but the Mana Pools basin may not contain units massive enough to affect the resistivity measurements. The conductor within the Mana Pools basin can be confined to the Upper Karoo while that in the deeper Lower Zambezi basin extends into the seismic basement. Due to its thinness and depth, the Lower Karoo layer is not resolved as a separate layer in either basin. The Mana Pools basin appears to be underlain by extremely low resistivity material. This may be due to alteration of both the basement rocks and the cratonic material

to the south of the Mana Pools basin, which also has a surprisingly low resistivity. The cratonic material to the north of the Mana Pools basin is more resistive confirming that it could have acted as the foot wall during formation of the half-graben basin. The high resistivity of the craton to the south of the Lower Zambezi basin may indicate that it also played no part in the tectonic processes by which the basin was formed.

Chapter 8

Conclusions and Suggestions for Further Work

This thesis has taken both new LMT and existing AMT data from the Mana Pools basin and combined them to generate for the first time a two-dimensional model of its resistivity structure. The model agrees closely with the structural interpretation of the basin, firmly established by reflection seismic data (Hiller and Buttkus, 1996). The resistivity section shows a half graben basin with a northward dipping basement and a depocentre of approximately 7 km, adjacent to the northern margin. The layering observed within the basin by Whaler and Zengeni (1993) is not observed here, probably because of the use of a minimum structure two-dimensional technique rather than the stitched one-dimensional models they used. The division by resistivity of the sedimentary fill of the Mana Pools basin into three layers by Whaler and Zengeni, on the evidence of the new model, is not justified by the data.

There is a marked contrast in the modelled resistivity of the cratons bounding the Mana Pools basin to the north and south. The northern block, in Zambia, lies outside the survey area and there are no data for it. It is expected to be resistive, however, and such a feature is required to model the increasing separation of the apparent resistivity curves at long periods as the basin is traversed from south to north. All of the models derived in chapter 6 struggle to match this separation but indicate that a resistivity of the order of 2000 Ωm is required for the northern craton. The southern craton has a much lower resistivity of 100 Ωm, which may be a feature of the modelling strategy used. The tensor decomposition results of chapter 5 show that the LMT data from sites 10 and 11 have significantly different regional azimuths to the majority of the rest of the data. Treating the data as two-dimensional involves a rotation of the LMT data from these two sites to a regional azimuth which disagrees with that of the Groom and Bailey (1989) decomposition. This reduces the anisotropy in apparent resistivity at site 11 and will affect the resistivity of this region of the model; certainly some uncertainty is associated with this area. Also apparent from the data curves at site 11 is a static shift effect. This necessitates the omission of the apparent resistivity data from modelling; the resistivity of the southern craton is determined by the phase data and the data from adjacent sites. The separation of site 11 from site 10 is approximately 25 km and the smoothing inherent in the modelling strategy may also have reduced its resistivity. All of these factors may be important, but the data curves for site 11 and the lack of

separation of the apparent resistivity curves at the adjacent sites suggest the resistivity of the southern craton is considerably lower than that of the northern. This may indicate disruption of the southern escarpment during basin formation and supports the suggestion that the southern boundary acted as a hinged flank (Orpen *et al.*, 1989). Some disruption of this southern section of the basin is clearly shown by the warping of the basement in this region of the seismic model. While the Mzarabani fault, believed to bound the Mana Pools basin to the south (Orpen *et al.*, 1989), is seen in the resistivity section, it does not correspond to a major resistivity contrast. The sharp resistivity contrast at the basin's northern boundary indicates a fault, believed to splay off the Luangwa trough system (Orpen *et al.*, 1989).

The acquisition of new LMT data allows the resolution of the Mana Pools basement, previously at the penetration limit of the AMT data (Whaler and Zengeni, 1993). The basement is remarkably conductive at 20-30 Ωm, suggesting that it must be heavily fractured or tectonically altered. No zone of concentrated extremely low resistivity, as little as 0.2 Ωm, such as that in the Lower Zambezi basin (Losecke *et al.*, 1988) or the Damara belt (De Beer *et al.*, 1976, 1982a), is seen in the basement. Problems with the data, between periods of approximately 1 and 400 s, leave a gap in the models between 10 and 25 km at some sites. The findings from the ρ^+ algorithm (Parker and Booker, 1996) of chapter 6 indicate that the apparent resistivity data in this frequency range are downward biased. Their inclusion would place a conductive structure within the basement, similar to that seen in the Lower Zambezi basin, but due to their poor quality this cannot be justified although neither can it be ruled out. The use of the ρ^+ technique, as a measure of data consistency, was extremely useful and its use in such situations is strongly recommended.

The work in chapter 7 on the BGR data (Losecke *et al.*, 1988) from the Lower Zambezi basin is the first two-dimensional inverse model of the region. The findings support those of Losecke *et al.*, showing a three layer basin that is difficult to reconcile with the structure in the seismic models of Hiller and Buttkus (1996). Comparison of the two is made by calculating MT forward models from the seismic structure with layer resistivities determined from the MT resistivity sections. There is good agreement between the two techniques for the Mana Pools basin and their combination indicates that the conductive feature seen is contained within the Upper Karoo sedimentary layer. By contrast, the conductor in the Lower Zambezi basin extends to at least 20 km and a more resistive electrical basement is not detected. Correlation with the seismic structure shows that the Lower Zambezi conductor lies mainly within the seismic basement. Static shifting of the data on the southern craton is again seen, but even after this is taken into account a resistivity of the order of 10000 Ωm is obtained. This feature forms a major, near vertical resistivity discontinuity and supports the suggestion that the basin is bounded by the Mzarabani fault (Orpen *et al.*, 1989). The large resistivity change across the Mzarabani fault here is in contrast to the small difference in the Mana Pools basin where the southern craton has a much lower resistivity. A resistive feature is found within the sedimentary fill which is not seen in the seismic section, and the seismic basement at approximately 10 km depth does not represent a resistivity contrast. It is the resistive feature in the sediments that is the main difficulty in reconciling the seismic model of the basin with the MT resistivity model. The Upper Karoo layer where this feature is found has completely different responses in the E- and H-polarisations and both the MT model derived here and that of Losecke *et al.* have concentrated on the fit to the E-polarisation data. Macroscopic anisotropy is suggested as an explanation for the incompatibility between the two responses and the MT and seismic models. The consistent splitting of the E- and H-polarisation apparent resistivity and phase curves at

all sites within the basin could be modelled by an Upper Karoo layer containing intercalated northward striking basalt dykes (eg. Kellett *et al.*, 1992). It is also plausible that these dykes would not be detected by the seismic data and would not appear on the structural section. While the incorporation of the positions of two aeromagnetic horizons into the resistivity model found no corresponding changes in resistivity, they do approximately bound the Upper Karoo layer. The layer between these two horizons contains magnetic material (Bosum and Geipel, 1988), which also agrees with the presence of dykes in the sediments.

The resistivity section of the Lower Zambezi basin does not help in the determination of its origin. Orpen *et al.* (1989) suggested that it is a pull-apart structure and the new MT model neither contradicts nor supports this. A better comparison of the Lower Zambezi and Mana Pools basins than that utilising the layering of Whaler and Zengeni (1993) and Losecke *et al.* (1988) can be made using the lithological identifications of Hiller and Buttkus (1996). There are a number of similarities between the two basin's layering. Both have a variable resistivity Post Karoo layer to a depth of between 1 and 2 km which can be approximated by resistivities of 5 and 10 Ωm for the Lower Zambezi and Mana Pools basins respectively. Beneath this, the Upper Karoo sedimentary layer in each basin has a similar resistivity, 1 to 5 Ωm, and the thin Lower Karoo layer beneath is not resolved in either case. There are also differences between the basins. The Lower Zambezi basin is deeper at 11.6 km (Hiller and Buttkus, 1996) and its Upper Karoo layer contains a resistive feature which, it is suggested, is due to anisotropy caused by the intercalation of resistive basalt dykes within the sediments. The basements beneath the basins are also different. The Mana Pools basement is more resistive at 20-30 Ωm than the Lower Zambezi at 2 Ωm. The resistivity beneath the Mana Pools basin is extremely low for basement rock but does not represent a localised conductive zone; it may just be heavily fractured and deformed. Deformation of the seismic basement is apparent from the structural cross sections and the Mana Pools basin is known to lie at the junction of the Lower and Mid Zambezi rift systems. The resistivity of the basement beneath the Lower Zambezi basin is an order of magnitude lower and, unlike the Mana Pools dataset, the apparent resistivity curves continue to descend at long periods. The basement in this case appears to contain a localised conductor. The relationship of the conductor to the layering in the Lower Zambezi is similar to that in the Damara belt to the west with the conductor lying in the basement. The conductive structure seen in Mana Pools is quite different, being a feature just of the sedimentary fill. It is not clear therefore whether, and if so how, these two features are related and whether they form an eastward extension of the southwest African conductor through the Zambezi valley. It is easier to suggest a link between the Lower Zambezi conductor and the southwest African conductor as there are more similarities between them, but this presents the problem of explaining the conductor's absence beneath the Mana Pools basin. Excepting the region between approximately 10 and 25 km, where the presence of a conductive feature cannot be rejected, the 2-D model of the Mana Pools basin is resolved to a depth of 40-50 km. Even in the cratonic regions bordering the Damara belt, the conductor has not been detected below this depth. The results from a new MT dataset, recently acquired in the Damara belt by Dr. O. Ritter, will provide more information about the southwest African conductor and may help to answer some of these questions.

The main question remaining unanswered is the origin of these conductive features, but there is little possibility of answering this definitively until more information, including borehole logs and heat flow measurements, are taken from the area. The main possibilities for the origin of the feature in the

Damara belt and probably that beneath the Lower Zambezi basin are: a high heat flow anomaly, a fractured zone exploited by saline fluids, or a serpentinised ultramafic body emplaced by subduction or from the asthenosphere. For the first hypothesis, the lack of a basement conductor beneath the adjacent Mana Pools basin would imply a rapid change of heat flow characteristics between the two basins which seems unlikely due to their proximity. Fracturing of the basement is likely to be an important factor but there is evidence from the seismic structural interpretation of the Mana Pools basin that the basement is deformed and probably significantly fractured. The low resistivities measured support this but a localised conductor similar to that beneath the Lower Zambezi is not seen. This is difficult to explain, the Mana Pools basin lies at the intersection of two rift zones and it is unlikely to be less fractured at depth than the Lower Zambezi basin. It is also difficult to see why the fluid exploiting these fractures should be less saline beneath the Mana Pools basin than the Lower Zambezi basin. There are also difficulties with the third hypothesis such as the source of the large quantities of water required for the serpentinisation process (Van Zijl and De Beer, 1983). Of the three, the first hypothesis seems the least likely, there are problems with the other two but the probability of extensive fracturing at depth favours the simpler second explanation. While it will be difficult to answer the 'origin' question, more could still be gained from further MT work. The gap between the AMT and LMT data in the Mana Pools basin is a problem and it would be useful to fill it and confirm that a conductive feature is not seen in the corresponding depth region. This would be possible with a broad band MT survey using modern equipment with more sensitive magnetic sensors and a remote reference processing technique. The links between the Mana Pools and Lower Zambezi basins are unclear. There is no conductor seen beneath the Mana Pools basin. A joint MT and DC resistivity survey in the Chewore region separating the two basins would be useful to map the lateral extent of the Lower Zambezi conductor. While the topography of the escarpments bounding the Mana Pools basin make the location of MT sites impossible there, some kind of electrical data from these regions would be useful. DC resistivity data would be particularly valuable for constraining the resistivities of both the Zimbabwe and Zambian escarpment regions. The contrast in resistivity between these two may be important for understanding the evolution of the Mana Pools basin. Evidence of three-dimensionality was seen in the LMT data at sites 10 and 11 but no three-dimensional modelling was attempted. It was deemed not worthwhile because the data were collected along a two-dimensional profile and the fraction showing three-dimensional characteristics was very small. A full 3-D survey of the basin would be extremely useful, in particular for a better understanding of its relation to the Chewore block and to trace the behaviour of the sedimentary conductor in this part of the basin. This would go a long way to answering the question of whether the conductor in the Mana Pools basin is related to that beneath the Lower Zambezi. Logistically, due to the lack of roads and danger of animals, it is a near impossibility. A more realistic target may be to attempt some complete north-south profiles of both basins. Currently we have no data from the Zambian side of the border.

Finally, two other areas of interest are directly apparent from this work. A quantitative investigation of the anisotropy in the Lower Zambezi basin would be useful to test the hypothesis presented here. This could be done if full tensor information from the Lower Zambezi basin was available. It is also a limitation of current two-dimensional modelling techniques that they cannot incorporate anisotropy, instead preferentially fitting one data polarisation. If this feature could be incorporated it would be a great aid to the modelling of datasets such as that from the Lower Zambezi basin. Secondly, a better method for the assessment of the sensitivity of the model features would be welcomed. This again could be included within a modelling routine. Plans for the latest release of RRI include the passing of

information on the performance of the inversion grid to the user. The inclusion of parameter resolution information would also be a useful step to a better sensitivity analysis. These features may be difficult to incorporate into the software currently available, but their existence would have significantly contributed to this study of the Mana Pools and Lower Zambezi basins.

Appendix A

The RRI Misfit Calculation

Normalised Residuals

RRI determines the model misfit by first determining the normalised model residuals. For the magnitude data,

$$e_k = \frac{\ln d_k - \ln m_k}{\ln w_k} \qquad k = 1, t \tag{1.1}$$

where d_k is an individual observed data point, m_k is the model response at the same discrete frequency, t is the total number of observed data and w_k is the uncertainty associated with the data point. The uncertainty can be specified either as an absolute value or relative to the observation itself; ln is the natural logarithm.

For the phase data,

$$e_k = \frac{d_k - m_k}{w_k} \qquad k = 1, t \tag{1.2}$$

where the terms have the same meaning as in equation 1.1 and the data and calculated model response are in radians.

The rms Misfit by Mode by Site (S)

The rms misfit by mode for each site (S) where the E and H-polarisations each comprise a phase and magnitude mode, is given by,

$$S_{(i,j)} = \sqrt{\frac{\sum_{i=1}^{N_{(i,j)}} e_k^2}{N_{(i,j)}}} \tag{1.3}$$

where e_k are the normalised magnitude or phase residuals for either the E or H-polarisation data and $N_{(i,j)}$ is the number of observed data at site i for mode j.

The rms Misfit by Mode (M)

The rms misfit by mode (M) is given by,

$$M_j = \sqrt{\frac{\sum_{i=1}^{n}(S^2_{(i,j)} \times N_{(i,j)})}{\sum_{i=1}^{n} N_{(i,j)}}} \tag{1.4}$$

where n is the number of sites, $S_{(i,j)}$ is the mode misfit and $N_{(i,j)}$ the number of data at site i for mode j.

Mean Squared Misfit by Site (T)

The mean squared misfit by site (T) is given by,

$$T_i = \frac{\sum_{j=1}^{m}(S^2_{(i,j)} \times N_{(i,j)})}{\sum_{j=1}^{m} N_{(i,j)}} \tag{1.5}$$

where m is the total number of modes and is equal to four. $S_{(i,j)}$ is the misfit of mode j at site i and $N_{(i,j)}$ is the number of observed data points for mode j at site i.

The Model RMS (R)

The root mean squared error of the model is calculated as,

$$R = \sqrt{\frac{\sum_{i=1}^{n}\left(T_i \times 2\left[\sum_{j=1}^{m} N_{(i,j)}\right]\right)}{\sum_{i=1}^{n}\left[2\left[\sum_{j=1}^{m} N_{(i,j)}\right]\right]}} \tag{1.6}$$

where T_i is the mean squared misfit for each site, n is the number of sites and m the number of modes. The total number of data $N_{(i,j)}$ is doubled to give the sum of the number of data points plus the number of model responses obtained.

Bibliography

Bahr, K. (1988). Interpretation of the magnetotelluric impedance tensor: regional induction and local telluric distortion. *J. Geophys.*, **62**, 119–127.

Bahr, K. (1991). Geological noise in magnetotelluric data: a classification of distortion types. *Phys. Earth Planet. Interiors*, **66**, 24–38.

Barber, B. (1994). *The Geology and Coal Potential of the Karoo Supergroup and Younger Rocks in Zimbabwe*. Ph.D. thesis, University of Zimbabwe.

Berdichevski, M. N. (1960). Principles of the theory of magnetotelluric profiling. *Applied Geophys.*, **28**.

Blohm, E. K., Worzyk, P., and Scriba, H. (1977). Geoelectrical deep soundings in southern Africa using the Cabora Bassa power line. *J. Geophys.*, **43**, 665–679.

Booker, J. R. (1997). *Documentation for rapid relaxation inverse (RRI 3.1)*. Geophysics, Box 351650, University of Washington, Seattle, WA, 98195, USA.

Bostick, F. X. and Smith, H. W. (1962). Investigation of large-scale inhomogeneities in the Earth by the magnetotelluric method. In K. Vozoff, editor, *Magnetotelluric Methods*, number 5 in Geophysics Reprints, pages 148–155. Society of Exploration Geophysicists.

Bosum, W. (1985). Interpretation of the aeromagnetic survey of the Zambezi valley, Zimbabwe. Technical Report 97681, Bundesanstalt Für Geowissenschaften und Rohstoffe, Hanover.

Bosum, W. and Geipel, H. (1988). Reinterpretation of an aeromagnetic profile in the Zambezi valley of Zimbabwe on the basis of magnetotelluric and gravimetric data. Technical report, Bundesanstalt Für Geowissenschaften und Rohstoffe, Hanover.

Brewitt-Taylor, C. R. and Weaver, J. T. (1976). On the finite difference solution of two-dimensional induction problems. *Geophys. J. R. astr. Soc.*, **47**, 375–396.

Bryan, W. B. (1986). Tectonic controls on initial continental rifting and evolution of young ocean basins - a planetary perspective. *Tectonophys.*, **132**, 103–115.

Burke, K. and Dewey, J. F. (1973). Plume generated triple junctions: key indications in applying plate tectonics to old rocks. *J. Geol*, **81**, 406–433.

Burke, K., Dewey, J. F., and Kidd, W. S. F. (1977). World distribution of sutures - the sites of former oceans. *Tectonophys.*, **40**, 69–99.

Cagniard, L. (1953). Basic theory of the magneto-telluric method of geophysical prospecting. *Geophys.*, **18**, 605–635.

Cannon, R. T., Simiyusiambi, W. M. N., and Karanja, F. M. (1981). The Proto-Indian ocean and a probable Palaeozoic/Mesozoic triradial rift system in Africa. *Earth and Planetary Science Letters*, **52**, 419–426.

Cantwell, T. (1960). *Detection and Analysis of Low-Frequency Magnetotelluric Signals*. Ph.D. thesis, MIT.

Chakiridi, R., Chouteau, M., and Mareschal, M. (1992). A simple technique for analysing and partly removing galvanic distortion from the magnetotelluric impedance tensor: Application to Abitibi and Kapuskasing data (Canada). *Geophys. J. Int.*, **108**, 917–929.

Chant, I. J. and Hastie, L. M. (1992). Time-frequency analysis of magnetotelluric data. *Geophys. J. Int.*, **111**(2), 399–413.

Chave, A. D. and Smith, J. T. (1994). On electric and magnetic galvanic distortion tensor decompositions. *J. Geophys. Res.*, **199**(B3), 4669–4682.

Chave, A. D. and Thomson, D. J. (1989). Some comments on magnetotelluric response function estimation. *J. Geophys. Res.*, **94**(B10), 14215–14225.

Coggon, J. H. (1971). Electromagnetic and electrical modelling by the finite element method. *Geophys.*, **36**, 132–155.

Constable, S. C., Parker, R. L., and Constable, C. G. (1987). Occam's inversion: a practical algorithm for generating smooth models from electromagnetic sounding data. *Geophys.*, **52**(3), 289–300.

Coward, M. P. and Daly, M. C. (1984). Crustal lineaments and shear zones in Africa: their relationship to plate movements. *Precamb. Res.*, **24**, 27–45.

Daly, M. C. (1986). Crustal shear zones and thrust belts: their geometry and continuity in central Africa. *Phil. Trans. Royal Soc.*, **A317**, 111–128.

Daly, M. C., Chorowicz, J., and Fairhead, J. D. (1987). The reactivation of steep basement shear-zones and their influence on rift basins in Africa. In G. Williams and M. A. Cooper, editors, *Inversion Tectonics*, number 29 in Geological Society Special Publications. Blackwell, Oxford.

Dawes, G. J. K. (1984). Short period automatic magnetotelluric (SPAM) system. EEC Report Series, Final Report, Contract No. EG-A2-031-UK.

De Beer, J. H., Gough, D. I., and Van Zijl, J. S. V. (1975). An electrical conductivity anomaly and rifting in southern Africa. *Nature*, **255**, 678–680.

De Beer, J. H., Van Zijl, J. S. V., Huyssen, R. M. J., Hugo, P. L. V., Joubert, S. J., and Meyer, R. (1976). A magnetometer array study in South - West Africa, Botswana and Rhodesia. *Geophys. J. R. astr. Soc.*, **45**, 1–17.

De Beer, J. H., Huyssen, R. M. J., Joubert, S. J., and Van Zijl, J. S. V. (1982a). Magnetometer array studies and deep Schlumberger soundings in the Damara orogenic belt, South West Africa. *Geophys. J. R. astr. Soc.*, **70**, 11–29.

De Beer, J. H., Van Zijl, J. S. V., and Gough, D. I. (1982b). The southern Cape conductive belt (South Africa): Its composition and tectonic significance. *Tectonophys.*, **83**, 205–225.

De Swardt, A. M. J., Garrard, P., and Simpson, J. G. (1965). Major zones of transcurrent dislocation and super-position of orogenic belts in part of central Africa. *Geol. Soc. Am. Bull.*, **76**, 89–102.

deGroot Hedlin, C. and Constable, S. (1990). Occam's inversion to generate smooth, two-dimensional models from magnetotelluric data. *Geophys.*, **55**, 1613–1624.

Drury, M. J. and Hyndman, R. D. (1979). Electrical resistivity of oceanic basalts. *J. Geophys. Res.*, **84**, 4537–4546.

Efron, B. (1982). *The Jacknife, the Bootstrap, and Other Resampling Plans*. Society for Industrial and Applied Mathematics, Philadelphia.

Egbert, G. D. and Booker, J. R. (1986). Robust estimation of geomagnetic transfer functions. *Geophys. J. R. astr. Soc.*, **87**, 173–194.

Egbert, G. D. and Livelybrooks, D. W. (1996). Single station magnetotelluric impedance estimation: coherence weighting and the regression M-estimate. *Geophys.*, **61**(4), 964–970.

Eggers, D. E. (1982). An eigenstate formulation of the magnetotelluric impedance tensor. *Geophys.*, **47**(8), 1204–1214.

Fischer, G. and Masero, W. (1994). Rotational properties of the magnetotelluric impedance tensor: the example of the Araguainha impact crater, Brazil. *Geophys. J. Int.*, **119**, 548–560.

Gamble, T. D., Goubau, W. M., and Clarke, J. (1979). Magnetotellurics with a remote reference. *Geophys.*, **44**, 53–68.

Gough, D. I. (1974). Electrical conductivity under western North America, in relation to heat flow, seismology and structure. *J. Geomagn. Geoelect., Kyoto*, **26**, 105–123.

Graybill, F. A. (1976). *Theory and Application of the Linear Model*. Duxbury Press.

Groom, R. W. and Bahr, K. (1992). Corrections for near surface effects: decomposition of the magnetotelluric impedance tensor and scaling corrections for regional resistivities: a tutorial. *Surveys in Geophys.*, **13**, 341–379.

Groom, R. W. and Bailey, R. C. (1989). Decomposition of magnetotelluric impedance tensors in the presence of local three-dimensional galvanic distortion. *J. Geophys. Res.*, **93**, 1913–1925.

Groom, R. W. and Bailey, R. C. (1991). Analytic investigations of the effects of near-surface three-dimensional galvanic scatterers on MT tensor decompositions. *Geophys.*, **56**(4), 496–518.

Haak, V. and Hutton, R. (1986). Electrical resistivity in continental lower crust. In J. B. Dawson, D. A. Carswell, J. Hall, and K. H. Wedepohl, editors, *The Nature of the Lower Continental Crust*, number 24 in Geological Society Special Publications, pages 35–49. Blackwell Scientific Publications.

Habashy, T. M., Groom, R. W., and Spies, B. R. (1993). Beyond the Born and Rytov approximations: a nonlinear approach to electromagnetic scattering. *J. Geophys. Res.*, **98**(B2), 1759–1775.

Hiller, K. and Buttkus, B. (1996). Structural style and sedimentary thicknesses in the Zambezi rift valley, Zimbabwe - investigations of the potential for hydrocarbons. *Z. angew. Geol.*, **42**(2), 132–137.

Hobbs, B. A. (1992). Terminology and symbols for use in studies of electromagnetic induction in the Earth. *Surveys in Geophys.*, **13**, 489–515.

Hohmann, G. W. (1975). Three-dimensional induced polarization and electromagnetic modeling. *Geophys.*, **40**, 309–324.

Huber, P. J. (1981). *Robust Statistics*. John Wiley, New York.

Jiracek, G. R. (1990). Near-surface and topographic distortion in electromagnetic induction. *Surveys in Geophys.*, **11**, 163–203.

Jones, A. G. (1983). The problem of current channelling: a critical review. *Geophys. Surveys*, **6**, 79–122.

Jones, A. G. (1988). Static shift of magnetotelluric data and its removal in a sedimentary basin environment. *Geophys.*, **53**(7), 967–978.

Jones, A. G. and Groom, R. W. (1993). Strike-angle determination from the magnetotelluric impedance tensor in the presence of noise and local distortion: rotate at your peril! *Geophys. J. Int.*, **113**, 524–534.

Kaufman, A. A. (1985). Tutorial: distribution of alternating electrical charges in a conducting medium. *Geophys. Prospecting*, **33**, 171–184.

Kaufman, A. A. and Keller, G. V. (1981). *The Magnetotelluric Sounding Method*. Number 15 in Methods in Geochemistry and Geophysics. Elsevier Scientific Publishing.

Kellett, R. L., Mareschal, M., and Kurtz, R. D. (1992). A model of lower crustal electrical anisotropy for the Pontiac subprovince of the Canadian shield. *Geophys. J. Int.*, **111**, 141–150.

La Torraca, G. A., Madden, T. R., and Korringa, J. (1986). An analysis of the magnetotelluric impedance for three-dimensional conductivity structures. *Geophys.*, **51**(9), 1819–1829.

Lambiase, J. J. (1989). The framework of African rifting during the Phanerozoic. *J. Afr. Earth Sci.*, **8**(2-4), 183–190.

Larsen, J. C. (1989). Transfer functions: smooth robust estimates by least-squares and remote reference methods. *Geophys. J. Int.*, **99**(3), 645–663.

Larsen, J. C., Mackie, R. L., Manzella, A., Fiordelisi, A., and Rieven, S. (1996). Robust smooth magnetotelluric transfer-functions. *Geophys. J. Int.*, **124**(3), 801–819.

Lilley, F. E. M. (1976). Diagrams for magnetotelluric data. *Geophys.*, **41**(4), 766–770.

Lilley, F. E. M. (1993a). Magnetotelluric analysis using mohr circles. *Geophys.*, **58**(10), 1498–1506.

Lilley, F. E. M. (1993b). Mohr circles in magnetotelluric interpretation (i) simple static shift; (ii) Bahr's analysis. *J. Geomag. Geoelectr.*, **45**, 833–839.

Livelybrooks, D., Banks, R. J., Parr, R. S., and Hutton, V. R. S. (1993). Inversion of electromagnetic induction data for the Iapetus suture zone in the UK. *Phys. Earth Planet. Interiors*, **81**, 67–84.

Losecke, W., Knodel, K., and Muller, W. (1988). Magnetotelluric survey in the northern Zambezi valley of Zimbabwe. Technical Report 84.2171.1, Bundesanstalt für Geowissenschaften und Rohstoffe, Hanover.

Lynn, P. A. (1989). *An Introduction to the Analysis and Processing of Signals.* Hemisphere Publishing Corporation, 3rd edition.

Mackie, R. L., Madden, T. R., and Wannamaker, P. E. (1993). Three-dimensional magnetotelluric modeling using difference equations- theory and comparisons to integral equation solutions. *Geophys.*, **58**(2), 215–226.

Madden, T. and Nelson, P. (1964). A defense of Cagniard's magnetotelluric method. In K. Vozoff, editor, *Magnetotelluric Methods*, number 5 in Geophysics Reprints, pages 89–102. Society of Exploration Geophysicists.

Mann, P., Hempton, M. R., Bradley, D. C., and Burke, K. (1983). Development of pull-apart basins. *J. Geol*, **91**, 529–554.

Martin, A. K. and Hartnady, C. J. H. (1986). Plate tectonic development of the south west Indian ocean: a revised reconstruction of east Antarctica and Africa. *J. Geophys. Res.*, pages 4767–4786.

Martin, H. (1983). Alternative geodynamic models for the Damara orogeny. A critical discussion. In H. Martin and F. W. Eder, editors, *Intracontinental Fold Belts*, pages 913–945. Springer-Verlag Berlin Heidelberg.

Martin, H. and Porada, H. (1977). The intracratonic branch of the Damara orogen in South-West Africa. I. Discussion of geodynamic models. *Precamb. Res.*, **5**, 311–338.

McKenzie, D. (1978). Some remarks on the development of sedimentary basins. *Earth Planet. Sci. Lett.*, **40**, 25–32.

Meju, M. A. (1994). *Geophysical Data Analysis: Understanding Inverse Problem Theory and Practice*, volume 6 of *Course Notes Series*. Society of Exploration Geophysicists.

Menke, W. (1984). *Geophysical Data Analysis: Discrete Inverse Theory*. Academic Press, Orlando.

Miller, R. M. (1979). The Okahanja lineament, a fundamental tectonic boundary in the Damara orogen of South West Africa/Namibia. *Trans. geol. Soc. S. Afr.*, **82**, 349–361.

MOBIL (1993). Republic of Zimbabwe, hydrocarbon exploration areas I-IV Cabora Bassa, Mana Pools and Mid-Zambezi basins. Initial Exploration Phase. Final Report, Mobil Exploration Zimbabwe Incorporated.

O'Brien, D. P. and Morrison, H. F. (1967). Electromagnetic fields in an n-layer anisotropic half space. *Geophys.*, **32**, 668–677.

Orpen, J. L., Swain, C. J., Nugent, C., and Zhou, P. P. (1989). Wrench-fault and half-graben tectonics in the development of the Palaeozoic Zambezi Karoo basins in Zimbabwe - the Lower Zambezi and Mid-Zambezi basins respectively - and regional implications. *J. Afr. Earth Sci.*, **8**, 215–229.

Pain, H. J. (1993). *The Physics of Vibrations and Waves*. John Wiley and Sons Ltd, 4 edition.

Park, S. K. (1989). Quantitative interpretation of rotationally invariant parameters in magnetotellurics. *Geophys.*, **54**(11), 1483–1490.

Park, S. K., Hirasuna, B., Jiracek, G. R., and Kinn, C. (1996). Magnetotelluric evidence of lithospheric mantle thinning beneath the southern Sierra Nevada. *J. Geophys. Res.*, **101**(B7), 16241–16255.

Parker, R. L. (1980). The inverse problem of electromagnetic induction: Existence and construction of solutions based on incomplete data. *J. Geophys. Res.*, **85**(B8), 4421–4428.

Parker, R. L. (1982). The existence of a region inaccessible to magnetotelluric sounding. *Geophys. J. R. atr. Soc.*, **68**, 165–170.

Parker, R. L. (1994). *Geophysical Inverse Theory*. Princeton University Press, Chichester, West Sussex.

Parker, R. L. and Booker, J. R. (1996). Optimal one-dimensional inversion and bounding of magnetotelluric apparent resistivity and phase measurements. *Phys. Earth Planet. Interiors*, **98**, 269–282.

Parker, R. L. and Whaler, K. A. (1981). Numerical methods for establishing solutions to the inverse problem of electromagnetic induction. *J. Geophys. Res.*, **86**(B10), 9574–9584.

Parkinson, W. D. (1959). Directions of rapid geomagnetic fluctuations. *Geophys. J. R. astr. Soc.*, **2**(1), 1–14.

Parkinson, W. D. (1962). The influence of continents and oceans on geomagnetic variations. *Geophys. J. R. astr. Soc.*, **6**, 441449.

Percival, D. B. and Walden, A. T. (1993). *Spectral Analysis for Physical Applications. Multitaper and Conventional Univariate Techniques.* Cambridge University Press.

Price, A. T. (1962). The theory of magnetotelluric methods when the source field is considered. In K. Vozoff, editor, *Magnetotelluric Methods*, number 5 in Geophysics Reprints, pages 44–55. Society of Exploration Geophysicists.

Price, A. T. (1973). The theory of geomagnetic induction. *Phys. Earth Planet. Interiors*, **7**, 227–233.

Ranganai, R. T. (1995). *Geophysical Investigations of the Granite-Greenstone Terrain in the South-Central Zimbabwe Archaean Craton*. Ph.D. thesis, The University of Leeds.

Reeves, C. V. (1972). Rifting in the Kalahari? *Nature*, **237**, 95–96.

Ritter, O. (1995). *An Audiomagnetotelluric Investigation of the Southern Upland Fault: Novel Instrumentation, Field Procedures and 3D Modelling*. Ph.D. thesis, University of Edinburgh.

Rokityanski, I. I. (1961). On the application of the magnetotelluric method to anisotropic and inhomogeneous masses. In K. Vozoff, editor, *Magnetotelluric Methods*, number 5 in Geophysics reprints, pages 143–147. Society of Exploration Geophysicists.

Rosendahl, B. R., Reynolds, D. J., Lorber, P. M., Burgess, C. F., McGill, J., Scott, D., Lambiase, J. J., and Derksen, S. E. (1986). Structural expressions of rift: lessons from lake Tanganika, Africa. sedimentation in the African rifts. *Geol. Soc. London, Sp. Pub.*, **25**, 29–43.

Schnegg, P. A. (1996). Comparison of 2-D modelling methods: rapid inversion vs. polynomial fitting. *Kolloquium Elektromagnetische Tiefenforschung.*, **16**, 74–79.

Sims, W. E., Bostick, F. X., Smith, J. R., and Smith, H. W. (1971). The estimation of magnetotelluric impedance tensor elements from measured data. *Geophys.*, **36**, 938–942.

Smith, J. T. and Booker, J. R. (1988). Magnetotelluric inversion for minimum structure. *Geophys.*, **53**(12), 1565–1576.

Smith, J. T. and Booker, J. R. (1991). Rapid inversion of two- and three-dimensional magnetotelluric data. *J. Geophys. Res.*, **96**(B3), 3905–3922.

Spitz, S. (1985). The magnetotelluric impedance tensor properties with respect to rotations. *Geophys.*, **50**(10), 1610–1617.

Stesky, R. M. and Brace, W. F. (1973). Electrical conductivity of serpentinized rocks to 6 kilobars. *J. Geophys. Res.*, **78**, 7614–7621.

Strangway, D. W., Swift, C. M., and Holmer, . C. (1973). The application of audiofrequency magnetotellurics (AMT) to mineral exploration. *Geophys.*, **38**, 1159–1175.

Sutarno, D. and Vozoff, K. (1991). Phase-smoothed robust M-estimation of magnetotelluric impedance functions. *Geophys.*, **56**(12), 1999–2007.

Swift, C. M. (1967). A magnetotelluric investigation of an electrical conductivity anomaly in the southwestern United States. In K. Vozoff, editor, *Magnetotelluric Methods*, number 5 in Geophysics Reprints, pages 156–166. Society of Exploration Geophysicists.

Sykes, L. R. (1978). Intraplate seismicity, reactivation of pre-existing zones of weakness, alkaline magmatism and other tectonism postdating continental fragmentation. *Rev. Geophys. Space Phys.*, **16**, 621–688.

Szarka, L. and Menvielle, M. (1997). Analysis of rotational invariants of the magnetotelluric impedance tensor. *Geophys. J. Int.*, **129**(1), 133–142.

Telford, W. M., Geldart, L. P., and Sheriff, R. (1990). *Applied Geophysics*. Cambridge University Press, 2 edition.

Thomson, D. J. (1982). Spectrum estimation and harmonic analysis. *Proceedings of the IEEE*, **70**(9), 1055–1096.

Thomson, D. J. and Chave, A. D. (1989). Jacknife error estimates for spectra, coherences, and transfer functions. In S. Haykin, editor, *Advances in Spectral Analysis and Array Processing*. Prentice-Hall, Englewood Cliffs, NJ.

Tikhonov, A. N. (1950). On determining electrical characteristics of the deep layers of the Earth's crust. In K. Vozoff, editor, *Magnetotelluric Methods*, number 5 in Geophysics Reprints, pages 295–297. Society of Exploration Geophysicists.

Travassos, J. M. and Beamish, D. (1988). Magnetotelluric data processing - a case study. *Geophys. J.*, **93**(2), 377–391.

Van Zijl, J. S. V. (1977). Electrical studies of the deep crust in various tectonic provinces of southern Africa. In J. G. Heacock, editor, *The Earth's Crust*, volume 20 of *Monogr. Am. geophys. Un.*, pages 470–500.

Van Zijl, J. S. V. (1978). The relationship between the deep electrical resistivity structure and tectonic provinces in southern Africa. part i. results obtained by Schlumberger soundings. *Trans. geol. Soc. S. Afr.*, **81**, 129–142.

Van Zijl, J. S. V. and De Beer, J. H. (1983). Electrical structure of the Damara orogen and it's tectonic significance. *Special Publication of the Geological Society Of South Africa.*, **11**, 369–379.

Vozoff, K. (1972). The magnetotelluric method in the exploration of sedimentary basins. *Geophys.*, **37**, 98–141.

Wait, J. R. (1954). On the relation between telluric currents and the Earth's magnetic field. In K. Vozoff, editor, *Magnetotelluric Methods*, number 5 in Geophysics Reprints, pages 35–43. Society of Exploration Geophysicists.

Wait, J. R. (1962). Theory of magneto-telluric fields. In K. Vozoff, editor, *Magnetotelluric Methods*, number 5 in Geophysics Reprints, pages 56–88. Society of Exploration geophysicists.

Wannamaker, P. E., Stodt, J. A., and Rijo, L. (1987). A stable finite-element solution for two-dimensional magnetotelluric modeling. *Geophys. J. Roy. Astr. Soc.*, **88**, 277–296.

Weidelt, P. (1972). The inverse problem of geomagnetic induction. *Z. Geophys.*, **38**, 257–289.

Weidelt, P. (1975). Electromagnetic induction in three-dimensional structures. *J. Geophys.*, **41**, 85–109.

Weidelt, P. and Kaikkonen, P. (1994). Local 1-D interpretation of magnetotelluric B-polarization impedances. *Geophys. J. Int.*, **117**, 733–748.

Whaler, K. A. and Zengeni, T. G. (1993). An audiofrequency magnetotelluric traverse across the Mana Pool Basin, northern Zimbabwe. *Geophys. J. Int.*, **114**, 673–686.

Wight, D. E. and Bostick, F. X. (1986). Cascade decimation - a technique for real time estimation of power spectra. In K. Vozoff, editor, *Magnetotelluric Methods*, number 5 in Geophysics Reprints, pages 215–218. Society of Exploration Geophysicists.

Windley, B. F. (1995). *The Evolving Continents*. John Wiley and Sons, Chichester, 3rd edition edition.

Yee, E. and Paulson, K. V. (1987). The canonical decomposition and its relationship to other forms of magnetotelluric impedance tensor analysis. *J. Geophys.*, **61**, 173–189.

Zhang, P., Roberts, R. G., and Pedersen, L. B. (1987). Magnetotelluric strike rules. *Geophys.*, **52**(3), 267–278.

Zhang, P., Pedersen, L. B., Mareschal, M., and Choteau, M. (1993). Channelling contribution to tipper vectors: a magnetic equivalent to electrical distortion. *Geophys. J. Int.*, **113**, 693–700.

Zhou, P. P. (1988). The gravity survey of the Zambezi valley east of Chirundu. Technical report, Zimbabwe Geological Survey, Harare.